

**Imperial College
London**

DEPARTMENT OF BIOENGINEERING

**Information-theoretic investigation of
multi-unit activity properties under
different stimulus conditions in mouse
primary visual cortex**

L. MARIE F. TOLKIEHN

of Hamburg, Germany

September 2017

Submitted in partial fulfilment of the requirements for the degree of
Doctor of Philosophy in Bioengineering of Imperial College London
and the Diploma of Imperial College London

Copyright Declaration

The copyright of this thesis rests with the author and is made available under a Creative Commons Attribution Non-Commercial No Derivatives licence. Researchers are free to copy, distribute or transmit the thesis on the condition that they attribute it, that they do not use it for commercial purposes and that they do not alter, transform or build upon it. For any reuse or redistribution, researchers must make clear to others the licence terms of this work.

Declaration of Originality

I hereby declare that this thesis and all the work therein are my own original research and my own work and that, to the best of my knowledge, it neither contains material previously published or written by another person or myself, nor material which to a substantial extent has been accepted for the award of any other unit, except where due acknowledgement is made in the text. Only, a subset of the behavioural experiments and training in Chapter 4 was performed by Aleksandra Berditchevskaia (AB), which is clearly indicated throughout. I also declare that the intellectual content of this thesis is the product of my own work, except to the extent that assistance from others in the project's design or in style and linguistic expression is acknowledged. Any concepts, ideas, methods or data which I did not develop myself are duly cited and a list of references given in the bibliography.

Marie Tolkiehn

Abstract

MARIE TOLKIEHN: Information-theoretic investigation of multi-unit activity properties under different stimulus conditions in mouse primary visual cortex (Under the direction of Dr. Claudia Clopath and Dr. Simon Schultz)

Primary visual cortex (V1) is the first cortical processing level receiving topographically mapped inputs from the retina, relayed through thalamus. Electrophysiological studies discovered its important role in early sensory processing particularly in edge detection in single cells. To this end, little is investigated how these activities relate on a population level. Orientation tuning in mouse V1 has long been reported as salt-and-pepper organised, lacking apparent structure as was found in e.g. cat or primates.

This is a novel synthesis of specially designed in-vivo electrophysiological experiments aiming to make certain information-theoretic data analysis approaches viable. Sophisticated state-of-the-art data analysis techniques are applied to answer questions about stimulus information in mouse V1. Multi-unit electrophysiological experiments were devised, performed and evaluated in the anaesthetised and in left hemisphere V1 of the awake behaving, head-fixed mouse. A detailed laboratory and computational analysis is presented validating the use of Multi-Unit-Activity (MUA) and information-theoretic measures. Our results indicate left forward drifting gratings (moving from the temporal to nasal visual field) elicit consistently highest neuronal responses across cortical layers and columns, challenging the common understanding of random organisation. These directional biases of MUA were also observable on the population level.

In addition to individual multi-unit analyses, population responses in terms of binary word distributions appear more similar between spontaneous activity and responses to natural movies than either/both to moving gratings, suggesting that mouse V1 processes natural scenes differently from sinusoidal drifting gratings. Response pattern distributions for different gratings emerge to be spatially but not orientationally clustered. Further computational analysis suggests population firing rates can partially account for these differences. Electrophysiological experiments in the awake behaving mouse indicate V1 to contain information about behavioural outcome in a GO/NOGO task. This, along with other statistical measures is examined with statistical models such as the population tracking model, which suggest that population interactions are required to explain these observations.

Preface

The work described in this thesis was performed between September 2013 and September 2017 in the Schultz Lab, Department of Bioengineering, Imperial College London.

One poster including an abstract containing parts of the methodology and preliminary results of Chapter 2 was accepted for publication in the proceedings of the Society for Neuroscience Conference held in Chicago, IL, USA in October 2015, with the title "Decoding grating spatial frequency and direction from Multi- Unit-Activity in mouse visual cortex" by MARIE TOLKIEHN, Simon Schultz. Their collaboration included initial academic advice and proofreading the abstract.

A second poster and abstract containing preliminary results of Chapter 4 was accepted for publication in the proceedings of the Society for Neuroscience Conference held in San Diego, CA, USA in November 2016, with the title "The entropy of neural ensemble firing patterns in mouse primary visual cortex correlates with behavioural performance" by MARIE TOLKIEHN, Aleksandra Berditchevskaia, Simon Schultz. Their collaboration included initial academic advice (SS), support in data collection (AB) and proofreading of the abstract (SS).

A four-page publication and subsequent oral presentation at the conference containing parts of the methodology and results of Chapter 2 was accepted for publication in the proceedings of the Annual International Conference of the IEEE Engineering in Medicine and Biology Society, EMBS, in Milano, Italy in August 2015, with the title "Multi-Unit Activity contains information about spatial stimulus structure in mouse primary visual cortex" by MARIE TOLKIEHN, Simon Schultz (Vol. 2015-Novem, pp. 3771–3774). <http://doi.org/10.1109/EMBC.2015.7319214>. Their collaboration included initial academic advice, and proofreading the manuscript.

Acknowledgements

"Sabbel nich', dat geit!"

Saying, Hamburg

It is a pleasure for me to thank those who supported me throughout the completion of this thesis. I am grateful for all the things I have learnt, both academically and otherwise. This work would not have been possible without the Department of Bioengineering PhD scholarship.

I am thankful to my supervisor, Dr. Simon Schultz, whose confidence in me led me to become an independent researcher. Thanks to the entire Schultz lab, especially to Sarah Jarvis, Caroline Copeland, Silvia C. Ardila Jimenéz, and Tomaso Muzzu. Further thanks Susanna Mitolo, Stefania Garasto, Renaud Schuck, Aleksandra Berditchevskaia, Ann Go and Romain Cazé.

In addition, I would like to thank my co-supervisor, Dr. Claudia Clopath, particularly for adopting me at a late stage of my PhD. Thanks to the legendary Clopath lab, especially to Dr. Katharina Wilmes, and Wilten Nicola for making me walk the extra mile ("Marie, we're South Kensington!").

A sincere and whistling thanks to Dr. Paul Chadderton and the whole Chadderton lab, past and present, for all their support and encouragements. Paul, thank you for giving me your equipment when all of mine failed. And Joseph Sollini: huge thanks for your support during write-up! Thanks and hugs also to Susu Chen, Alex *Redfern* Morris and Matt TC Brown. Go raibh maith agat Caroline Golden! All groups: Thanks for countless hours of discussions, advice, and laughter. Thanks for lunch, coffee, hops and hugs (or elbow-rubs).

I would also like to take this opportunity to thank my examiners Dr. Cian O'Donnell and Dr. Tobias Reichenbach for their valuable comments and discussions. Further, I owe gratitude to my cohort mentor Prof. Holger Krapp for his managerial advice, and to the Director of Postgraduate Studies, Dr. Anil Bharath, for his insights during write-up. Thanks to Dr. Friedrich Sommer of UC Berkeley for his academic advice at various stages. I also very much appreciate the Drakakis and Tanaka labs for always happily adopting me on their premises. Thanks Graham Peyton, Hamid Soleimani, and Paolo Cadinu (it is happening!).

Größten herzlichsten Dank an Britta Ross for all her help, advice and positive thoughts! A great thanks to the administrative and teaching staff of the Bioengineering Department. Thanks to the whole past Bessemer 438 research office - our home until the Hamlyn Centre annexed it.

I want to express my gratitude to my 53 Averill Street PhD family: Gaëlle Chapuis, Martina Fonseca, and Ana and Jonathan Ball. Pineapples forever!

I am also indebted to many of my friends and colleagues who walked this path with me: Octave Etard, Ariadne Whitby, Andreas Thomik, Martin Ebner, James McIntosh, Luke Bashford, and the exceptional Cypriot: Harris Konnaris. Big shout to my RSD wolf pack: Davide Moia (I have the ball!), fantastic ~~Mr. Fox~~ Ilan Grossman, Ben Zelenay and the wonderful Markéta Kubánková. We did it! My final year also would not have been the same without the ever-bickering Panayiotis Christodoulides and Georgios Zafeiropoulos.

Above all, thanks to Dr. Ed Johns for proofreading my acknowledgements section and offering valuable suggestions, such as thanking himself.

Thanks to all the wonderful friends who provided me with food and/or shelter while I was homeless in London. And thanks to all the other people I have not personally listed here.

I am happy about all the moral support by my friends from Hamburg. Thanks for being there Pauline Schulz, Andreas Schulze, Andreas Hörstel, Felix Wenzel. Danke an die Superfreunde VII: Mads Rohde, Christoph Antonczyk, Tjard Pröfrock, Flip and Mariechen Albright, Martje Friedrich, Rona ~~Pätzold~~ Jung, Isabel Schommburg und Joey Blümel. Und Eva und Yoko. Ευχαριστω Dr. Melina Vogiatzi and Dr. Steffen Tiedt for hosting me so many good times!

Further, my sweets drawer, lemon poppyseed muffins, coffee and my ukulele played crucial parts in the completion of my thesis.

Finally, and most importantly, I would like to thank my family:

Vielen allerherzlichsten Dank Mama und Papa! Ohne eure Unterstützung und Aufmunterungen hätte ich vielleicht irgendwann aufgegeben. Danke auch an den Rest meiner wundervollen, buckligen Verwandtschaft. Jan und Kiki, Niels und Julia, Fritzchen, Tina, Marion, Maxi, Tomas, Julia W. und Annika. Unvergessen sind auch Oma Lilo, Oma Gertrud und Opa Uli, und Tante Mücke, die mich immer unterstützt und an mich geglaubt haben.

Dedication

Für meine Eltern.

Contents

1	Introduction	1
1.1	Overview	1
1.2	The mouse visual system	3
1.3	Learning and sensory processing in primary visual cortex	7
1.4	Decision-making	9
1.5	Multi-Unit-Activity as a methodological choice	11
1.6	Information-theoretic concepts	13
1.6.1	Shannon entropy	13
1.6.2	Mutual Information	16
2	Multi-Unit Activity contains information about stimulus structure in mouse V1	17
2.1	Introduction	17
2.2	Methodology - surgeries and animal preparation	18
2.2.1	Anaesthetics and drugs	19
2.2.2	Surgical procedures	19
2.2.3	Electrophysiology rig	21
2.2.4	Stimuli and data acquisition	22
2.3	Analysis methods	24
2.3.1	MUA analysis and processing	24
2.3.2	Multi-Unit tuning properties	25
2.3.3	Decoding, feature detection and performance measures	27
2.4	Results	30
2.4.1	Visual responses to both gratings and natural movies were observed using MUA recordings	30
2.4.2	Tuning to moving gratings of different directions and spatial frequencies in V1	31
2.4.3	Spatial frequency tuning in V1 shows bandpass and low-pass properties	32
2.4.4	Direction tuning in left V1 is biased towards leftward moving gratings	34
2.4.5	Tuning in V1 is highly correlated between sites	36
2.4.6	Direction tuning depends on spatial frequencies	40
2.4.7	High performance in spatial frequency and direction decoding from MUA	43
2.5	Discussion and conclusions	45
3	Distinct stimuli sample from different binary pattern distributions	51
3.1	Introduction	51

3.2	Methodology and concepts	54
3.2.1	Spatial patterns	54
3.2.2	Kullback-Leibler Divergence (KLD)	54
3.2.3	Jensen-Shannon Divergence (JSD)	55
3.2.4	Multidimensional Scaling	56
3.3	Results	57
3.3.1	Stimulus types influence activity levels and numbers of uniquely evoked patterns	57
3.3.2	Neural ensemble spatial pattern entropy weakly resembles MUA tuning functions	61
3.3.3	Mutual Information between neural activity and stimuli	62
3.3.4	Pattern probabilities evoked by natural movies and spontaneous activity resemble each other more than either moving gratings	65
3.3.5	Spatial frequencies are clustered in pattern space	70
3.4	Discussion and conclusions	72
4	Mouse V1 contains information about behavioural outcome in a visual discrimination task	79
4.1	Introduction	79
4.2	Materials, procedures and methods	81
4.2.1	Behavioural visual discrimination task and set-up	81
4.2.2	Surgical and electrophysiological procedures	84
4.2.3	Hardware and software specifications	90
4.2.4	Behavioural training protocol and habituation	92
4.2.5	Performance markers and signal detection theory	95
4.3	Results	97
4.3.1	Training protocol affects learning speed	98
4.3.2	Behaviour summaries of electrophysiological recordings	102
4.3.3	Mean firing rates differ between gratings, outcomes and experimenters	103
4.3.4	Mutual Information indicates behavioural correlate in V1	108
4.3.5	JSD between outcomes differs between experimenters	111
4.3.6	High Mutual Information between shanks indicates cross-columnar co-activation	114
4.4	Discussion and conclusions	115
5	Population interactions are required to emulate observations of GO/NOGO data	123
5.1	Introduction	123
5.2	Methods - computational models	126
5.2.1	Independent model	126
5.2.2	Energy-Based-Models	126
5.2.3	Population tracking model	129

5.2.4	Homogeneous Poisson surrogate data	130
5.2.5	Modelling parameter details and model evaluation measures . . .	130
5.3	Results	132
5.3.1	Evaluation of entropy estimators with surrogate homogeneous Poisson spiking data	133
5.3.2	Homogeneous Poisson data fails to match features observed in empirical data	134
5.3.3	Loglikelihood gain and RMSE imply pairwise interactions are cru- cial	138
5.3.4	Models successfully approximate empirical pattern probabilities .	143
5.3.5	Ising coupling matrices indicate consistent laminar connections .	145
5.4	Discussion and conclusions	145
6	Conclusions and outlook	151
6.1	Summary	151
6.2	Shortcomings	153
6.3	Future work	153
	Bibliography	155
	Appendices	175
1	Statistical Tests	175
2	Supplementary figures of 2	176
2.1	Direction decoding performances of different decoders as a func- tion of bin size and number of shanks	176
2.2	Spatial frequency decoding performances of different decoders as a function of bin size and number of shanks	179
3	Supplementary figures of Chapter 3	182
4	Dosage calculation table	183
5	Copyright permissions	184

List of Figures

1.1	Orientation selectivity maps	6
2.1	Stimulus presentation structure.	23
2.2	Grating stimuli with increasing Spatial Frequency (SF).	24
2.3	Decoding features	29
2.4	Visually evoked responses vary for stimuli.	31
2.5	Response patterns vary between moving gratings and natural movies.	32
2.6	Multi-Units (MU) show strong Firing Rate (FR) modulations for both directions and SF.	33
2.7	SF peak and cutoff distributions.	34
2.8	Preferred direction is not uniformly distributed.	35
2.9	Direction tuning depends on SF.	37
2.10	Signal correlation is high for directional tuning.	38
2.11	SF tuning is very similar across sites.	39
2.12	SF signal correlation is high, and noise correlations centred around zero.	40
2.13	Direction tuning depends on the mixture of SFs.	41
2.14	Maximum and minimum FR affected by SF.	42
2.15	FR mode at each SF.	43
2.16	Good predictions for SFs and high performance on all direction predictions.	44
3.1	Number of patterns differs for different stimuli	58
3.2	Number of patterns per sample correlates with mean population firing rate	60
3.3	Pattern entropies resemble mean population firing rate across all stimuli and also seem to weakly qualitatively approximate the tuning curves.	65
3.4	Empirical pattern probabilities vary under different stimulus conditions for 16-bit spatial patterns.	66
3.5	FR difference and JSD are correlated.	68
3.6	Stimulus types probability distributions reside in different pattern subspaces.	69
3.7	Pattern distributions conditioned on all stimuli appear clustered for spatial frequencies, and less structured for directions	71
4.1	Behavioural task description.	82
4.2	Behaviour grating stimuli.	83
4.3	Head-fixed mouse ready for training.	92
4.4	The meaning of d' in Signal Detection Theory (SDT) and Receiver Operating Characteristic (ROC) space.	96
4.5	Behavioural progress indicates ten days to learn the task.	99
4.6	Behavioural progress over sessions, experimenter AB.	101
4.7	Mean FR between stimulation conditions.	104

4.8	Mean FR between outcome conditions.	105
4.9	Average PSTH reveals differences in FR time course.	106
4.10	PSTH at high accuracy differs vastly from low.	107
4.11	MI between neural response and behavioural outcomes is non-zero . . .	109
4.12	Median MI as a function of bin size and number of shanks.	110
4.13	JSD between response types at 8 bit patterns.	112
4.14	JSD differs between experimenters at 16-bit patterns.	113
4.15	High MI between signals and shanks.	114
5.1	EBM connection schematics.	128
5.2	Fractional bias as function of sample size.	134
5.3	Entropy of homogeneous Poisson exceeds that of empirical.	136
5.4	MI on surrogate data is larger than empirical data.	137
5.5	Poisson surrogate MI between shanks matches data MI.	138
5.6	JSD of data exceeds surrogate data.	139
5.7	Loglikelihood gains over independent model.	140
5.8	Model success depends on training and test subsets.	142
5.9	Pattern probability scatter plots between all models and p_{emp}	143
5.10	Example pattern probability scatters between models and p_{emp}	144
5.11	Ising coupling matrices for six example mice.	146
1	Direction decoding, NB classifier.	177
2	Direction decoding, knn classifier.	177
3	Direction decoding, classification tree classifier.	178
4	Direction decoding, LDA classifier.	178
5	SF decoding, NB classifier.	179
6	SF decoding, knn classifier.	180
7	SF decoding, classification tree classifier.	180
8	SF decoding, LDA classifier.	181
9	All graphs.	182

List of Abbreviations

AB	Aleksandra Berditchevskaia.
ACC	Anterior Cingulate Cortex.
acc	accuracy.
AIS	Annealed Importance Sampling.
ANCOVA	Analysis of covariance.
ANOVA	Analysis of Variance.
BMI	Brain Machine Interfaces.
CDF	Cumulative Distribution Function.
CDM	Centred-Dirichlet-Mixture.
cpd	cycles per degree.
CR	Correct Rejection, true negative, <i>Glossary</i> : CR.
DIR	Direction.
DoG	Difference of Gaussian.
DSI	Direction Selectivity Index.
EBM	Energy-Based-Model.
FA	False Alarm, false positive, <i>Glossary</i> : False Alarm.
FN	False Negative.
FP	False Positive.
FPR	False Positive Rate, or False Alarm Rate.
FR	Firing Rate.
IND	Independent model.
ITI	Inter-Trial-Interval.
JSD	Jensen-Shannon-Divergence.

List of Abbreviations

KLD	Kullback-Leibler Divergence.
knn	k-nearest neighbour.
LDA	Linear Discriminant Analysis.
LFP	Local Field Potential.
LGN	Lateral Geniculate Nucleus.
LTD	Long-Term Depression.
LTP	Long-Term Potentiation.
MAP	Maximum A Posteriori.
MDS	Multi-Dimensional Scaling.
mG	moving Gratings.
MI	Mutual Information.
MPF	Minimum Probability Flow.
mPFC	medial Prefrontal Cortex.
MT	Marie Tolkiehn.
MU	Multi-Units.
MUA	Multi-Unit-Activity.
MWU	Mann-Whitney-U test.
nat	natural movie.
NB	Naive Bayes.
NSB	Nemenman-Shafee-Bialek.
OSI	Orientation Selectivity Index.
PBS	Phosphate Buffered Saline.
PFA	Paraformaldehyde.
PSTH	Peri-Stimulus Time Histogram.
PYM	Pitman-Yor-Mixture.

- RBM** Restricted Boltzmann Machine.
- RMSE** Root Mean Square Error.
- ROC** Receiver Operating Characteristic.
- S1** Spontaneous Activity 1.
- S2** Spontaneous Activity 2.
- S3** Spontaneous Activity 3.
- SA** Spontaneous Activity.
- SC** Spike Count.
- SDT** Signal Detection Theory.
- SEM** Standard Error of the Mean.
- sem** standard error of the mean.
- SF** Spatial Frequency.
- sRBM** semi-Restricted Boltzmann Machine.
- SRP** Stimulus-selective Response Potentiation.
- STMUA** Spatio-temporal Multi-Unit Activity.
- SUA** Single Unit Activity.
- TF** Temporal Frequency.
- TN** True Negative.
- TNR** True Negative Rate.
- TP** True Positive.
- TPR** True Positive Rate, or Hit Rate.
- V1** Primary Visual Cortex.
- VEP** Visually Evoked Potentials.

Nomenclature

CR Correct Rejection, True Negative. The mouse successfully withheld the lick until the end of the stimulus presentation, 2s after onset. No reward or punishment was given and the trial ended after the Inter-Trial-Interval (ITI) .

False Alarm False Positive. The mouse incorrectly licked before the stimulus was turned off. The lick triggered a short air puff and a change of stimulus to a black screen. The combination of the air puff and the 5 s long full-field visual stimulus served as negative reinforcement. After this, the trial ended after the ITI .

HIT True Positive. The mouse licked when the positive stimulus was presented. A water reward was triggered by the lick, and was available during a 1.75 s window. During this time the animal was free to drink without restrictions while the stimulus was presented continuously. After this, the trial ended with the ITI .

MISS False Negative. The mouse incorrectly withheld the lick until the end of the stimulus presentation, 2s after onset. No additional stimulus was given for positive or negative reinforcement and the trial ended after the ITI .

pattern Discretised, binned and binarised spike events of N channels or neurons. Here, a single *spatial* pattern consists of $N \times 1$ bin (binary firing vector), also often referred to as *word*. A spatiotemporal pattern of t bins will have a $N \times t$ pattern, which is not investigated in this study..

sensitivity Sensitivity describes the True Positive Rate, or Hit Rate (TPR) and describes the probability of detection. $TPR = \text{True Positive (TP)} / (\text{TP} + \text{False Negative (FN)})$.

specificity Specificity is the True Negative Rate (TNR), and describes the fraction correctly classified as negatives. It is calculated as $TNR = \text{True Negative (TN)} / (\text{TN} + \text{False Positive (FP)})$.

support all occurring symbols or words in the state space with non-zero possibility .



Introduction

This work addresses sensory processing questions at individual unit and population level of Primary Visual Cortex (V1) both in anaesthetised and awake behaving mice. The following sections outline an overview of the background and literature required to follow the overall course of this work. Each chapter provides an individual introduction and brief summary of relevant work tailored to the methods and questions posed therein.

1.1 Overview

The brain is a peculiar processing system capable of handling and integrating vast amounts of multisensory inputs in form of electrical activities from both localised and diverse populations. In contrast to the function and engineering of most organs such as kidney or heart, which are understood in great detail, deciphering how the brain processes information is still the aim of modern neuroscience. Vision is one of the sensory systems most crucial for survival for many animals, e.g. when fleeing from a predator. But vision is also heavily involved in other fields such as navigation (and spatial memory) or object identification. Thus, vision has been a major field of research in neuroscience, under healthy conditions and in interventional research.

Sensory processing controls our perception: how we feel, hear, think and see. Reproducing and understanding how the multisensory integration and cortical microcircuits function is a main research goal in neural engineering. Neural Coding — the attempt at describing the relationship between stimulus and neuronal response, has created a wide range of coding techniques to map electrical and chemical responses to a stimulus, e.g. rate codes (the number of spikes in a time window) or temporal codes (the specific timing of spikes). Efficient coding (H. B. Barlow 2012) and characterising high-dimensional neural recordings of different domains at the same time has been the topic of many studies (K. Zhang et al. 1998; Panzeri and S. R. Schultz 2001), in both exploratory analyses and computational modelling.

Mouse V1, with its similar cell types and functional characteristics to other mammals (Niell and Stryker 2008), has become one of the main models to study visual information processing, given the wide range of molecular and genetic manipulations available (Huberman and Niell 2011) — despite the mouse not being a paragon of animal vision (Prusky and R. M. Douglas 2004). V1, located at the most posterior part of the occipital lobe is the entry point to cortex on the visual processing path. It is retinotopically mapped, where adjacent inputs on the retina are located in adjacent areas in cortex. Neural inputs arriving here are solely relayed through Lateral Geniculate Nucleus (LGN), rendering it a prominent model for probing low-level sensory processing. Electrophysiological studies in cat V1 already discovered half a century ago orientation-selective neurons (Hubel and Wiesel 1962; Hubel and Wiesel 1959), their organisation in orientation columns, and ocular dominance columns (Hubel and Wiesel 1974). Preferred orientations were not only found to be organised in columns of the same preferred orientations, but also spatially arranged in pin-wheel like structures (Bonhoeffer and Grinvald 1991), progressing in small systematic increments forming a map across the entire orientation field (Espinosa and Stryker 2012). However, this organisation of preferred orientations or orientation maps was not reproduced in mice or rats. Instead, random connectivity and orientation preferences in salt-and-pepper organisations were described (Ohki et al. 2005; Tan, B. D. Brown et al. 2011; Carrillo-Reid et al. 2015; Chklovskii and Koulakov 2004; Kaschube 2014). Yet, a reason why mice lacked this organisation has so far not been presented. This, along with other aspects of multi-unit tuning properties, is explored in Chapter 2, where a novel in-vivo electrophysiological dataset was acquired to address these questions.

While there has been considerable success in improving recording techniques yielding increasing numbers of simultaneously recorded neurons (Stevenson and Körding 2011), the neural code has not been deciphered yet. It is not clear if there is a single set of codes that can be used by several processing units at different cortical stages. Larger numbers of simultaneously recorded neurons require efficient, sophisticated data analysis techniques. Information theory can be used to quantitatively test theories about how the brain encodes stimulus-relevant information under different functional or sensory conditions, which can be useful to probe how ensemble responses differ from individual responses. A key metric in information theory is Shannon entropy (Shannon 1948), which quantifies how deterministic a system is: if there are many varying activity states (flat activity probability distribution) entropy is high, and if only a subset of all possible states dominate (peaked probability distribution), entropy is low.

Information-theoretic approaches allow enquiring into how population rates may contain similar amounts of information as individual units, or if the precise temporal and spatial arrangement of a neural response is relevant or necessary for a successful information transmission. Population responses (and thus processing) of natural scenes may differ from those driven by artificial stimuli. This is further explored in Chapter 3, which investigates groups of binary firing vector distributions evoked under different stimulus conditions.

Such differences in spatio-temporal population responses may also play an important role in the successful execution of a visual discrimination task, which is addressed in Chapter 4, where neural correlates of task outcomes are examined in V1 of the awake behaving mouse. Electrophysiological data is recorded and analysed from mice that are trained to perform a dichotomous choice upon presentation of one of two drifting gratings at orthogonal directions. This also permits examination of visual signal processing in the awake state.

Finally, with increasing population sizes to record from, interactions between individual units gain importance too. By developing computational models that mimic specific aspects of the experimental data, it is possible to incrementally approximate the neural response while explaining and investigating the structure that gave rise to the data. When a simplistic model fails to explain a certain statistical feature, more complex models are required to recreate the observed structures. Alternatively, such models can be used to verify findings of small data sample sizes, to test if the results were indeed attributable to insufficient sample sizes or could otherwise be easily explained by low-level (statistical) features. A short investigation of computational models based on the dataset of Chapter 4 is assessed in Chapter 5.

1.2 The mouse visual system

Processing of visual inputs in the mouse begins when photons arrive on the retina, where the photo signal is transduced into an electrical signal in a process called phototransduction. Rods, cones and photosensitive retinal ganglion cells are the involved cells. Both rods and cones transduce photons into electrical signals in what is called the photocascade. Upon arrival of a photon, transduction is initiated by a protein, an opsin, called rhodopsin, that undergoes a conformation change from 11-cis retinal to all-trans retinal. The conformation change activates a G-protein (in cones, transducin in rods), which in turn activates a molecule called cyclic Guanosine 3'-5' monophosphate

(cGMP) phosphodiesterase, breaking down the cGMP to 5'-GMP thereby reducing the concentration of cGMP within the cell. This causes cGMP-gated Na-channels to close, reducing the inward current and hyperpolarizing the photoreceptor membrane. The signal of several adjacent photoreceptors is then integrated by horizontal cells. Bipolar cells relay the graded membrane potential to amacrine cells or directly to retinal ganglion cells, whose axons form the optical nerve. Retinal ganglion cells then transmit the signal in form of spikes to the superior colliculus, which is involved in eye movements, the pretectum (playing a role in papillary reflex), and the LGN. On the way to the LGN, parts of the optic nerve cross at the optic chiasm, after which the optic nerve is called optic tract, which synapses onto the contralateral thalamus (LGN). This decussation entails that visual input from the right hemifield reaches the left hemisphere and vice versa. LGN projects in optic radiations to V1.

V1, also known as the striate cortex, is a 6-layered cortical structure located at the most posterior part of the brain's occipital lobe, receiving input through LGN in layer 4 on spiny stellate cells. It is the first cortical level of visual processing, having only passed through thalamus (LGN). In mammals such as carnivores or primates, V1 exhibits topographical mapping, or more specifically, retinotopic mapping, where nearby portions of visual space are represented at adjacent anatomical locations in V1. Rodent V1 also manifests this retinotopic organisation, which could be successfully mapped using optical approaches (Schuett, Bonhoeffer and Hübener 2002).

In addition to retinotopic mapping, V1 can also be characterised by exhibiting orientation selectivity as has been first described and discovered in cats and monkeys by (Hubel and Wiesel 1959; Hubel and Wiesel 1962; Hubel, Wiesel and LeVay 1976). Hubel and Wiesel discovered then that differently orientated bars presented as visual stimulation elicited responses differing in spiking frequency during electrophysiological recordings from V1. Some orientations generated strong spiking responses, whereas others would consistently elicit weaker spike activity. A common way of quantifying and visualising these differences in neural responses to orientated bars or gratings are tuning functions, which capture each neuron's mean spiking activity as a function of orientation or direction. Often, neurons have one preferred orientation eliciting the maximum response, after which other directions are generally best described to follow e.g. cosine or mixtures of von Mises functions.

This discovery led to widespread research into orientated bars and the assumption of V1 fulfilling low-level visual processing (such as edge detection), which will lead to more complicated object recognition in higher visual areas. V1 became a well-researched area,

both experimentally, and in the realm of computational models (Olshausen and Field 2005; Köster and Olshausen 2013; Niell 2013; Olshausen 2013; Sadeh and Rotter 2015).

In higher-level mammals such as cats or monkeys, these orientation-selective neurons are organised in orientation columns ("hypercolumns", (Hubel and Wiesel 1974)), stretching across cortical layers, where neighbouring cells exhibit similar orientation preferences (Espinosa and Stryker 2012). These "orientation columns" progress in small systematic increments covering the whole orientation field, forming an arrangement resembling pin wheels of a 30 - 100 μm (Bonhoeffer and Grinvald 1991), parallel to the surface of the cortex. While these orientation columns are commonly found in cats and monkeys, these are not observed in rodents such as rats and mice, whose V1 neurons responsive to orientations seem to be randomly organised throughout (Ohki et al. 2005; Tan, B. D. Brown et al. 2011). This is often described as salt-and-pepper organisation (Carrillo-Reid et al. 2015; Chklovskii and Koulakov 2004), with one cell's preferred orientation not bearing information about the one below or beside it, due to the lack of the functional architecture found in other carnivore and primates. Both orientation selectivity arrangements are presented in Fig. 1.1. Hansel and van Vreeswijk argue that achieving orientation selectivity in V1 of species, which lack clear topographic orientation organisation (i.e. rodents), it is sufficient to display random connectivity (Hansel and van Vreeswijk 2012). This means, selectivity may emerge through random connections, challenging the belief that orientation selectivity requires a functional organisation of neuronal response properties (Corey and Scholl 2012). Little has been suggested as to why rodents appear to lack the orientation maps apparent in carnivores.

In addition to orientation columns, the neurons in V1 also exhibit ocular dominance columns where the visual field is covered by both eyes (binocular area). They can be characterised as columns of neurons that are predominantly monocularly driven, and typically alternate between left and right eye. While these areas are large in humans and primates, the binocular field of vision is fairly small in rodents, and does not normally exist in fish and frogs.

Experimental investigations in mouse visual processing often involve receptive field mapping and characterising single and complex cell properties or contrast sensitivity measures (Ringach 2004; Histed, Carvalho and Maunsell 2012; Hansel and van Vreeswijk 2012). Important findings showed the dependency of stimulus exposure in the critical period on the development of preferred orientations and the effects of monocular deprivation (Espinosa and Stryker 2012).

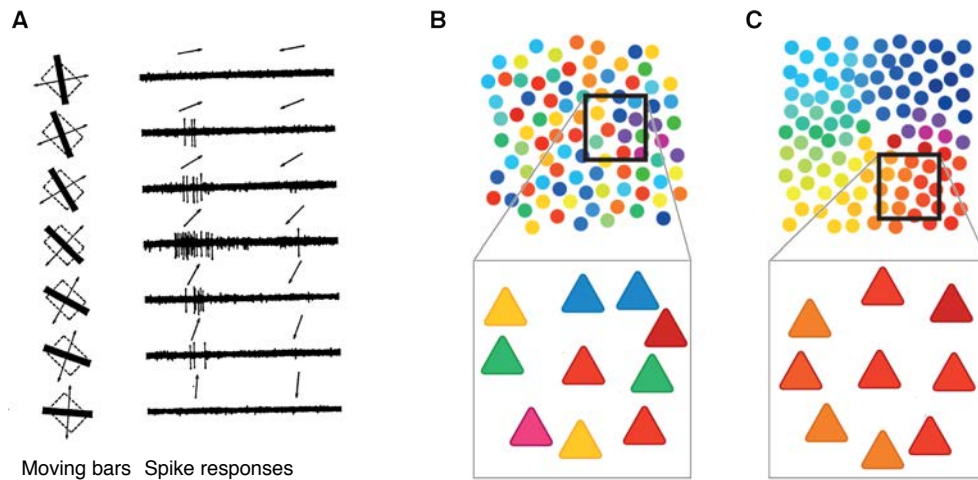


Figure 1.1: Orientation selectivity in V1. (A) Spike responses to moving bars at varying orientations in one neuron differ in strength, indicating orientation selectivity. (B) Different neighbouring neurons with differing preferred orientations (similar shades correspond to similar preferred orientations) in mouse V1 display salt-and-pepper organisation. (C) Neighbouring neurons in cat V1 show a clear organisation of orientation preference. Both insets show zoomed-in versions. Figure (A) taken with permission from (Hubel and Wiesel 1968), Figure (B) and (C) taken with permission from (Harris and Mrsic-Flogel 2013).

This apparent lack of systematic organisation in rodents may pose a problem when using Multi-Unit-Activity (MUA) from different depths of a cortical column to recover orientation selectivity, as this is not preserved across layers. Pooling over a number of neurons that are arranged in orientation columns will strengthen a neuronal signal derived extracellularly due to the positive support of similar preferred orientations. However, pooling over a number of neurons of different preferred orientations as would be the case in salt-and-pepper organisations will deteriorate signal since opposing preferred directions may cancel each other out.

Recent studies proposed that neurons of mouse V1 are more correlated in their preferred orientation that was previously thought. Neurons of similar preferences were clustered both horizontal and vertical scales (Kondo, Yoshida and Ohki 2016; Ringach et al. 2016). This work challenges the current understanding of mouse V1 as being randomly or salt-and-pepper organised, by investigating direction selectivity via in vivo extracellular electrophysiology across cortical layers (with a linear probe spanning all layers) and columns (by using several shanks).

1.3 Learning and sensory processing in primary visual cortex

In order to learn to respond to a stimulus in a certain way, a whole cascade of sensory processing needs to be executed. Even more so if a stimulus is behaviourally relevant to the individual. Evoked responses to first-time exposures may be biased by previous similar experience (a prior), or innate preferences (such as experience-independent development factors (Espinosa and Stryker 2012)), but a meaningful association of this particular stimulus is still lacking. Learning to respond to a stimulus in a beneficial way modulates and alters the initial, neutral-valued connectivity pattern induced by the response (Goltstein et al. 2013). These modulations can differ in strength, direction or sign of the connections. Thus, if a stimulus becomes associated with a certain value, such as a positive reward or the avoidance or removal of a noxious stimulus, this may alter the evoked activity. Formerly unresponsive neurons may change or enhance their response behaviour (Hager and Dringenberg 2010), e.g. through gain modulation to occupy a stimulus-selective state (J. Zhang and L. Abbott 2000)

Before being able to predict a certain pattern of activity, the cortical columnar activation is mainly achieved by sensory stimulation of Layer 4 (L4) receiving input from thalamus or primary sensory cortex (Constantinople and Bruno 2013). After learning, Barlow stated that the cortical column may also be driven by other sources not primarily concerned with vision (H. B. Barlow 1997) or under the influence of later (visual) areas (Tse and Cavanagh 2000). In other words, initially, activity is mainly driven by a bottom-up approach (Rauss and Pourtois 2013), and later, after learning, top-down regulations may affect the sensory response (Makino and Komiyama 2015; Moldakarimov, Bazhenov and Sejnowski 2014; A. Fiser et al. 2016).

The laminar structure and columnar organisation of the neocortex is arguably part of a small processing unit (Mountcastle 1997; Horton and Adams 2005). New circuits for sensory processing are still being discovered (Hirsch and Martinez 2006; Jiang et al. 2013; R. J. Douglas and K. A. C. Martin 2004), and cortical processing and modulation of functional connectivity in the visual cortical column is not entirely understood yet. A recent study by Olsen et al. (2012) revealed that strong projections from L6 target L4 interneurons. This was shown by an optogenetic stimulation of L6 in vivo, which led to a translaminar inhibition in both L4 and L2/3, while sensory stimulation of L2/3 had only little effect on L4 (Adesnik and Scanziani 2010; Petersen and Crochet 2013). Different types of inhibitory cells in L4 were also shown to be involved in mechanisms of gain control (Hirsch, Martinez et al. 2003), which plays a pivotal role in sensory representation (Salinas and Thier 2000): A changing amplitude of neuronal responses

can be induced by a downstream neuron, allowing to switch from being unresponsive to a stimulus to responsive (J. Zhang and L. Abbott 2000), potentially indicating a learnt pattern (Makino and Komiyama 2015).

In the superficial cortex, it was reported that activity patterns are organised into a small number of attractor-like neuronal assemblies (Bathellier, Ushakova and Rumpel 2012; Harris 2012). A very small number of firing patterns was induced by stimuli, leading to discrete response modes whose neurons belonging to the same mode exhibited similar tuning, although receptive fields in L4 and L2/3 were not the same. Thus, the responses of cells in superficial layers differed from those in L4 (Hirsch and Martinez 2006; Martinez et al. 2005; Niell and Stryker 2008; Cossell et al. 2015). Differing responses were also observed in neighbouring neurons, which can have strongly correlated activity but the probability of observing these high correlations falls rapidly with distance between neurons (Rothschild, Nelken and Mizrahi 2010; Sakata and Harris 2009).

Another example of how visual experience may alter the response properties of a stimulus-selective subpopulation of V1 was presented by (Goltstein et al. 2013): In 2-photon imaging experiments, they repeatedly exposed the mouse with a directional visual stimulus linked to a reward and observed how this reward association affected tuning properties. The result revealed a broadened orientation tuning and sharpened direction tuning for an assembly of V1 neurons selective for that stimulus. This translated also to population responses in L2/3 in experiments done by (Poort et al. 2015), where it was shown that task performance correlated with increasingly distinct population-level representations.

Another target of learning was shown by Jeanne, Sharpee and Gentner (2013), who demonstrated in songbirds how forming a behaviourally relevant association with a specific stimulus modified the correlational patterns between neurons. Thus, the response properties for noise and signal correlations were altered, illustrating how correlation can act as a measure of recognition weights and be the target of learning.

Stimulus-selective Response Potentiation (SRP) discussed in Frenkel et al. (2006) and Cooke and Bear (2010), demonstrates how experience-dependent plasticity in a perceptual learning task is achieved by inserting AMPA receptors (α -Amino-3-hydroxy-5-methyl-4-isoxazolepropionic acid receptors) into the membrane. Further, they showed that the early visual system was able to recognise and predict a learnt sequence of visual stimuli (Gavornik and Bear 2014).

These aforementioned phenomena illustrate the history-dependence of synapses, in

that a repeated stimulus exposure can increase the response (Zucker and Regehr 2002) - unlike the phenomenon of adaptation, where a repeated or prolonged stimulus presentation (Patterson, Wissig and Kohn 2013), quite contrarily, can reduce the amplitude of the evoked response (Kohn and Movshon 2003; Kohn 2007). Taken together, these changes may also lead to a shift or remapping of the preferred direction of the receptive field (Jeyabalaratnam et al. 2013; Jin et al. 2005), typically sharpening it up (Chaderton et al. 2014), which can be compensated for using low stimulus repetition rates and presentation durations.

1.4 Decision-making

Behaviour is a directly observable result of a (sensory) perception that was processed, evaluated and integrated in a decision process, which then evoked a (motor) response or the omission of it (e.g. fleeing or freezing responses). Thus, decisions are a fundamental part of behaviour. Forming a decision requires integrating prior knowledge (what happened last time, what is the value of the current decision?), current internal and external states (e.g. motivational state, hunger, danger) and other factors (is immediate action required or can the decision be deferred?). To this date, little is known about how decisions are made on a neural basis (Gold and Shadlen 2007). Intertwined in decision-making is the consideration of potential outcomes, and thus, the benefits and costs of choosing one decision over another. Hence, the ability to predict the outcome and reward associated with it are tightly linked. Unfortunately, this means decision-making is unlikely to be directly observable in one brain area alone, but to be the result of a multiregional integrative process.

When this question is investigated in a laboratory environment, external factors that may exacerbate interpretation are attempted to be minimised. One way of probing decision-making is to create new (reward) associations with novel or neutral stimuli, avoiding confounding effects from prior experience. These associations are often formed using reinforcement learning techniques to condition animals to produce a desired behaviour (Huberman and Niell 2011; Guo et al. 2014). A common behavioural paradigm to do this is the two-category GO/NOGO task, where the GO stimulus is paired with a reward and requires a behavioural action, while the NOGO cue expects no action and may be punished. Thus, the animal needs to make a perceptually-driven decision based on its prediction of reward or punishment. With a given behavioural task, the next question is in which brain structure to probe decision-making.

Anterior Cingulate Cortex (ACC) and medial Prefrontal Cortex (mPFC) are regions known to be involved in decision-making processes (Euston, Gruber and McNaughton 2012). Damage to mPFC or ACC often results in difficulties making choices and impaired abilities in learning or predicting the consequences of a choice (Kennerley and Walton 2011). Areas that have long been known to be involved in reward-dependent learning, and which directly showed neural substrates of reward predictions are the midbrain structures ventral tegmental area (VTA) and substantia nigra (W. Schultz, Dayan and Montague 1997). After reward association, these structures increase their firing already on cue onset, and decrease markedly if the reward is omitted, indicating that expected reward timing is also encoded (Hollerman and W. Schultz 1998). All these areas have been reported to be involved in value assignment, reward-directed and Pavlovian learning (Balleine 2007; Gold and Shadlen 2007; Carandini and Churchland 2013).

However, the decision-making process starts with the sensory percept, which is why investigations in sensory areas have become more common in decision-making research (Huberman and Niell 2011; Carandini and Churchland 2013; Stüttgen, Schwarz and Jäkel 2011). Here, electrophysiological recordings are performed in primary sensory cortices after animals were conditioned to a stimulus, often paired with an operant conditioning component that requires a certain action, e.g. licking or pressing a lever as conditioned behaviour (Skinner 1938). Different variables have since been shown to be linked to decision-making. Pupil diameter has been reported to be an observable parameter in decision-making (C. R. Lee and Margolis 2016) as well as in arousal (Vinck et al. 2015). In a GO/NOGO tactile discrimination task, C. R. Lee and Margolis (2016) was able to use pupil diameter as a predictor for lick response, where learning increased the dilation magnitude and latency between pupil dynamics and lick response. Further, recently several studies pointed at the role of V1 in decision-making: Namboodiri et al. (2015) suggested V1 to play a role in decision-learning in questions involving visually cued actions, and St. John-Saaltink et al. (2016) reported decision-making not only to be subject to the stimulus itself, but also the preceding stimulus sequence.

The recently formed International Brain Laboratory is trying to address the problem of multiple brain regions being involved in decision-making. Their aim is to perform the same behavioural experiment in different labs, while recording in different regions with different recording techniques to create a comprehensive data set to be analysed by computational partners (L. F. Abbott et al. 2017). Hopefully, this will help unravel how decisions are formed, from the sensory percept to a motor response.

1.5 Multi-Unit-Activity as a methodological choice

Single Unit Activity (SUA) describes the activity of a single neuron. Their electrical potentials can be measured extracellularly using microelectrodes or glass micropipettes placed closely to the cell membrane. Common methods in extracellular recordings involve microwires small enough to pick up signals from only the closest neuron, inserted as bundles into the brain (J. C. Williams, Rennaker and Kipke 1999; Kralik et al. 2001), having only little control over the actual positioning of each electrode site in the brain since individual wires may diverge from the bundle in unforeseeable ways. Alternatively, silicon microelectrode arrays have the advantage of providing better mechanical stiffness and the control over multiple recording sites in defined geometric organisation on a single or on multiple shanks (Kipke et al. 2003). The increased mechanical stiffness and the option to define the recording sites (i.e. the size and positioning) enables study over a larger neural tissue volume at defined locations. These larger recording sites increase the yield (Obien et al. 2015), which may also lead to picking up neural signals from more than one neuron in the vicinity. This is called MUA and describes the aggregate spiking of a local population of cells. MUA recordings require a few processing steps to obtain the neural signal. Firstly, it requires high-pass filtering the neurophysiological signal. Secondly, thresholding it on each channel of the multi-electrode recording array results in MUA. Here, it is also possible to simultaneously collect low frequency electrical signals from each channel, the Local Field Potential (LFP) (believed to represent the aggregate input into a particular region), which is low-pass filtered with a cut-off frequency of 250 Hz. Both MUA and LFP show improved robustness in comparison with SUA over long recording sessions (Land et al. 2013; Nelson 2012).

Unfortunately, the standard technique for observing neural activity, i.e. neurophysiological recording of SUA, is not particularly well suited for long recordings over multiple behavioural sessions. This is because individual units are lost, often due to drift or damage if recording probes are left *in situ* (Kozai, Li et al. 2014; Biran, D. C. Martin and Tresco 2005; Kozai, Catt et al. 2014), despite some reported success with long-term recordings with immovable probes (Okun, Lak et al. 2016). This technical reality often means the researcher is better served investigating MUA, when making recordings in behaving animals and over long behavioural sessions.

Summing over multiple neurons to increase information and robustness is not a new idea, but has, for example, already been used in decoders such as population vector (Georgopoulos, Schwartz and Kettner 1986; Stark and Abeles 2007). This has led to their use in Brain Machine Interfaces (BMI) applications (Flint et al. 2013; Stark and

Abeles 2007), and suggests that their use may be advantageous in probing the neural substrates of learning or behaviour mechanisms in the cortical circuit. Thus, using MUA instead of SUA targets different questions, mainly those concerning populations of neurons with the aim of transferability to being utilised in long term studies (Flint et al. 2013). Luckily, studies that included both MUA and SUA generally found that MUA on a given site/shank behave similarly to the rest of the local population. This can be beneficial, particularly in areas such as auditory cortex with its tonotopic mapping. Here, local populations are generally homogeneous, where integrating over a local area may lead to signal amplification. Yet, summing signals may be detrimental for signal quality in heterogeneous regions such as mouse visual cortex, which, unlike cats and primates, does not show orientation columnar organisation. It instead exhibits a salt-and-pepper organisation (Ohki et al. 2005), whilst still displaying a high orientation selectivity (E. Gao, DeAngelis and Burkhalter 2010; Niell and Stryker 2008; Espinosa and Stryker 2012). Because of this fine-scale random organisation, it might be expected that MUA and LFP in mouse visual cortex contain little information about the spatial structure of a stimulus beyond retinotopy. However, it was recently shown that the median similarity in tuning preference is significantly higher between neurons in close proximity (100 μm) than further (200 μm) separated ones (Ringach et al. 2016). Thus, we conjecture that a residual bias in the orientation or SF tuning sampled by the MUA on a single channel may leave a substantial amount of information, and that although orientation preference may be randomly scattered, their occurrence may not be uniformly distributed. Indeed, it has recently been shown in rat hippocampus (which also manifests random organisation) that LFP alone can be accurately used to decode spatial position of a rat (Agarwal et al. 2014).

If required, MUA can also be transformed into SUA with a time-consuming process called spike-sorting (Harris, Quian Quiroga et al. 2016), which requires clustering the waveforms of each spike incident and assigning them to different neurons with specialised software such as Klustakwik (Rossant et al. 2016; Kadir, Goodman and Harris 2014). Although clustering techniques exist that may correctly find clusters, the manual cluster merging step is still time-devouring and the experimenter may suffer from decision fatigue that a consistent accurate classification cannot automatically be warranted, particularly over long recordings in which spike waveforms or activity levels change or deteriorate (Flint et al. 2013; Harris, Quian Quiroga et al. 2016; Rossant et al. 2016; Buzsáki 2004). In this study, spike-sorting was performed but not further analysed, because the questions posed did not rely on whether the signal was generated

by one, or two or perhaps three distinct neurons. Instead, the existence of a source in close proximity to the recording site is acknowledged, as we are investigating the population response, i.e. the local activity. Thus, the devised and applied techniques would allow examination of neural signals in real-time, which will be particularly useful for cases that cannot rely on offline spike-sorting such as in neuroprosthetic BMI applications or in repeated or long recordings.

While studies involving SUA mainly targeted individual cell properties, two-photon imaging based methods are able to record from multiple individual cells simultaneously, albeit all from the same or similar superficial cortical depths. Both methods lack the power to record from all layers and different cortical columns at the same time, while summing over as much cortical volume as attainable whilst retaining the spatial resolution that is possible with MUA.

1.6 Information-theoretic concepts

Information theory describes the systematic study of information transfer, retrieval and storage. It focusses on the coding of sequences of symbols and how these can be transmitted through communication channels. Claude Shannon lay the cornerstone to information theory in his work searching for limits on signal processing and data compression (Shannon 1948). Already in 1952, his principles were applied to neuroscience in describing the transmission capacity of neurons (MacKay and McCulloch 1952), and has since been found a plethora of applications from the study of consciousness to analytic approaches designed to decipher the neural code (Dimitrov, Lazar and Victor 2011). One of the key measures in Information theory is Shannon entropy, which is a quantity typically measured in bits that determines the amount of uncertainty in a random variable or process.

1.6.1 Shannon entropy

Shannon entropy (Shannon 1948) is a measure to quantify the amount of potential information contained in a signal. It is calculated as a weighted average of $\log \frac{1}{p(x)}$, in which $p(x)$ represents the amount of surprise in an event x . If the occurrence of event x is very unlikely (low probability), a large amount of information is conveyed by knowing x happened. Likewise, if all events occurred at equal probability, knowing that any event happened does not explain anything about any other, thus maximising the surprise and uncertainty.

Entropy is a measure that is maximal when the underlying probability distribution is uniform, which means observing a particular state bears no information about observing any other particular state, and each state has equal probability. Shannon entropy then also depends on the number of possible observable states, which means if in a particular system each state occurs with equal probability, the (theoretical limit of the) entropy depends on the size of the state space. Without correlations between sites, and given a uniform probability distribution, in infinite time each unique **pattern** is traversed, and no **pattern** would provide information about observing another, thus, reaching maximum entropy. However, given that neural data contain signal and noise correlations, as well as the problem of finite sample sizes, often only a (small) subset of all possible **patterns** are observed. This leads us to the finite sampling problem.

(Spatial) spike **patterns** can also be characterised by their (Shannon) entropy, which is part and parcel of ongoing research in Information Theory (Strong et al. 1998; Averbeck, Latham and Pouget 2006; Ince, Panzeri and S. R. Schultz 2015) since it is surprisingly difficult to get an accurate estimate of the Shannon Entropy from a finite number of observations (Panzeri, Senatore et al. 2007; Tkačik and Bialek 2014; Victor 2002). It is very common to lack adequate amounts of observations (samples) compared with the numbers of possible states (or possible symbols). This is particularly obvious when considering the case of all possible binary **patterns** with 32 channels, which give us $2^{32} \approx 4.3 \cdot 10^9$ possible states. With a minimum bin size of 1 ms (considering that neurons have a refractory period of 1-2 ms), observing each **pattern** only once would require ≈ 49 days of data. Thus, severe problems can occur in the so-called undersampled regime, where not all events with non-zero probability are observed, or certain states end up being misrepresented.

The first entropy estimator described here is the *plug-in* estimator (Panzeri, Senatore et al. 2007; Archer, Park and Pillow 2012; Ince, Mazzoni et al. 2012; Nemenman, Bialek and de Ruyter van Steveninck 2004). It is calculated as $H(X) = -\sum_{x \in X} p(x) \log_2 p(x)$, and suffers from a severe negative bias for low sample sizes. There are many techniques focussing on how to estimate and correct this bias, e.g. (Treves and Panzeri 1995; Ince, Mazzoni et al. 2012; Panzeri, Senatore et al. 2007; Paninski 2003), sometimes at the cost of increased variability (Strong et al. 1998). When choosing an entropy estimator for discrete data, the following questions need to be considered: (i) Is knowledge about the shape of the distribution available? (ii) Are the samples binary vectors? (iii) Is the support of our observations known? (iv) Is the support known and finite? (v) Is following a Bayesian approach an option? (vi) If the range is unknown or infinite, is

anything about the tail of the distribution known? E.g. exponential or power-law tail? (Park 2014).

Unfortunately, there are no unbiased entropy estimators (Paninski 2003). However, luckily, there are many estimators with low bias and/or low variance (Park et al. 2013; Paninski 2003; Panzeri, Senatore et al. 2007). Using a reliable entropy estimator is pivotal when calculating **Mutual Information (MI)** or other metrics that derive from a good entropy estimator. Often, the joint probability distribution or the cross-entropy required to calculate MI cannot readily be estimated, while the marginal distributions are known or can be inferred. One particularly effective technique follows a Bayesian approach, using a suitable prior on the probability distributions, which has been shown to be effective in approximating entropy particularly in the undersampled regime (Archer, Park and Pillow 2013a; Archer, Park and Pillow 2013b; Archer, Park and Pillow 2014; Nemenman 2011; Nemenman, Shafee and Bialek 2002; Tkačik and Bialek 2014).

Notably, the **Centred-Dirichlet-Mixture (CDM)** estimator developed by (Archer, Park and Pillow 2013b) deals with the problem of low samples sizes and unknown support with an appropriate prior, and is particularly suitable for binary spike train data. In short, the CDM is a novel Bayesian estimator with a prior designed specifically for binary data, reflecting observations that are either close to independent or to the synchrony distribution (i.e. the sum of simultaneously active neurons, or population spike count). An extension of the CDM-entropy estimator for countable, discrete distributions such as population FRs is the **Pitman-Yor-Mixture (PYM)** entropy estimator, also developed by (Archer, Park and Pillow 2014), which includes a nice feature by being able to deal with unknown support.

Another entropy estimator often used in the literature is **Nemenman-Shafee-Bialek (NSB)**, which uses a mixture of Dirichlets to create an approximately flat prior (uninformative) on entropy, thereby also reducing the bias in the undersampled regime (Nemenman, Shafee and Bialek 2002; Nemenman, Bialek and de Ruyter van Steveninck 2004; Nemenman 2011).

This study applies the CDM and PYM, since these Bayesian estimators, albeit having explicit probabilistic assumptions, perform well in the undersampled regime and their assumptions do not need to be valid for them to produce good entropy estimates. More information can be found in e.g. (Park 2014) and (Archer, Park and Pillow 2014). The implementations can be accessed on <https://github.com/pillowlab/CDMentropy> and <https://github.com/pillowlab/PYMENTROPY>.

1.6.2 Mutual Information

MI is a measure quantifying how much one random variable explains about another. It is a symmetric, non-negative quantity, explaining in units of bits the reduction of uncertainty about one variable given information about another (Tkačik and Bialek 2014; Cover and Thomas 1991; Brunel and Nadal 1998; Pola et al. 2003). If the two random variables are independent, MI is zero, and (provided a bijective mapping) $I(S, R) = H(X) = H(Y)$ if there is a deterministic relationship, where $H(X)$ is the entropy of X and $H(Y)$ the entropy of Y . MI is defined as: $I(S, R) = \sum_{s \in S} \sum_{r \in R} p(s, r) \log_2 \left(\frac{p(s, r)}{p(s)p(r)} \right)$ where $p(s, r)$ denotes the joint probability distribution function of discrete variables S and R (e.g. stimulus and response), and $p(s)$ and $p(r)$ are the marginal probability distribution functions. This, however, is a mathematical depiction of MI and unless the estimate for our probability distributions is good, which cannot be guaranteed at low sample sizes, similar problems as with the plug-in estimator may be encountered. Another way of calculating MI is via entropies: $I(S, R) = H(R) - H(R|S) = H(S) - H(S|R)$, where $H(R|S)$ is the (sample-size weighted) sum of entropies conditioned on each stimulus. $H(R|S)$ is called conditional entropy, and can be interpreted as the mean uncertainty about R after observing a second random variable S .

In practice and when working with probability distributions of very unequal sample sizes encountered in experimental work, MI estimates can result in (small) negative values. This may be exacerbated by poor entropy estimates when calculating MI. For example, there may be classes with sufficiently large sample sizes resulting in a reliable entropy estimate, and another class being heavily undersampled. Even by weighing the inputs adequately to account for differences in sample sizes the entropy estimate of the undersampled class may be so poor (and therefore possibly negatively biased) that the sum results in a negative MI estimate. This emphasises the need for a good entropy estimator and sufficiently large sample sizes. The true MI cannot be negative, as stipulated by Jensen's inequality (Cover and Thomas 1991). This can be easily proved, and a proof can be found e.g. in the notes of (Vu 2012).

Since the plug-in entropy estimator suffers from substantial negative bias, MI based on the plug-in estimator suffers from substantial positive bias. To minimise these effects, binary data applied the CDM entropy estimator, and discrete data such as population FR, employed the PYM entropy estimator, which reduce the negative bias (Archer, Park and Pillow 2014; Archer, Park and Pillow 2013b).

2

Multi-Unit Activity contains information about stimulus structure in mouse V1

2.1 Introduction

Cortical microcircuits govern our perception: how we see, hear and think. Reverse-engineering the functionality of these circuits is a major project of modern neuroscience, and of the emerging field of neural engineering. Mouse Primary Visual Cortex (V1) is a prime candidate for studying the principles of information processing in a cortical circuit, as it possesses a similar range of cell types and receptive field classes to that of other mammals (Niell and Stryker 2008), while allowing numerous recently developed molecular and optogenetic tools to be applied (Huberman and Niell 2011). Moreover, its position at the earliest cortical stage receiving topographically mapped inputs from the retina, solely relayed through thalamus makes it a suitable candidate for investigating early sensory processing. Electrophysiological studies demonstrated its importance in low-level sensory processing, particularly in edge detection in single cells (Niell 2013).

Already in the 1950s it was discovered that moving bars at different orientations elicited responses of varying strength. This led to the discovery of orientation-selective neurons (Hubel and Wiesel 1962; Hubel and Wiesel 1959), and their apparent organisation in orientation columns (Hubel and Wiesel 1974), consisting of neurons of the same or similar preferred orientation spanning multiple cortical layers. Beside this functional arrangement orthogonal to the cortical surface, orientation-selectivity was found to be organised in pin wheel structures (Bonhoeffer and Grinvald 1991), in which preferred orientation progressed in small increments, lateral to the cortical surface, covering the entire orientation field (Espinosa and Stryker 2012). These orientation maps can mainly be found in higher-level mammals such as cats, ferrets, or monkeys (Koulakov and Chklovskii 2002), but are missing in rodents such as rats and mice. Yet, rat and mouse V1 do display orientation selectivity, appearing to be randomly organised (Tan, B. D. Brown

et al. 2011) in what has been termed "salt-and-pepper" organisation (Carrillo-Reid et al. 2015; Chklovskii and Koulakov 2004; Kaschube 2014). Thus, mice are said to lack both the columnar structure of orientation preference, and the pinwheel organisation. It is not clear why rodents lack an orientation map found in cats. Hansel and van Vreeswijk (2012) argued random connectivity would be enough to create orientation selectivity in animals lacking topographic organisation, in contrast to the belief that the generation of orientation selectivity required a functional organisation (Corey and Scholl 2012). Only recently, studies began to revisit preferred orientation in mouse V1 and detected more structure than was thought, as preferred orientations were found to cluster both on cross-columnar and laminar scales (Kondo, Yoshida and Ohki 2016; Ringach et al. 2016).

This study challenges the widespread understanding of orientation tuning and selectivity in mouse V1 by in-vivo electrophysiology across different layers and cortical columns. It is demonstrated that individual Multi-Units (MU) contain significant amount of information about the direction and Spatial Frequency (SF) of drifting gratings. To do this, an anaesthetised in-vivo electrophysiology experiment is devised in which novel electrophysiological MU data from the left hemisphere of mouse V1 is acquired. In addition, MU analysis reveals that low SF gratings moving from the temporal to nasal visual field reliably evoke highest neural responses across layers and columns indicating a strong bias in direction selectivity. Further, a high signal correlation between directions, and between SF tuning functions from different cortical locations is presented, questioning salt-and-pepper organisation in mouse V1.

It is shown that it is possible to decode direction and SF from the pattern of Multi-Unit-Activity (MUA) across channels with a high degree of confidence, emphasising that Single Unit Activity (SUA) might not be required for decoding tasks. This may provide an extremely useful tool for probing changes in cortical circuit information representation during behavioural learning paradigms.

The following sections contain material taken from and expanded upon ©2015 IEEE, reprinted, with permission, from (Tolkieln and S. R. Schultz 2015).

2.2 Methodology - surgeries and animal preparation

4x8-shank translaminar linear Neuronexus silicon microelectrodes were used to record neural activity in left hemisphere mouse primary visual cortex. Four shanks enabled recordings to be made from neurons in different layers and columns, maximising the

area and population recorded from.

All experiments were designed, implemented and performed by Marie Tolkiehn in accordance with the Animals (scientific procedures) Act 1986 (UK) and the Home Office (UK) under protocol 19b2 of PPL 70/7355 and personal licences. Mice were kept in a reversed 12h dark/light cycle and recordings were performed during the early dark phase.

2.2.1 Anaesthetics and drugs

The acute experiments were performed with $n=12$ female young adult wild-type C57BL/6 mice with mean age 2.2 months. The animals were sedated intraperitoneally with chlorprothixene (0.5 mg/kg, Sigma-Aldrich, UK) and anaesthetised with Isoflurane (2% for induction, 1 - 2% for surgery, 1% for electrophysiology in 1.2% O₂, Harvard Apparatus, UK). Isoflurane concentration was controlled via vaporizer, and superfluous anaesthetic retrieved using a scavenger. Further, to maintain clear airways and avoid tracheal secretions, 0.3 mg/kg (injected 0.01 ml dilution, Animalcare, UK) atropine sulphate was injected subcutaneously; and 2 mg/kg dexamethasone (injected volume 0.01 ml, Organon, UK) was also administered subcutaneously to prevent oedema. Depth of anaesthesia was controlled continually by checking the pedal-withdrawal reflex.

2.2.2 Surgical procedures

The anaesthetised animal was moved onto a feedback-regulated heating pad and body temperature was measured with a rectal thermometer, and maintained at $37.1 \pm 0.5^\circ\text{C}$. To prevent corneal dehydration whilst maintaining clear optical transmission, the eye to be recorded from was kept moist throughout the procedure by eye ointment (silicone oil, Sigma-Aldrich), applied continually, and covered from the microscope light with a stripe of black tape when in use. The head was initially kept in position using ear bars, a custom-built nose cone and an incisor adaptor. Vaseline was applied over the head to glue together the hair, easing the hair removal with scissors and to avoid stray hairs in the surgical area from the surrounding areas. An incision was made over the skull and the skin removed to expose the skull between Bregma and Lambda, approximately an area of 1 cm². A sterile cotton bud and sticky tape helped clearing the skull surface of connective tissue (gelatinous periosteum) and stray hair. With a sterile cotton bud, the muscle at the back of the head was gently pushed away in a rotating movement, making space for a ground screw site over the contralateral cerebellum.

The distance between Bregma and Lambda was measured by inserting a recycled electrode into the head stage of the electrode mount. Operated through a Scientifica[®] PatchStar micromanipulator and controlled with LinLab[®] software, the target location for the acute recording was the monocular region of the primary visual cortex (V1m) at -3.55 mm posterior Bregma and 2.5 mm lateral from the midline. With the measured distance Bregma-Lambda, the corrected target area was calculated with $x_{LOC} = -3.55 \text{ mm} * z[\text{mm}] / 4.2 \text{ mm}$ and $y_{LOC} = 2.5 * z[\text{mm}] / 4.2 \text{ mm}$, with z the individual distance between Bregma and Lambda and 4.2 mm being the average distance between them. The corrected target area at x_{LOC} and y_{LOC} was marked with a permanent marker and the location for the ground screw over contralateral cerebellum, on the interparietal bone near the lambdoid suture was identified with Phosphate Buffered Saline (PBS) application to check for superficial blood vessels. One small craniotomy (1 mm diameter) was drilled for the ground screw with a hand-held dental drill (Osada Success 40, 0.5 mm drill bit), and the ground screw-socket complex (Precision Technology Supplies, M1.0x2.0 Slot Cheese Machine Screw DIN84 A2 St/St and socket connector, MILL MAX, 851-43-050-10-001000 connector, sip socket), which had been prepared and connected before the procedure, was gently inserted into the craniotomy with a precision screwdriver after having removed the dura with a small needle (27G).

An elastic ring, cut from a syringe tip or a PVC tube was placed onto the target area and glued with super glue (Henkel Loctite). The height of the well was dependent on the use of internal electrode reference vs. external (which required an extra wire). Using the internal reference entailed a higher well allowing for a larger amount of PBS filled in the well, keeping the brain moist and the internal reference site connected, since the distance between electrode sites and reference was fixed, and given our superficial cortical recordings would lie outside of the brain tissue with the reference site located 1000 μm from the top site. For the external reference, which was connected to the ground screw, a smaller rubber ring sufficed. Once the superglue was cured, the ground screw and well were secured in place with dental cement (Kemdent Simplex Rapid[®], cold cure acrylic). Dental cement was then also used to cover the exposed skull and to form a head plate, joining the skull with a horizontal metal bar, which was screwed onto the frame. When the dental cement was set, ear bars were removed, the mouth piece (nose cone) unscrewed and brought forward along with the mouse to place it in the recording position, thereby removing the stereotaxic frame from the field-of-view, and readjusting the nose cone in the forward position.

Subsequently, a craniotomy of approximately 3 mm in diameter was performed in the

region of interest inside the rubber well (with a 0.5 mm drill bit). In doing so, the skull was thinned at the outer part of the ROI (the stereotaxic frame may be rotated for better visual control), and when it was thin enough to form cracks along the thinned bone, PBS was applied to soak the skull and thereby ease the bone fragment removal. Soaking the skull in PBS facilitates the separation of skull and dura, minimizing potential damage due to skull-dura adhesion. With a bent needle used as a hook, the skull fragment could be lifted slightly off the brain. Fine forceps 5 (Dumont #5) then lift the skull fragment gently off the brain. Similarly, to remove the dura, a small incision was made into the dura, lateral to the recording site, and retract it with fine forceps #5. The mouse was then moved into recording position and DiI (fluorescent lipophilic cationic indocarbocyanine dye, DM282, Molecular Probes[®], Life Technologies) solution (20 mg DiI in 300 μ l DMSO) was prepared (vortexed), for histological identification of the electrode trace. The recording electrode was manually dipped into the DiI. Alternatively, the DiI Eppendorf tube was placed into a boss head and a magnetic rod fixed onto the optical table, and the electrode was inserted into the DiI through a micromanipulator. The coated electrode was then inserted into the brain at the desired location. This has to happen in quick succession with the coating, as the DiI may evaporate or dry, rendering it ineffective.

The silicon microelectrode was lowered slowly into the brain to a depth between 800 μ m and 1050 μ m, at a speed of a few 10 μ m/s. In these experiments, the probe was equipped with four shanks, 200 μ m apart, with 8 linearly arranged recording sites of size 177 μ m², each separated by 100 μ m. Once the required depth was reached, the electrode was left to settle for 20-30 minutes.

2.2.3 Electrophysiology rig

The electrophysiology rig was modified from the set-up designed and used by Tang (2015). It was built on an air-pressure stabilised optical table with aluminium plates on four sides to form a Faraday cage, minimizing electromagnetic noise artefacts and scattered light. For the recordings, all lights were switched off in the room to avoid stray light that could interfere with the recording. To cover the front/operating part of the rig, a conductive fabric curtain (Wavetame, UK) was drawn during recording, thus, further keeping light and noise, e.g. from observing computer screens, away from the recording sites ensuring the display presenting stimuli being the only light source to the animal.

The stimulus monitor was a Samsung SyncMaster 2233Z, 22" LCD monitor, 60 Hz

refresh rate, which was reported as particularly suitable because of its temporal reliability for visual research (Wang and Nikolić 2011). The stimuli on the gamma-corrected monitor were displayed on 255 grey scale with mean screen luminance at 46.93 cd/m².

2.2.4 Stimuli and data acquisition

The stimuli comprised a set of 5 different individual subsequently presented conditions:

1. 5 minutes of spontaneous activity (not used in this study)
2. 400 repetitions of 600 ms flashes (black, white, maximum and minimum luminance), full-field to detect transient and sustained responses (not used for analysis).
3. A set of pseudorandomly presented sinusoidal drifting gratings, full contrast, 20 repetitions each, of 6 different SFs at 8 directions (1 s stimulus-ON time, with 1 s pre-stimulus time) at a constant 1.6 Hz temporal frequency, interleaved with 1 minute spontaneous activity after each full set at medium luminance (grey screen), which is common practice to use to estimate ongoing activity (Kenet et al. 2003; Niell and Stryker 2008; Jurjut et al. 2017). Throughout this manuscript, this stimulus type is termed **moving Gratings (mG)**, and its associated interleaved **Spontaneous Activity 1 (S1)**.
4. 4 repetitions of 10 different temporal frequencies at a SF of 0.03 cycles per degree (cpd) (stimulus-ON time 14 s, pre- and post-stimulus time 1 s each). The stimulus type is referred to **Temporal Frequency (TF)** and the **Spontaneous Activity 3 (S3)**.
5. 15 repetitions of a 60 s grey-scale natural movie consisting of 2 continuous presentations of the same 30 s natural movie showing natural scenes such as grass and trees. Each 60 s of movie presentation is followed by 1 minute break from stimulation (grey screen, as a proxy for **Spontaneous Activity (SA)**). Movie stimuli are referred to as **natural movie (nat)** and its SA as **Spontaneous Activity 2 (S2)**.

The order of stimulus type presentations was kept the same to improve comparability across mice at similar anaesthesia lengths. Fig. 2.1 outlines the stimulus type presentation structure described above.

The mouse was placed 25 cm away from the monitor (Samsung SyncMaster 2233Z, 22" LCD monitor, 60 Hz refresh rate), covering approximately 60°x75° of the visual field of the right eye. The left eye was treated with eye ointment (Allergan Lacrilube) and covered with black tape to avoid confounding effects attributable to the binocular zone of vision or inputs from the contralateral eye.

Stimuli were generated with FlyMouse, a software based on FlyFly, a Matlab Psychophysics Toolbox-based interface developed by the Motion Vision Group at Uppsala

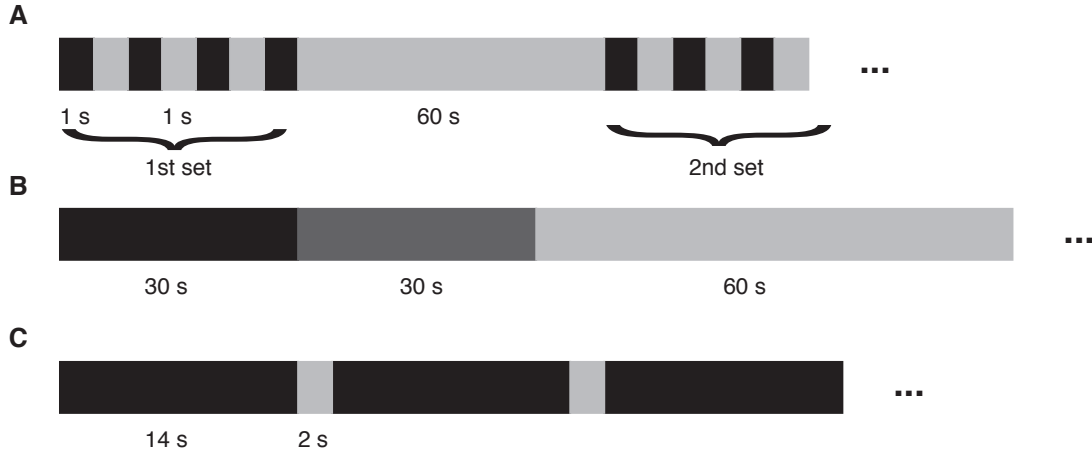


Figure 2.1: Stimulus presentation (black) structure with interleaved spontaneous activity (grey). (A) Moving gratings are presented with 1 s on and 1 s off time, interleaved with 60 s grey screen, S1. (B) Natural movies are 2 concatenated presentations of the same 30 s segments, followed by 60 s grey screen. (C) TF are presented for 14 s, followed by 2 s OFF screen periods.

University (<http://www.flyfly.se/about.html>) and customized by Silvia Ardila Jimenéz and Marie Tolkiehn. Examples of the Direction (DIR) and SF stimulus battery are depicted in Fig. 2.2. SFs were [0.01, 0.02, 0.04, 0.08, 0.16, 0.32] cpd and directions [0°, 45°, 90°, 135°, 180°, 225°, 270°, 325°]. Temporal frequencies were [0.2, 0.4, 0.6, 1.2, 1.6, 2.4, 3.2, 4.8, 6.4, 9.6] Hz.

Drifting gratings were presented at a constant temporal frequency (1.6 Hz), implying that the perceived stimulus speed decreases at higher SF.

Signals were acquired by Ripple Grapevine (Scout Processor), amplified with a single-reference amplifier with on-board filtering and digitization at 16 bit resolution and 0.2 μ V/bit (Grapevine Nano front end), and software Trellis, which was equipped with a live display of the channels during the recording. This set-up was best used with an Intel GIGABIT CT DESKTOP RJ45 PCIE B networks card to ensure a safe signal transmission. The Grapevine Nano front end enables the user to switch between different references, selecting between reference floating, R2 ignored, R2 as reference, or a tied reference bus. In these recordings, the built-in electrode reference located 1 mm from the top electrode site was used, as it provided a much clearer signal. Broad-band signals sampled at 30 kHz were recorded, filtered between 0.3 Hz and 7.5 kHz (3rd order Butterworth filter) and Local Field Potential (LFP) signals sampled at 1 kHz, low-pass

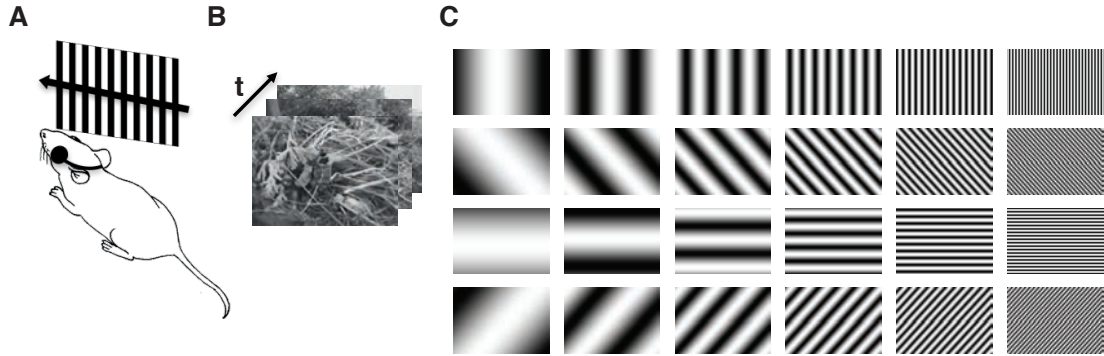


Figure 2.2: Grating stimuli with increasing SF. (A,B) Moving gratings and natural movies are presented on a monitor covering approximately $60^\circ \times 75^\circ$ of the visual field of the right eye, while the contralateral eye is covered to avoid confounding effects from inputs from the contralateral eye; and in-vivo electrophysiological recordings were made from left hemisphere V1. Mouse sketch by Susanna Mitolo. (C) From left to right increasing spatial frequencies from 0.01 to 0.32 cpd, and from top to bottom increasing orientations at 45 degree steps, from 0/180 to 135/325.

(250 Hz) 4th order Butterworth filter, from each of the channels.

The screen output signal and stimulus presentation triggers were synchronised with a custom-built photo-diode circuit board and photo-sensor (LCM555CN), which was attached to the bottom left corner of the monitor, where stimulus presentation differed from the rest of the monitor. Here, on stimulus onset and offset, a small rectangle flashed, which was detected by the photo-diode, relayed to the data acquisition system and used as a sync pulse.

2.3 Analysis methods

2.3.1 MUA analysis and processing

For the MUA analysis, the electrophysiological data was high-pass filtered, and thresholded at 4 standard deviations, in a spike detection algorithm developed by Aman Saleem (unpublished), providing the time stamps of spiking events used (albeit binned) throughout the analysis as our binarised spiking data. As mentioned in the introduction, we refrained from spike-sorting the data.

To investigate the quality of the signals, first the visual responsiveness of each electrode site was evaluated. A Mann-Whitney-U test (MWU) test identified those electrode

sites that showed a significant change in average Firing Rate (FR) between the pre-stimulus time (1 s) and during stimulus presentation (1 s). This resulted in 92% of the channels (354 of 384 electrode sites) exhibiting a significant difference in firing.

2.3.2 Multi-Unit tuning properties

Direction tuning of the MU was evaluated with the sum of two modified von Mises functions similar to those described in (E. Gao, DeAngelis and Burkhalter 2010; Swindale 1998; Gatto and Jammalamadaka 2007). SF tuning curves were fit with a Difference of Gaussian (DoG) function (Grubb and Thompson 2003; So and Shapley 1981; Rodieck 1965). In both cases, these fits were used to estimate peak response (preferred direction or preferred SF) and cut-off frequency.

The DoG function was of the form $y = b + (k_c - b)(e^{-(\pi r_c(v-v_p))^2} - k_s e^{-(\pi r_s(v-v_p))^2})$, with b baseline response, k_c area under RF centre's Gaussian function, r_c radius of centre Gaussian function, k_s relative area under RF surround's Gaussian function, r_s radius of surround Gaussian function and v spatial frequency, and v_p preferred SF (Grubb and Thompson 2003). The advantage of fitting the SF with a DoG over a log-Gaussian allows the possibility to model the centre and surround mechanisms as symmetrical antagonistic Gaussian functions. Moreover, the nature of the fit allows us to accurately calculate the cell's peak and cut-off frequency.

The goodness of the function fits was estimated with an R^2 estimate, which is also called the coefficient of determination, where $R^2 = 1 - sse/sstotal$, with sse denoting the sum of squared errors, and $sstotal = (n-1)var(x)$ the total variation. It is the ratio of the sum of squared deviations and the "total" sum of squares around the mean. When $R^2 \leq 0.9$ in a MU for both SF and directional fit, the MU is discarded from further tuning analysis. For example, if the R^2 of an individual unit was too low (indicating a poor fit), it was not included in calculating full population tuning functions in this study.

For population tuning curve calculations, the FRs were normalised across directions (or SF) to fall between 0 and 1 for each repetition, enabling us to compare across channels while accounting for slow temporal changes in excitability and different FR of the channels. Normalisation ensured the minimum value of each dimension (e.g. each SF in one trial) and for all data points to be 0 and the maximum value respectively 1. In the following, this is referred to as [0,1]-normalisation.

Tuning curves were estimated by fitting the trial-averaged FR of each direction (or SF) to the basis functions. Preferred direction was determined at the maximum of the

fitted function. In addition, determining solely which direction elicited the maximum and minimum mean firing response (without the fitting), allows the investigation if this is consistent over animals or channels. We then compared the fitted tuning functions across sites by calculating the pairwise Pearson correlation coefficient between channels (r_{signal}), as well as the noise correlation, estimated as the Pearson correlation of deviations of each trial from the mean at each direction.

Orientation and direction selectivity were calculated with the Orientation Selectivity Index (OSI) and Direction Selectivity Index (DSI), which were defined as:

$$OSI = \frac{R_{pref} + R_{null} - (R_{ortho+} + R_{ortho-})}{R_{pref} + R_{null}} \quad (2.1)$$

with R_{pref} as the preferred direction, R_{null} the opposite direction, and $R_{ortho\pm}$ denoting the orthogonal directions (Hansel and van Vreeswijk 2012). DSI was defined as:

$$DSI = \frac{R_{pref} - R_{null}}{R_{pref}} \quad (2.2)$$

An OSI of 1 represents high selectivity, an OSI of 0 means each stimulus produces an equal numbers of spikes.

One known problem using OSI or DSI is the positive bias in selectivity. These indices only make use of subsets of the tuning information and thus may artificially increase their selectivity. This is discussed at length in (Mazurek, Kager and Van Hooser 2014), where instead an approach using circular variance is pursued. Thus, this more conservative estimate of the direction and orientation selectivity was additionally estimated with L_{OSI} and L_{DSI} .

$$L_{OSI} = \left| \frac{\sum_k R(\phi_k) e^{2j\phi_k}}{\sum_k R(\phi_k)} \right| \quad (2.3)$$

where $R(\phi_k)$ is the mean response to the k^{th} direction. Hence, having computed both estimates, the real selectivity is assumed to lie between the two. Before calculating the mean, the responses were [0,1]-normalised (i.e. normalised such that all responses fall into the interval [0,1]), and the average is then taken across repetitions. Analogously, the DSI is calculated in Eq. 2.4.

$$L_{DSI} = \left| \frac{\sum_k R(\phi_k) e^{j\phi_k}}{\sum_k R(\phi_k)} \right| \quad (2.4)$$

In addition to the aforementioned methods, the average vector over FRs was calcu-

lated as a method encompassing spiking magnitudes of all directions at the same time. It was computed by first $[0,1]$ -normalising the data over each repetition and averaging them. Normalisation allowed us to compare vectors of different FRs and animals. It may also adjust for FR changes during a recording, when the general activity level increased or dropped. This ensured that during each repetition relative maximum and minimum responses were emphasised. Subsequently, the vectors were broken into their x and y components via trigonometric transformations and summed to get their vector sum ($R_x = \sum_k R_k \cos(k)$). The preferred angle was then the atan2 of the component sums $\phi_{pref} = \text{atan2}(R_y, R_x)$, and its magnitude the square root of its squared components. These components were then used in rose diagrams (polar histogram graphs) or polar diagrams to compare across sites and animals.

2.3.3 Decoding, feature detection and performance measures

In order to investigate how stimulus information is encoded in the neural signal, in particular, which features tell us more about certain aspects of the stimuli, three neural features were evaluated: a) binned, binarised spikes (Spatio-temporal Multi-Unit Activity (STMUA)), b) Spike Count (SC) and c) population rate, all at bin width 5 ms. For the multinomial classification of the grating stimuli, decoding performance was evaluated using four classifiers: Linear Discriminant Analysis (LDA), Naive Bayes (NB), classification-Tree and k-nearest neighbour. These features and classifiers were chosen over a more complicated feature extraction at this stage as a proof of concept that MU signals can be used to significantly decode different stimuli from these types of neural responses. In order to use the spatiotemporal information more effectively, the MUA matrix was vectorised. The binned, binarised MUA allowed us to use all the spatiotemporal features in the data. Summing over the time course results in the SC, thus greatly reducing the feature space to the number of channels or neurons. Summing over all neurons then gives us the population rate, which retains the temporal information, yet loses information about neuron-specific contributions. An example of how to extract each feature is given in Fig. 2.3.

A short summary of the classifiers is given here. For more information, please see e.g. (Bishop 2006). The LDA classifier works by seeking a projection vector w^* such that the separability of the scalars is maximised: $w^* = \arg \max_w \frac{w^T S_B w}{w^T S_\Delta w}$, where S_B is the between-class scatter matrix and S_Δ the intra-class scatter matrix. It is also known as Fisher's Linear Discriminant (1936) and assumes that class covariances are identical and have full rank. To do this, it tries to find a discriminant function of linear

combinations of independent variables which best explain the data by focussing on the differences between the classes of data. The LDA classifier was trained and tested using MATLAB's *fitcdiscr*, with discriminant type pseudolinear (all classes have the same covariance matrix), and predict functions.

The NB is a classifier using Bayes' theorem with naive assumptions between features (i.e. they are assumed to be conditionally independent given the target value). Bayes' theorem is defined as $P(c|x) = \frac{P(x|c)P(c)}{P(x)}$, where $P(c|x)$ is the posterior probability, $P(x|c)$ the likelihood, $P(c)$ the prior, and $P(x)$ the normalisation constant, c the parameters and x the observations. Once the posterior probability is known, classification is achieved by choosing the hypothesis with the highest probability Maximum A Posteriori (MAP). MATLAB's *fitcnb* function with a multinomial distribution input parameter was used in this task.

The classification tree is a subtype of a decision tree where the leaves represent class labels and branches the path or jointly occurring features that lead to the class label. This study employed a method similar to the one described in (Breiman et al. 1984), using MATLAB's *ClassificationTree* function.

Finally, the *k*-nearest neighbour (knn) is a non-parametric classification method. It classifies an input by comparing it to the *k* nearest training samples in feature space. This is normally achieved by calculating the e.g. Euclidean distances between test and training samples. Dependent on the class label of the *k* nearest neighbours, it then assigns an output label accordingly. The knn classifier was trained and tested with MATLAB's *ClassificationKNN* and predict function.

The decoding task comprised two parts for each feature type: *A*) Decoding the Spatial Frequency (1 of 6 SFs), and *B*) Decoding the direction from the responses (1 of 8 directions). Training and testing data consisted of random uniformly sampled partitions of 50% training and 50% for testing, using MATLAB's *datasample* function without replacement. For the SF decoding task, all training and testing data was taken at the same direction, 180°. For direction decoding, training and testing data was taken at 0.02 cpd. This was to ensure the stimuli were in a detectable range.

Classification accuracy was evaluated against chance level, validated with a 2-fold cross-validation and averaged over 100 repetitions with random permutations of the partitions, and averaged across all mice. To do this, the same random repetition indices were chosen over all sample stimuli, to ensure training and testing samples were taken in close temporal coherence. This ensures being able to avoid training on e.g. $[SF_1, trial_1]$, $[SF_2, trial_{14}]$, but instead had $SF_{1:6}$ all at $trial_1$ etc.

All stimuli occurred with equal probability. This means that chance level was defined at 16.67% for SF and 12.5% for the directions. Consistent classification above chance level suggests the decoder's successful use of inherent structures about SF or direction in the MUA.

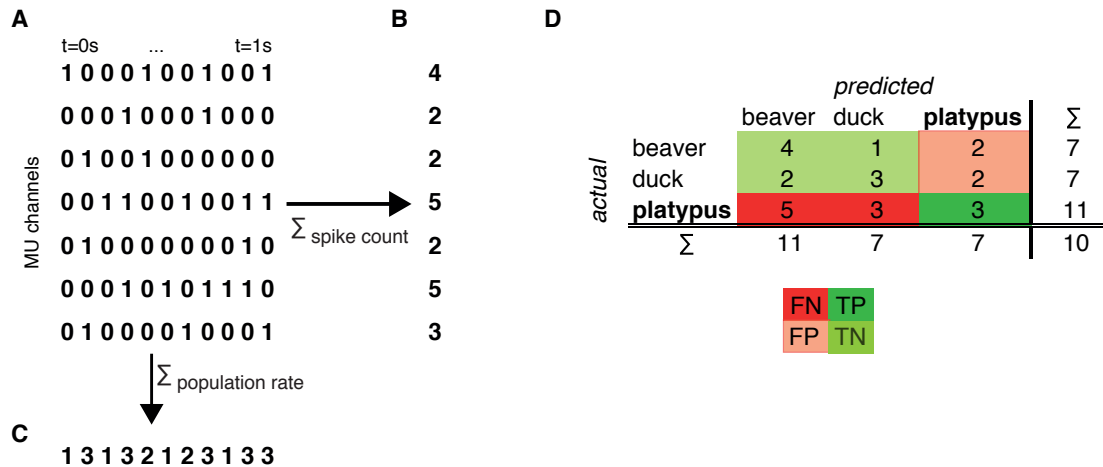


Figure 2.3: Decoding features are spatiotemporal MUA, spike count and population rate. Example fake trial to visualise feature extraction. (A) Binned, binarised MUA of 32 sites are used in the spatiotemporal feature based decoding, which is summed over all bins to get the spike count (B) feature, or summed across neurons to get the population rate (C). The population rate retains the temporal structure, whilst the spike count keeps the MUA-specific firing at the expense of losing temporal information. (D) Conceptual confusion matrix illustrating where True Negative (TN), True Positive (TP), False Negative (FN), False Positive (FP) are attributed for the example of platypus classification.

Performance accuracy was estimated with a confusion matrix and the fraction of correctly classified samples, cross-validated over 100 repetitions. A confusion matrix is a table that displays predicted classes on the y-axis over actual, real classes on the x-axis. With this display, it is possible to detect which classes are commonly misclassified as another, as well as the overall misclassification. Fig. 2.3 (D) illustrates a toy example of the structure of a confusion matrix in a beaver/duck/platypus classification task. Highlighted is the classification success of platypuses. Summing over the rows of the table gives us the number of actual samples in each class, whilst summing over the columns yields the number of predicted class elements. The diagonal contains all correctly classified samples in each class, and its sum corresponds to True Positive (TP).

Focussing on each class individually, it is then possible to look at False Positive (FP), False Negative (FN) and True Negative (TN). The confusion matrix is thus a versatile visualisation of a classification task. In the example of Fig. 2.3 (D), out of 11 platypuses (sum over rows), only 3 were correctly identified (TP). 5 were mistaken for beaver, and 3 misclassified as ducks, making a total of 8 FN. Instead, 2 beavers and 2 ducks were wrongly allocated to the platypus class amounting to 4 FP. The remaining 4 fields are TN from the view of platypus classification. With the knowledge of TP, TN, FN, and FP, it is possible to estimate properties such as sensitivity and specificity of the classifier. The sensitivity of detection (i.e. the probability of detecting), also called True Positive Rate, or Hit Rate (TPR), is computed by $TPR = TP / (TP + FN)$. Specificity is the True Negative Rate (TNR), and describes the fraction correctly classified as negatives. It is calculated as $TNR = TN / (TN + FP)$

2.4 Results

In-vivo extracellular electrophysiological data was acquired from left hemisphere V1 of the Isoflurane-anaesthetised mouse. Each recording followed the same stimulation protocol. Using 4-shank linear translaminar silicon microelectrodes, MUA was recorded from different cortical layers and columns under visual stimulation of monocular full-field drifting gratings. MUA properties such as directional or spatial tunings are characterised and compared among different MU.

2.4.1 Visual responses to both gratings and natural movies were observed using MUA recordings

Fig. 2.4 highlights the visual responsiveness to 48 moving gratings at 6 SFs and 8 directions, grouped by SF and repetitions, for 32 channels on in one mouse. The red line at the top indicates stimulus presentation. Higher grating indices correspond to higher SFs and appear to induce weaker visual responses at larger variability. Subpanel (B) visualises the same stimuli in the same animal as a probability- Peri-Stimulus Time Histogram (PSTH) summed over 32 channels. It is visible from the figure that the temporal structure differs between gratings, which can be linked to stimulus differences. From the raster plot and the PSTH we can observe that most channels were consistently visually responsive and that their activity was highly modulated by the stimuli.

Having a closer look at a subset of these stimuli, Fig. 2.5 (A) visualises example responses on 32 channels to 20 repetitions of 6 directions (0-225° in 45° steps) at a

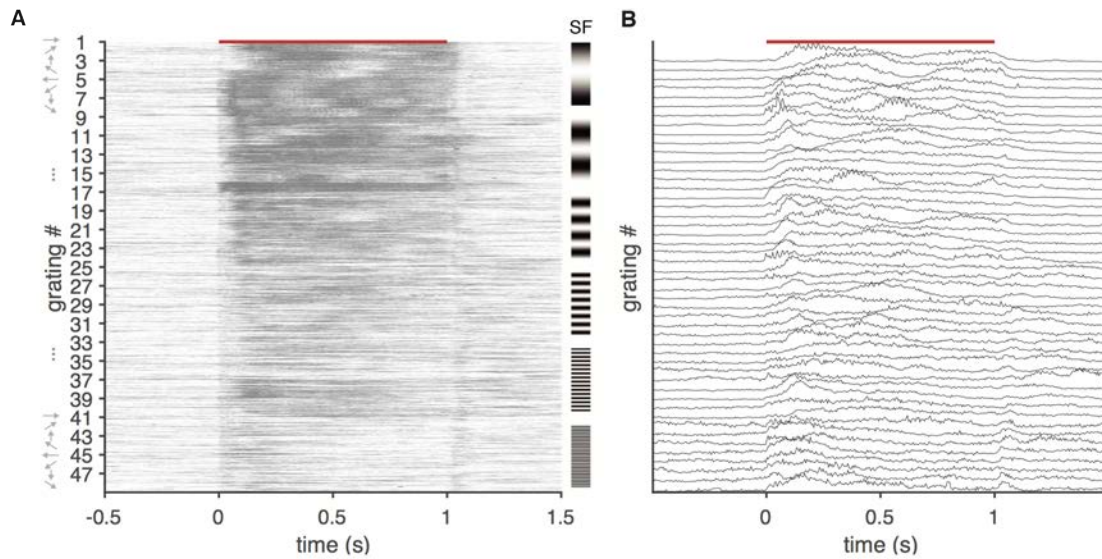


Figure 2.4: Visually evoked responses vary in their intensity for different moving gratings. (A) Example raster plot of all 48 moving gratings, grouped by SF with 20 repetitions per stimulus and all 32 channels indicates visual responsiveness of most channels to most gratings, with a decreasing intensity for gratings of higher indices. (B) The PSTH of the same stimuli emphasises the difference in temporal structure of the moving gratings.

static SF of 0.01 cpd, and (B) 15 repetitions of the natural movie on 32 channels in the same animal. (C) and (D) reveal the normalised probability PSTH for the same data. As can be observed from the figure, a high fraction of channels demonstrate strongly driven responses to visual stimuli, with different response shapes evoked by varying stimulus conditions. Moving gratings appear to evoke strong, reliable responses during stimulus presentation (indicated by a red line atop of the figure), whereas natural movies seem to induce spiking at a higher trial-to-trial variability, but high population activity. The most reliable population response in the excerpt of the 30 s movie appears to be the onset response at $t=0$ s.

2.4.2 Tuning to moving gratings of different directions and spatial frequencies in V1

A large number of MU proved to be significantly modulated by moving gratings. An example of three strongly tuned MU in different animals is presented in Fig. 2.6. Direction tuning fits of a combination of von-Mises functions on the baseline-subtracted

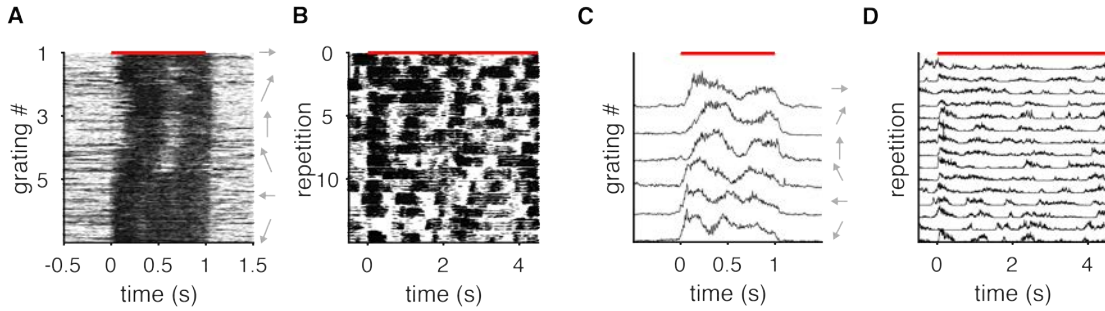


Figure 2.5: Response patterns vary between moving gratings and natural movies, and a high fraction of channels is stimulus-responsive. (A, B) Example raster plots on 32 grouped channels to moving gratings at 6 directions ($0-225^\circ$ in 45° steps) at the same SF (0.01 cpd) for 20 repetitions (A), and to 15 repetitions of the first 4 seconds of the natural movie (B) illustrate visual responsiveness and spiking reliability across repetitions. Each line highlights a spike incident. (C-D) show the PSTH for the same data, (C) shows the PSTH over the population response to each grating, averaged over 20 repetitions, and (D) shows the population response for natural movies, repetition by repetition. (A-D) are taken from the same mouse. Red line indicates stimulus presentation period.

MU of the mean response over the first two SFs indicated a weak to strong modulation across channels and shanks. Mean FRs peaked for directions around 180° , with a median preferred direction of 171.8° . (A-C) show the tuning fit for a mixture of two von-Mises functions on the MUA of three channels in three mice. Although FRs differ, the shape of the tuning functions is highly similar with troughs at 90° and peaks around 180° .

Example tuning functions in Fig. 2.6 appear qualitatively similar in tuning preference in mouse V1. The majority of sites across animals exhibited tuning functions similar in shape to those presented in the figure. This modulation appears to be a feature present at different average FRs. In particular, the tuning functions of the examples reveal a global minimum at 90° , and a maximum at 180° . It is also evident that the direction 180° appears to drive the activity slightly more than its collinear direction at 0° .

2.4.3 Spatial frequency tuning in V1 shows bandpass and low-pass properties

Similar to directional tuning, all visually responsive MU indicated substantial SF tuning. With SFs exceeding 0.04 cpd, activity decreased drastically, as can be observed in Fig. 2.6 (D-F), where sites (D-F) are the same as in (A-C). These DoG fits are estimated using the average of all 8 directions and stimulus repetitions, thus decreasing the SEM

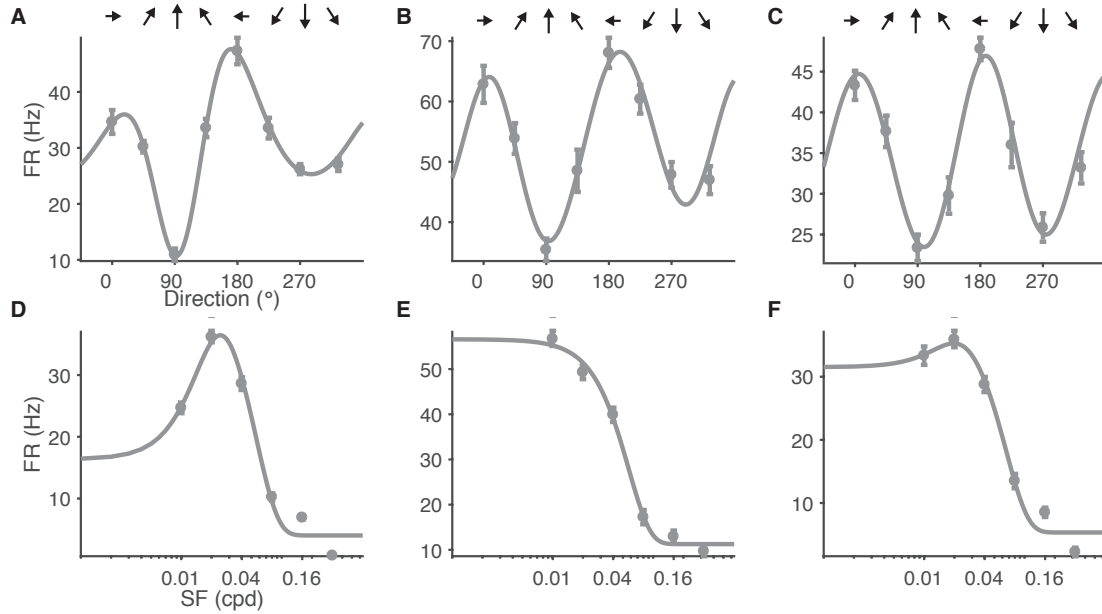


Figure 2.6: Baseline FR-subtracted MU show strong FR modulations over differently orientated drifting gratings. Direction and SF tuning curves appear stereotyped across mice. (A-C) show von-Mises function fits on baseline-subtracted data with directional peaks around 180° (horizontally moving grating) for MUA of 3 example sites from 3 different mice. Mean responses for directions were averaged across the two lowest SFs. (D-F) present the SF tuning on the same electrode sites as in (A-C), illustrating bandpass and low-pass properties, respectively. Note logarithmic scale of x-axis in (D-F). Mean FR of SFs were averaged across all 8 directions. Error bars denote Standard Error of the Mean (SEM). Note different y-axes scales.

relative to the ones in directional tuning. The most commonly observed tuning shapes appear with bandpass (D, F) or low-pass (E) properties, where low-pass properties are defined by a monotone decreasing shape, and bandpass behaviour by a rise-fall shape in the amplitude-frequency plot. In particular, the three lowest SFs elicit high responses, whereas the three highest SFs induce lower activity levels. Fig. 2.7 summarises (A) the distribution of peak SF for $n = 353$ sites. The distribution of peak frequencies appears bimodal, with a sharp peak at zero, which has been truncated in the plot to the lowest SF, 0.01 cpd. (B) presents the distribution of 3-dB cut-off frequencies, whose median lies at 0.12 cpd.

The corresponding SF tuning functions, fitted with a DoG function, show low-pass and bandpass properties, with a mean preferred SF of 0.017 cpd, which is in line with previously reported results. Ignoring the cases where preferred SF is 0 (140 out of 384

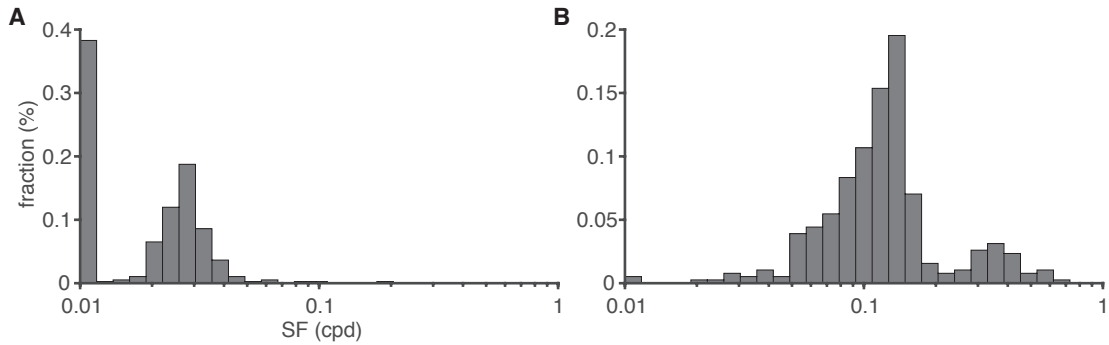


Figure 2.7: SF peak and 3-dB cut-off distributions summarise their low-pass and band-pass properties. (A) Peak SF appears bimodal with a large peak at the lowest SF, and a secondary peak at 0.028 cpd. Axis is truncated to 0.01 cpd given the log-scale. (B) Distribution of -3 dB cut-off frequencies across all mice with a mode at 0.13 cpd.

cases), the mean preferred SF is 0.029 cpd, median 0.027 cpd, which is also visible in the secondary peak of Fig. 2.7 (A).

The overall median preferred SF was 0.022 cpd. About half of the MU (207) revealed bandpass properties indicated by a drop in response at the lowest SF, 0.01 cpd, which is illustrated by the example of panel (D) of Fig. 2.6. Our analysis showed a median cut-off SF of 0.12 cpd (as determined by the -3 dB cut-off from the preferred SF). Most MU revealed a preferred SF of around 0.02-0.03 cpd. Variation was low and only occasionally a peak SF response exceeding 0.04 cpd was observed, as given in Fig. 2.7.

2.4.4 Direction tuning in left V1 is biased towards leftward moving gratings

The tuning functions in Fig. 2.6 indicated similarity between tuning functions in the three example sites of three different mice. Summarising these findings by estimating the maximum responses for all sites in all animals lets us compare which direction elicits the highest responses across animals. If there was no underlying directional preference or an even representation, the directions evoking maximum FR should average out over many samples and approximate a uniform distribution on the circle. Similarly, comparing the frequencies that evoke minimum responses may support this finding.

The tuning curves in Fig. 2.6 indicate a bias in directional preference for leftward moving gratings (corresponding to a movement from temporal to nasal visual field). This corresponds to the direction that elicited the highest FR, as shown in Fig. 2.8

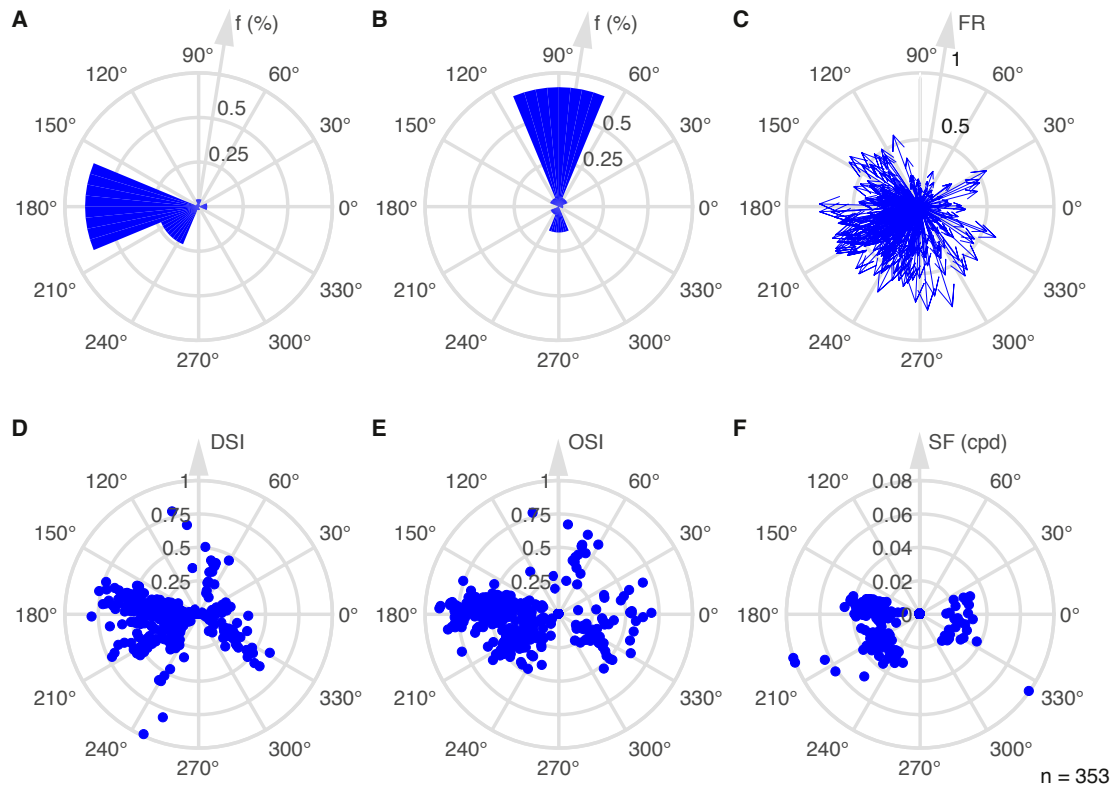


Figure 2.8: Preferred direction is not uniformly distributed. Polar histograms of average *maximum* FR and the direction which elicited the average *minimum* FR are shown in (A) and (B) in frequency (% of MU), respectively, which evidently illustrate the directional bias, calculated at SFs 0.01 and 0.02 cpd together. Leftward moving gratings evoke maximal responses in the majority of $n = 353$ sites, and upward moving gratings (90°) typically minimal responses. (C) illustrates the [0,1]-normalised average vectors of 353 sites in all 12 mice, where vector direction and length result from the vector sum of the normalised firing responses to all directions. In (D-F), each dot represents properties of one electrode site of a total $n=353$ sites from 12 animals. (D) Polar plot of preferred direction (taken from peak tuning fit) against DSI. (E) Preferred direction against OSI. (F) Preferred direction against preferred SF.

(A), 180° . Polar histograms of the average *maximum* FR and those directions evoking the average *minimum* FRs are presented in Fig. 2.8 (A) and (B). It is striking that the distribution of directions evoking maximum and minimum is not at all uniformly distributed (both $p < 0.001$, Rayleigh test for non-uniformity of circular data), but shows a high preference of 180° for maximal firing, and 90° for minimum average FRs. Over 68% of the 353 visually responsive sites show mean maximum firing at 180° (Fig. 2.8 (A)). Another striking feature is the consistency of which direction elicited minimal responses across all sites, at 90° (B).

Computing the average vectors over $[0,1]$ -normalised FR responses for each site emphasises the directional bias towards left and downward moving gratings further (C), which corresponds to the largest two fractions of directions generating maximum firing in (A).

Using knowledge inferred via von-Mises function fits, a better estimate of the preferred directions may be obtained by taking the peak of the fit as the preferred direction. Fig. 2.8 (D-F) reveal polar scatter plots with DSI, OSI and preferred SF on the radial axes, and preferred direction on the angular coordinates. Each dot represents one site in one of 12 mice, with $n=353$ total sites included, having rejected sites whose tuning fits are worse than $R^2 \geq 0.9$. The majority of direction- and orientation-selective cells show preferences in areas of leftward moving gratings.

The polar plots in Fig. 2.8 indicate that certain directions are overrepresented across the visual field. Here, the graph of preferred SF against preferred direction of 353 MU for 12 mice revealed a majority of SF/direction pairs appearing clustered around 0.02-0.03 cpd and 180° . The polar plot in (D) of Fig. 2.8 showing DSI against preferred direction further illustrates this bias towards horizontal leftward moving gratings, and it appears to manifest in sites that range from low to high direction and orientation selectivity.

2.4.5 Tuning in V1 is highly correlated between sites

Directional tuning in primary visual cortex appears to be distinctly correlated across sites, both longitudinally and laterally.

The assumption of salt-and-pepper organised orientation maps may require the tuning functions to roughly tile the whole direction space. Yet, normalising the FRs over directions for each repetition, and averaging across repetitions reveals a different picture, as presented in Fig. 2.9, which also shows the dependency of tuning on SF. The tuning functions of 32 sites in all mice seem to align approximately with the example curves

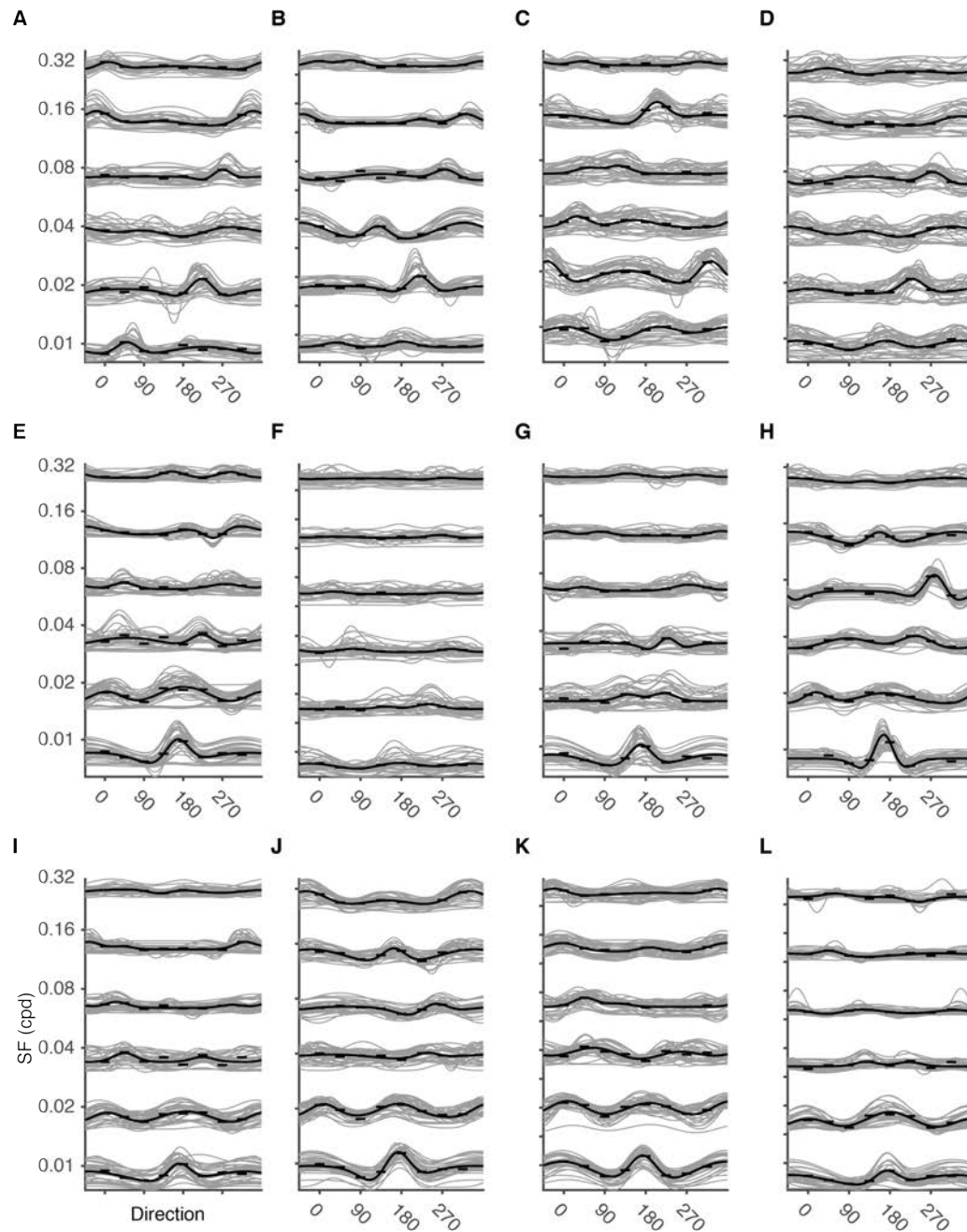


Figure 2.9: Direction tuning depends on underlying SF and is highly correlated between sites, even across shanks. Bottom to top: tuning function estimated over increasing SF. (A-L) show [0,1]-normalised tuning functions of all sites (grey, thin lines) in one mouse per panel. Thick black line indicates tuning fit of the mean across all ([0,1]-normalised) sites.

from Fig. 2.6 for the lowest SF, with differing tuning function shapes for higher SFs. Fitting the mean over all sites and repetitions gives us the overall tuning function of the population. Comparably, the SF tuning is highly similar across channels.

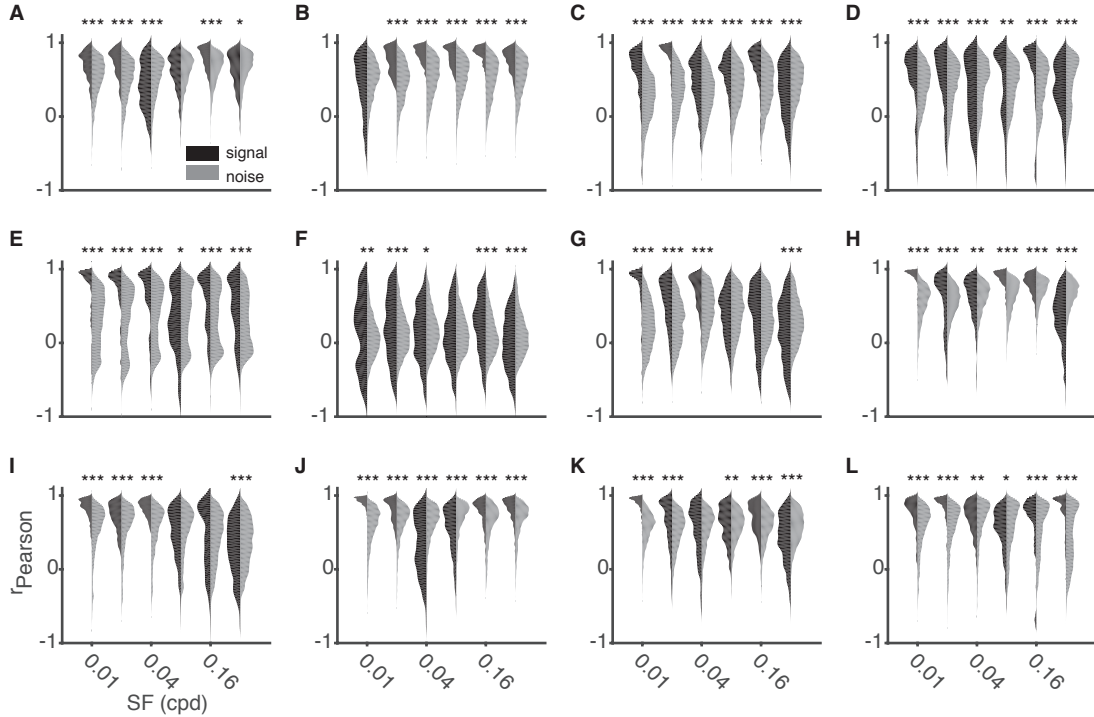


Figure 2.10: Pairwise signal correlation coefficients between directional tuning functions of all sites in each mouse are high for low SF, with few negative correlations indicating opposing tuning curves. Noise correlation is generally lower for directions. (A-L) indicate different mice. Black is signal correlation, grey noise correlations. Statistics MWU, where * indicates $p < 0.05$, ** $p < 0.01$ and *** $p < 0.001$.

Extending this over $n=12$ mice, signal correlation between individual (within-mouse) tuning curves is high, with few highly negative correlations indicating opposing tuning curves, which may speak for an optimal code. This is illustrated in Fig. 2.10 in violin plots over all (within-mouse) pairwise correlations for all mice. Comparison of Figs. 2.10 and 2.9 shows that tuning function reliability and signal correlation correspond well in describing the relationship. For example, in Fig. 2.9 (F), no strong overall tuning is observed on any of the SFs. In accordance with this, signal correlation indicates a large spread over many values for all SFs, while noise correlation centres around zero with a fairly low spread. Similarly, Fig. 2.9 (H) reveals a very strong population tuning for the lowest SF, which is also reflected in Fig. 2.10 (H) indicating a very high signal

correlation tightly located around 1, with substantially lower noise correlations visible.

These findings are consonant with averaged population tuning functions for SF tuning calculated by pooling over all directions, demonstrating a high reliability over sites and shanks, visualising the similarity even across mice, as is depicted in Fig. 2.11. Individual averaged site responses as well as the averaged population responses mainly show low-pass or band-pass properties, which was illustrated in Fig. 2.7.

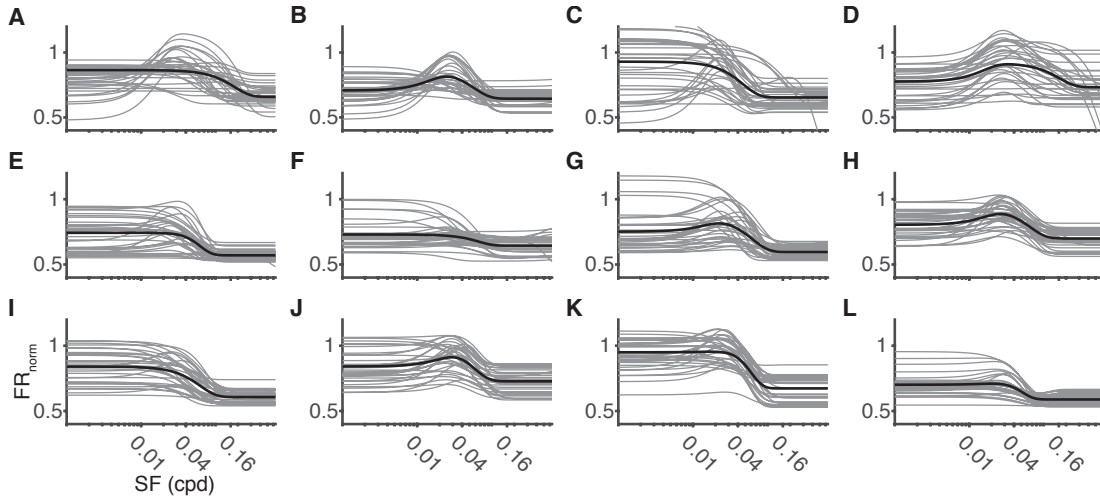


Figure 2.11: SF tuning function fits of [0,1]-normalised responses reveal high similarities across sites and shanks. (A-L) show [0,1]-normalised tuning functions of all sites (grey, thin lines) in one mouse each. Thick black line indicates tuning fit of the mean across all ([0,1]-normalised) sites. Generally, function fits indicate low-pass or band-pass properties.

As expected, correlation coefficients for SF tunings are all high, significantly different from zero, as is revealed in Fig. 2.12 (A) ($p < 0.001$, 1-sample sign test). Particularly SF signal correlation is tightly located near a correlation coefficient of 1. In contrast, noise correlation is much lower, with a mean approximately centred around zero, but significantly different from zero ($p < 0.001$, 1-sample sign test). Further, signal correlations are significantly higher ($p < 0.001$, MWU) than noise correlations, as is evident from the distributions in Fig. 2.12 (A), demonstrating this is not noise but driven activity.

DSI and OSI distribution values lie mainly between 0.2 and 0.6, with DSI occupying lower indices than OSI, as is expected. This demonstrates a pronounced direction and orientation selectivity of the MU. However, the selectivity was subject to the choice of SF. Estimating selectivity indices over all SFs resulted in a median OSI of 0.28, and a median DSI of 0.20. The much more conservative selectivity measures L_{osi} and L_{dir} ,

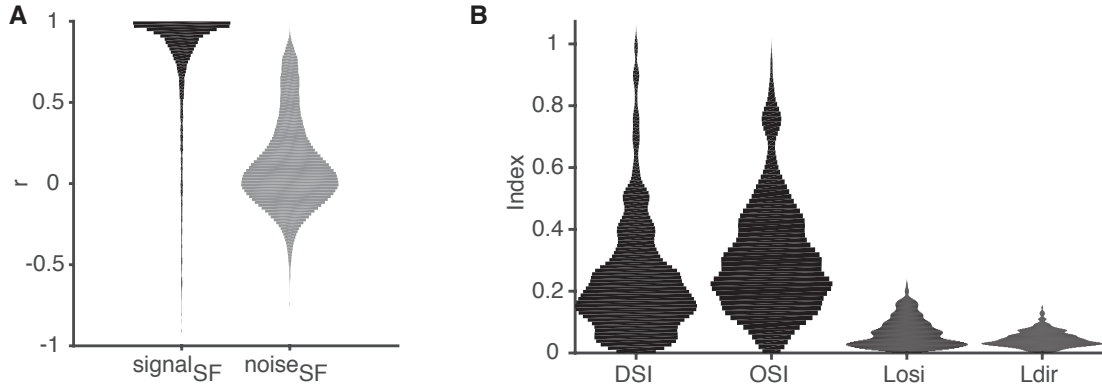


Figure 2.12: SF indicate high signal correlations, and much lower noise correlations. (A) Signal correlations for SF tuning fits are high with a centre of mass near a correlation coefficient of 1, with only few strongly opposing negative values. Noise correlations appear generally centred around zero. Correlations were estimated over all 6 SFs. (B) DSI and OSI distributions demonstrate pronounced stimulus selectivity, which is also reflected in the more conservative stimulus selectivity estimates L_{osi} and L_{dir} , which have much lower values. All selectivity indices were estimated over all SFs and directions.

which were defined and discussed in Eq. 2.3 and Eq. 2.4, occupy a much smaller range between 0 and 0.2, with direction selectivity centred around yet smaller values, concordant OSI and DSI. Estimated across all SFs, the median L_{osi} and L_{dir} are 0.06 and 0.04, respectively. Estimating the selectivity indices for 0.01 cpd only, resulted in much higher values, at OSI 0.49, DSI 0.36, L_{osi} 0.20 and L_{dir} 0.10.

2.4.6 Direction tuning depends on spatial frequencies

Preferred directions appear mainly clustered around 180° , fairly consistently across mice. Yet, computing the preferred and maximum FRs may be a property related to the SF used. That is why the mean FR and tuning fits for all [0,1]-normalised channels were computed at different SF. Since FR decrease rapidly at high SFs, instead of investigating these metrics for each SF individually, results were compared by varying the number of SFs included in the averages (visualised in Fig. 2.13).

Each panel in Fig. 2.13 corresponds to one mouse, and each group of lines stands for one tuning fit group of SF used. From top to bottom, SF were [0.01, 0.01:0.02, 0.01:0.04, 0.01:0.08, 0.01:0.16 and 0.01:0.32] cpd frequencies to pool over. In agreement with the decrease in FR observed in SF tuning functions from Fig. 2.6, tuning curve modulation decreases when including higher SFs to almost straight lines. Strong tuning

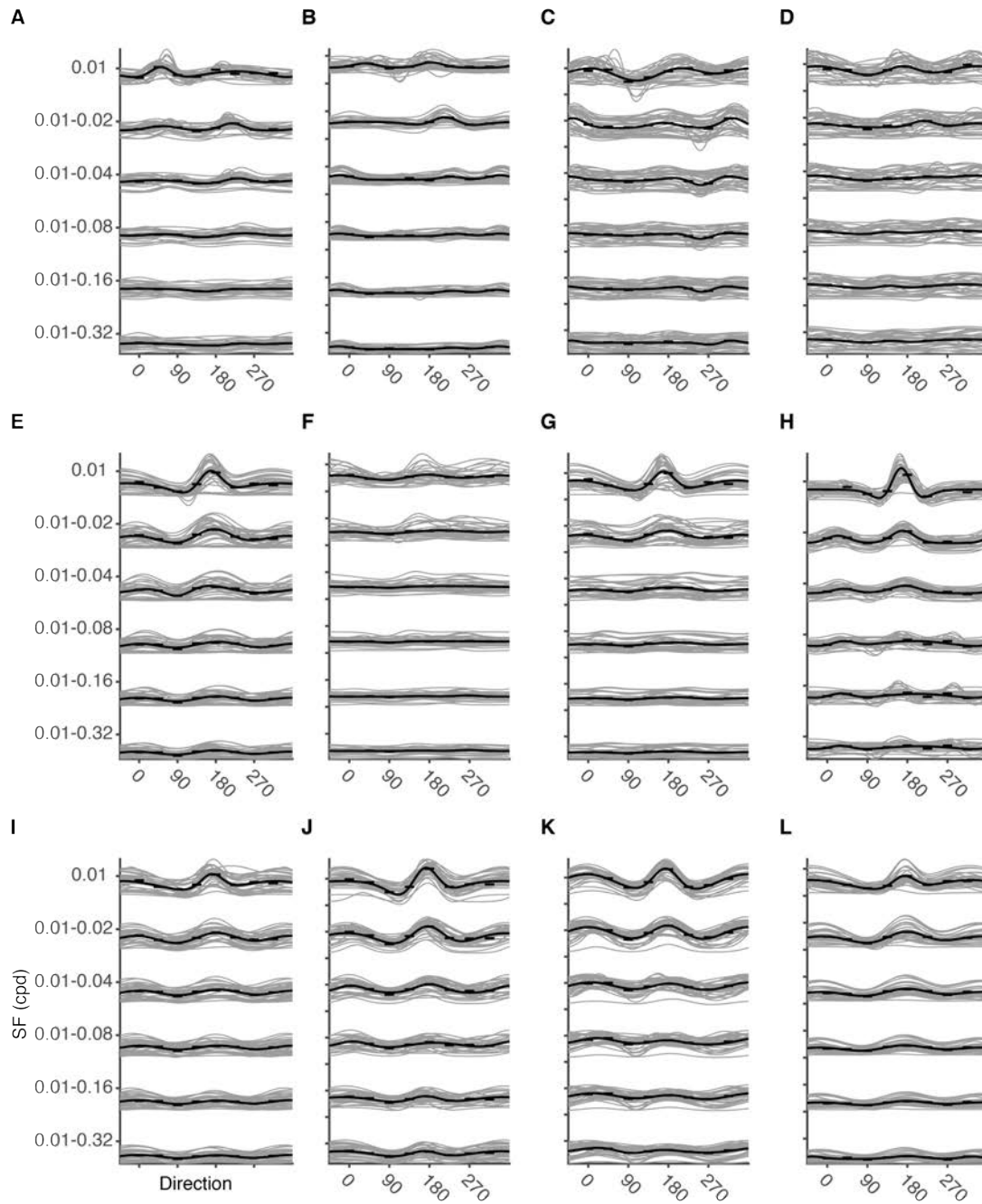


Figure 2.13: Direction tuning depends on the mixture of SFs used. Top to bottom: tuning functions pool over increasing numbers of SF. (A-L) show [0,1]-normalised tuning functions of all sites for each mouse.

modulations are manifest for low SFs, mainly using 1, and 1:2 SFs, particularly for the mice depicted in (E, G H, I J, K and L). At decreased level, the dip at 90° is still apparent at groups including higher SFs. These results show that while the tuning preference is strongest at low SF it does seldom change for higher SFs. In contrast, when calculating directional tuning functions at each SF differently, a different picture emerges as could be seen in Fig. 2.9. Directional tuning may depend on the SF and is not necessarily a property that is unrelated to the SF at which it is displayed.

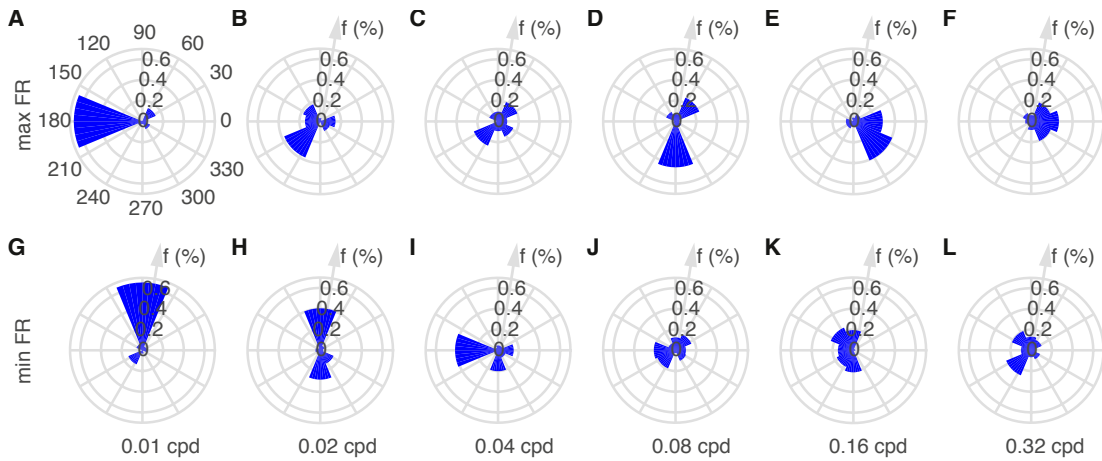


Figure 2.14: Frequency of maximum and minimum FR of each MU is affected by the underlying SF. (A-F) show the polar histograms of the average maximum FR for each SF, with SFs at increasing order, left to right. (G-L) corresponding for minimum FR.

Mean FR maxima and minima are affected by SF. Fig. 2.14 illustrates the differences in mean maximum and minimum FR for each SF used in this study. At low SF the maximum evoked FR appears to be 180° with a large majority of cells across animals. This drops off at higher SF and is washed out. (A-F) show average maximum FR at each presented SF, (G-L) present the mean minimum FR for the same SF, left to right increasing SF.

Apart from the different FR, it can be seen that polarity in responses decreases at higher SFs, with the effect of more uniform and less uniquely peaking polar histograms. Whilst for low SF at (A, B) and (G, H) histogram counts reach levels of 40-60% similar directions, higher SFs appear more evenly distributed with several directions accumulating levels around 20%.

A summary of the modes of each polar histogram of Fig. 2.14 is presented in Fig. 2.15. (A) depicts the directions that most frequently elicited the maximum FR responses

for each SF. The relationship between SF and directions that elicited the minimum FRs is given in (B). It is evident from the depiction that the relationship for the minimum FRs is not as smooth as for the modes of maximum FRs, which was also apparent in Fig. 2.8 (G-L).

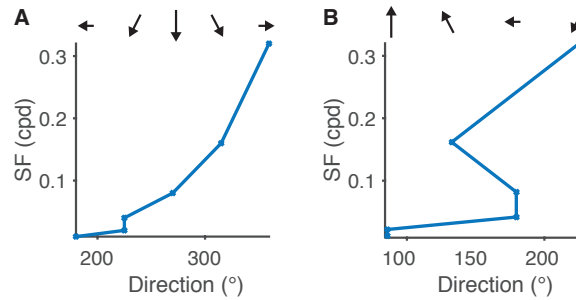


Figure 2.15: Mode of maximum and minimum FR at each SF indicate a clear progression of preferred directions. (A) illustrates the mode direction eliciting maximum FR at each SF. (B) Visualisation of the modes of the minimum FR distributions at each SF.

2.4.7 High performance in spatial frequency and direction decoding from MUA

Using either spatiotemporal MUA, SC or population rate (compare with Fig. 2.3), high classification accuracies of around 50% for SF decoding were achieved, against a chance level of 16.6% in the SF-decoding task. Decoding was done per individual mouse and then averaged. In the direction decoding task, there was a significant difference ($p < 0.001$, MWU, and $p < 0.01$ MWU) in performance for using MUA over the summed features, where STMUA reached a median classification performance of 70% (against a chance level of 12.5%), and SC and population rate attained approximately 40%. Decoding performance was determined with a confusion matrix and percentage correctly decoded samples.

Fig. 2.16 (A) shows the average confusion matrix for decoding SF from spike responses for the best decoder (Naive Bayes in both decoding tasks), where circle size and colour corresponds to %-correct classification. Decoding performance varied across experiments and animals, Fig. 2.16 (C-D) demonstrate 2-fold cross-validated decoding performances, averaged over 100 repetitions over all mice for all feature types and decoding targets (SF, direction). The dotted grey lines indicate chance level, which amounted to 12.5% and 16.6% for direction and SF, respectively. It is apparent that

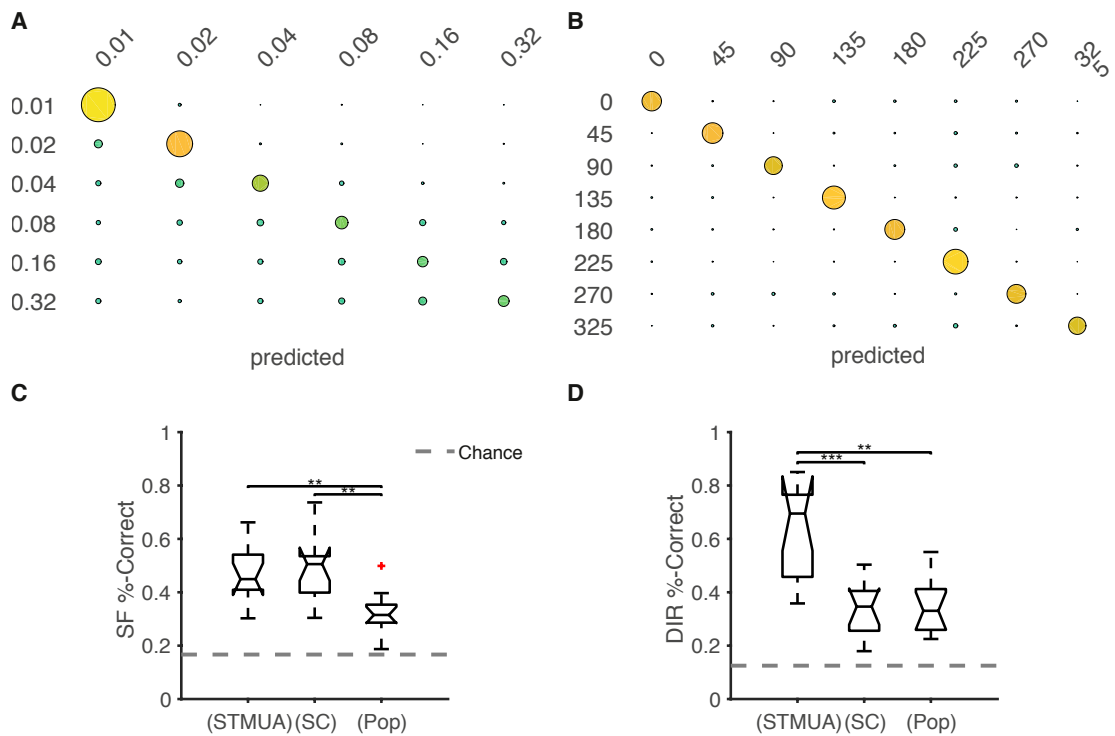


Figure 2.16: Good predictions for SFs and high performance on all direction predictions. Confusion matrices for (A) SF and (B) direction decoding, where circle radius and colour correspond to correctly classified parameters, on 5 ms binned data, 4 shanks. (A) shows the averaged confusion matrix of the Naive Bayes classifier on SF decoding, indicating a high prediction success for low SFs, and a tendency to underestimate higher SFs, indicated by misclassifications under the identity line. (B) same as in (A) on direction decoding, demonstrating a consistently high correspondence between predictions (x-axis) and actual directions (y-axis). (C) depicts correct classification rates for SF-decoding of 2-fold cross-validation averaged over 100 repetitions, for binned spike responses STMUA, vector of spike counts of all channels SC and population rate (Pop). (D) same as in (C) but for direction decoding. Dashed line (grey) denotes chance levels. MWU, where ** indicates $p < 0.01$ and *** $p < 0.001$

particularly low SFs scored high decoding accuracy.

Panel (B) of Fig. 2.16 reveals the average confusion matrix for directional decoding achieving an evenly high classification performance for all directions, albeit reaching slightly lower average performance levels than with peak SF decoding. Median performance for SF decoding with the Naive Bayes classifier as depicted in panel (C) of Fig. 2.16 was 50.2% (chance level 16.67%) with SC, whereas the median direction decoding performance (D) achieved 69.1% with STMUA features (chance level 12.5%). In

the boxplots, the central mark represents the median, the bottom and top edges the 25th and 75th percentiles. The top and bottom whiskers indicate the extreme data points which are not considered outliers, while the outliers are indicated individually in red crosses. The different features excelled with varying degrees of success, in particular in (C), SC marginally outperformed STMUA ($p > 0.05$, MWU), but both STMUA and SC outperformed the population rate ($p < 0.01$, MWU). However, for direction decoding, STMUA features perform significantly better than SC ($p < 0.001$, MWU test) and population rate ($p < 0.01$, MWU test).

In the direction decoding task, 80 samples (10 samples for 8 directions) were classified at 0.02 cpd, for which an *error* rate of $< 70\%$ against chance level of 12.5% corresponds to a significant classification performance at $p < 10^{-4}$, which resulted in $p < 0.001$, 1-sample sign test against chance level. The SF decoding task involved 60 samples (10 samples at 6 SF), as SF decoding was only estimated at peak direction of 180° .

The different decoders achieved comparable results in decoding SF and direction. For SF decoding, STMUA median decoding performance varied between 45.5% for Naive Bayes and 34.7% for the classification tree. The SC features achieved medians between 51.2% knn and 42.6% (classification tree), and population rate features between 34.5% (knn) and 30.0% (NB). Direction decoding attained medians between 33.8% (classification tree) and 69.1% (NB), SC features 27.7% (classification tree) and 40.1% (LDA), whereas population FR revealed medians between 23.3% (LDA) and 31.1% (NB). All results showed statistically significant classification performance ($p < 0.001$, 1-sample sign test against chance level).

A comparison of decoders and their dependency on numbers of shank and bin width is presented in Appendix 2.

2.5 Discussion and conclusions

In-vivo extracellular MU electrophysiological experiments were developed, performed and evaluated in primary visual cortex of the anaesthetised mouse, to address questions about stimulus information at the earliest cortical processing stage. Analysis of the in-vivo electrophysiology experiments in left hemisphere V1 of the Isoflurane-anaesthetised mouse presented here revealed that left forward drifting gratings consistently evoked the highest neuronal responses. This is a result at odds with the widespread understanding of random organisation of orientation selectivity in rodents. Spatial and directional tuning properties of MUA appeared very similar among animals, with a high signal

correlations of the tuning functions, and a lower noise correlation. Further, direction selectivity, in particular the preferred direction, may be dependent on the SF, and change with the SF. Finally, different MUA features reached high classification rates in spatial and directional decoding tasks. In direction decoding STMUA features attained much higher classification rates than population rate or SC features, whereas SC reached better results than the other features in decoding SF, suggesting that different stimulus parameters are encoded differently, and confirming that MUA contains spatial stimulus information.

Strongest responses to gratings moving into the visual field

As already described by Ringach et al. (2016) who found that the direction tuning similarity decreased with cortical distance, this study confirms a high similarity between MUA tuning (both SF and direction) across different locations. In particular, we found an overrepresentation of preferred responses to leftward moving gratings (equivalent to an object moving from right temporal to nasal visual field) in left V1.

This overrepresentation does not necessarily contradict the current understanding of rodent visual cortex being randomly organised, as it could be seen as a salt-and-pepper organisation with particularly large "pepper" grains representing, in this case, leftward moving gratings. It has been known that cardinal directions exhibit stronger or more stereotyped responses, yet, it is notable to see that visual movements in the opposite direction of the optical flow during running evoke highest responses. Rightward moving objects, e.g. during forward movement (roughly corresponding to 0°), might thus be the more commonly observed visual stimulus, but maybe not the behaviourally most relevant.

Rodents are prey animals and close to the ground, and their eye position is more lateral and superior than e.g. cats, which enables them to identify and flee when pursued by a predator, which may come from the back, and most certainly from above. Looming stimuli and overhead sweeping discs were indeed shown to induce flight or freeze responses in mice (Yilmaz and Meister 2013; De Franceschi et al. 2016) and thus their detection is very behaviourally relevant. The inward drifting gratings at a large SF resembling an object moving into the field of view are perhaps the most resemblant to such looming stimuli, and as such similar to the "attacking" direction from behind. The average vector in Fig. 2.8 (C) points mainly both in leftward and downward direction, which may represent the movement of an attacking predator, which is thus in line with the overrepresentation observed in this study. The dip in 90° might be

less behaviourally relevant, as an object or the world moving upwards are cases not frequently observed or simply do not pose a threat to the animal. This may play an important role in the detection of predators (i.e. it would be easier to detect a target stimulus that approaches from behind rather than one the mouse approaches).

Spatially-selective tuning in MUA

MUA recorded from mouse primary visual cortex were selective to SFs and exhibited either bandpass or low-pass properties. The MU studies could confirm the median preferred spatial frequency to lie around 0.02 cpd, consistent with data reported for single units elsewhere (Niell and Stryker 2008; E. Gao, DeAngelis and Burkhalter 2010; Prusky, Alam et al. 2004; Umino, Solessio and R. B. Barlow 2008; Vreysen et al. 2012). Peak SFs revealed a bimodal distribution, with one peak at the lowest SF, and the secondary peak at 0.028 cpd. This is in accordance with the observed bandpass (peak unequal to zero) and low-pass (monotone decreasing) properties. The median -3 dB cut-off frequency lay at 0.12 cpd, which is exactly the SF limit used in the literature to generate noise movies that drive a maximum number of neurons, e.g. by (Niell and Stryker 2008).

Direction-selective tuning in MUA

Analysis of MUA of multi-shank laminar electrophysiological data from left mouse V1 indicates a directional preference of moving gratings around 180° (leftward moving) at varying modulation depths. This was particularly prominent at low SF of 0.01 cpd and deteriorated at higher SFs (Fig. 2.9), suggesting that direction tuning may depend on the SF, in agreement with other recent reports (Ayzenshtat, Jackson and Yuste 2016).

Strong and reliable directional tuning was observed at low SFs of 0.01 - 0.02 cpd of similar shape between sites and mice (Fig. 2.11). Directional tuning functions resembled each other across cortical depths and between mice as was evident from the Pearson signal correlations between tuning functions (Fig. 2.10 and Fig. 2.12). The same tuning functions were less correlated for tuning functions calculated for fits at high SF. This high correlation of tuning functions contradicts the widespread understanding of random connectivity in mouse V1, however recent studies, e.g. (Kondo, Yoshida and Ohki 2016; Ringach et al. 2016), also support that there may be more structure in V1 than was previously reported.

Directional tuning functions on the normalised responses also visually showed a high similarity for some of the mice, as was shown in Fig. 2.9, particularly at low SFs. This

tuning rapidly decreased at high spatial frequencies, flattening out the tuning functions. Tuning peak sometimes shifted towards different preferred directions at higher SF, which was also observed by (Ayzenshtat, Jackson and Yuste 2016). The modes of directions that elicited maximum FR appeared to smoothly transition from 180 to 360°. This suggests that if direction selectivity varies with SF, it could be possible to encode both size and direction information in the same population, given a sparse code.

Pooling over a larger number of SF to increase the amount of trials when calculating normalised tuning functions emphasised the strong influence of responses at the lowest SF on the tuning functions (Fig. 2.13), as the higher average FR of the low SF strongly influence the average used to compute the tuning function fit.

Maximum FRs indicated that specific directions were preferentially distributed around 180° (leftward moving grating, Fig. 2.8 (A)) - a result at odds with previous studies (E. Gao, DeAngelis and Burkhalter 2010; Prusky, Alam et al. 2004; Niell and Stryker 2008). In contrast to what has been suggested in the literature (E. Gao, DeAngelis and Burkhalter 2010), these polar plots indicated that certain directions were overrepresented across the visual field (Fig. 2.8). Preferred directions, and anti-preferred directions (distribution of minimum FR) were not uniformly distributed (both $p < 0.001$, Rayleigh test for non-uniformity of circular data).

Orientation and direction selectivity was subject to the underlying SF used, a result which has recently been shown by (Ayzenshtat, Jackson and Yuste 2016) in Ca^{2+} -Imaging study of Layer 2/3 neurons. Calculating the selectivity indices over all SF resulted in a median OSI of 0.28, and a median DSI of 0.20 further illustrate the selectivity of MU data. Yet, one may argue that the measure of DSI and OSI may overestimate the true underlying selectivity (Mazurek, Kager and Van Hooser 2014), which is why the more conservative measures L_{osi} and L_{dir} were also included. These provide lower and concordant values to DSI and OSI at much lower values. L_{osi} and L_{dir} are 0.06 and 0.04, respectively. All measures reveal significant non-zero selectivity ($p < 0.001$, 1-sample sign test).

Selectivity indices estimated at 0.01 cpd only resulted in much higher values, at OSI 0.49, DSI 0.36, L_{osi} 0.20 and L_{dir} 0.10, suggesting a dependency on SF involved.

Decoding performance well above chance indicates substantial information in MUA

The use of MUA to classify multiple visual stimuli was demonstrated. Solely using MUA features for decoding directions or SF of drifting gratings, performances well above

chance level were achieved. This suggests MUA can be used to efficiently decode different visual stimuli, with a directional decoding performance of 69.9%, indicating MU contain substantial information about spatial stimulus structure in mouse V1. In particular, comparing different stimulus features such as spatiotemporal patterns STMUA, SC and temporal population responses illustrated how different stimulus features are encoded differently. With a NB decoder that keeps assumptions about the data minimal (naive implying a strong independence assumption), direction decoding achieved highest performance with STMUA features, at great superiority over the other SC based features. For SF decoding, however, SC and STMUA features achieved similar predictions with SCs attaining slightly higher correct classifications than STMUA. This implies that SF may be more strongly represented as a SC feature, whereas directions follow a spatiotemporal pattern, or are encoded in a more population-wide response, where spatial or temporal information is required to decode the stimulus.

Further, while performances well above chance level were achieved, classification rates were highest for low SFs and introduced more false predictions at higher SFs, as was visible from the confusion matrix where performance dropped in a similar fashion as in the SF tuning functions. One factor that may play a role in this is that if SF were indeed encoded mostly via SC, higher SF do not evoke strong responses, and particularly at higher SF similarly low mean FRs in the SF tuning functions emerged. This was not the case for direction decoding, which attained equally high performances throughout the decoded directions.

Together, the findings propose MUA contains substantial information about stimulus structure in V1 and that MUA can be used to efficiently decode direction and SF, potentially a useful tool for investigating changes in cortical circuit representation in behavioural learning paradigms. In addition, mouse cortex may in fact be more similar in their processing strategies to monkey and cat than previously postulated (Juavinett and Callaway 2015). This an important step in extracting information inherent in neural signals for applications, which cannot rely on SUA stability, or which do not have the capacity for time consuming spike-sorting.

3

Distinct stimuli sample from different binary pattern distributions

In Chapter 2, examination of mean Firing Rate (FR)s revealed differences in direction selectivity, which was reliable across Multi-Units (MU) at different locations. This chapter aims to dig deeper by investigating the statistics of binary firing vectors, exploring the neural code on a finer time scale and in spatial relation to each other. Thus, this chapter goes beyond single-channel analysis of Chapter 2, and based on the datasets described in Section 2.2, extends the neural coding question to the population responses to the different stimuli, and stimulus types.

3.1 Introduction

Neural coding in the brain can be explored at different levels: at a microscopic level, where the composition and interactions of different proteins may be studied, over individual neurons and their dendritic trees, or at a macroscopic scale, examining neural ensembles and the signalling strategies between different groups of neurons. Progress in experimental recording techniques allowed researchers to increase the number of simultaneously recorded neurons (Stevenson and Körding 2011). However, to analyse large amounts of neurons and their interactions requires sophisticated analysis techniques that differ from individual cell analyses since population responses may act differently from isolated neurons.

Population activity studies showed that different ensembles can be linked to certain stimuli and prefer to fire together (Agetsuma et al. 2017; Womelsdorf, Bosman and Fries 2013; Rikhye and Sur 2015), that they can be inherently linked (Miller et al. 2014), that the population activity is in fact coupled to the overall excitability (up or down states) (Saleem, Chadderton et al. 2010), and less influenced by visual stimulation itself (Harris, Csicsvari et al. 2003; Schneidman 2016; Harris and Shepherd 2015), or

related to the strength of the stimulation (Reig et al. 2015). Ensemble responses are often characterised in terms of population FR (i.e. the summed activity of all simultaneously active cells in the population, i.e. their synchrony distribution), spatial or temporal correlations, or the distinct spike trains evoked by a certain stimulus, which are compared to the spike train profiles under varying conditions (Montijn, Vinck and Pennartz 2014).

One measure that lends itself to compare neural data under different conditions is the simultaneous firing configuration (Luczak, McNaughton and Harris 2015) of discretised and binarised individual spike times of each channel or neuron. In the following, the simultaneous firing of discretised (binned), binarised Multi-Unit-Activity (MUA) of spatially distinct channels is defined as *patterns*. Information-theoretic approaches are a method of particular interest for investigating these *patterns* as they allow quantification and characterisation of the information content and their transmission features of these high-dimensional neural signals.

These *patterns* may have different probabilities of occurring depending on what process or context generated them. For example, a *pattern* reliably evoked under visual stimulation of e.g. a drifting grating may be unlikely to be observed under grey screen (representing lack of stimulation) or a different type of stimulus (Miller et al. 2014). It has been shown that activity of populations, discriminability and spiking reliability are contingent on both sensory inputs and internal states (Gutnisky et al. 2016; Rikhye and Sur 2015). Spontaneous Activity (SA), neural events present during quiescent wakefulness and passive attention, has been hypothesised to play a role in memory recall and consolidation, and in gating of sensory inputs (Luczak, Barthó and Harris 2013; Romano et al. 2015). SA may be similar in shape and appearance (e.g. synchronous events, correlated activities) to sensory responses (Luczak, Barthó and Harris 2009; Han, Caporale and Dan 2008; Berkes et al. 2011; Carrillo-Reid et al. 2015). This implies that the same networks underlie cell activity in both SA and driven contexts, or: There should be no difference between intrinsic probability of observing a particular *pattern* and under visual stimulation. Yet, other effects such as locomotion have been shown to enhance stimulus encoding and thus influence *pattern* probability (Dadarlat and Stryker 2017). With these differences in *pattern* occurrence, comparing *pattern* distributions under varying stimulus conditions is non-trivial particularly for large state spaces.

Different mechanisms or stimulus components can be responsible for *pattern* generation (Montijn, Vinck and Pennartz 2014; Miller et al. 2014), which may lead to distinct

subsets of the state space being activated under certain stimulus conditions. For example, Carrillo-Reid et al. (2015) showed that neurons were part of ensembles that fire in precise spatiotemporal sequences both under stimulation and absence of sensory inputs. They further showed it was possible to use these intrinsic activities to predict future temporal sequences under stimulation. While this may be an extreme case, variations of overlapping subsets (Sadovsky and MacLean 2014) or sampling biases disguising the origin of differing populations may exacerbate the quantification process. Comparing individual **pattern** probabilities quickly becomes infeasible given limited sample sizes and many unobserved states (Pillow and Latham 2007; Kass, Ventura and E. N. Brown 2005; O'Donnell et al. 2017).

That is why it is important to identify statistical derivatives and to pursue more holistic approaches, particularly those that can handle such problems (Park et al. 2013). Information theory describes the mathematical study of coding of information, and is, thus, a suitable field to quantitatively examine theories how the brain encodes and processes stimulus information. Shannon entropy (Shannon 1948; Ré and Azad 2014; Cover and Thomas 1991) is an information-theoretic measure quantifying the amount of uncertainty in a signal. It is minimal in deterministic systems and maximal if each possible state is equiprobable. It may vary under different stimulus conditions informing about **pattern** diversity. It is an often used metric in decoding (Quiñero Quiroga and Panzeri 2009; Borst and Theunissen 1999) and was used in quantifying information in retinal ganglion cells (Palmer et al. 2015). Similarly, comparing information content in terms of Mutual Information (MI) can cast light on how a neural population carries information about different types of stimuli or other properties (Kraskov, Stögbauer and Grassberger 2004).

This chapter applies state-of-the-art data analysis techniques with particular focus on information-theoretic approaches such as Shannon entropy and MI on MUA **pattern** responses. It seeks to address questions about how different stimulus conditions and ongoing activity affect population level responses in Primary Visual Cortex (V1) in anaesthetised mice. Information content is quantified for spatial **patterns** and contrasted with that contained in the population rate (i.e. summed activity across the neurons or channels, thus, discarding spatial information). With the help of Shannon entropies, Jensen-Shannon-Divergence (JSD) divergences between **pattern** distributions are computed and used to examine how similar the distributions are during varying stimulus conditions, probing if the traversed **pattern** spaces are stereotyped for certain stimuli or stable under all stimulus and quiescent conditions. This is an important step in trying

to unveil how the brain encodes and transmits stimulus-dependent information.

3.2 Methodology and concepts

All data analysis in this chapter focusses on the same data sets in anaesthetised mouse V1 described in Chapter 2, Section 2.2. In this chapter, *stimulus type* or *stimulus condition* refer to the sets of electrophysiological recordings involving moving Gratings (mG), Spontaneous Activity 1 (S1), natural movie (nat), Spontaneous Activity 2 (S2), Temporal Frequency (TF) and Spontaneous Activity 3 (S3). Shannon entropy and MI are detailed in the Introduction, Chapter 1 Section 1.6.1.

3.2.1 Spatial patterns

Analysis is based on spatial patterns of varying sizes 8x1, 16x1 and 32x1 corresponding to 1, 2 and 4 shanks, and not taking into account temporal correlations (i.e. bins are assumed temporally independent). 16x1 and 32x1 pattern are created by concatenating adjacent 8x1 shanks (given the probe geometry) of each mouse. For 16x1 patterns, this results in 24 non-overlapping experimental sets (i.e. 2 for each of n=12 mice). A subset of the channels is used, because for entropy estimates of 2^{32} possible pattern states to be reliable would require many more samples. A spatial pattern, thus, denotes the binary firing vector (word) at one time bin. Entropy is estimated on 16x1 binary patterns, unless otherwise declared. In addition to patterns, population FR, i.e. the spatial sum across channels (illustrated in Fig. 2.3 of Chapter 2), are investigated to probe population activity without its spatial component.

3.2.2 Kullback-Leibler Divergence (KLD)

When dealing with ensemble patterns, a comparison of the empirical pattern distributions under varying conditions or among different populations may be of interest as well. Differences in these distributions may indicate that varying neural ensembles may be involved in generating them, or that the underlying statistics differed (e.g. cortical state changes), implying different encoding strategies. One way of measuring the distance between probability distributions is the Kullback-Leibler Divergence (KLD) (Kullback and Leibler 1951), a measure closely related to MI (Shlens 2007; Ré and Azad 2014; Nielsen 2010). KLD is often used in variational learning and approaches that seek to minimize the distance between a model and a data distribution. That

means the KLD describes the amount of information required to explain the data distribution P , when it is approximated by model distribution Q . It can be calculated as $D_{KL}(P||Q) = \sum_x P(x) \log \frac{P(x)}{Q(x)}$, where P is the true data distribution and Q is often called the model or approximating distribution, and $D_{KL}(P||Q)$ is pronounced the *Kullback-Leibler divergence from Q to P* . The KLD can also be calculated via entropy terms, $D_{KL}(P||Q) = H(P, Q) - H(P)$, with $H(P, Q)$ denoting the cross-entropy, and $H(P)$ the entropy of P .

It denotes the information gain, or how many bits are required to decode samples from P using model distribution Q , or equivalently, the amount of information lost when Q is used to approximate P (Boyd and Vandenberghe 2004; Sohl-Dickstein, Battaglini and DeWeese 2009; Roudi, Aurell and Hertz 2009). For the case $P(x) = 0$, the measure is interpreted as 0, since $\lim_{x \rightarrow 0} x \log(x) = 0$, and $Q(x) = 0$ requires $P(x) = 0$. It strictly requires P and Q to have the same **support**. Support here refers to the set of possible values of a random variable with that distribution, so the **support** of a function is the set of points where the function is not zero valued.

It is a non-negative, *non - symmetric* measure that does not obey the triangle inequality and is zero only if $P(x) = Q(x)$ (Cover and Thomas 1991; Shlens 2007). Thus, it is not a real distance, and $D_{KL}(P||Q) \neq D_{KL}(Q||P)$.

3.2.3 Jensen-Shannon Divergence (JSD)

The JSD is based on the KLD with the difference in that it is a real metric: It is symmetric and obeys the triangle inequality, and thus, unlike the KLD it measures an actual distance (Lin 1991). This makes it a preferable alternative to the KLD, suitable for comparing probability distributions letting us measure the similarity or distance between probability distributions (Ré and Azad 2014; Nielsen 2010; Cover and Thomas 2012; Tkačik, Marre, Amodei et al. 2014). It can be calculated as the average KLD between a mixture distribution M , and X and Y , respectively ($JSD = \frac{1}{2}D_{KL}(P||M) + \frac{1}{2}D_{KL}(Q||M)$, where $M = \frac{P+Q}{2}$). Alternatively, it can be calculated as *the entropy of the mixture distribution minus the mixture of the entropies*:

$$JSD = H\left(\frac{P+Q}{2}\right) - \frac{H(P) + H(Q)}{2} \quad (3.1)$$

For two probability distributions, and provided using the base-2 logarithm in the entropy estimators, the JSD is bounded between 0 and 1: $0 \leq JSD \leq 1$.

Although the KLD is often used in the literature, the JSD has its advantages in com-

paring distributions since it is a real metric. Yet, when instead of a model distribution and the true distribution, two true distributions are sought to be compared, the JSD is the favourable metric in this case.

One problem in comparing probability distributions that were created under different conditions is that they might not have the same **support**, i.e. one probability distribution may (only) contain distinct symbols from the other (Archer, Park and Pillow 2014). This is often dealt with by using a Dirichlet prior with α and β parameters of 1, which is equivalent to adding a pseudocount of 1 to the probability distributions (Granot-Atedgi et al. 2013; Archer, Park and Pillow 2013b). For probability distributions of small size (e.g. an 8-bit **pattern** space of $2^8=256$ possible states), this may be a straightforward solution. However, for distributions of higher order, where most of the non-zero probability states are not or never observed, this can introduce a substantial bias. Instead, in this case, it is possible to only add pseudocounts to the union of observed states in both distributions, giving them full **support** over observed **patterns**. This in conjunction with a suitable approximation method, e.g. an appropriate prior that can deal with unknown finite **support**, such as Centred-Dirichlet-Mixture (CDM), will lead to more reliable results.

Similar to finite sampling problems observed in MI and entropies, empirical estimates may result in negative JSD, particularly for very similar distributions (Raj and Wiggins 2008). This can e.g. happen when the distributions compared are based on very unequal numbers of samples, which can partially be accounted for by weighing the mixture distribution accordingly.

3.2.4 Multidimensional Scaling

Multi-Dimensional Scaling (MDS) is a data dimensionality reduction technique whose main use lies in visualising distance information in a dataset. Points that are close in a (high-dimensional) input space appear close after applying MDS. It takes as input a distance (or similarity) matrix, and tries to preserve edges (distances) between nodes (features) in input space (T. F. Cox and M. A. A. Cox 2000; Wickelmaier 2003). A distance (or similarity) matrix is a symmetric matrix consisting of pairwise distances (using a real distance metric such as Euclidean distance) between features or nodes. For example, let nodes represent London, Paris and New York, and edges denoting the distances between them, the similarity matrix will contain distances London-New York, London-Paris, and Paris-New York (all to all). MDS will try to retain the edges and cluster London with Paris while New York will be positioned further away.

Using the JSD as our distance matrix, it is possible to visualise similarities among probability distributions in a principled manner. This study uses the non-metric MDS technique employing Kruskal’s normalised stress criterion, where stress is normalised by the sum of squares of the inter-point distances. This was implemented as the *mdscale* function in Matlab (2017a) with default parameters.

3.3 Results

This chapter extends the study of the anaesthetised electrophysiological experiments of left hemisphere V1 under the visual stimulation of monocular full-field drifting gratings, natural scene movies and SA (grey screen mean luminance) described in the previous chapter. In particular, the binary firing vectors or (word/pattern distributions) and population FR are investigated. Information-theoretic approaches such as Shannon entropy are used to evaluate the similarities of SA and evoked responses. Analysis was based on simultaneous firing activities on recording sites of varying numbers of adjacent shanks (one, two and four), permitting information-theoretic analyses at different state spaces sizes, to examine low-level visual processing and neural encoding.

3.3.1 Stimulus types influence activity levels and numbers of uniquely evoked patterns

The first metric to compare neural activities (here **patterns**, binary firing vectors of one time bin) under different stimulus conditions is the number of unique **patterns** occurring during each stimulus type as an indicator for stimulus modulation. Fig. 3.1 (A) visualises the distributions of number of unique **patterns** in box-and-whisker plots over all 32×1 **patterns** for the different stimulus conditions for all mice. Of $2^{32} = 4.3 \cdot 10^9$ possible **patterns**, during spontaneous activity (S1, S2 and S3) only approximately half the **patterns** of those realised during stimulus presentation are generated. The median number of **patterns** during mG amounts to almost twice those of its associated SA, with similar yet less pronounced differences for nat movies and its associated SA, S2. Another decrease in total number of **patterns** is visible for TF and S3, which is attributable to reduced recording length (only 80 s for S3, as it was only 2 s per presentation in contrast to 14 s stimulus duration per trial in the TF set, in contrast to approximately 1200 s in S1 and 900 s in S2). A Friedman test yielded $p < 0.001$, suggesting that stimulus type affects the number of **patterns**. Concentrating on the differences between each distribution, some yield particularly significant differences in median ($p < 0.001$,

Wilcoxon signed ranks, Bonferroni corrected).

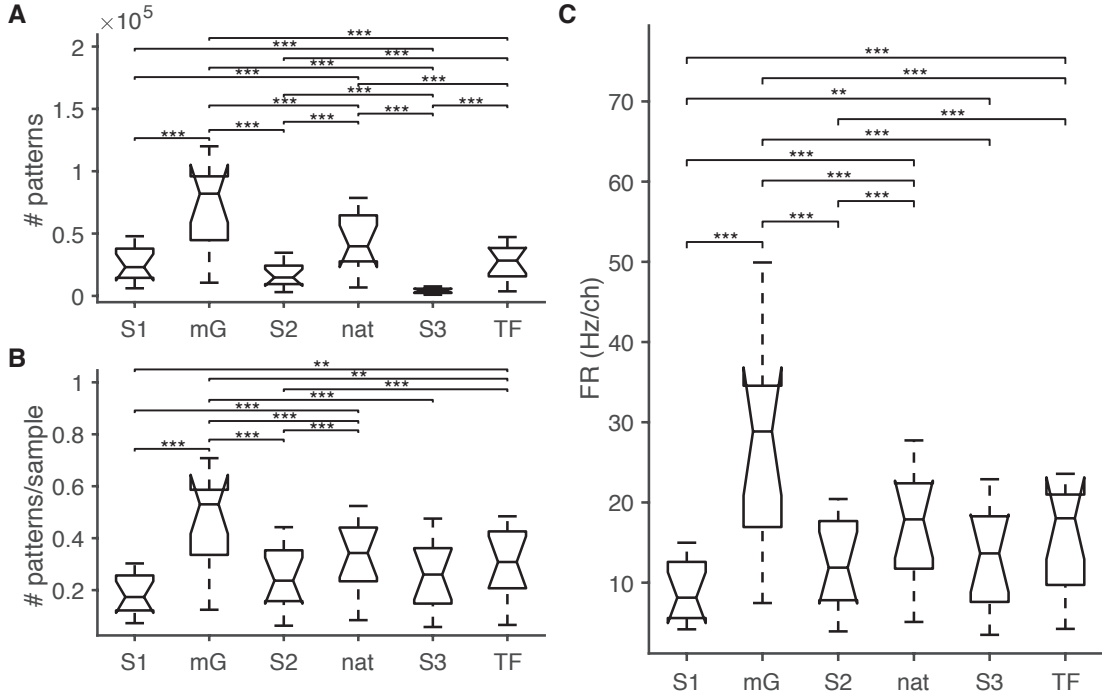


Figure 3.1: Number of unique 32-bit patterns per sample differs under different stimulus conditions. (A) Spontaneous activity generally traverses a smaller subset of unique patterns than evoked activities. (B) Accounting for recording lengths changes the impression of (A) in the number of unique patterns per sample. Values are averages of subsampling each category 30 times at the lowest number of samples (16 000). (C) Mean population FR/channel vary with different stimulus conditions, but the differences are not as severe as the difference in number of unique patterns, resembling the number of patterns per sample. ** indicates $p < 0.01$ and *** $p < 0.001$, Wilcoxon signed ranks, Bonferroni corrected.

Attempting to account for differences in recording lengths, we subsampled from all categories 30 times and calculated the average number of patterns and divided it by sample length (16 000 samples for all stimulus conditions). Fig. 3.1 (B) provides the number of patterns per sample. Subsampling and thus reducing the influence of recording length is changing the impression despite still indicating a highly significant influence of stimulus type on the number of uniquely evoked patterns/sample ($p < 0.001$, Friedman test).

For example, SA recorded interleaved with nat movies attains higher pattern numbers per sample than S1 ($p < 0.01$, Wilcoxon signed ranks, Bonferroni corrected), while mG

is significantly different from all stimulus types (all $p < 0.001$ apart from TF at $p < 0.01$, Wilcoxon signed ranks, Bonferroni corrected). According to Fig. 3.1 (B), the median number of unique patterns per sample lies approximately around 0.25 for most of the stimulus types, and is significantly higher during mG with a median over 0.5 patterns / sample, and a decreased value at S1 with a median just under 0.2 patterns per sample. Stimuli generally increase the number of patterns per sample to 0.3. Moreover, it is apparent that the number of patterns per sample during S3 is approximately the same as the number of patterns per sample during stimulus presentation TF, which was not apparent in (A). Performing multiple comparisons among medians of the distributions reveals significant differences among some of the medians (all $p < 0.01$, Wilcoxon signed ranks, Bonferroni corrected). Particularly differences among S1 and all other conditions (S2 $p < 0.01$, remainder $p < 0.001$) are striking (all Wilcoxon signed ranks, Bonferroni corrected).

Evoking sensory responses by visual stimulation modulates the FR, which may play a pivotal role in the numbers of patterns realised under different stimulus conditions. To see how FRs differ among the stimulus types, Fig. 3.1 (C) illustrates mean population FR per channel for each stimulus type. This is expressed as mean population FR per channel to obtain the same numbers of data points as in (A) and (B). Undoubtedly, the two measures form concordant pairs wrt. stimulus types. SA appears generally lowest, mG arises with highest median FR, and nat and TF exceed their respective SA. However, the differences among FR distributions do not seem as pronounced as for the numbers of patterns, particularly for S2, nat, S3 and TF. One interesting observation is that while in (B), S1 and S2 differed significantly in patterns per sample ($p < 0.01$, Wilcoxon signed ranks), there is no significant difference found in their FR in (C). Although FR differences are still significant for some stimulus types, the differences among stimulus types are more pronounced in the deviation of total number of patterns under each condition. The difference in FRs between evoked and spontaneous cases appears more pronounced than for the numbers of patterns per sample, particularly for TF and S3. In accordance with results of (A) and (B), stimulus type significantly influences mean population FR, μ_{popFR} ($p < 0.001$, Friedman test). Multiple comparisons of the medians pinpoints the highly significant difference in medians among mG and all other stimulus types (all $p < 0.001$ Wilcoxon signed ranks, Bonferroni corrected).

The concordance of medians in Fig. 3.1 insinuated a relationship between number of patterns and μ_{popFR} . This is further explored in Fig. 3.2, which depicts the number of patterns (n_p) per number of samples (n_s) against the mean population FR, for stimulus

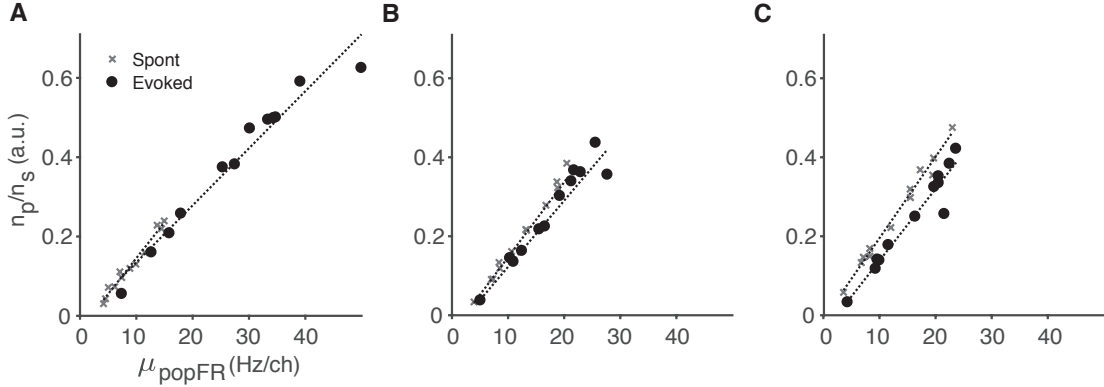


Figure 3.2: Number of patterns per sample correlates with mean population FR. The number of patterns per sample and μ_{popFR} are strongly positively and significantly correlated ($p < 0.0001$, correlation coefficient $r_{Pearson} > 0.96$ for each condition). (A) The linear fit of number of patterns per sample and mean population FR appears similar for S1 and mG. (B) S2 and nat have slightly (insignificantly) different slopes ($p = 0.055$, Analysis of covariance (ANCOVA)), which is also the case for S3 and TF (C), in addition to different y-intercepts. Axes in (A-C) are the same, with number of patterns (n_p) per number of samples (n_s) on the y-axes, and μ_{popFR} in Hz/ch on the x-axes.

conditions mG, nat and TF and their SA for 32-bit patterns at 5 ms bin sizes. The number of patterns per sample is highly positively correlated with the μ_{popFR} for all stimulus types and SAs ($p < 0.0001$, Pearson correlation coefficient > 0.96 for each condition, mean correlation coefficient 0.98 ± 0.005 standard error of the mean (sem)). Each group was fitted with a linear function of the type $y = mx + b$ and obtained a minimum R^2 of 0.88 (mean $R^2 = 0.94 \pm 0.02$ sem). Function fits are all very similar across stimulus conditions, and the function parameters are presented in Tab. 3.1. Y-intercept is slightly negative throughout, and the slopes range between 0.01 and 0.02 (a.u.), with all of the SA slopes exceeding the evoked ones. Evaluating regression results across all 6 stimulus conditions together, the six slopes indicated no significant difference ($p = 0.06$, F-statistic 2.29, ANCOVA).

Pooling each stimulus with their concurrent SA is an option allowing the comparison of slopes between stimulus types. ANCOVA found a significant difference of slopes at $p = 0.004$ (F-statistic 6.04). Similarly, the difference of slopes between grouped SAs and pooled stimuli resulted to be highly significant at $p < 10^{-6}$ (F-statistic 29.87, ANCOVA).

	intercept b (a.u.)	slope x (1/Hz)
S1	-0.0352	0.0181
mG	-0.0093	0.0144
S2	-0.0429	0.0190
nat	-0.0451	0.0168
S3	-0.0086	0.0206
TF	-0.0415	0.0182
Grouped SA	-0.0457	0.0211
Grouped evoked	-0.0022	0.0147

Table 3.1: Parameter values for linear fits depicted in Fig. 3.2. Fitting functions are of the type $y = mx + b$. Individual slopes are not significantly different ($p=0.06$, F-statistic 2.29 ANCOVA), but slopes between grouped SA and grouped evoked conditions differ highly significantly ($p < 10^{-6}$, F-statistic 29.87 ANCOVA).

3.3.2 Neural ensemble spatial pattern entropy weakly resembles MUA tuning functions

The tuning analysis of Chapter 2 focussing on MUA of individual sites is now expanded to spatial 16x1 binary word Shannon entropies. Pattern statistics are estimated over 16 sites unless otherwise declared, bins are assumed temporally independent. Comparison of the entropy properties for each stimulus case shows that neural ensemble pattern entropies resemble MUA tuning properties from the previous chapter (see Chapter 1 Section 1.6.1 for more details on entropy estimation).

Fig. 3.3 visualises pattern entropies (A-B) for different stimulus groups and types, where (A) groups directions, and (B) Spatial Frequency (SF)s. The mean population FRs across the same set is shown in (C-D). Grating pattern entropies in (A) are estimated on the probability distributions over all directions at the lowest four SF, in order to condense information about directions, as was presented in Chapter 2 that MUA at higher SFs evoked responses were less distinguishable (cf. Figs. 2.9 and 2.16 (A)). Pooling across all SF might thus even out or conceal directional differences. To complement this, in (B), entropies are estimated over the pattern distributions over all directions for each SF separately.

In Fig. 3.3, each line represents entropies of one of 24 experimental sets. In (A) and (C) the x-axis is ordered as follows: S1, moving gratings (0-325° in 45° steps, or 0.01-0.32 cycles per degree (cpd)), S2 and nat, S3 and TF. In (B) and (D) instead of directions, steps are 0.01-0.32 cpd.

This grouping also allows enquiry into where the other stimulus types, S2, nat, S3 and TF approximately lie in relation to the tuning functions of Chapter 2. As illustrated in Fig. 3.3 (A), S1 and S2 manifest the lowest entropies apart from TF, with nat displaying an entropy not much higher. Inspection of Fig. 3.3 (A-D) suggests that **pattern** entropies resemble mean population FRs across all stimuli and also seem to weakly approximate the tuning curves (cf. Fig. 2.9 and Fig. 2.11), with peaks around 180° and troughs around 90° across mice for the directions. Correspondingly, entropy over SFs roughly resemble the Difference of Gaussian (DoG) tuning fits observed for MUA in Fig. 2.11, with higher values at low SFs and lower values at high SFs.

In accordance with this, in (C, D) mean population FRs (μ_{popFR} in Hz/channel) estimated over the same samples of (A, B) exhibit the same qualitative shapes across stimuli. μ_{popFR} is low for spontaneous activities, shows a dip around 90° , a peak at 180° . Similar to the entropies, μ_{popFR} increases slightly again for nat movies.

Panels (A-D) insinuate a relationship between entropy and average population FR, which is further explored and illustrated in Fig. 3.3 (E). A positive sublinear relationship is apparent between entropy and average population FR. This is not only true for **pattern** entropies, but also entropies estimated using population FRs alone (entropies calculated with the Pitman-Yor-Mixture (PYM) estimator on the population FR). Population FR entropy is much lower than **pattern** entropy (17 vs 2^{16} possible states for **patterns**, $p < 0.001$, Wilcoxon signed ranks test), but both increase sublinearly with mean population FR. They are fitted with a cubic of the form $ax^3 + bx^2 + cx + d$ at high R^2 values of 0.98 and 0.99, respectively. Each symbol corresponds to one of 62 (48 gratings, 10 TF, 1 nat, three SA) stimulus cases in 24 independent experiment sets.

3.3.3 Mutual Information between neural activity and stimuli

Quantifying the information content of the spatial **patterns** and stimulus (total 62 stimuli) in terms of MI reveals that the spatial **patterns** contain 0.26 bits of information (median, cf. Fig. 3.3, (F)) for 5 ms bins. MI is maximal for empirical spatial **patterns**, in contrast to estimating MI in terms of population FR (sum over the sites), where the median lies at 0.09 bits (at 5 ms bins). Increasing bin widths greatly increase MI estimates. Yet, larger bin sizes may positively bias the estimate since the number of samples decreases (thus negatively biasing entropy).

Fig. 3.3 (G) is a reminder of how **patterns** are defined. Neural ensemble firing **patterns** are binarised, binned spike events. Time is discretised into bins of size Δt . A single spike **pattern** is a 16×1 binary vector whose entries are 1 or 0 corresponding to whether

the neuron spiked or not. Frequencies of occurring **patterns** are computed to estimate the empirical **pattern** probabilities.

MI is highest when estimated using **spatial patterns**. Fig. 3.3 (H) illustrates MI computed for **patterns** and population FR at 5 ms bins, and how the estimates are affected by randomly shuffling stimulus identities (labels) for each sample, or randomly shuffling **spatial patterns** site-by-site for each bin. **Spatial pattern** shuffling does not affect population FR, since the sum across sites remains unchanged.

Shuffling stimulus labels greatly reduces MI over the unshuffled results, as is evident from Fig. 3.3 (H). This is particularly striking for MI calculated via population FR, where MI is reduced to nearly zero (small positive fluctuations) for shuffled labels (shL, $p < 0.001$, 2-sample sign test). MI estimated via **pattern** entropies is greatly reduced for shuffled labels ($p < 0.001$, 2-sample sign test), but indicates residual information possibly attributable to negative entropy biases. In addition, randomly shuffling bins within a sample (**spatial shuffling**, shBin) reduces the MI estimates greatly for **patterns** ($p < 0.001$, 2-sample sign test), without affecting MI computed with population FR, as expected.

3 Distinct stimuli sample from different binary pattern distributions

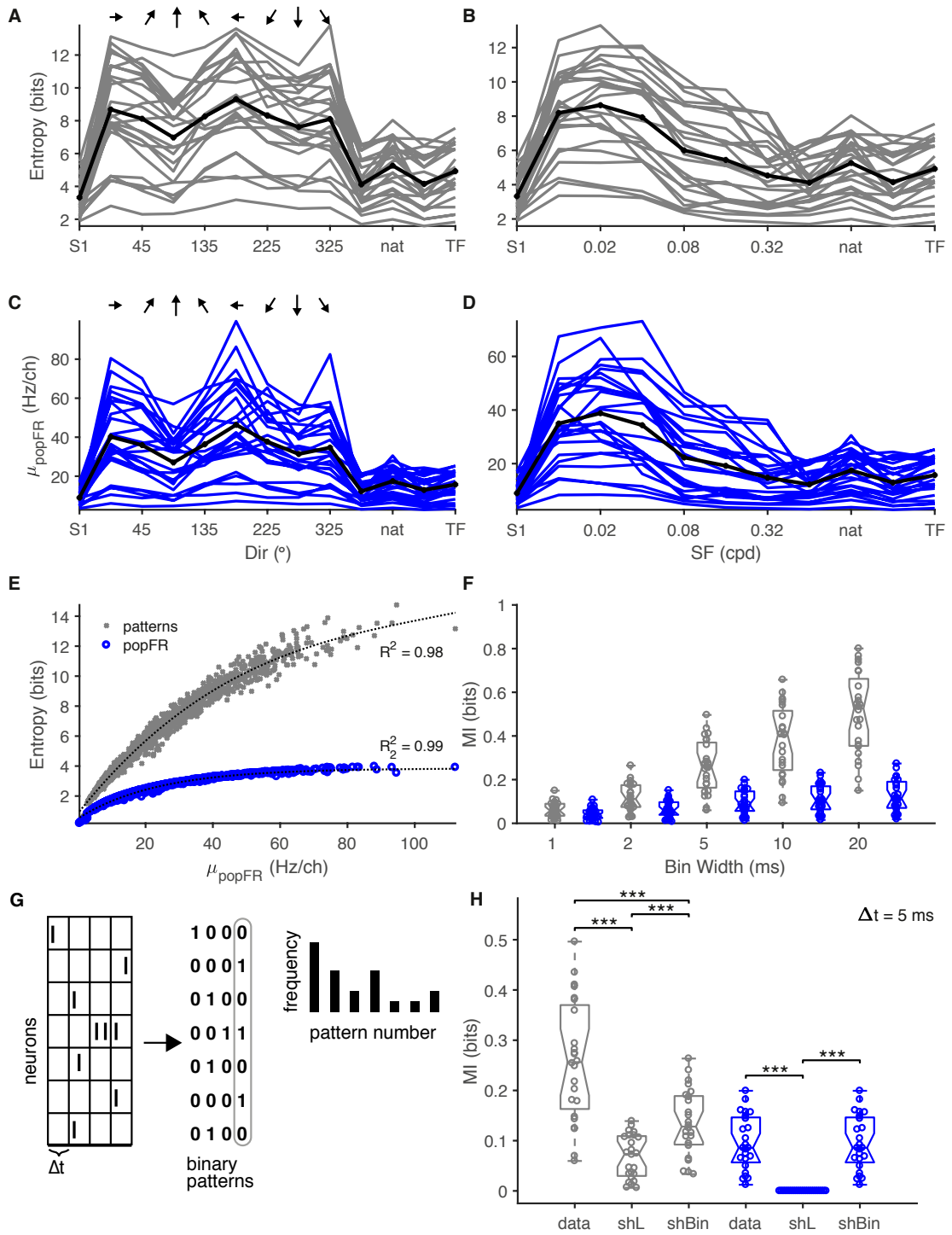


Figure 3.3 (previous page): Pattern entropies resemble μ_{popFR} across all stimuli and also seem to weakly (qualitatively) approximate the tuning curves (cf. Fig. 2.9 and Fig. 2.11). As in MUA tuning curves, peaks emerge around 180° and troughs at 90° for the directions. SFs roughly follow the DoG tuning fits observed for MUA in Fig. 2.11. Each line represents entropies computed over 16x1 binary patterns at 5 ms bins for each stimulus type. X-axis shows S1, moving gratings ($0-325^\circ$ in 45° steps, or 0.01-0.32 cpd), S2 and nat movies, S3 and TF. (A) Pattern entropy across all directions, pooled over the four lowest SFs. (B) SF entropies, pooled over all eight directions. (C-D) same as in (A-B) but for mean population FR in Hz/channel computed over the same samples. (E) Entropy increases with average population FR. Entropies of patterns and population FR alone (lower trace) increase sublinearly with μ_{popFR} . Each symbol corresponds to one of 62 stimulus cases (48 gratings, 10 TF, 1 nat, three SA) in 24 independent experiment sets. (F) MI between spatial 16x1 patterns and 62 stimuli emphasises the superiority of patterns over population FR, particularly with increasing bin size. (G) Neural ensemble firing patterns are binarised, binned spike events. Time is discretised into bins of size Δt . A single spike pattern is a 16x1 binary vector whose entries are 1 or 0 corresponding to whether the neuron spiked or not. Frequencies of occurring patterns are computed to estimate the empirical pattern probabilities. (H) MI between pattern and stimuli at 5 ms bins for patterns (grey) and population FR and shuffled labels (shL) and shuffled bins (shBin). *** indicates $p < 0.001$, 2-sample sign test.

3.3.4 Pattern probabilities evoked by natural movies and spontaneous activity resemble each other more than either moving gratings

Fig. 3.3 depicted that population FRs and entropies differed under mG, SA and nat movies. Comparing the probability of occurrence of each observed pattern under all stimulus conditions allows enquiry into whether the pattern statistics vary with stimulus types, or if distinct neural ensembles may be involved. This could be visible as differing probabilities.

Fig. 3.4 (A-I) displays scatter plots of pattern probabilities under different stimulus conditions in three example mice, for 16-bit patterns on log-log axes. Colour map corresponds to number of simultaneously active channels (0-16, blue to red), with a black diamond indicating the zero-pattern, which is the most frequent one in all sets and animals. In all cases, patterns with a small number of simultaneously active channels exhibit high probabilities, and patterns with a large number of co-active sites have generally lower probabilities, accumulated in the lower left corners. As can be seen in Fig. 3.4 (A), the zero-pattern, visualised as a black diamond, occurs at a slightly higher probability in S1 than during mG evoked activity. Analogously, a vast subset of patterns

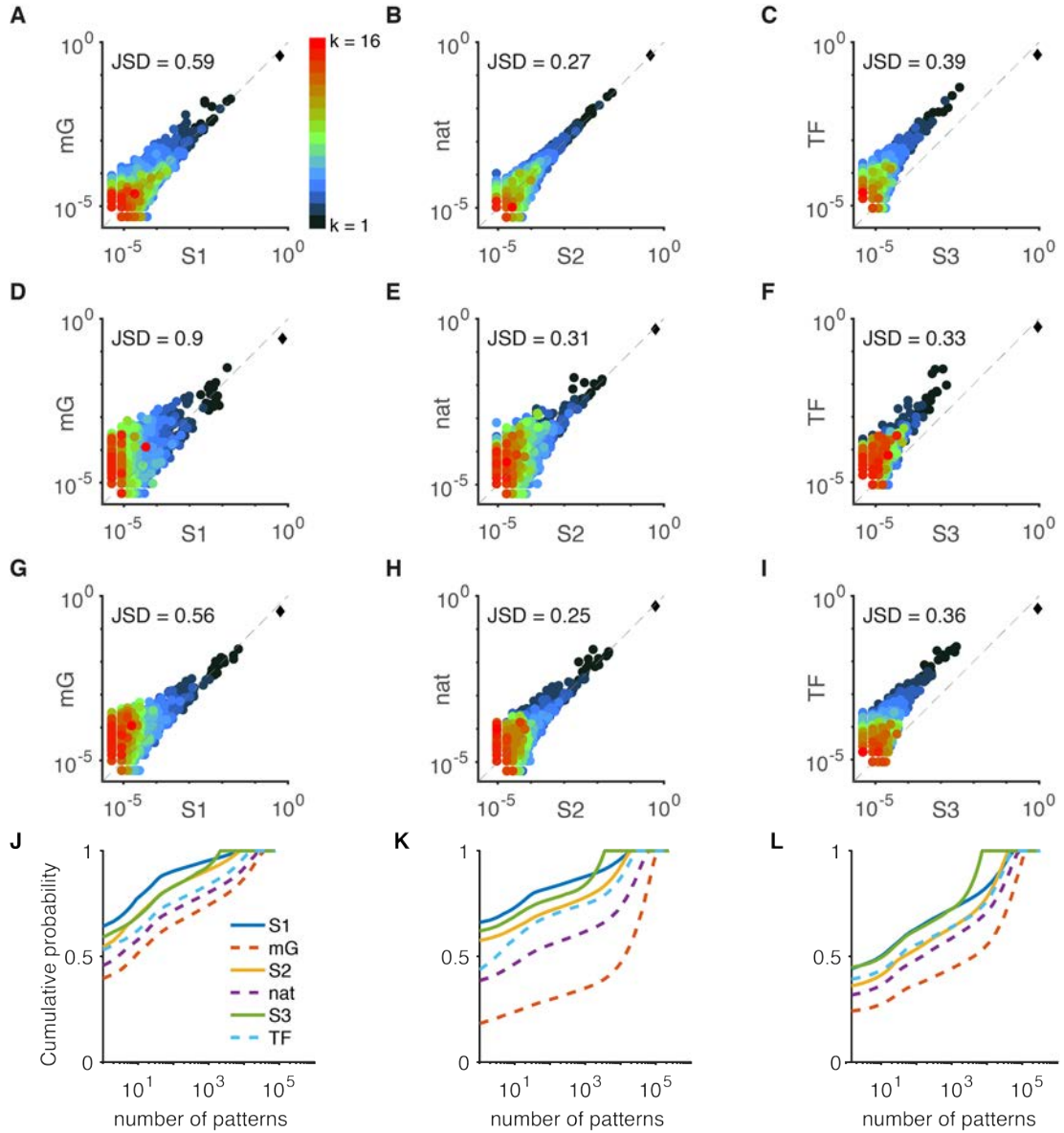


Figure 3.4: Empirical pattern probabilities vary under different stimulus conditions for 16-bit spatial patterns. (A-I) show the empirical 16-bit pattern probabilities between evoked and their associated SA for three mice. Panel (A) shows the pattern probabilities during mG against those of S1. The diagonal line indicates identity. Each dot represents one unique pattern (probability). Shades indicate number of simultaneously active channels (0-16). Diamond shape represents zero-pattern. (B) same as (A) for nat and S2. (C) same for S3 and TF. (D-F) and (G-I) follow the same structure for two more example mice. (J-L) show the (subsamped and averaged) cumulative probability as a function of the number of patterns for each stimulus type in 32-bit patterns for three example mice. Stimuli are shown in dashed lines, SA in full.

occurring during SA arises under mG-evoked activity with much higher probability, shifting away upwards from the identity line. This is particularly obvious for higher spike count patterns, which cluster more above the identity line at low probability values. This is reflected well by the fairly large JSD between the two distributions, which amounts to 0.59 bits. Panel (B) reflects the probability scatter between nat and its associated SA, S2. No activity, i.e. the zero-pattern, appears to be almost equally frequent between the two conditions, as suggested by the black diamond on the identity line. In addition, most pattern probabilities distribute axisymmetrical around the identity line for both low and high spike-count patterns, with increasing spread at low probabilities. The JSD is substantially lower than during gratings and their SA at 0.27 bits. Finally, (C) compares TF and S3, which appear in shape similar to (B), with a tight spread shifted away from the identity line towards TF, with considerably higher pattern probabilities for the evoked case. The zero-pattern is again displaced from the identity line, and JSD amounts to 0.39 bits.

These findings are qualitatively similar across mice, as is illustrated by two more mice in (D-F) and (G-I). Generally, the JSD is highest between S1 and mG, and lowest between nat and S2.

Fig. 3.4 (J-L) illustrate the cumulative probabilities of 32-bit patterns as a function of number of patterns for three example mice. Probabilities were repeatedly subsampled and averaged to account for different recording lengths. The y-intercept corresponds to the zero-pattern, which is visibly lower under stimulus presentation (dashed lines). Especially mG indicate many more activity patterns to account for the same probability mass as e.g. S1, which is particularly evident in (K).

It is difficult to disentangle influences by differences in FR from the disparity in pattern probability distribution induced by the different stimuli themselves. To investigate this further, Fig. 3.5 depicts the distributions of JSD and the distributions of the *difference* in mean population FR among stimulus conditions. There appears to be a relationship between JSD and the difference in μ_{popFR} across stimulus conditions, $\Delta\mu_{popFR}$. Fig. 3.5 (A) summarises the JSD of all stimulus presentation types, again illustrating the large divergences between e.g. mG and its associated SA, S1. The box plots indicate, as before the median as the central mark, the bottom and top edges the 25 and 75th percentile. Whiskers point to the most extreme data points, and outliers are illustrated as red crosses. Data points are classified as outliers if they exceed $q3 + w \times (q3 - q1)$ or less than $q1 - w \times (q3 - q1)$, where w stands for maximum whisker length, and $q1$ and $q3$ are the 25th and 75th percentiles. To compare the qualitative progress of JSD

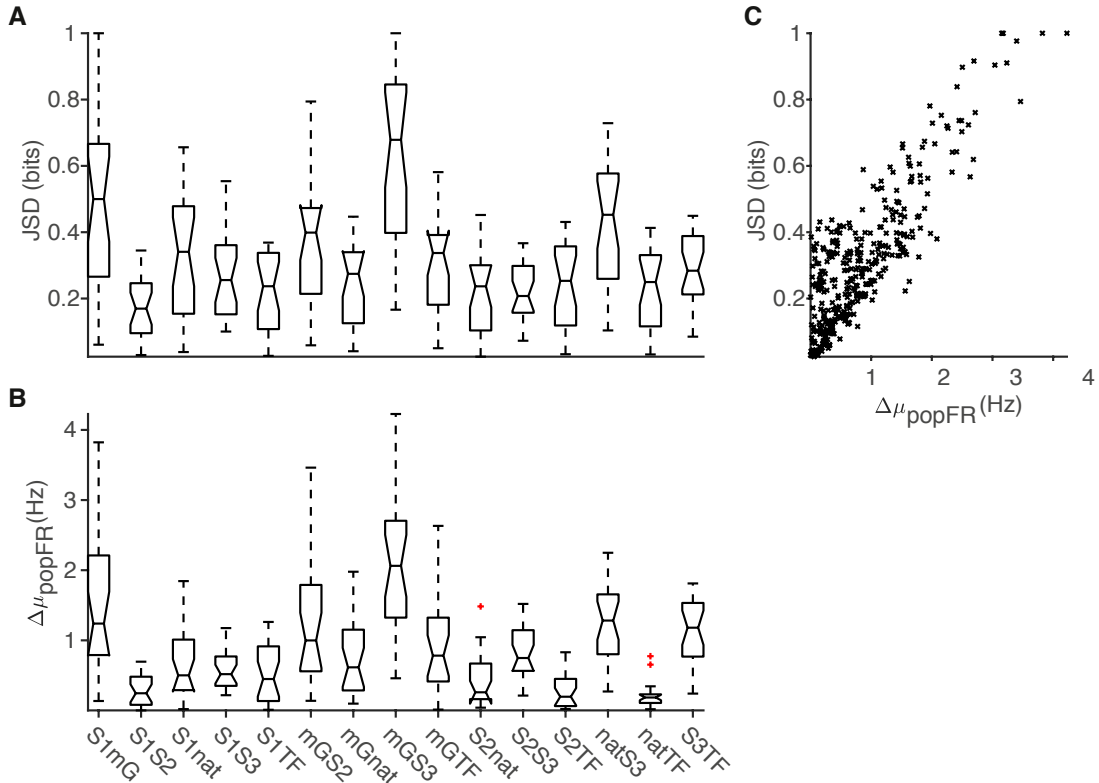


Figure 3.5: 16-bit pattern JSD and $\Delta\mu_{popFR}$ between all pairwise combinations of stimulus types are correlated. (A) Pairwise JSD distributions over stimulus presentation types show e.g. large divergences between S1 and mG and small divergences between e.g. S1 and S2. (B) $\Delta\mu_{popFR}$ between the same conditions as in (A) in Hz/channel appear in concordance with divergences from (A). This is further illustrated in (C), which shows one 'x' per stimulus condition for all mice indicating a strong positive correlation between difference in FRs and JSD ($r=0.85$, $p<0.0001$, Pearson).

values to the differences in FR, Fig. 3.5 (B) discloses $\Delta\mu_{popFR}$ for the same presentation types, in Hz/channel. Contrasting (A) and (B), a concordance in value progression is evident, which is further highlighted in (C) illustrating all JSD - FR pairs of all mice and stimulus conditions with an 'x'. Fig. 3.5 (C) suggests a positive correlation between divergences and difference in $\Delta\mu_{popFR}$, despite displaying a large variance particularly at low values ($r=0.85$, $p<0.0001$, Pearson, $n=24 \times 15$).

Using pairwise JSD versus stimulus presentation types, it is possible to compare pattern distributions beyond number of patterns and quantify how dissimilar the distributions are. This may indicate that certain stimulus types traverse similar patterns with similar probabilities or that some patterns in fact belong to a different distribution,

if they do not or rarely occur in other stimulus types. MDS is a technique that takes in a distance matrix and transforms it into a lower dimensional space whilst seeking to preserve distances (between distributions in our case). Using pairwise JSD as the input distance matrix, it is possible to visualise the pattern similarities in a simple graph illustrating how distributed the stimulus types are in relation to each other. This is delineated in Fig. 3.6, indicating where the pattern distributions lie with respect to each other in an artificial space.

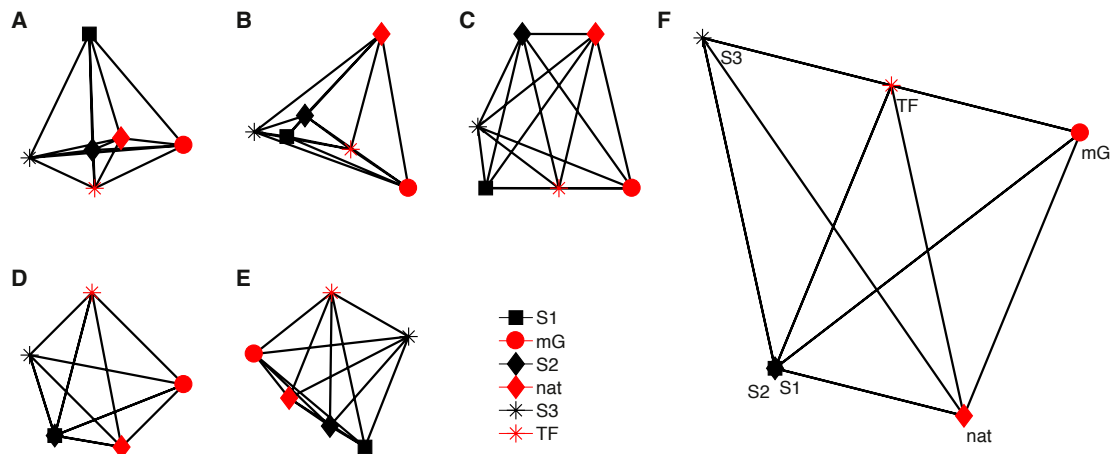


Figure 3.6: Stimulus types probability distributions reside in different pattern subspaces. Each symbol represents one stimulus type, colour indicates spontaneous activity (black) or stimulation (red). (A-E) illustrate five example sets of the low dimensional mapping using the JSD matrix as input to MDS. (F) shows the graph calculated on the average JSD over all mice.

Fig. 3.6 visualises the lower dimensional mapping (a.u.) for 5 example data sets (estimated on 16-bit patterns of 5 mice). (A-E) each represent one mouse. Each symbol stands for one stimulus type, colour code indicates visual stimulation (red) and spontaneous activity (black). Scrutiny of (A) evinces a close relation between *nat* and *S2* in the centre of the graph (diamond shapes), while the remaining evoked types (*mG* and *TF*) appear in the vicinity and the spontaneous cases are located further away. (B) offers a different graph in that *SA* and evoked types are much more distinctly clustered, with all *SA* in a tight neighbourhood, and evoked activities displaced, where *TF* is on a trajectory between *SA* towards *mG*, and *nat* appears in a different regime. The mouse in (C) also highlights a clear distinction between *SA* and visual stimulation, yet again indicating neighbouring regimes for *nat* and *S2*. Here, *mG* appears furthest from the centroid, yet gratings (*TF* and *mG* plus their interleaved *SA*) could be interpreted as

forming a cluster of its own, given the distance to **nat** and **S2**. The instance in (D) maps **SA** of **S1** and **S2** in the same spot, with the nearest evoked distribution again being **nat**. Fig. 3.6 (E) displays a symmetric graph with the symmetry line at roughly 45° marking the difference between evoked and spontaneous distributions. The edges between **nat** and **S2** is the shortest, with **mG** and **S1** aligned to it on either side, and **TF** and **S3** further removed, forming a trapezoidal shape.

Graph (F) is the low-dimensional MDS mapping on the *mouse-averaged JSD* matrix. The mean JSD over all mice results in a short edge length between **nat** and **SA** in contrast to drifting gratings (both **mG** and **TF**), which are located further away.

3.3.5 Spatial frequencies are clustered in pattern space

The JSD technique was next elaborated to build the JSD distance matrix across all stimuli (**S1**, 48 **mG**, **S2** and **nat**, **S3** and ten **TFs**, creating a 63x63 matrix). This allows visualisation of the combinations of **SF** and directions in pattern space. In this case, divergences are estimated over unequal numbers of samples. Sample sizes for spontaneous activities and **nat** movies are unchanged from before, but grating sample sizes are now reduced to 20 repetitions of 200 5 ms bins (i.e. 20 000 samples each).

Fig. 3.7 (A) highlights the map resulting from MDS over the mouse-averaged JSD distance matrix. Each circular symbol represents one grating type (of defined **SF**-direction specification), and colour of circular symbols corresponds to their **SF**. Black symbols depict spontaneous activity, diamonds the set of **nat** movie, the star **S3** and plus signs **TF**. It is evident from the figure that the arrangement is not random, but that gratings, in particular spatial frequencies form clusters in the transformed space. Again, it is apparent that **nat** movie patterns seem to be displaced from gratings at the top right corner (red diamond). However, **SA** recorded interleaved with **mG** appears to be in close proximity to mid-frequency gratings (green, 0.04 cpd), and almost central in the graph. The circular symbols appear not only clustered but also to be following a path at increasing **SF**, from blue to red, whilst decreasing inter-symbol-distance or scatter as well. All **TF** are far removed from the remaining stimulus types in the lower right corner, also following an apparent order of increasing **TF** (black to pale grey).

Fig. 3.7 (B) illustrates the same mapping with a different colour code, where each colour represents one direction on a circular colour map. The appearance is much more scattered, with some local clusters of directions, but no apparent overall structure in it. Local structures emerged e.g. for $45/225^\circ$ (green) in the centre of the graph, corresponding to the lowest three **SF** in (A). Direct comparison between (A) and (B)

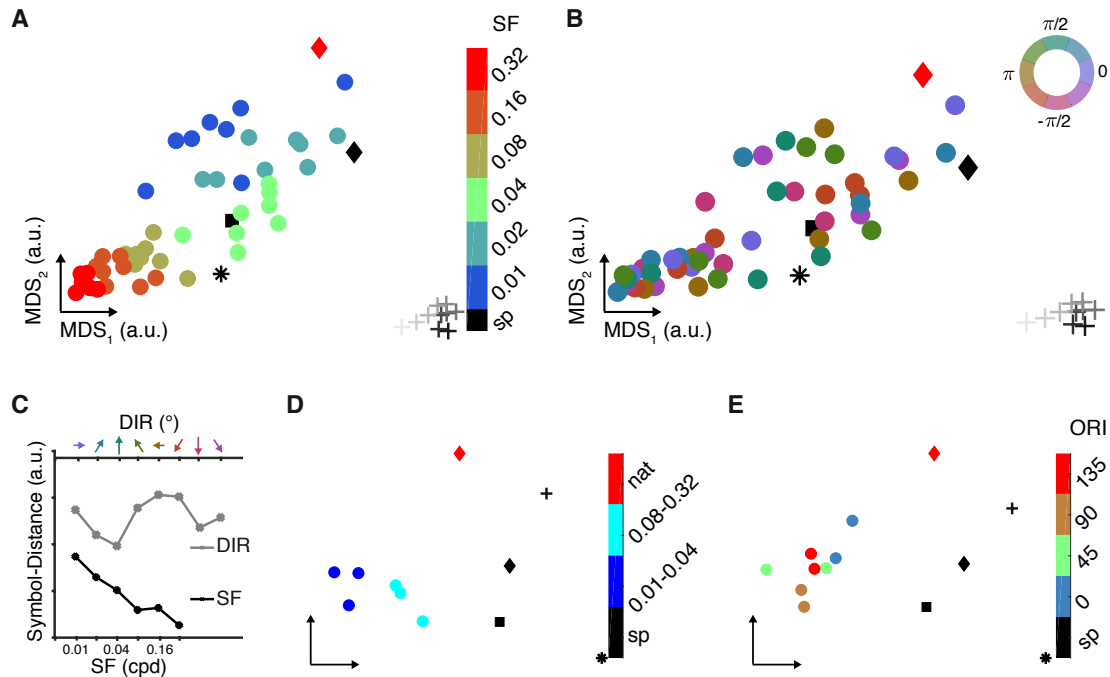


Figure 3.7: Pattern distributions conditioned on all stimuli appear clustered for spatial frequencies, and less structured for directions. (A) MDS on the mouse-averaged JSD distance matrices of the pattern probability distributions unveils a map clustering in SFs, whereas Direction (DIR) seem less globally structured in (B) with a circular colour map. In all subpanels, natural movie sets, both S2 (black diamond) and evoked (red diamond), are consistently at a distance from mG. Colours represent same SF or direction, respectively. Square indicates S1, diamonds S2 (black) and nat (red), plus signs TF (grey scale) and S3 (black star). (C) Intra-class symbol distances decrease for SFs, but not for directions. NB: different x-axes. (D) Pooled directions at each SF cluster into high and low spatial frequencies. (E) DIRs pooled across SFs appear very similar to each other in contrast to S1, S2, S3 and nat and TF. Colour code represents same orientations, for clarity.

suggests that orientations at the same SF tend to appear in close proximity to each other (e.g. two circular symbols at 0.02 cpd in (A), moss green, appear in brown 90/270° in (B)). Fig. 3.7 (C) shows the average within-class distances between symbols to quantify their scatter. Individual symbol distance was calculated as the Euclidean distance between symbols. Intra-class distance for SF decreases at higher SFs. Intra-class distances are generally higher for directions and do not appear to follow a clear structure. Inter-class distances were high for SF (not shown), given their localised clusters. Average distance between directions was small, given the large overlap among groups.

This observation is reinforced when grouping the data for SF alone (pooling trials over all directions for each SF), which is portrayed in Fig. 3.7 (D). Here, each circular symbol represents one of six SF, and JSD is calculated over all directions at the same SF. Again, the figure suggests a difference between nat movies, mG and spontaneous activities. S1 appears in the general SA area, further away from mG, or, the mGs form a cluster distant from the remaining presentation types. Between mGs, we can identify a sub-clustering of SFs in lower (blue) and higher (turquoise) SFs, with lower SFs further away from the centre of the graph, and thus further away from SA of the right side. The other visual stimulations, nat and TF emerge at the top right corner forming a distinct contrast to the SF clusters.

Similarly, Fig. 3.7 (E) pools all SFs with the same direction and calculating the pairwise JSD between the remaining 8+2+3 stimulus types reveals directionally distinct clusters: nat movies, TF, S1, S2 and S3 appear far away from the directions in similar locations as in the previous panel. In this representation, some of the directions emerge close to their collinear direction.

3.4 Discussion and conclusions

This chapter applied information-theoretic approaches such as Shannon entropy and MI to binary MUA pattern responses, to investigate how neural population activity is affected by stimulus types in V1 of anaesthetised mice. The brain is an epitome of an information processing device. Here, we examined how neurons encode and process stimulus-dependent information and how and if it differed in the absence of stimulation.

This study revealed that results found on single channel level (in Chapter 2) were also reflected at a population level. Shannon entropy of pattern probability distributions evoked by mGs roughly resembled directional and spatial tuning functions of Fig. 2.6,

and formed a distinct relationship with μ_{popFR} . MI was highest when estimated with **patterns**, i.e. including spatial knowledge, in contrast to population rates that only utilise the total population spike count (cf. Fig. 3.3). In addition, the number of unique **patterns** in each experimental condition depended on the stimulus type, which was tightly linked to mean population firing rate, μ_{popFR} .

Individual **pattern** distributions differed distinctly in direct comparison across stimulus types, which was quantified with the JSD. With the JSD, it was possible to visualise **pattern** probability distributions as graphs where edge length reflected the distance between distributions, and nodes representing stimulus types. This representation revealed that **nat** movies evoked **pattern** probability distributions most similar to those evoked during **SA**.

Spontaneous activity evokes more unique patterns than stimulus-driven activity when accounting for firing rates

As detailed in Fig. 3.1, the number of unique 16-bit **patterns** varied over stimulus presentation cases. The absolute number of unique **patterns** was highest for **mG** for all mice, and lowest for **S3**. One problem with this representation was that it did not consider recording lengths, thus, longer recordings naturally provided a larger number of unique **patterns** (assuming non-zero FRs and variation in timing, jitter etc.). This problem was addressed by normalising each stimulus type by the total number of samples, resulting in the total of unique **patterns** evoked per sample. With this normalisation, variability over stimulus types did not appear as pronounced any more. However, **mG** still emerged as significantly evoking a larger amount of unique **patterns** per sample than all other stimulus cases ($p < 0.001$, Wilcoxon signed ranks, Bonferroni corrected). **S3** was notable in its homogeneity of response patterns ($p < 0.001$, Wilcoxon signed ranks, Bonferroni corrected), demonstrating natural movies (which preceded the **S3** period) evoked periods of stereotyped activity after cessation. Yet, through normalisation by recording length **S3** surfaced in the same ballpark as **TF**, thus reducing its impact. One drawback of normalising by sample size (duration) is that the short presentation time of **S3** may bias the results as it could artificially increase the ratio of **patterns** / sample if there was an actual minimum number of total **patterns** in that regime. Balanced recording lengths would have eliminated this concern. The results in Fig. 3.1 (C) finally detailed the effects of stimulus cases on μ_{popFR} . In line with increased unique **patterns** per sample, the μ_{popFR} was highest during **mG**. While **S1** and **S2** differed significantly in their **patterns** per sample ($p < 0.01$), their FR were not found to differ significantly, suggesting a higher

pattern yield in S2 that cannot be explained by FR alone. It was shown that stimulus types had a highly significant influence on the number of patterns/sample ($p < 0.001$, Friedman test), as well as on the μ_{popFR} ($p < 0.001$, Friedman test).

The behaviour between number of unique patterns per sample and μ_{popFR} suggested a relationship, which was then further explored in Fig. 3.2. It highlighted a strong positive correlation ($r_{Pearson} > 0.96$, $p < 0.0001$), which was linearly fitted with a minimum R^2 of 0.88. All stimulus types revealed strong positive relationships between numbers of patterns per sample and μ_{popFR} . Grouping SA and evoked responses resulted in highly significant differences between slopes ($p < 10^{-6}$, F-statistic 29.87 ANCOVA). In addition, the slope computed over the aggregated SA exceeded that of grouped evoked slope by approximately 40%. This implies that the pattern variety during SA is larger than in evoked activities, when accounting for the smaller population FR. Also, patterns during evoked activity appear more reliable or stereotyped as has been reported elsewhere (Sakata and Harris 2009; Buzsáki and Mizuseki 2014), even to the degree that stimuli reduce the dimensionality of activity in line with findings by Mazzucato, Fontanini and La Camera (2016).

Entropies resemble MUA spatial and directional tuning profiles

A comparison of Fig. 2.6 and Fig. 3.3 revealed a distinct similarity between MUA spatial and directional tuning fits and entropies. With entropies and μ_{popFR} being modalities computed across spatial locations, it was possible to emulate earlier observations from population tuning fits seen in Fig. 2.6. There, it had already been shown that tuning functions of individual sites resembled each other. Taken together, it is evident that tuning properties are visible at both single-site and population level. Entropy properties appear to be fairly stable across locations and mice (apart from scaling differences).

Fig. 3.3 (E) disclosed a strong positive relationship between entropy and μ_{popFR} for both entropies estimated via spatial patterns and population FR. Entropies against μ_{popFR} were fitted with a cubic polynomial and achieved an R^2 of 0.98 (patterns) and 0.99 (population FR). The fitted function indicated a plateau at about 4 bits (theoretical maximum is $\log_2(17) = 4.0875$ bits) for population FR-entropies, while entropy estimated via patterns attained higher values tending to its theoretical maximum of 16 bits. A sublinear relationship between entropy and μ_{popFR} may reflect the sparsity of neural data. At low population FR, only few sites are active, and thus, only few patterns are observed, resulting in low entropy. At higher population FRs, more patterns can be traversed, resulting in higher entropy under the assumption of each site firing with equal

probability. Equally, at higher population FR, the number of simultaneously active channels is increased. This must reach a plateau once a certain FR is passed, and then decrease again. The conditional entropy of a response R given the number n of simultaneously active channels $H(R|n)$ is Bernoulli distributed for independent channels. A toy example proves for a 2^{16} pattern, that $\binom{16}{1} = 16$ and $\binom{16}{8} = 12870$, representing the number of possible combinations of patterns with one and eight simultaneously active sites. Picking the maximum μ_{popFR} of approximately 100 Hz/ch (from Fig. 3.3 (C)), we can estimate how many channels were active on average, per bin. Given 100 Hz/ch was estimated over bins of size $\Delta t = 5ms$. This means 200 bins of size 5 ms contained 0.5 spikes per bin and channel. FR were averaged across 16 channels, leading to averagely 8 sites being active simultaneously. Having 8 channels simultaneously active results in $\binom{16}{8} = 12870$ possible states, amounting to $H(R|8) = 13.65$ bits, which is roughly given in (E). This relationship must decrease at high μ_{popFR} . For example, at 200 Hz/ch, each channel requires to be active simultaneously (the all-ones pattern), and entropy of only one state is zero.

In conjunction with this, MI between stimulus and response estimated via population FR obtained values around 0.1 bits, whereas MI computed using patterns attained values more than twice as high, largely increasing at higher bin widths, emphasising the importance of their spatial representation. MI between spatial 16x1 patterns (for 2 shanks) and the 62 stimuli indicates a superiority in information content of spatial patterns over population FR, particularly with increasing bin size. However, larger bin widths may positively bias the estimate since the numbers of samples decrease (c.f. negative bias from entropy), which may affect the pattern-derived entropies more than the population FR one. Shuffling labels reduced this information to zero for population FR ($p < 0.001$, 2-sample sign test), and resulted in a small positive bias for MI calculated via patterns, as was evident from Fig. 3.3 (H). Spatially shuffling bins in the patterns significantly ($p < 0.001$, 2-sample sign test) reduced the MI estimate, again supporting the importance of spatial spiking configuration.

Natural movies may be processed differently from moving gratings

Pattern probabilities during SA (grey screen) and nat movies appeared to be fairly similar, both visually (Fig. 3.4) and in terms of the JSD, whilst mG seem to modulate pattern probabilities differently. The experimental design allowed for comparing SA recorded at different times during the experiment, which enabled us to account for different brain states or network excitability levels (Saleem, Chadderton et al. 2010;

Harris and Shepherd 2015; Gutnisky et al. 2016). Particularly *nat* movies and *S2* recorded in close temporal coherence (interleaved between stimulus repetitions) revealed a low divergence of *pattern* distributions with values comparable to divergences between *SA* recorded at early and late experimental phases. Fig. 3.6 illustrated a graph whose edge lengths corresponded to the JSD between stimuli types. It was evident that *nat* and *S2* were consistently placed within each other's neighbourhoods. It was argued by Luczak, Barthó and Harris (2009) that responses during *SA* may delineate the set of cortical responses, and the influence of *SA* on sensory processing (Schölvinck, Friston and Rees 2012; Luczak, Barthó and Harris 2013). The fact that *TF* and *S3* appeared furthest away in e.g. Fig. 3.7 may be linked to the timing in the experiment plus the difference in recording lengths, which may influence minimum possible probability. This may reflect different brain states, a change in excitability or gain, or that these stimuli are processed differently, with *nat* movies being closer to the default firing states. Natural movies with their high SFs and large amount of spatial detail drive the neurons at a highly fluctuating pace, whereas *mG* can evoke responses that are more sustained during the presentation period because of their high contrast and generally large spatial edges. Yet, non-optimal gratings, which have similar average FRs as *nat* movie-evoked responses still elicit very different spatial patterns, as was evident from Fig. 3.7 (A).

Berkes presented similar findings in ferrets (Berkes et al. 2011), which have structured orientation maps like cats, where particularly in adult ferrets *mGs* were most dissimilar to *SA* and *nat* movies. They postulated that a statistical model that is optimally adapted to a stimulus ensemble must have had prior experience to match the occurrence frequency and investigated the difference in *pattern* distributions (with a symmetrised version of the KLD) over the developmental period. (Miller et al. 2014) also argued for patterns observed during spontaneous activity to be linked to ensembles activated and formed during prior stimulus exposure. The current study ties in nicely here and confirms Berkes's observation for adult anaesthetised mice.

Okun, Yger, Marguet et al. (2012) argued that word distributions differed between *cortical states*, where brain state was estimated as the coefficient of variation as derived in Renart et al. (2010). In their paper (on rats and cats primary visual and auditory cortex), brain state was the main factor for *pattern* similarity, more so than the presented stimulus (or lack thereof) and all correlations were subject to population rate dynamics. Unfortunately, their model was a poor fit if strong correlations between subgroups of neurons existed that could not be explained by population FR dynamics. This sparked lively discussions between the groups (Okun, Yger and Harris 2013; J. Fiser et al. 2013).

In a similar investigation in behaving monkeys (Tan, Chen et al. 2014) observed that visual stimulation shifts cortical state to the asynchronous state.

However, the present study confirms that the pattern distribution during SA is, also in mice, more similar to nat movies than to gratings, as was shown in ferrets (Berkes et al. 2011), rats and cats (Okun, Yger, Marguet et al. 2012). Further, our findings do not contradict Okun's, that population rate dynamics may play an important role, as we recorded nat movies interleaved with SA in an attempt of matching or accounting for brain states throughout the recording. This should, thus, be encompassed in our estimates.

Spatial frequencies cluster in pattern space

Investigation of patterns induced by a battery of mGs revealed via JSD and MDS that SFs appear clustered in the MDS-transformed pattern space. SA and nat movies emerged at the periphery of pattern space, whereas SFs tiled the majority of it. Low SFs were clustered while retaining a high spread, and traversed in an orderly fashion to more densely packed patterns of higher SFs. The increase in pattern similarity at high SFs may reflect the detectability of the grating. High SFs may be more difficult for the mouse to detect, and thus evoked patterns may be represented similarly, and therefore, cluster. The large spread for low SFs on the other hand may correspond to the differences in directions. Tuning curves from Chapter 2 observed for both population and MUs were most dominant at low SF, where large differential responses were present at different directions. This directional difference may be washed out at higher SFs, resulting in less diverse pattern distributions. This may suggest that SF were the main driver for pattern space in the subcategory of mGs, and that this clustering can be subdivided at low SF to achieve a secondary tiling corresponding to directions of a grating.

Mean firing rates may account for some of the pattern distribution divergences

Dissimilarities in pattern distributions between stimuli may be attributable to different FRs induced by the choice of stimuli (optimal gratings evoke high FRs whereas nat movies may induce on average lower FRs with instantaneously high peaks). Spontaneous and nat movie evoked activity displayed a lower JSD than both/each to artificial gratings (Fig. 3.6). If neurons are more driven by (optimal) artificial stimuli, one might argue that this could automatically change the pattern distribution. However, non-optimal gratings with FRs similar to nat movies still appeared to elicit different responses. One

weakness in the current analysis may be that by grouping all of the `nat` movie frames together rather than looking at it frame by frame or e.g. in 1 s chunks (to get the same dimensionality as the gratings), we might lose information. Also, by splitting the movie in chunks, we may be able to investigate different FRs during the movie, or condition on certain frames.

One way to check individual FR influences could be to create surrogate data (e.g. homogeneous independent Poisson that match the individual site firing statistics, which is the maximum entropy solution given FR constraints (Schneidman et al. 2006)). This would use the mean FR for each stimulus, but will not reflect population FRs. Alternatively, surrogate data that match only the μ_{popFR} for each condition could be used to check if this dissimilarity is indeed dependent on population FRs induced by the stimuli.

In addition, it has been suggested (Okun, Yger, Marguet et al. 2012; Okun, Yger and Harris 2013) that instead of pairwise correlations between spike trains, population FR fluctuations may be responsible for the different `pattern` distributions and that considering population rate dynamics over simply mean FR was required to account for FR statistics (Tkačik, Marre, Mora et al. 2013) and that fluctuations in ongoing activity play an important role in population FR (Gutnisky et al. 2016). There has been considerable research into this with different models (Okun, Steinmetz et al. 2015; O'Donnell et al. 2017; Tkačik, Marre, Mora et al. 2013; Okun, Yger, Marguet et al. 2012; Gutnisky et al. 2016), and will be further addressed in Chapter 5.

Population dynamics, and population FR differences between the various stimulus regimes could be implicated in the observed divergences. Fig. 3.5 depicted a strong positive relationship between JSD and $\Delta\mu_{popFR}$ with $r_{Pearson} = 0.85$ ($p < 0.0001$). Okun, Steinmetz et al. (2015) investigated the relationship between one neuron and the population. They coined the terms `choristers` and `soloists` for neurons that showed a tendency to be highly linked to population FR and independent thereof, respectively. `Choristers` appeared to be affected by sensory stimulation, while `soloists` are much less influenced by the ensemble or network activity. They further suggested that the coupling of neurons to the population FR explained pairwise correlations. Both `soloists` and `choristers` are reflected in $\Delta\mu_{popFR}$, and thus, the `choristers`' robustness in sensory stimulation (Okun, Steinmetz et al. 2015) could partially explain the consistency in our results.

4

Mouse V1 contains information about behavioural outcome in a visual discrimination task

Neural activity differs between anaesthetised, sleeping and awake states (Greenberg, Houweling and Kerr 2008; Aasebø et al. 2017). Chapters 2 and 3 concentrated on neural processing of varying stimulus conditions in the anaesthetised state. The following chapter is an ethological study elaborating on information contained in binary patterns in V1 of the awake mouse during a GO/NOGO visual discrimination task, based on two datasets, acquired by Aleksandra Berditchevskaia (AB) and Marie Tolkieln (MT). AB's dataset has been focus of two independent studies, one on behaviour and motivation (Berditchevskaia 2014), and one involving Local Field Potential (LFP) analysis (Ardila Jimenéz 2016).

4.1 Introduction

Ethology, the study of animal behaviour from a biological point of view, attempts to classify, define and predict the determinants and components of interacting animals. *Behaviour* denotes an animal's response to a particular stimulus or situation. How a neural signal results in behaviour and cognition, and how particular neural activities induce certain behavioural actions is one of the key question in neuroscience. A fundamental challenge of this question is the large number of processing steps that lie between stimulus presentation and the observed behavioural response, rendering it difficult to confidentially match a detected neural response to the stimulus, particularly in higher cortical processing levels where sensory inputs may have been integrated with signals from other areas. Neural correlates of behaviour have often been successfully found in areas such as medial prefrontal cortex, which receives input from all other cortical regions, and is implemented in various cognitive and decision tasks (Kolb et al. 2012;

Euston, Gruber and McNaughton 2012). Yet, it does not receive direct projections from sensory cortices hindering to infer a mapping between stimulus and behavioural outcome.

A prominent model to examine cortical processing is mouse V1, conveniently located at an early cortical processing stage, with retinotopic mapping allowing to relate neural activity to visual stimuli more concretely. Simultaneous extracellular in-vivo electrophysiology in populations of neurons is a common technique to probe neural activity. In order to understand how cortical circuits function during a task involving decision making and the activation of memory processes, it is essential to analyse its operation during behaviour. In particular, recording how activity in different elements of the circuit bears information about the behavioural states may elucidate how and if neural correlates of behavioural outcome can already be found at such an early processing stage, or if V1 purely acts as a cortical input stage. Indeed, neural activity in V1 has been shown to be modulated by locomotion and running speed (Saleem, Ayaz et al. 2013; Polack, Friedman and Golshani 2013; Niell and Stryker 2010), attentional state (S. Zhang et al. 2014), or potentially even motor intention (Zagha et al. 2013), proposing that V1 activity may be more involved in behavioural outputs than previously understood.

While it has been known that individual neurons can adapt their tuning functions to behaviourally relevant properties (e.g. sharpening tuning in perceptual learning tasks (Goltstein et al. 2013)), this study did not expect to observe a differential response at the population level, since V1 is not thought to be directly involved in decision-making or learning processes. V1 was reported to show signs of plasticity in perceptual learning tasks, e.g. in experiments near the perception thresholds e.g. with Vernier lines (Saarinen and Levi 1995), however the SFs used in this study are sufficiently large to be easily detectable by the mouse. Behavioural paradigms often require repeated presentation of a stimuli to train the animal to react in a particular way to learn the desired behaviour. Repeated stimulus presentation may have other effects than are behaviourally apparent. For instance, Stimulus-selective Response Potentiation (SRP) is a form of cortical plasticity, which typically shows an increase in visually evoked potentials upon repeated exposure to e.g. sinusoidal gratings (Frenkel et al. 2006). It is a type of perceptual learning, which is NMDA receptor (N-methyl-D-aspartate receptor) activation dependent and occurs already at processing stages as early as V1 (Furmanski, Schluppeck and Engel 2004). In line with this, it was shown that learning and habituation (Cooke and Bear 2010) can strengthen sensory representations in V1

(Poort et al. 2015).

However, how and if these representations are affected by behaviour and reward association has not been fully understood yet, despite some indication of behavioural state being implicated in cortical gain control (Fu et al. 2014). A recent study in humans suggested a serial dependence of stimulus-induced activity patterns proposing previously observed stimuli may make subsequent stimuli appear more similar to the prior perceived ones than they may otherwise be (St. John-Saaltink et al. 2016), another indicator for top-down regulations that reach V1.

Thus, the aim of this chapter is to investigate how the activity of simultaneously recorded populations of neurons in mouse V1 relates to task state and if the behavioural action has an impact on the neural representation. A novel behavioural training protocol for head-fixed mice is designed and successfully implemented. The behavioural aspect comprises a GO/NOGO visual discrimination task involving operant conditioning, in which the mouse is required to initiate or withhold a response (licking) upon visual presentation of a drifting grating. Water-restricted, head-fixed C57BL/6 wild type young adult female mice are trained to respond differentially to vertical and horizontal moving gratings. One grating is associated with a positive reinforcement (water supplement), and one with a punishment (compressed air puff to the flank). Upon satisfactory learning of the task, multi-shank multi-laminar MUA is recorded in-vivo in left hemisphere V1 of the awake behaving mouse. MUA is then analysed with information-theoretic techniques probing if evoked population responses in V1 contain information about behavioural task outcome, and the similarity of evoked binary firing pattern distributions under varying behavioural outcomes is assessed.

4.2 Materials, procedures and methods

All experiments were performed in accordance with the Animals (scientific procedures) Act 1986 (UK) and the Home Office (UK) under protocol 19b3 of PPL 70/7355 and personal licences, in female C57BL/6 wild type mice. Mice were kept in a reversed 12h dark/light cycle. Surgeries, behavioural training and recordings were performed during the dark phase.

4.2.1 Behavioural visual discrimination task and set-up

The behavioural paradigm involved a GO/NOGO task in water-restricted head-fixed mice, in which mice have to make a dichotomous decision to either stimulus by per-

forming a motor task (lick) to the GO stimulus (S+), or withhold a response (no lick) to the aversive stimulus (NOGO, S-).

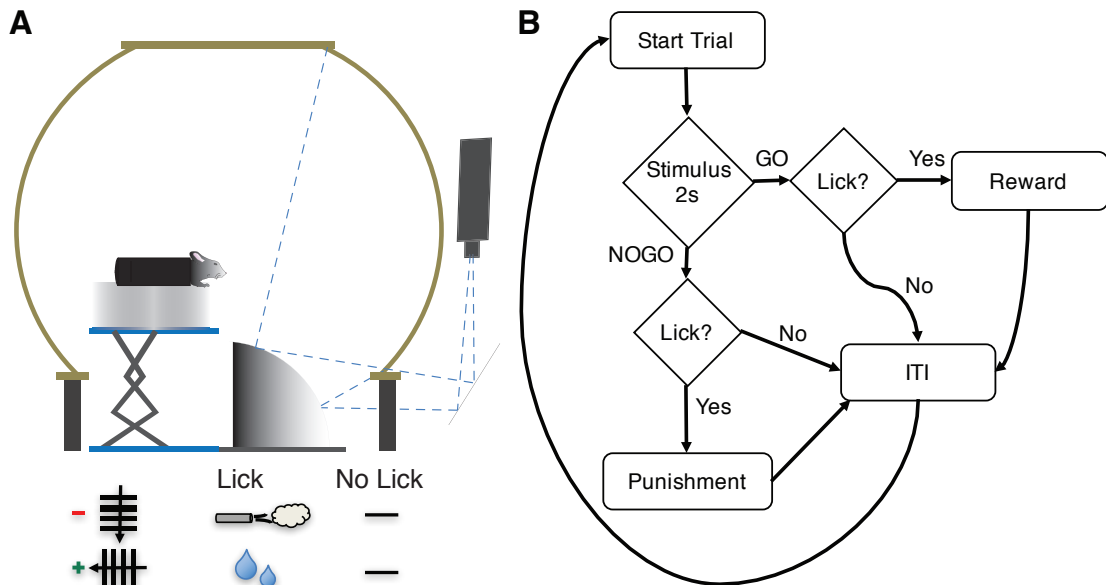


Figure 4.1: Behavioural task description. (A) Top: The mouse was placed in a small plastic tube in the centre of a dome and head-fixed, with its paws reaching over the ledge. Monocular stimuli (moving gratings) were projected onto a convex mirror reflecting into the dome. Bottom: A downward moving horizontal grating was the aversive stimulus, which negatively reinforced with an air puff to the flank. A leftward moving vertical grating was the GO stimulus, rewarded with a small water release in the lick port. In both cases, withholding a lick bore no consequences. (B) Flow-chart of the trial structure. A trial started with a stimulus presentation of 2 s. Stimulus choice was pseudo-randomised (maximum consecutive presentation of the same stimulus was limited to 5 repetitions) by sampling from a Bernoulli distribution with probability 0.5. If a lick occurred for the GO stimulus after a grace period of 500 ms but before presentation was over, the mouse was rewarded with a small water release. If a lick occurred during the NOGO stimulus, a short air puff to the flank (300 ms) was used as a punishment. If no lick occurred during the stimulus presentation, and after reward or punishment, the trial went into a Inter-Trial-Interval of variable duration, which was sampled from a Poisson distribution with mean 4 s. *Fig. (A) top taken with permission from (Berdichevskaia 2014).*

Animals were trained to respond differently to two discriminant moving grating stimuli at orthogonal orientations, visualised in Fig. 4.2. Early training sessions showed that it was easier for mice to discriminate when SFs differed slightly. One stimulus,

S+, a vertical grating moving forward, was rewarded with a water release upon correct behavioural response (licking within a window of 1.5 s during stimulus presentation). The aversive stimulus, S-, a horizontal downward moving grating, resulted in punishment by an air puff to the left flank. This was a conditioning task that involved aspects of classical and operant conditioning (Rescorla and Wagner 1972; Busse et al. 2011). Initially, the animal was conditioned to associate water (unconditioned stimulus) and licking (unconditioned response) with the lick port/screen (conditioned stimulus). Once this association was made, the animal would start licking the lick port to quench its thirst, even if there was no water present (conditioned response). This was the classical conditioning part. Then, in the discriminative part, the animal needed to learn through operant conditioning how to adapt its response to the different gratings.

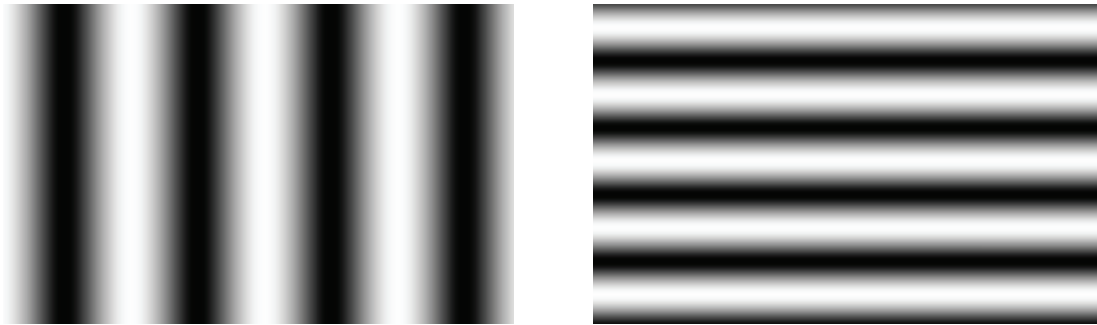


Figure 4.2: Grating stimuli. The left stimulus was the positively reinforced, water-rewarded stimulus, moving in leftward direction. The right horizontal grating illustrates the punished, unrewarded grating, at a slightly higher spatial frequency than the positive one.

The trial structure is illustrated in Fig. 4.1 (B). A trial began by pseudo-randomised stimulus initiation. Consecutive presentation of the same stimulus was restricted to 5 repetitions of the same stimulus by sampling from a Bernoulli distribution with equal probability. In early training phases, this probability was modifiable from the control panel to ease the early conditioning task. Both stimuli were presented for 2 s. The first 500 ms served as a grace period, in which a lick bore no consequences. If a lick occurred in the 1.5 s after the grace period during a GO trial, the mouse was rewarded with a small water release (1-4 μ l). Contrarily, if a lick occurred during presentation of the aversive stimulus, the mouse was punished with a short air puff to the flank (300 ms) and the stimulus remained on screen for an extra second. Passive behaviour was not punished. If no lick occurred during stimulus presentation, and after reward

or punishment, the trial entered an Inter-Trial-Interval (ITI) of variable length, in which the screen was grey (mean luminance), as a proxy for inferring spontaneous activity (Kenet et al. 2003; Niell and Stryker 2010). ITI duration was sampled from a Poisson distribution with mean 4 s and limited to a maximum of 13 s. The choice to sample from a Poisson distribution was to avoid effects from the mouse "anticipating" a trial start. Licks during the ITI period were also neither punished nor rewarded.

4.2.2 Surgical and electrophysiological procedures

Head-plate surgeries

Preparation started a few days before surgery by habituating the mice to being handled by the experimenter. Habituation involved different kinds of interactions such as holding, weighing, or feeding them Hartley's[®] raspberry jelly.

The head plate surgery was performed under general Isoflurane anaesthesia, Carprofen and Buprenorphine analgesia, following aseptic technique, in order to implant a custom-built metal head plate and ground screw under protocol 19b3 of PPL 70/7355.

Anaesthesia was induced with 4-5% Isoflurane in an induction chamber and maintained through a nose cone at 1.5-2% throughout the procedure, with a carrier gas of 1.2% O₂. Isoflurane was the choice of anaesthetic as it allowed a quick induction, variable depth of anaesthesia throughout the procedure and a fast recovery time. After inducing anaesthesia in the induction chamber, the animal was placed on a feedback-controlled heat pad (FHC) on a KOPF[®] small animal stereotaxic frame. Body temperature was monitored throughout the procedure with a rectal thermometer, and maintained at 37.1 ± 0.5°C. Depth of anaesthesia was controlled continually by checking the pedal-withdrawal reflex and breathing.

Immediately after moving the mouse onto the stereotaxic frame, 0.2 ml of NSAID (non-steroidal anti-inflammatory drug) analgesic Carprofen (of a 0.5 mg/ml diluted solution, dose 5 mg/kg, Rimadyl[®]), and 0.06 ml of the opioid analgesic Buprenorphine (0.03 mg/ml diluted solution, dose 0.1 mg/kg, Vetergesic[®]) were injected subcutaneously to reduce post-operative pain and help recovery time. The Buprenorphine dose gave 6-12 hours of analgesia (as advised by in-house vet Francisco Diaz), and Carprofen approximately 24 hours. In addition, sterile saline was injected subcutaneously to account for the volume of fluid the mouse would normally intake over the duration of the surgery. Per hour of surgery, the prescribed dose was 10 ml/kg, which amounts to 0.15 ml/h for a 15 g mouse. For this study, a reference sheet for calculating the correct dilutions was devised and can be found in the Appendix, 3. Calculations were

confirmed by Georgina Wilkinson, BSc BVetMed MRCVS, Deputy Named Veterinary Surgeon at the time.

Once the mouse was mounted to the nose cone, Lacrilube[®] was applied onto the mouse's eyes to keep them hydrated. Lacrilube, being more viscous than eye oil, is more suitable for surgeries as it does not need to be applied as often as e.g. silicone eye oil. The head was gently fixed in position using ear bars (whose tips were coated in EMLA[®] cream, which contains local anaesthetics lidocaine/prilocaine, to improve comfort), while making sure not to puncture the tympanic membrane. Lidocaine, a local anaesthetic with rapid onset and duration of 1-2 hours, was injected subcutaneously across a few equally spaced points around the head. Scalp hair was carefully shaved with an electric trimmer. The remaining hair on the sides of the skull was covered in Vaseline to avoid stray hairs in the surgical site when exposing the skull.

To further reduce recovery time, analgesic (Buprenorphine) jelly (Hartley's[®], raspberry flavour) for recovery post-surgery was added into the home cage. Ideally, jelly without analgesic should be introduced into the cage of surgery candidates at least a couple of days prior to surgery for the mice to habituate to. Introducing the analgesic jelly after the surgery, without prior exposure, the mice would likely be suspicious of it and not eat it (and thus miss out on the pain relief).

Before an incision was made to expose the skull, Povidone-Iodine was applied with sterile cotton swabs to reduce infection risk, particularly around the incision sites. An incision was made to expose the skull; hair and skin were removed or retracted. The connective tissue was thoroughly and carefully removed with sterile cotton swabs, small scissors, and an Austin chisel. A drop of 5% H_2O_2 (hydrogen peroxide, 1.5 ml of 30% H_2O_2 in 7.5 ml distilled water) was used to carefully clean the skull surface, removing the gelatinous periosteum. Particular focus was laid to the muscle at the back of the head. It was carefully scraped away with an Austin chisel, specifically on the left side (target side). It was very important to clean the skull as meticulously as possible, since any remaining tissue might regrow and jeopardise a secure adhesion of the head plate. Another step in augmenting the adhesion of the head plate to the skull was to scrape incisions at different orientations into the skull, either with a scalpel blade, or with a slow turning dental drill. These incisions increased the surface area of the glue, and thus, improved adhesion.

The target area, the monocular area of V1 in the left hemisphere, was identified with a ruler or micromanipulator device and marked with a permanent surgical marker at 2.5-3.2 mm lateral to lambda (S.-H. Lee et al. 2012; Glickfeld, Histed and Maunsell

2013).

The custom-made design metal head plates (design by AB) were moulded to the skull with pliers to fit the shape of the skull as accurately as possible, leaving as little gaps as achievable. For the later behavioural training, it was important that the tongue of the head plate remained horizontal as otherwise the mouse's performance might have been affected by an uncomfortable head position attributable to a tilted head in the fixture. Once the head plate fit was acceptable, it was attached to the skull with Histoacryl[®], a liquid topical skin adhesive, which polymerized in seconds upon being exposed to water or water-containing substances such as tissue (TissueSeal LLC, TS1050071FP). This step involved firm and cautious pressure for a few seconds to ensure a tight adhesion. Optionally, the craniotomy area and possible minor gaps between skull and head plate could be covered in a thin layer of cyanoacrylate (super glue, Henkel Loctite), sealing the skull and minimising regrowth. Introducing an extra layer of super glue noticeably minimised head plate detachment or tissue regrowth under the head plate.

A small craniotomy of \varnothing 1 mm was performed over the contralateral hemisphere over the cerebellum for a ground screw. After a careful durotomy, the ground screw (Precision Technology Supplies, M1.0x2.0 SLOT CHEESE MACHINE SCREW DIN 84 A2 ST/ST) was inserted into the craniotomy site with a precision screwdriver without perforating the brain, and subsequently secured in place with dental cement (Kemdent). The ground screws were prepared prior to the surgery. They contained a connector (MILL MAX, 851-43-050-10-001000 connector, sip socket), which was placed into the slot of the screw and bent upwards to enable an easy connection to the ground cable during electrophysiological recordings.

Dental cement was used to fill any gaps between the head plate and skull. It was applied through a pipette tip and syringe, superficially around the edges of the head plate. It helped reinforce the connection between skull and head plate and to seal the exposed skull from the environment. Once the dental cement had cured, the retracted skin around the surgical site was attached to the dental cement and head plate (if applicable) with Histoacryl[®]. Finally, the future craniotomy site was covered with Kwik-Cast[®] (World Precision Instruments), a two component silicone elastomer, and a layer of nail varnish to secure the craniotomy site even more, particularly for group-caged mice. An alternative to Kwik-Cast[®] was Smooth-on Body Double[®], a two component platinum-cure silicone rubber. The cured Kwik-Cast[®] was covered with a thin layer of nail varnish, and the head plate was marked with a unique symbol identifying the mouse. While the nail varnish was curing, the Isoflurane was turned off to minimise

anaesthesia time. The mouse was released from the ear bars and, once it showed signs of recovery, put into the recovery chamber.

During recovery period the mouse was under observation in a heat box for approximately 60 minutes with access to water and softened food. Once it appeared to have fully recovered, it was returned to its home cage where it was group-housed with its litter. Group-housing ensured mice would not suffer from social isolation, which may render behavioural tests inconclusive or influence their outcome in any other way (Võikar et al. 2005).

Craniotomy and preparation for extracellular recording

On the day of the electrophysiological recording, the mouse was taken to the aseptic procedure room and anaesthetised in the induction chamber with 4 – 5% Isoflurane in 1.2% O_2 and moved onto the KOPF stereotaxic frame. Anaesthesia was maintained through a nose cone at 1.5 – 2% Isoflurane and excess Isoflurane was retracted with a scavenger. All procedures followed aseptic technique.

The mouse was placed on a feedback-regulated heat pad, and its body temperature was kept at $37.1 \pm 0.5^\circ C$. The eyes were covered in eye ointment Lacrilube (Allergan). Analgesia was ensured by subcutaneously injecting NSAID Carprofen (0.5 mg / ml diluted solution at a dose of 5 mg/kg, Rimadyl) and Buprenorphine (0.03 mg/ml diluted solution, dose 0.1 mg/kg, Vetergesic). Sterile saline was injected subcutaneously to make up for the volume of fluid lost during the surgery. The head was gently fixed in position using EMLA cream covered ear bars (to improve comfort). Next, the nail varnish seal was removed using acetone-based solution on a sterile cotton bud. With the help of forceps (Dumont #7, Fine Science Tools), the silicon elastomer Kwik-Cast[®] sealing the marked craniotomy site was removed.

With a dental drill (Osada Success 40, 0.5 mm drill bit), a small circular craniotomy of 1-3 mm diameter was made, with particular caution not to damage the cortex. To achieve the craniotomy, the skull was thinned evenly over the craniotomy site. As the location of V1 was very close to the parietal suture, bone thickness varied, requiring to adapt the drilling to the thickness of the skull. When the skull was sufficiently thinned, the final separation could be achieved by pressing gently onto the centre of the piece of skull that was to be removed, thereby cracking and separating the bone plate from the skull. Adding Phosphate Buffered Saline (PBS) onto the cracked skull fragment and waiting a short moment eased removal, as it helped disconnect the dura from the skull, minimizing potential damage attributable to skull-dura adhesion. Then, the plate

could be easily removed using a bent needle and fine forceps (Dumont #5, Fine Science Tools).

For the durotomy, a sharp needle tip (27G) perforated the dura mater, lifted it slightly, with great care not to puncture the brain tissue. The dura flap was retracted carefully with fine forceps (Dumont #5, Fine Science Tools). The cortex was kept moist by applying a drop of PBS, and 1.2% agarose (Sigma, in 1xPBS (Life Technologies)) which was heated up and applied through a pasteur pipette once the temperature was low enough and the agarose still fluid. Once the agar solidified, a layer of Kwik-Cast was applied to seal the craniotomy site further and to protect the cortex from other hazards.

To reduce surgical time, the Isoflurane was turned off, ear bars and thermometer withdrawn whilst the Kwik-Cast[®] was still curing, and the mouse was placed in a heat box for recovery with free access to water and softened food. The mouse remained under observation for approximately 60 minutes or until it appeared to have fully recovered. The mouse was then returned to its cage, in single housing, to recover further, before the first electrophysiological recording could begin approximately 6 hours later to ensure the mouse had recovered sufficiently from the surgery and readjusted to its normal cage behaviour.

In-vivo extracellular electrophysiology in the awake behaving mouse

With the mouse prepared as described in 4.2.2, the procedure for the in-vivo electrophysiology was the following.

Trying to match the time for the recording as closely as possible to the times behavioural training takes place, the mouse should be habituated to the extra steps required by the electrophysiology by mimicking them as closely as possible the days before the recording. This would include steps such as extra waiting periods, inserting the ground cable, lowering a sham probe with the micromanipulator or application of PBS and potential small spillages. On the recording day, the mouse was head-fixed as usual, and the ground cable was connected to the ground screw. Our electrode type allowed to use its built-in reference site, which was located on one of the shanks, approximately 1 mm from the most superior site, which with our superficial target depth happened to lie just outside the brain, but still within PBS.

Nail varnish, silicone elastomer and agarose were removed by blunt forceps and fine forceps (Dumont #5, Fine Science Tools). The craniotomy site was inspected for damage or infection through the microscope and kept hydrated with PBS. Mouse, lick port,

apparatus and micromanipulator (Scientifica[®] PatchStar) were positioned with a sham probe to warrant correct alignment. All recordings were performed with Neuronexus A4x8 linear probes (A4x8: 5mm-100-200-177, 100 μm linear site spacing, 200 μm shank spacing, 177 μm^2 site area).

Signals were acquired by a Ripple Grapevine (Scout Processor), amplified with a single-reference amplifier with on-board filtering and digitization (Grapevine Nano front end, 16 bit resolution and 0.2 $\mu\text{V}/\text{bit}$), and software Trellis, which enabled for a live display of the channels. This set-up required an Intel GIGABIT CT DESKTOP RJ45 PCIE B networks card to ensure a safe signal transmission without dropping frames. Each of the 32 channels provided a broad-band signal, filtered between 0.3 Hz - 7.5 kHz (3rd order Butterworth) sampled at 30 kHz, as well as an LFP signal (< 250 Hz, 4th order Butterworth filter) sampled at 1 kHz.

The probe was attached to the head stage, and dipped manually into a small vial of fluorescent lipophilic cationic indocarbocanine dye (DiI) to help histological identification of electrode position in the cortex. Before the DiI coating evaporated or dried, the probe was positioned on the brain surface with the micromanipulator, tared to zero before advancing into the brain at a speed of a few 10 $\mu\text{m}/\text{s}$ and 90° angle. The silicon microelectrode was lowered slowly into the brain to a depth between 800 μm and 1050 μm .

Once the target depth was reached and a signal found, agarose was applied via pasteur pipette to stabilise the probe and to prevent the brain from drying. The electrode was left to settle for 15 minutes. Through habituation and training, mice would generally be quiet and patient during this preparatory period.

The recording commenced with 5 minutes of SA in the absence of visual stimulation (black screen, dark room). The Trellis software enabled us to scrutinise signal quality on all 32 channels simultaneously, in both high-passed and low-passed filtered signal (MUA and LFP). Once the 5 minutes of SA finished, the behavioural task started as usual. At the beginning of each trial, a synchronisation pulse (a Boolean signal) was sent to the NI-DAQ card (National Instruments[®]) to help synchronise timestamps between data acquisition and visual stimulation. This synchronisation pulse indicated the start of the trial (and thus the visual stimulation), and was also visible in the Trellis software for an immediate comparison of visual evoked responses. In this study, eye movements were not monitored, although it was discussed and shown that correlates of motivation could be inferred from by pupil diameter (Reimer et al. 2014; C. R. Lee and Margolis 2016). In addition, however, previous studies in rodents suggested eye movements to be

generally low, with little effect on neural activity (Andermann, Kerlin and Reid 2010; Keller, Bonhoeffer and Hübener 2012), particularly in head-fixed animals (Wallace et al. 2013).

The session was concluded with another 5 minutes of SA (black screen, dark room) when the mouse stopped participating. The probe was slowly withdrawn and submerged in electrode cleaning solution. Agarose was removed and the state of the craniotomy site was assessed. If the state of the brain was acceptable, with no apparent bruising, contusion or any other damage, the animal was prepared for another recording the following day. For this, PBS was applied and 1.2% agarose was used to cover the craniotomy site. Kwik-Cast[®] was administered and set to cure before securing it in place with small drop of nail varnish. The mouse was released from the head-fix and its well-being was evaluated. If the session did not result in sufficient trials to cover the daily water rate, supplementary water was fed through a syringe before the mouse was returned to its single-housed home cage until the next recording.

If upon inspection, either at the beginning or at the end of the recording day, the brain seems too damaged, shows signs of an inflammatory response, dryness or otherwise affected tissue, the animal was sacrificed by either intraperitoneal injection (180 mg/kg) Pentobarbital (Euthatal; Merial Animal Health, Harlow, UK), and transcardially perfusion with PBS (Life Technologies, UK) and fixed with 4% Paraformaldehyde (PFA) (Sigma-Aldrich, UK) solution; or anaesthetised in an induction chamber (4-5% Isoflurane) followed by cervical dislocation. In both cases, the brain was dissected out and post-fixed over 4 days in 4% PFA at 4°C, before being transferred to PBS solution at 4°C for histological processing.

4.2.3 Hardware and software specifications

The experimental set-up was adjusted from AB's efforts (Berditchevskaia 2014) to create an immersive virtual visual environment.

The dome depicted in Fig. 4.1 (A) consisted of an 800 mm spherical polystyrene (Ecclestone& Hart Ltd), covered in papier mâché and projection paint (Goo Systems, SKU6375 Max Contrast). This permitted to use a spherical projection field as opposed to linear ones with a screen, which closely resembled the visual field of rodents (Chalupa and R. W. Williams 2008; Sterratt et al. 2013). Visual stimuli and trial structure was based on code provided by (Berditchevskaia 2014), modified and extended for this study. The software used to control visual stimulation and trial progression was developed in LabVIEW connected to a National Instruments Data Acquisition Board (NI-DAQ).

Visual stimuli were coded as textures in an OpenGL framework using the GLFW library written in C, enabling us to map the grating textures to the interior surface of the dome (via a coordinate transformation) allowing for an undistorted presentation on a spherical surface. Dome coordinates for the transformation procedure were obtained manually (by Tomaso Muzzu) by measuring equiangular points of a polygon inside the dome.

Once the textures were bound, the signals were sent to the dome via a digital projector (ViewSonic PJD 6533w, 120 Hz refresh rate, output brightness 3500 Lumens), installed vertically behind the Faraday cage, pointing at a rectangular mirror mounted at 35° , which reflected onto a 180° spherical mirror (Viso MS180 Indoor Dome Mirror) inside the dome projecting onto the surface of the dome, (c.f. Fig. 4.1 (A)).

Apart from stimulus generation, the experimental set-up required further hardware and software components to control lick detector, water release valve and air puffs. These components were also controlled by the LabVIEW environment.

The lick port comprised a blunted 19G needle attached to a 0.5 mm (inner diameter) silicone tube (RS Components, Stock No. 667-8438), leading to a single-channel peristaltic pump (Campden Instruments, Product No. 80204-0.5) operating at a flow rate 0.025 ml/s, picking up tap water from a small water reservoir in a glass vial, controlled by a TTL pulse coming from LabVIEW. Licks were optically detected via photo-microsensor at 8 mm aperture (Omron Electronics, EE-SX4070) sampled every 20 ms, which was well over the typical rhythmic lick rate in rodents at 5-8 Hz (Welzl and Bureš 1977). Every beam interruption was interpreted as a lick.

Air puffs were regulated by a miniature 2/2 way solenoid valve (Shako Company, PU220AR-01, 1/8 inch) and linked to a controllable in-house compressed air system allowing for adjustment of puff strength (0.7 -1 bar). The room's compressed air control outlet connected to the solenoid via high pressure resistant silicone tubing. The solenoid's output consisted of a 1 mm copper pipe allowing for manual adjustment in targeting the air puffs to the mouse's left hind flank, contralaterally to the monocular stimulus presentation.

Given the space constraints in the dome, the Scientifica Patch Star micromanipulator for probe insertion was placed in the left field of view, and the microscope attached to a separate aluminium construct on wheels.

Stimulus generation and data acquisition (including micromanipulator control software, LinLab[®]) were assigned to different computers to ensure stable signal transmission without risking running out of memory on either computer. The stimulus PC was running 64-bit Windows 7 OS with an Intel Core i7 CPU.

The LabVIEW-based controlling software incorporated a Graphical User Interface (GUI) allowing the user to interfere manually (air puff or water release), change training parameters (stimulus probability, field of view starting point, grating temporal frequency, air puff duration), scrutinise behaviour (lick raster plots), and analyse ongoing performance via Signal Detection Theory (SDT) measures such as sliding d' or accuracy. This dynamic interface enabled the user to intervene and tailor the behavioural program to the animal's individual performance and needs.

4.2.4 Behavioural training protocol and habituation

This is a novel and efficient behavioural training protocol devised in particular for head-fixed mice to learn a GO/NO-GO task involving visual stimulation in the monocular field of vision. The protocol includes a habituation phase and initiation of water restriction. Normally, this protocol can be started within 2 days after surgery. During the entire protocol, mice have ad libitum access to food. An example of a mouse in the behavioural set-up is presented in Fig. 4.3.

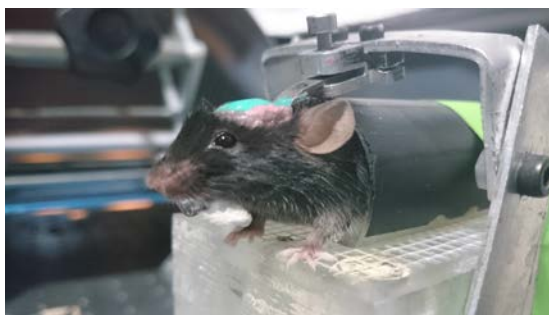


Figure 4.3: Head-fixed mouse ready for behavioural training. The mouse's body is located in a narrow tube on a custom-built Plexiglas head-fix mount, whose surface is topped with a mesh for more grip. Visible on the skull is dental cement (light rose), nail varnish (pink), and Kwik-Cast[®] (green). NB: Lights are on and the lick port was moved out of view for the photo.

This behavioural training protocol is based on but differs widely from the approach used in (Berditchevskaia 2014) by reducing the number of training stages thereby accelerating leaning progression. Where the previous protocol required training the mice on a full-field stimulus first, which is then replaced by a half-field and then monocular field stimulus, this approach instigates the monocular field from the start. This change is brought about in an attempt to circumvent the drawbacks from the previously im-

plemented training protocol, where mice appeared to have to learn the monocular task anew, as their performance had dropped substantially transitioning from full-field to monocular stimulation.

Unless explicitly noted, all lights in the behavioural training room were off apart from the stimulus projector, minimising distraction from other visual inputs.

Throughout the training phases and while one mouse is trained, the remaining mice of the batch were placed in a cage with enriched environment (including a running wheel, cardboard tubes and pieces).

Day 1

The mouse is acclimatised and habituated to the experimenter's hand. Starting a few days before the water restriction or head plate implant, the mouse is placed in the experimenter's hand and let free to explore. Further, the mouse is weighed and put back into the experimenter's hand. In addition, the hand is placed into the cage, letting the mouse explore it freely. This also helps the mouse to get accustomed with the experimenter's scent and presence. The head fix apparatus and tube are placed into the cage over night for the mouse to get used to. In the experimenter's hand, the mouse is head fixed a few times for <15 s by holding the head plate firmly with the other hand.

Day 2

The mouse is weighed, and taken to the experiment room to get used to the transport box and the daily transfers between mouse holding facility and behavioural training room. There, the mouse is briefly head-fixed (< 15 s) in the experimenter's hand and fed with water through a syringe (up to the daily supplement of 0.2 ml). This aims at building a positive connection between head-fix, interaction and being restrained. If the mouse does not struggle too much, the mouse can be put into the head-fix device tube and head-fixed for approximately 5 minutes, with water rewards starting immediately through the syringe and at increasing time intervals to build the association of water reward while being head-fixed whilst building patience in the restraint.

Day 3

Day 3 is similar to day 2, but the mouse is head-fixed in the apparatus for 15-20 minutes, with water rewards through a syringe every few minutes, until the daily allowance of

0.2 ml water is reached.

Day 4

Day 3's procedure is repeated, but the time in head-fix is extended to 30 minutes, depending on how well each candidate copes. If the mouse does not struggle too much, introduction to the lick port can be initiated (set-up habituation phase), building the association between lick port and water reward with a specially designed habituation program that simply delivers a droplet of water upon licking (i.e. interrupting an optical beam). Initially, the water delivery can be manually launched to indicate the mouse the function of the port. In classic operant conditioning terms, this stage may be referred to as *shaping* (Skinner 1938). In this training phase, any lick in the lick port will be rewarded. Next, we want the animal to learn to lick only when a particular stimulus is present (S+), so the transition from this stage to the next should be rapid to avoid building wrong or impartial associations.

Day 5

If the mouse showed participation on Day 4 in the habituation and shaping phase, the task training can begin. Before visual stimulation begins, the session begins with head-fixing and making the animal wait. This patience task is crucial to emulate the time required in the electrophysiological recording from removing the craniotomy seal, over inserting the probe to waiting to let the probe settle. Waiting time varies depending on how much the animal struggles, and can be built up from a few minutes to approximately 15 minutes. The positive stimulus (S+) is presented in the right half of the dome and automatically rewarded with water after 500 ms of stimulus presentation. Stimulus presentation is interleaved with periods of grey screen, ITI, of varying duration. ITI duration is randomly sampled from a Poisson distribution with mean 4 s and cut-off at 13 s. Stimulus probabilities are regulated depending on animal performance. Initially, S+ is assigned 100% of occurrence probability, to strengthen the lick association. Every day, this probability decreases with a simultaneous increase of S- until they reach 50%. Air puffs to the left flank are used to stop the mouse from licking to the negative stimulus.

Final stage

Behavioural training is in its final structure. Weight is logged before each session in the animal holding room. Reward and punishment is no longer automated but subject to the mouse licking at the specific times (between 500 ms and 2 s). At the start of each session, the mouse generally readily runs into the tube to be head-fixed and remains calm throughout. Stimulus probability is at 50% and generally, the mouse performs 200-300 trials. Stimulus presentation is fully moved to the monocular area of vision by reducing the stimulus presentation field to the rightmost area in the dome.

Each session starts with approximately 20 minutes of patience where no stimulus is shown, which mimic the preparation time for the electrophysiological recording. In early parts of the final stage, the animal may show impatience and struggle here, but it is crucial to mimic the recording as closely as possible to maintain performance. In the final few sessions before the in-vivo recording, mimicking similar movements, sounds, and interferences with the animal are advisable. This may involve tinkering with the head plate (i.e. a gentle tap with forceps to imitate Kwik-Cast[®] removal), releasing a drop of PBS, having the microscope light pointed at the head to emulate probe insertion, inserting the ground cable to the ground screw, or moving the micromanipulator with a sham probe up and down. Similarly, patience needs to be built to mimic probe removal, and the application of agar, Kwik-Cast[®] and nail varnish seal after each training session. Again, in the final sessions before the recording, introducing the right smells and interactions may be beneficial.

Behavioural performance and participation is automatically logged every day and compared in lick scatter plots.

Weights

Mouse weight was monitored throughout and it was ensured to never fall below 80% of the starting weight. Since very young mice (4 weeks old) were used, mice were expected to gain weight through growth, and they normally gained weight of about 15% above the starting weight.

4.2.5 Performance markers and signal detection theory

Behavioural outcomes can be classified according to binary classification tasks as described in SDT. The possible outcomes for a GO/NO-GO tasks were (I) HITS (true positives) (II) MISS (false negatives) (III) Correct Rejection, true negative, *Glossary*: CR

(CR), (true negatives) (IV) False Alarm, (false positives)

Performance was then monitored using the following methods commonly used in SDT, illustrated in Fig. 4.4:

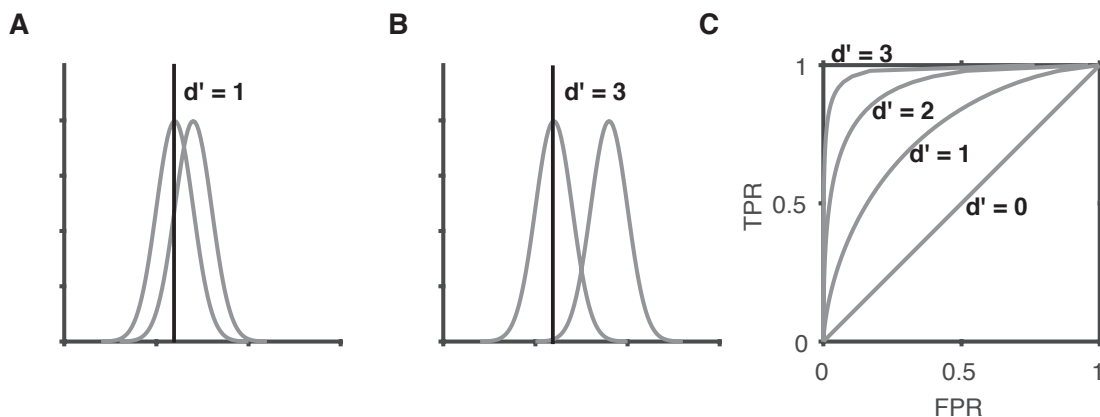


Figure 4.4: The meaning of d' in SDT and Receiver Operating Characteristic (ROC) space. (A) Noise and signal distribution have the same standard deviation and their means are separated by $d'=1$. Criterion C lies on the mean of the noise distribution. (B) Criterion remains in the same position, but the two distributions are separated by $d'=3$, increasing their discriminability. Here, the amount of false negatives (MISS) is massively reduced in comparison with (A). (C) Different curves in ROC space illustrate the meaning of d' . A d' of 0 corresponds to equal False Positive Rate, or False Alarm Rate (FPR) and True Positive Rate, or Hit Rate (TPR), with a discriminability of 0.

1. d' (d -prime), also referred to as sensitivity or discriminability index, describes the distance between means of signal and noise distribution. These were calculated via TPR and FPR. TPR is the proportion of HITS, $p(\text{yes}|\text{signal})$, FPR the proportion of False Alarm, false positive, *Glossary*: False Alarm (FA), $p(\text{yes}|\text{noise})$. Noise and signal distribution have the same standard deviation, but differ in their means. An often used approximation of d' is to use difference between the z-scored hit rate and z-scored false-alarm rate. $d' = Z(TPR) - Z(FPR)$. Z-score here refers to taking the inverse of the normal Cumulative Distribution Function (CDF). A d' of 0 means that noise and signal distributions overlap (identical); in ROC space, a d' of 0 corresponds to the main diagonal. A larger d' indicates that the two signals were more easily separable; in ROC space this would mean a curve tending towards the upper left corner, increasing the area under the curve.
2. Response bias (criterion), $C = -\frac{Z(TPR)+Z(FPR)}{2}$, which stipulates the tendency of

an agent's behavioural strategy. It describes the propensity to act and is related to the risk-taking or risk-averse strategies. For a risk-averse or conservative approach, the agent favours reduction in false alarms, resulting in a high criterion. A more risk-taking or liberal strategy (low criterion) accepts the cost of false alarms in fear of missing out. This means, criterion reflects the general tendency to act with "yes" (Stanislaw and Todorov 1999). Fig. 4.4 (A) and (B) demonstrate a criterion value on the mean of the noise distribution. In (A), the proportion of false negatives is large, with 50% false positives. In (B), the amount of false negatives is minimal, whilst the number of false positives remained the same. An unbiased agent would optimally choose the intersection of signal and noise distribution.

3. ROC, a common visualisation method of binary classification tasks in which the x-axis shows TPR, and y-axis FPR. The larger the area under the ROC curve, the better the performance.
4. Accuracy, computed according to Eq. ??, denotes the proportion of correct results (both true positives and true negatives) over the total number of trials examined. Accuracy may be referred to as *validity* in psychology literature and is calculated

$$\text{as } acc = \frac{CR + HITS}{FA + HITS + CR + MISS}$$

4.3 Results

In-vivo extracellular electrophysiology data from the awake mouse during a visual discrimination task was recorded by AB and MT. Both experimenters followed the same electrophysiological recording protocol, using 4-shank linear translaminar silicon microelectrodes, but pursued different training protocols leading up to the recordings. Ensuing from a broken shank, some of the experiments by AB used only three shanks of eight sites each. This limited the number of state spaces investigated to a maximum of three shanks (24 sites) in this chapter, where applicable. Number of shanks used is clearly marked throughout. On account of different training protocols, results of the two datasets were juxtaposed. Information-theoretic techniques inspected information content and state spaces between behavioural outcomes to investigate the influence of a dichotomous choice (to lick or not to lick) on firing patterns, and how this affected stimulus encoding.

4.3.1 Training protocol affects learning speed

Mice attain d' of 1 after 10 sessions

Training progression and success was evaluated using behavioural markers from SDT such as d' , ROC and response bias (criterion) C , as described in Sec. 4.2.5.

Fig. 4.5 illustrates progress in behavioural performance by means of d' , response bias, ROC, and smoothed lick profiles. Data in (A) suggests that it takes approximately 10 sessions to reach a d' of 1, which quickly progresses to a d' of around 2 after 20 training days. Progress seems to reach a plateau lasting around 30-40 sessions, after which some animals progress even further to a second plateau around d' of 3 (not shown). It is evident from (A) that the steepest learning occurs during the first 20 days as illustrated by the increase in d' . The dip in d' after 20 sessions observable in all four mice may be attributable to a one-off delay in behavioural training time from its usual schedule. Each line in (A) is smoothed via convolution with a normalised Hanning window of size 5.

In comparison, response bias in Fig. 4.5 (B) appears to start around zero and plummets down at the 10 session mark, before it fluctuates around -0.5. It appears to oscillate at low slightly negative values. Criterion does not reflect performance gain but indicates the animal's propensity to react (lick), and it is generally negative, resulting in generally high response rates or task participation. A negative criterion involves that $Z(\text{TPR})$ and $Z(\text{FPR})$ both increased. The high variance in response bias may reflect differences in internal strategies (increased thirst, motivation) between sessions. One animal in particular appears to oscillate around zero, which suggests it is least biased, whereas the other mice adopt a lower, negative criterion, indicating to be more responsive.

Progression in ROC space calculated over full training sessions visualises the learning. Fig. 4.5 (C-F) depict ROC progress during the first 20 days for the four mice of (A, B). Colour indicates training day, with blue shades corresponding to early days and red to later sessions. Most of the shown animals begin in the middle or upper right quadrant of ROC space, displaying participation but not particular good performance with high FPR and TPR. Then, the FAs are reduced whilst HITs remain stable, indicating a transition from an over-motivated to the optimal regime in the top left corner.

The animal presented in (E) follows a trajectory starting at the midline, with a higher FPR than TPR, transitions towards the over-motivated area in the top right corner at high FPRs and TPR, before reaching the optimal area by reducing FAs while maintaining

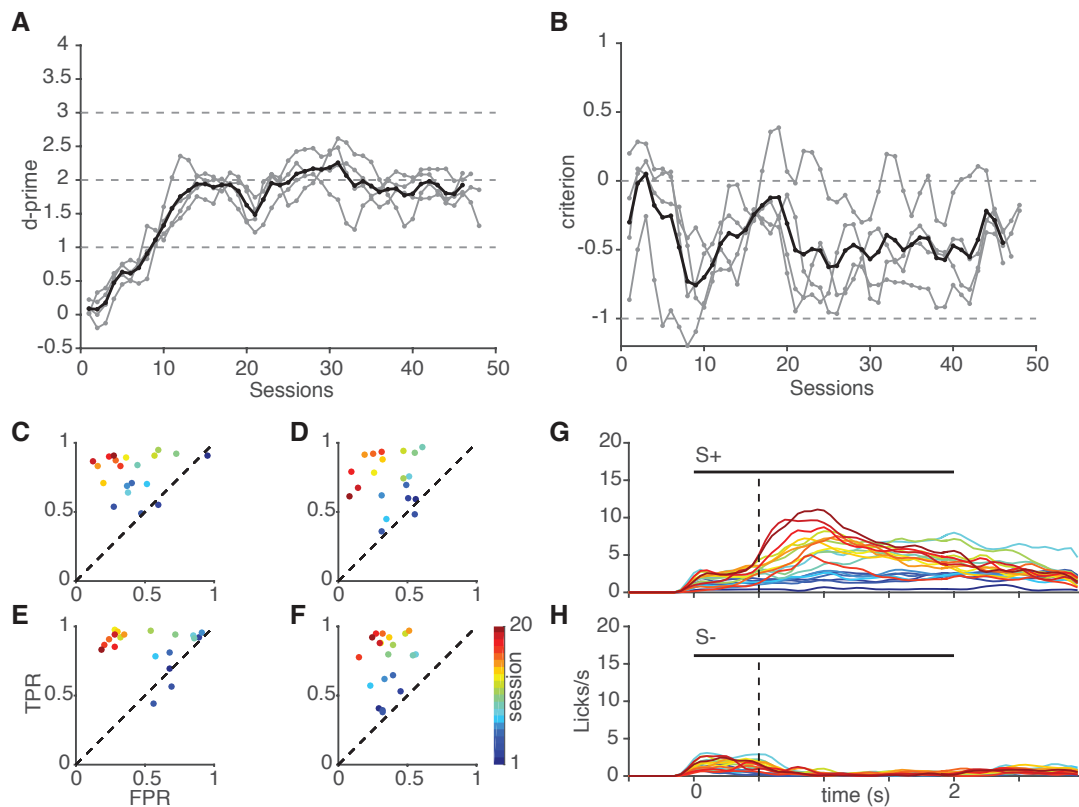


Figure 4.5: Behavioural progress over training days, indicates ten days are required to learn the task, experimenter MT. (A) Sensitivity measure d' over sessions (training days) increases rapidly during the first 20 days before reaching a plateau. Grey lines indicate individual mice in one batch (4 mice), black line mean across mice. Each line is convolved with a normalised Hanning window of size 5. (B) Criterion starts around zero, drops during the first 10 days towards -1 before levelling off at around -0.5 at high variability over training days. Only one animal appears to oscillate around an unbiased criterion (zero). Colours and mice as in (A). (C-F) ROC values for the first 20 training days in the 4 mice of (A, B). Colour indicates training day, with blue shades corresponding to early, and red shades to later stages. (E) illustrates a mouse following a trajectory starting from the middle, reaching into the over-motivated top right area at high FPR and TPR before reaching high discriminability in the optimal regime (top left), at high TPR and lower FPR. (F) The ROC training progression follows a different path from (E), starting at medium/low values for TPR and FPR and mainly improving on TPR without apparent reduction in FPR. (G) and (F) illustrate the corresponding Hanning-smoothed lick Peri-Stimulus Time Histogram (PSTH)s for GO (G) and NOGO (H) stimulus for the animal shown in (F), colour code as in (C-F). Initial lick profiles appear flat (blue) before evolving to a steep lick onset after the grace period for later training days. Both GO and NOGO stimuli show a low but positive initial response during 500 ms grace period. Horizontal black line (top) indicates stimulus presentation, vertical dashed line end of the grace period. Colour code same as in (C-F).

high TPR. Although other mice follow different trajectories, they all appear to reach the optimal regime after 20 sessions. In particular, the mouse from (F) appears to maintain a certain FPR whilst improving its TPR visibly. Focussing on the smoothed PSTH lick profiles in (G) and (H), (smoothing via Hanning window with 5 bins of length 50 ms), the lick profiles between (G) GO and (H) NOGO appear very dissimilar. A clear transition from almost flat lick profiles (G), blue shades, to a rapid onset after the 500 ms grace period emerges for the GO stimulus (G), whereas in (H) licks are generally suppressed in the NOGO stimulus (S-), particularly after the grace period. The onset response in the lick profiles during the 500 ms grace period for either stimulus illustrates classical conditioning and the animal's tendency to react to the visual stimulation.

Under a different training protocol, mice do not attain a d' of 1

The alternative protocol, described in Berdichevskaia (2014) involved multiple, staggered training stages, moving from binocular full-field, to half-field to monocular stimulus presentation. In contrast to the previous section, where mice attained a d' value of 1 after 10 sessions, Fig. 4.6 illustrates behavioural training progress of experimenter AB, where mice failed to maintain this discrimination level. Criterion, in (B), oscillates heavily around zero with a slightly positive mean across all sessions and mice, which is different from the mostly negative criteria (and thus suggesting higher lick propensity) from Fig. 4.5 (B). ROC in (C-F) do not show as clear a trend as was visible in Fig. 4.5 (C-F). Mice still showed signs of learning by decreasing the lick frequency for S-, which is particularly evident from Fig. 4.6 (H). However, the smoothed lick profiles also differ between experimenters. Whilst under MT, licks peaked after the grace period for S+, and were evidently reduced under S- particularly around the end of the grace period, mice under the protocol deployed by AB appear to differentiate less between the stimuli, by indicating high classical stimulus conditioning as apparent by high lick responses immediately following stimulus onset. Air puffs administered for licks after the grace period reduce lick frequency, but mice seem to fail to anticipate the punishment in AB's protocol. In accordance with this, lick frequency is only slightly increased for the positive stimulus, as is evident from the relatively flat lick profile following the grace period. This stands in contrast to the increased lick frequency of Fig. 4.5 (G), which indicates a strong peak particularly after the grace period during later sessions.

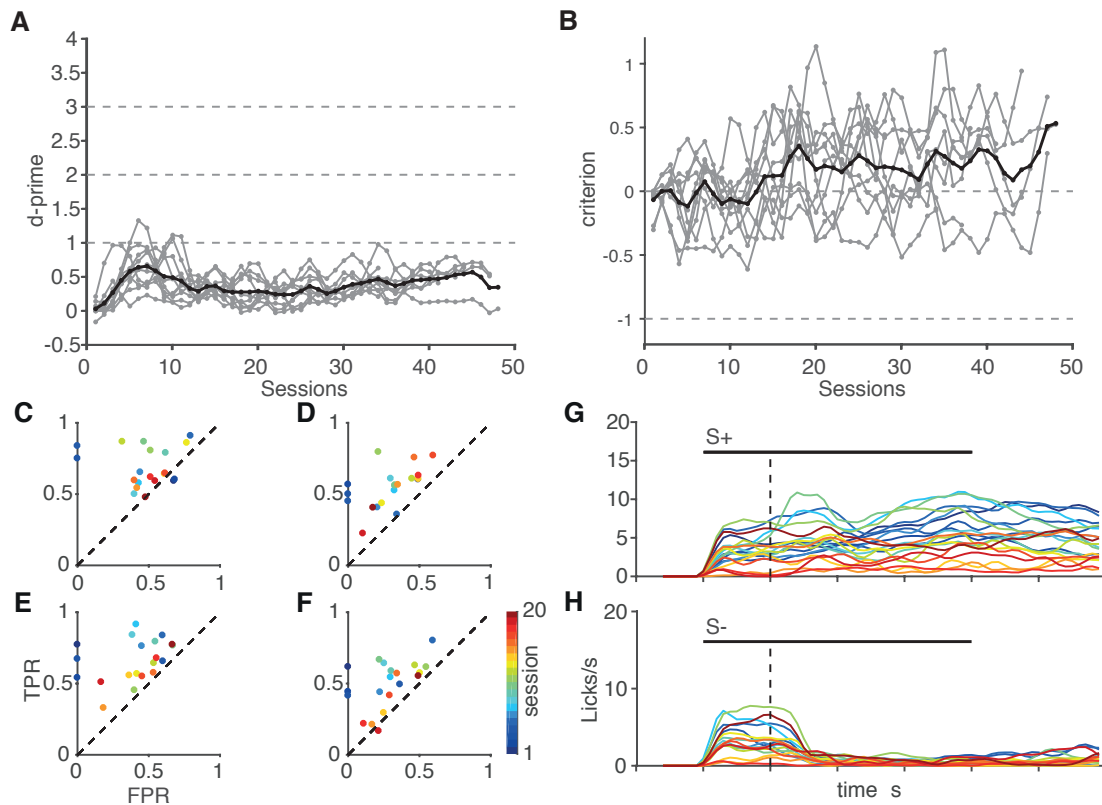


Figure 4.6: Behavioural progress is weak following protocol AB. (A) The sensitivity measure d' over sessions (training days) does not increase greatly over 50 days. Grey lines indicate individual mice in this batch (10 mice), black line mean across mice. (B) Criterion values oscillate around zero throughout sessions. (C-F) ROC values for the first 20 training days in 4 example mice used in later electrophysiology. Colour indicates training day, with blue shades corresponding to early, and red to later sessions. (G) and (H) illustrate the corresponding Hanning-smoothed lick PSTHs for (G) GO and (H) NOGO stimulus for the animal shown in (F). Initial lick profiles arise very similarly for both stimuli. Horizontal black line (top) indicates stimulus presentation, vertical dashed line end of the grace period. Colour code same as in (C-F).

4.3.2 Behaviour summaries of electrophysiological recordings

All data analysis unless otherwise stated is based on in-vivo electrophysiology data recorded by both MT and AB. It is clearly stated when which sets are used. Table 4.1 summarises all behaviour aspects during the electrophysiological recordings used in this study, and presents the number of trials for each behavioural outcome (FA, CR, MISS, HITS), and the performance attained during each recording (d' and accuracy (acc)). The first 9 experiments were conducted by MT, and the remainder by AB.

ID	FA	CR	MISS	HIT	d'	accuracy
G-13	1	100	60	35	1.9940	0.6888
G-14	15	119	64	71	1.2813	0.7063
G-15	8	108	46	64	1.6901	0.7611
G-16	6	111	43	42	1.6178	0.7574
H-10	47	85	23	115	1.3364	0.7407
H-11	23	125	50	87	1.3587	0.7439
H-12	20	115	65	62	1.0148	0.6756
J-20	41	95	9	111	1.9597	0.8047
J-21	17	107	34	87	1.6734	0.7918
mouse1_1a	5	64	61	7	0.1927	0.5182
mouse1_1b	6	59	61	1	-0.8145	0.4724
mouse1_1c	5	72	53	12	0.6167	0.5915
mouse1_2	12	198	188	34	0.5562	0.5370
mouse2_1	50	159	129	69	0.3387	0.5658
mouse2_2	39	106	76	71	0.5733	0.6062
mouse4_1	14	94	73	17	0.2461	0.5606
mouse4_2	27	123	78	71	0.8565	0.6488
mouse8_1	67	72	59	75	0.1953	0.5385
mouse8_2a	40	31	25	52	0.2951	0.5608
mouse8_2b	4	69	70	4	-0.0067	0.4966
mouse9_1a	32	42	50	28	-0.1910	0.4605
mouse9_1b	97	105	115	80	-0.1772	0.4660
mouse9_2	3	105	101	20	0.9416	0.5459
mouse9_3	8	67	52	20	0.6550	0.5918
raisa	15	81	78	23	0.2636	0.5279
renata_1a	76	83	81	82	0.0629	0.5124
renata_1b	1	38	35	2	0.3424	0.5263
sveta	7	83	77	8	0.1044	0.5200

Table 4.1: Trial outcomes of the behavioural experiments during electrophysiology, and the performances during the entire recording for all mice.

4.3.3 Mean firing rates differ between gratings, outcomes and experimenters

Fig. ?? illustrates box and whisker plots of the mean FR under varying behavioural conditions. As before, the central mark indicates the median, bottom and top edges the 25th and 75th percentiles. Whiskers extend to the extreme points which are not regarded outliers. Outliers are identified and marked as red crosses if they exceed $q3 + w \times (q3 - q1)$ or less than $q1 - w \times (q3 - q1)$, where w is maximum whisker length, and $q1$ and $q3$ refer to the 25th and 75th percentiles. Mean FR differ significantly (all $p < 0.001$, Kruskal-Wallis) between stimulus conditions S+ (rewarded stimulus), S- (negative stimulus), ITI, and SA recorded before (*pre*) and after (*post*) the behavioural session for both experimenters, regardless if FR are [0,1]-normalised or not. SA in *pre* and *post* was recorded in darkness (black screen, dark room). Scrutiny of the differences in mean FRs during stimulus presentation (S+, S-) reveals a significant difference ($p < 0.001$, 2-sample sign test, Bonferroni corrected) for experimenter MT (Fig. 4.7, (A)), whereas significance in the difference cannot be reported for experimenter AB (Fig. 4.7 (C), $p > 0.0167$, 2-sample sign test, Bonferroni corrected), although both stimuli differed significantly from ITI (for both experimenters $p < 0.001$, 2-sample sign test, Bonferroni corrected).

Dividing S- and S+ in their behavioural outcomes FA, CR, MISS and HITS, the mean FR appear even more significantly different within the same stimulus types (illustrated in Fig. 4.8). Fig. 4.8 (A) presents that although the same stimulus is presented, S-, mean FR differ significantly at $p < 0.001$ (2-sample sign test, Bonferroni corrected) between FA and CR. This is also the case for S+, where MISS and HITS significantly differ at $p < 0.001$ (2-sample sign test, Bonferroni corrected). The responses in passive behaviour, as indicated by withholding a lick in CR and MISS, also differs significantly at $p < 0.001$ (2-sample sign test, Bonferroni corrected). The distributions of CR and MISS both differ significantly from FA and HITS (each to MISS and CR $p < 0.001$, 2-sample sign test, Bonferroni corrected). CRs do not differ significantly from ITI, or SA *pre* or *post*, whereas MISS does in all cases at $p < 0.001$. Mean FR of HITS are significantly different from all but FA, as are FA (all $p < 0.001$).

Fig. 4.8 (B) visualises the [0,1]-normalised mean FR, making it easier to follow the qualitative shapes of (A). Fig. 4.8 (C) conveys the same as (A) for experimenter AB, in 520 MU. Qualitatively, the results are as in (A), with the exception of FA and HITS to significantly differ at $p < 0.001$ (2-sample sign test, Bonferroni corrected), but MISS and *post*, and ITI and *post* do not in (C).

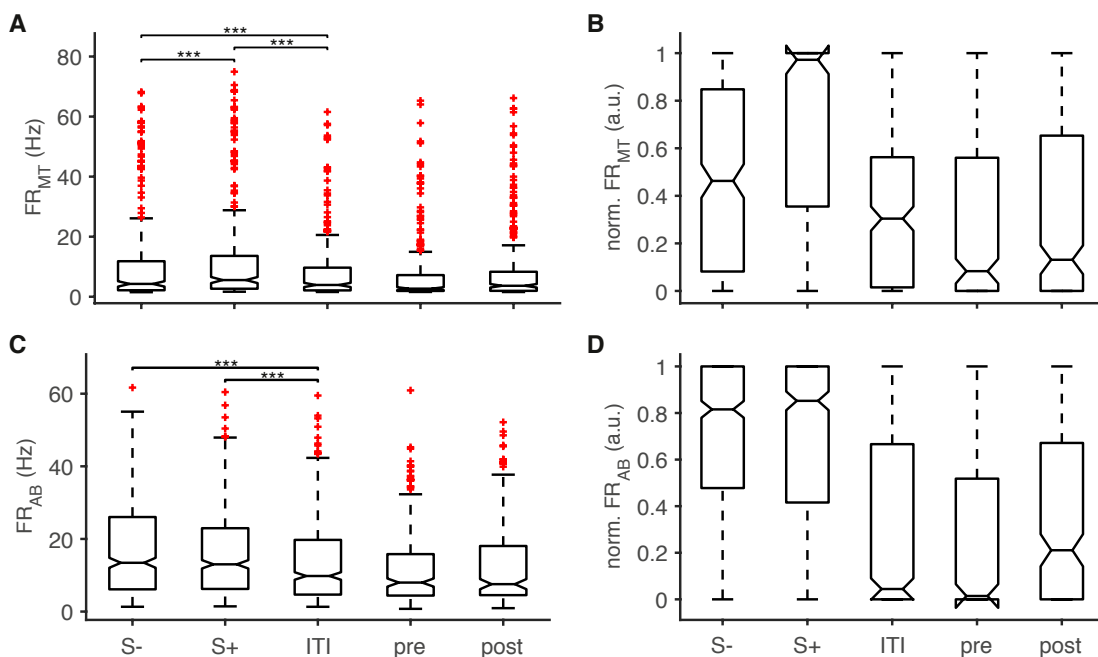


Figure 4.7: Mean FR differs between stimulus conditions and experimenters. (A) mean FRs of all MU and all experiments by MT show a significant difference between S+ and S- (***) indicates $p < 0.001$, 2-sample sign test, Bonferroni corrected). (B) [0,1]-normalised FR enhances this even further. (C, D) same as in (A) for experimenter AB. Medians were only compared for S-, S+ and ITI.

Behavioural outcome and performance may affect PSTH shape

The PSTH for each outcome (FA, CR, MISS, HITS, ITI) reveals useful information about how stimuli are (temporally) processed. Pooling all mice and all MUA, results in the mouse-channel-averaged PSTH in Fig. 4.9. Before averaging across mice, the PSTH was calculated over 5 ms bins, smoothed via convolution with a normalised Hanning window over 50 ms. It is evident from Fig. 4.9 (A) that the onset response is followed by a secondary peak around 250 ms. Comparing (A-D), the increased activity particularly for FA after 500 ms is striking. In (B, C), *NoLick* outcomes (CR and MISS), the PSTH responses look very similar, with high primary peaks around 50 ms followed by secondary peaks at 250 ms. This is succeeded by a low response until the end of stimulus presentation at 2 s. HITS appear with a strong onset response followed by a weaker secondary peak turning into sustained activity throughout stimulus presentation. All outcomes exceed average ITI activity as indicated by the grey line. Only CR in (B) appears to reach levels comparably low as during ITI in the latter part of stimulus

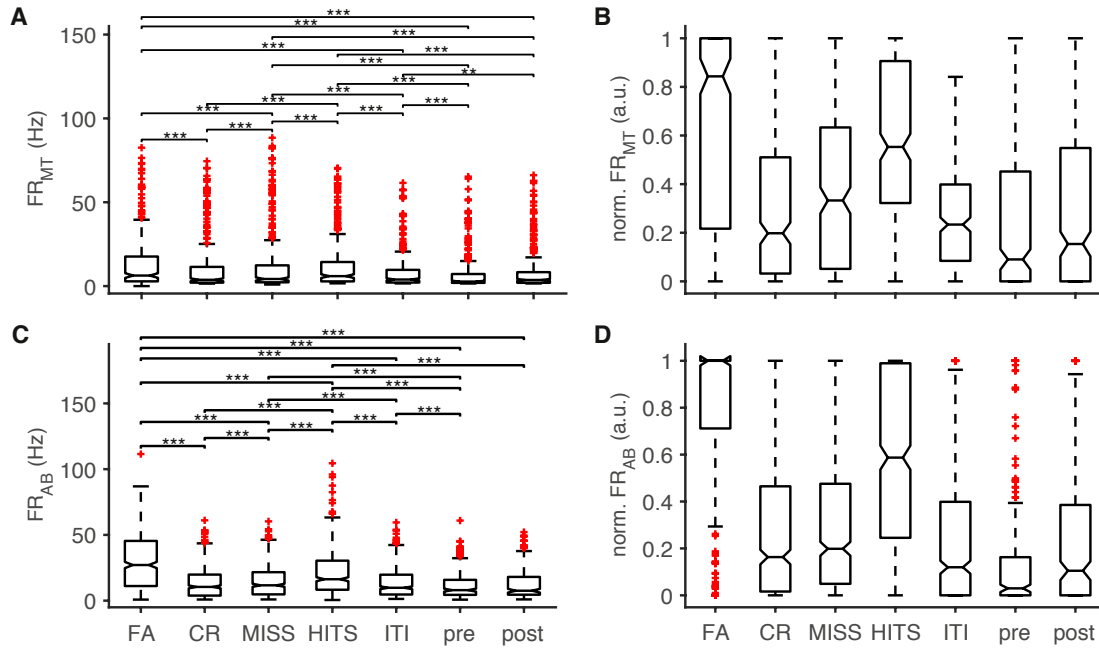


Figure 4.8: Mean FR differ among outcome conditions and experimenters. (A) mean FRs of all $n=288$ MU of experiments by MT across behavioural outcomes and stimulus conditions indicate significant differences within and across stimulus types (S+, S-) (***) indicates $p < 0.001$, 2-sample sign test, Bonferroni corrected for multiple comparisons). (B) $[0,1]$ -normalised FR enhances the qualitative shapes of (A). (C, D) same as in (A) for experimenter AB for 520 MU.

presentation.

Disentangling the PSTH using knowledge about animals' performances, dividing the mice into groups of high ($\text{acc} > 0.65$) and low accuracy (≤ 0.65) reveals a vastly different picture as presented in Fig. 4.10. The group sizes are 37% for high and 63% for low-performing mice. This group allocation happens to coincide with different experimenters. AB's animals belong to the group at accuracy < 0.65 , and MT's the high-performing.

Fig. 4.10 (A) indicates a strong difference in PSTH shapes at high and low performances for FA outcomes (or MT and AB). The low-performance group (red) displays a high average response throughout stimulus presentation (whole window), with a higher average FR in general. The onset response can be characterised with a peak followed by a secondary, weaker peak around 250 ms. Following this, a strong increase in FR was apparent for the remainder of the window from about 500 ms. This sustained high response reaches and exceeds levels of the onset peak. This may be ascribed to the

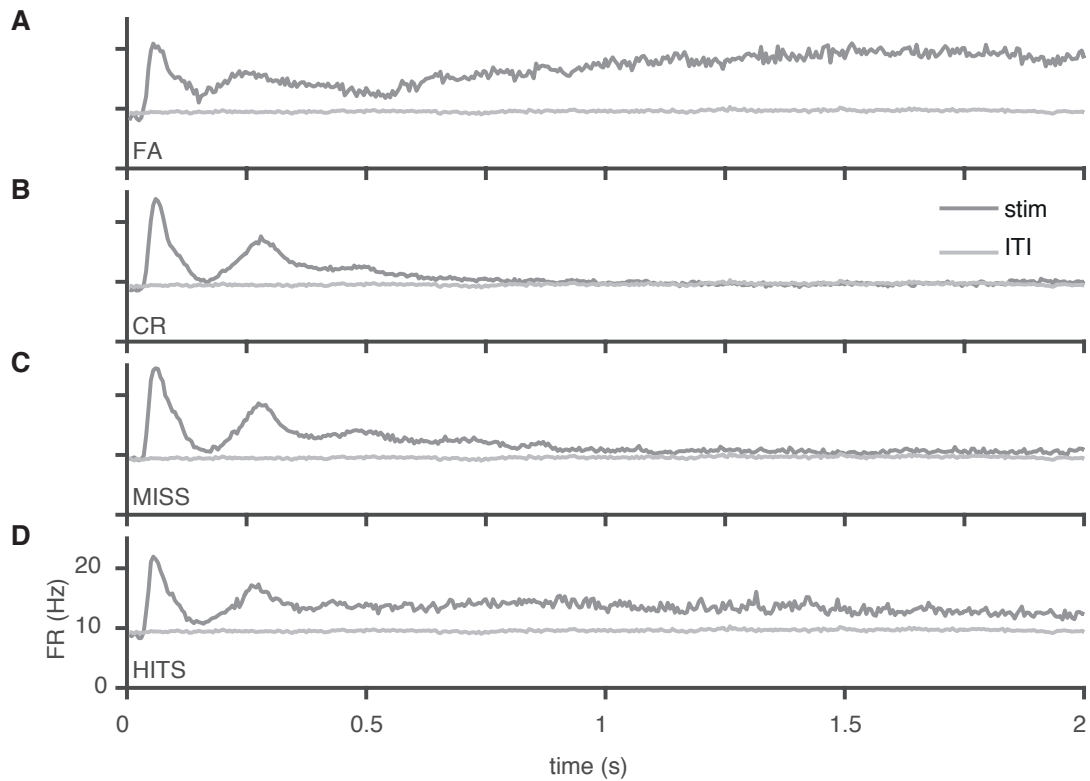


Figure 4.9: Average PSTH reveals differences in FR time course. Mouse-, trial and channel- averaged PSTH over 5 ms bins, smoothed with a Hanning filter over 50 ms for all outcomes with more than 9 trials. All outcomes reveal a strong onset response followed by a weaker secondary peak and differing stationary activities. (A) FA reveal weakest onset response and highest sustained activity during stimulus presentation. (B) PSTH as in (A) for CR outcomes show a double peak response with a strong onset and very low following activity. (C) PSTH for MISS is similar to CR responses with double peak and lower tail. (D) PSTH for HITS excels with a higher sustained responses after primary and secondary peak. All graphs show average ITI as a faint grey line to compare.

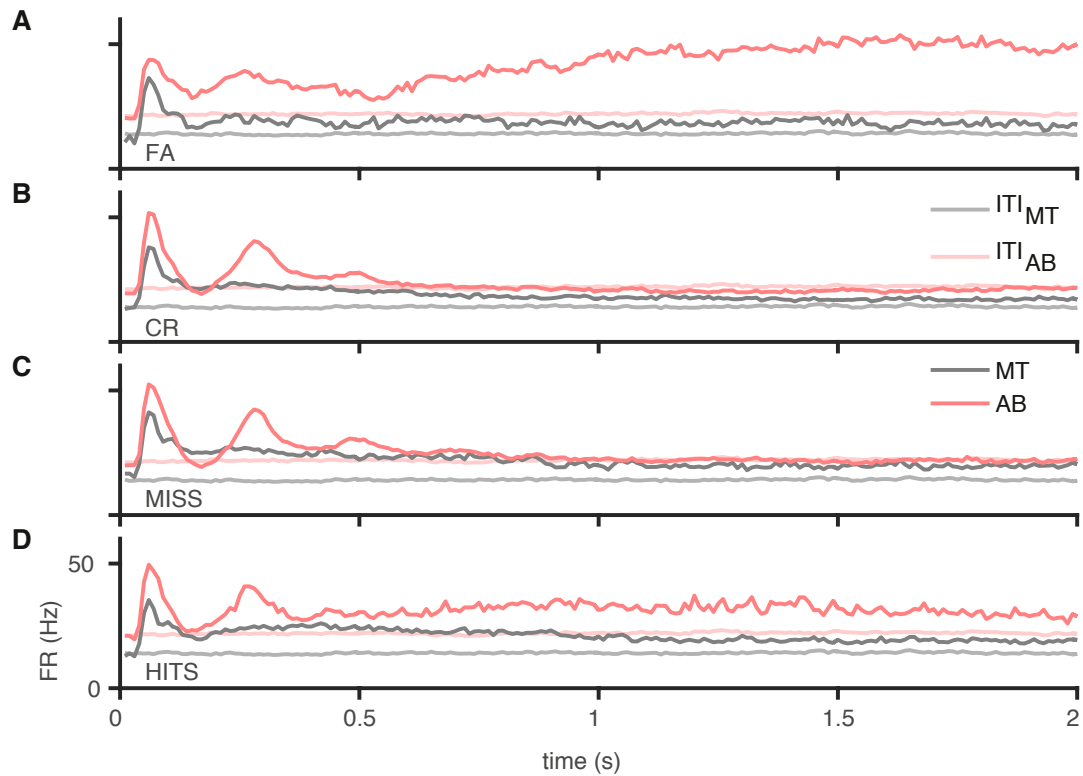


Figure 4.10: PSTH at high accuracy differs vastly from low. Description same as in Fig. 4.9. (A-D) FA, CR, MISS, HITS. Mice are split into high-performing (accuracy > 0.65) and low-performing (accuracy ≤ 0.65) groups. The double peaks seem to be prominent only in lAB's group. Sustained responses in FA and HITS also appear predominantly for AB's set. Average ITI is higher in low-performers than high-performers (faint red vs. faint grey line, respectively).

punishment (air puff) following a lick during S- presentation. Air puffs are immediately triggered upon a lick after 500 ms, which may blur out a clear temporal correlation between response and puff since licks may occur at any time. Unfortunately, in early recordings of AB, air puffs sometimes created artefacts, which may be the source of the visible increase after 500 ms. Luckily, these were not observed in MT's animals.

The high-performing group (dark grey) presents a PSTH demonstrating an onset peak starting at the average ITI line (faint grey) reaching a peak just below the low-performing animals, coinciding in time with them. After this initial peak, the remaining PSTH levels off slightly above the ITI line.

PSTHs for CR in Fig. 4.10 (B) also differ between groups. The low group (red) exhibits a strong onset response that plummets momentarily to ITI level (faint red) around 200 ms, before increasing to a secondary peak at approximately 80% of the primary peak around 250-300 ms. After this secondary peak there is a hint of a third one at 500 ms before finally levelling off for the remaining stimulation to values even slightly below ITI. The high-performance group, in dark grey, displays a strong primary peak with a small step on the falling flank. After this initial disruption, the PSTH levels off at a sustained plateau slightly above ITI throughout stimulus presentation.

AB's MISS trials, presented in Fig. 4.10 (C) appear with great similarity to CR trials in (B), with a strong onset response, momentarily dip at 200 ms and a secondary peak around 300 ms and a hint of a tertiary peak at 500 ms before tailing off afterwards for in the low-performing group. MISS trials in MT's group appear similar in shape to CR PSTH, only that the step on the downward flank is slightly more pronounced than in (B) and the general plateau in activity is slightly above CR outcomes.

Finally, AB's HIT trials, detailed in Fig. 4.10 (D) occur with the double peak previously described and remain at a noisy elevated activity level in low-performing group. High-performing HITS appear with an onset response similar to CR and MISS outcomes, again with a small step on the downward flank, but this time falling slightly below those values observed in MISS and CR, before marginally increasing and reaching a plateau until the end of the window.

These results suggest a difference in the datasets acquired by MT and AB, which is another reason why all following analysis is presented separately for the different sets.

4.3.4 Mutual Information indicates behavioural correlate in V1

MI between behavioural outcomes (HITS, CR, FA, MISS, ITI) and neural response suggests a substantial amount of information in the neural data about behavioural outcome

($p < 0.001$, 2-sample sign test between data and shuffled labels), with a mean at 0.02 bits, and peak values at 0.25 bits. As expected, MI between MUA patterns and behavioural outcomes is higher than that contained in population FR ($p < 0.001$, 2-sample sign test), as is evident from Fig. 4.11.

Fig. 4.11 (A) provides the MI between MUA and behavioural outcome estimated via entropies of 8-bit patterns at 5 ms bin widths, for shuffled labels (shL) and shuffled bins (shBin). Shuffling the outcome labels reduces the MI to zero (with some fluctuations attributable to entropy estimation, which is markedly higher for 16-bit or 24-bit calculations (not shown)), and spatially shuffling the bins significantly reduces MI ($p < 0.001$, 2-sample sign test), suggesting spatial arrangement adding information about behavioural outcome. In (B), MI is estimated using the population FR, i.e. the spatial sum over the same patterns as in (A). Using population FR, MI is generally lower than estimated via patterns ($p < 0.001$, 2-sample sign test). Shuffling labels reduces entropy to zero without any apparent fluctuations. As expected, taking the population FR on the shuffled bins (shBin) amounts to the same results as the unshuffled data, since spatially shuffling bins does not affect the bin sum. Further, MI estimated on patterns that were spatially shuffled bins, and that of population FR differ significantly at $p < 10^{-4}$ (Wilcoxon signed ranks).

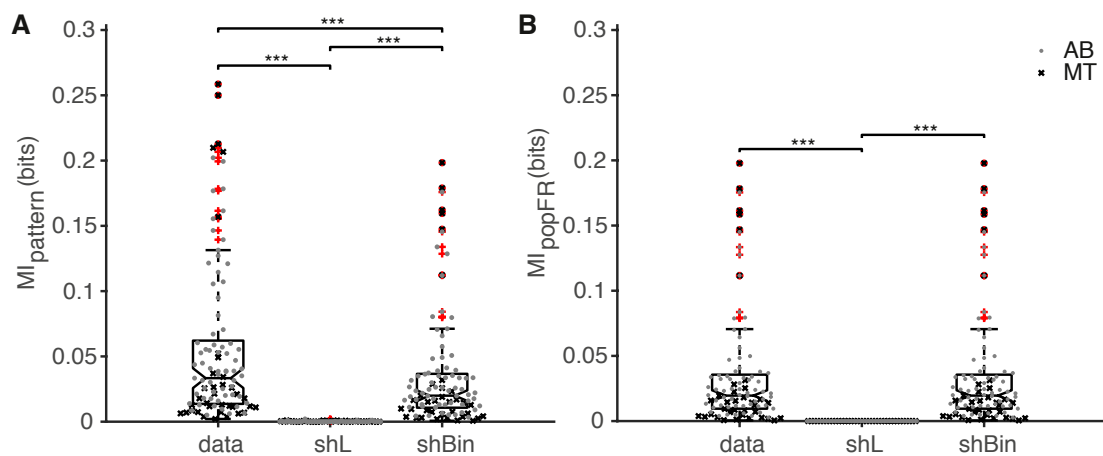


Figure 4.11: MI between behavioural outcomes including ITI, and neural response is non-zero. (A) MI between MUA and behavioural outcome is significantly greater than zero ($p < 0.001$, 1-sample sign test) for 8-bit patterns at 5 ms bins (one shank). Shuffling labels decreases MI to zero, and spatially shuffled bins significantly reduce MI over unshuffled patterns (all $p < 0.001$, 2-sample sign test, Bonferroni corrected). Different symbols correspond to experimenters. (B) Same as (A) but for *popFR*. *** indicates $p < 0.001$, 2-sample sign test.

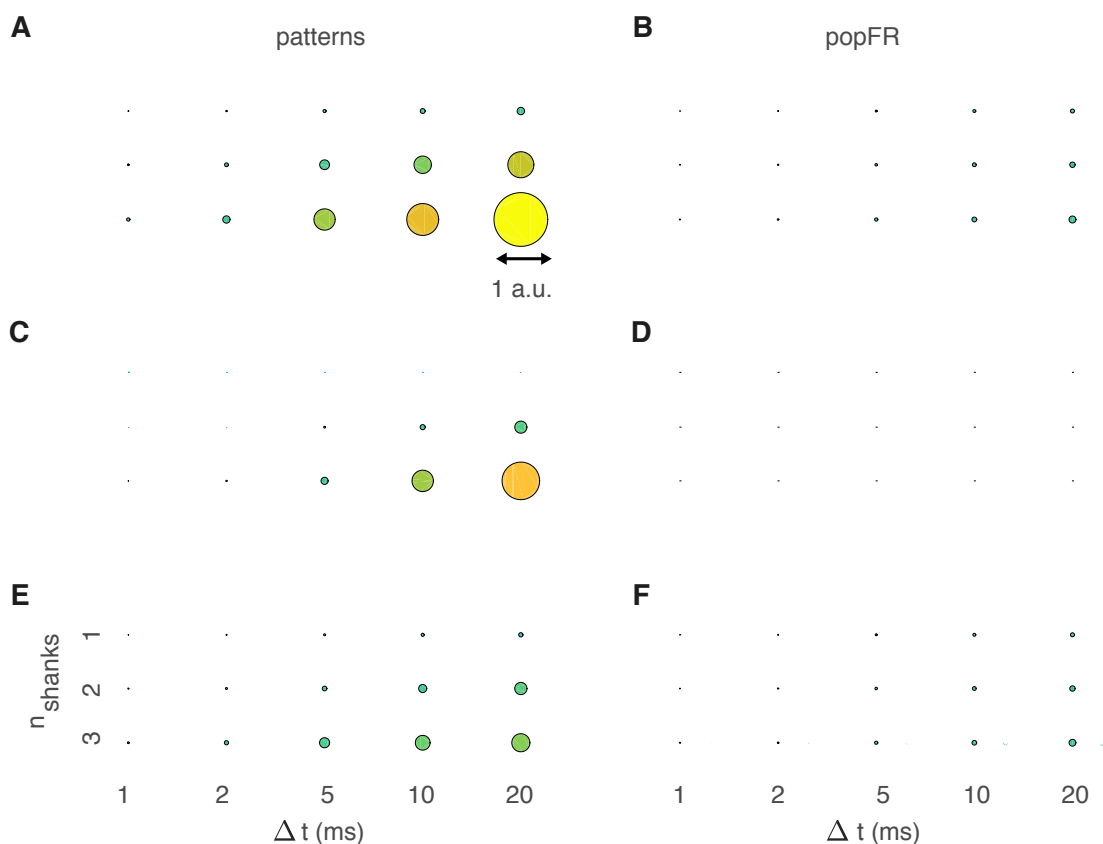


Figure 4.12: Median MI increases with bin width and number of shanks. (A) Median MI across mice is highest at 20 ms binned MUA using 3 shanks, where circle radius corresponds to MI normalised to the maximum occurring value. (B) Same as in (A) for population FR estimates. (C, E) Same as (A) for shuffled labels and shuffled bins, respectively. (D, F) same as (C, E) on population FR. Given the nature of the shuffle, (B) and (F) are exactly the same. (D) is zero for all points.

Fig. 4.12 highlights how MI is affected by bin width and number of shanks used, as indicated by the medians over experimental sets on data and shuffled data as in Fig. 4.11. For illustration and scaling purposes, MI values were normalised by the maximum occurring value (0.42 bits at $\Delta t=20$ ms and 3 shanks for unshuffled data).

Panels (A, C, E) reveal MI estimated on MUA patterns, and (B, D, F) its estimation on population FR. It is evident from (A) that MI increases slowly with bin width, and more visibly with the number of shanks included, leading to MI appearing highest at 20 ms bins for 3 shanks. Shuffled labels in (C) indicate zero values for 8-bit patterns (1 shank, first row), which increase slightly for 16-bit patterns, and peak at 20 ms for 3 shanks (0.3 bits). As was pinpointed in Fig. 4.11 for 8-bit patterns already, the shuffled

labels set does display residual information despite shuffling, which is even more visible for higher bit patterns (e.g. 3 shanks at 24-bit patterns at 20 ms bins). This should not be the case in a sufficiently sampled distribution and is indicative of a negative bias in entropy estimation. Overall, MI is reduced in comparison with (A). Spatially shuffling bins in (E) reveals reduced MI for each combination in relation to (A).

In contrast to MUA patterns, panels (B, D, F) provide the results for MI estimated via population FR. MI is smaller than (A) for all combinations. Qualitatively, MI still increases in a similar fashion when increasing bin width and number of shanks, while the differences between MI are marginal, yet leading to the largest MI at 0.04 bits, for 3-shanks (25 possible states) at 20 ms. For this type of data, distribution space appears sufficiently sampled, which is also evident from panel (D) revealing MI of shuffled labels being zero for all combinations, as would be expected. (F) then reports the same results as in (A) since shuffling bins does not affect population FR.

4.3.5 JSD between outcomes differs between experimenters

JSD lowest for non-licking behaviour for 8-bit patterns

Comparing patterns and their frequencies under the different behavioural outcomes lets us potentially investigate how distinct ensembles are more or less involved in experimental conditions. The PSTH from Fig. 4.10 reported that there was a significant difference between experimenters and/or performance level of animal training. Thus, also here, Fig. 4.14 juxtaposes the results in two subpanels for each experimenter. To provide a different reference for the conceptual meaning of the divergences between behavioural outcome types, Tab. 4.2 summarises response types. Divergences between groups FA and CR belong to stimulus S- (NOGO). Divergences between FA and MISS represent the wrong choice (incorrect lick and incorrect withholding of a lick) etc.

	FACR	FAMISS	FAHITS	CRMIS	CRHITS	MISSHITS
Response Type	S-	Wrong	Lick	No Lick	Correct	S+

Table 4.2: Combinations of behavioural response types. FACR corresponds to the case where S- was presented, comprised of FA and CR. FAMISS represents the wrong behavioural decision, etc.

Fig. 4.13 contrasts the JSD for each response type and evaluates whether the JSD differs significantly between categories. Subpanel (A), for all experiments by AB, depicts significant differences between all response types and *NoLick* ($p < 0.001$, Mann-Whitney-

U test (MWU), Bonferroni corrected for multiple comparisons), which emerged with a very low JSD at a median of 0.02 bits and low variation. JSD distributions also differ significantly ($p < 0.001$, MWU, Bonferroni corrected) between $S+$ and $S-$. Divergences of *Correct* decisions emerge with a lower median than those during *Wrong* outcomes ($p < 0.001$, MWU). Evaluating the distributions, divergences involving $S+$ are generally lower than $S-$ ($p < 0.001$, MWU). *Correct* and $S-$ also differ significantly at $p < 0.001$, as do *Wrong* and $S+$ (all MWU). Part (B) discloses the results for experimenter MT, which surface at overall lower values and spread than in (A). Like in (A), the lowest divergence is observed for *NoLick*, which is highly significantly different from all but one (*Correct*) other response category at $p < 0.001$ (MWU, Bonferroni corrected). As in (A), *Correct* and *Wrong* divergence distributions differ significantly at $p < 0.001$ (MWU), with *Wrong* types manifesting a higher median. In contrast to (A), $S+$ and $S-$ do not show a significant difference in their medians. In accordance with (A), both *Correct* and $S-$, and *Wrong* and $S+$ differ significantly at $p < 0.01$ and $p < 0.001$, respectively (MWU, Bonferroni corrected).

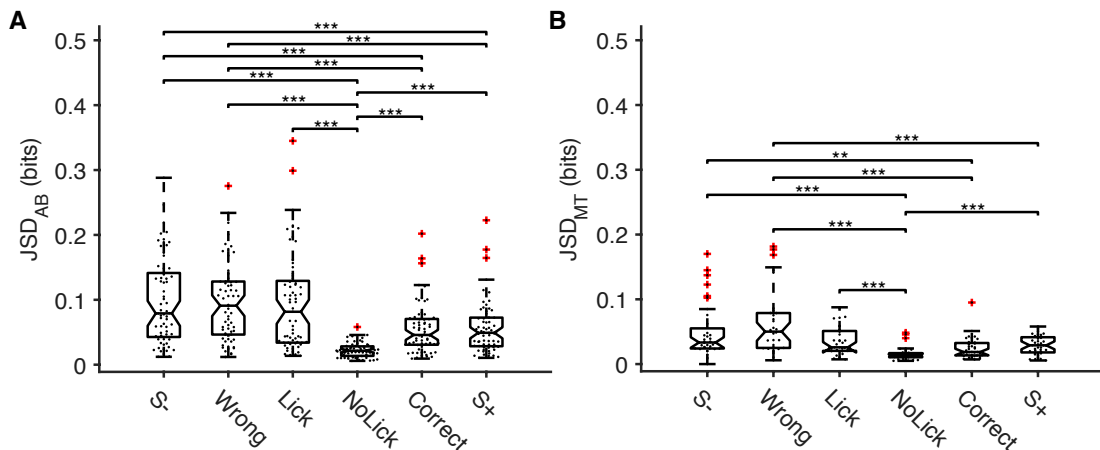


Figure 4.13: Substantial difference in JSD between outcome pairs at 8-bit patterns. (A) JSD of all patterns observed between pairs of behavioural outcomes for experimenter AB indicates significant differences between *NoLick* and all other outcomes at $p < 0.001$ (MWU, Bonferroni corrected). (B) The dataset by MT displays significant differences between some of the JSD distributions (** indicates $p < 0.01$ and *** $p < 0.001$, MWU, Bonferroni corrected for multiple comparisons). JSD was calculated for 8-bit patterns at 5 ms bin widths.

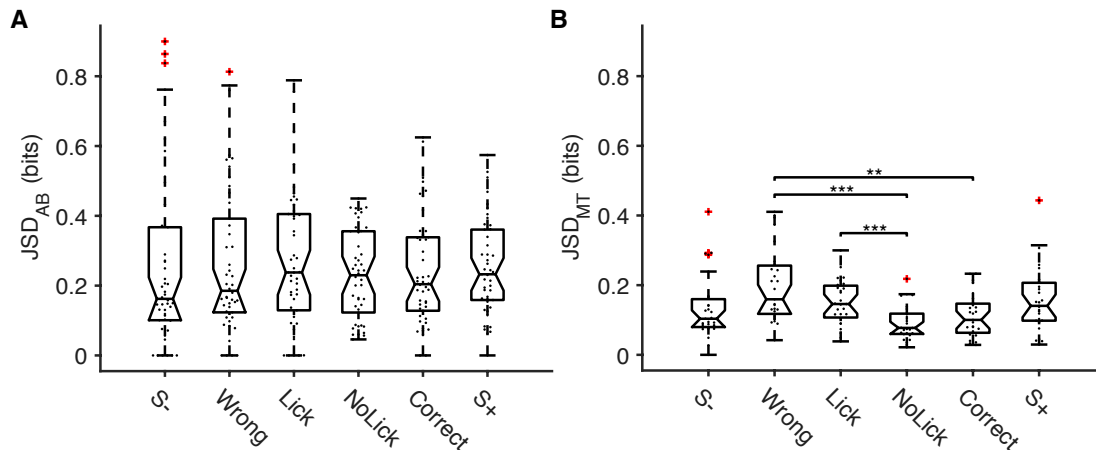


Figure 4.14: Substantial difference in JSD for one experimenter at 16-bit patterns. (A) JSD of all patterns observed between pairs of behavioural outcomes indicates no significant difference for pairwise outcome JSD distributions for experimenter AB (MWU, Bonferroni corrected). (B) The dataset by MT indicates significant differences between some of the divergence distributions (** indicates $p < 0.01$ and *** $p < 0.001$, MWU, Bonferroni corrected for multiple comparisons), most notably *Lick* and *NoLick*, or *Correct* and *Wrong*. JSD was calculated for 16-bit patterns at 5 ms bin widths.

JSD at 16-bit patterns varies between experimenters

Examination of 16-bit patterns provides a slightly different perspective from 8-bit patterns. Fig. 4.14 (A) contains the JSD for all pairwise behavioural outcome divergence distributions estimated on 16-bit patterns at 5 ms for recordings by AB. No JSD of any behavioural outcome combination appears to be deviating significantly for experimenter AB ($p > 0.05$, Kruskal-Wallis). The median lies around 0.2 bits for all categories.

In (B) significant differences between several response types for recordings done by MT emerge (** indicates $p < 0.01$ and *** $p < 0.001$, MWU, Bonferroni corrected for multiple comparisons). The qualitative shape of distributions, with e.g. the median of *Wrong* exceeding *Correct* and *NoLick* appears similar to the one observed for 8-bit patterns in Fig. 4.13. The spread is generally smaller than in (A) whose JSD reached values as high as 0.9 bits, in contrast to (B)'s maximum of 0.4 bits. Inspection of (B) suggests the JSD between *Wrong* and *NoLick* (non-active behaviour) differs significantly at $p < 0.001$ (MWU, Bonferroni corrected). Overall, non-active behaviour, *NoLick*, displays lowest JSD with also the lowest variance, whilst *Wrong* display the highest JSD. *Wrong* and *Correct* indicate a significant difference in JSD ($p < 0.01$, MWU, Bonferroni

corrected), which is interesting from a behavioural perspective as both combinations include non-active and active (licking) behaviour. In contrast, $S-$ and $S+$ do not appear significantly different (MWU). Divergences of *Lick* and *NoLick* also differ significantly at $p < 0.001$ (MWU, Bonferroni corrected). All significant differences observed here also differed significantly in 8-bit patterns.

4.3.6 High Mutual Information between shanks indicates cross-columnar co-activation

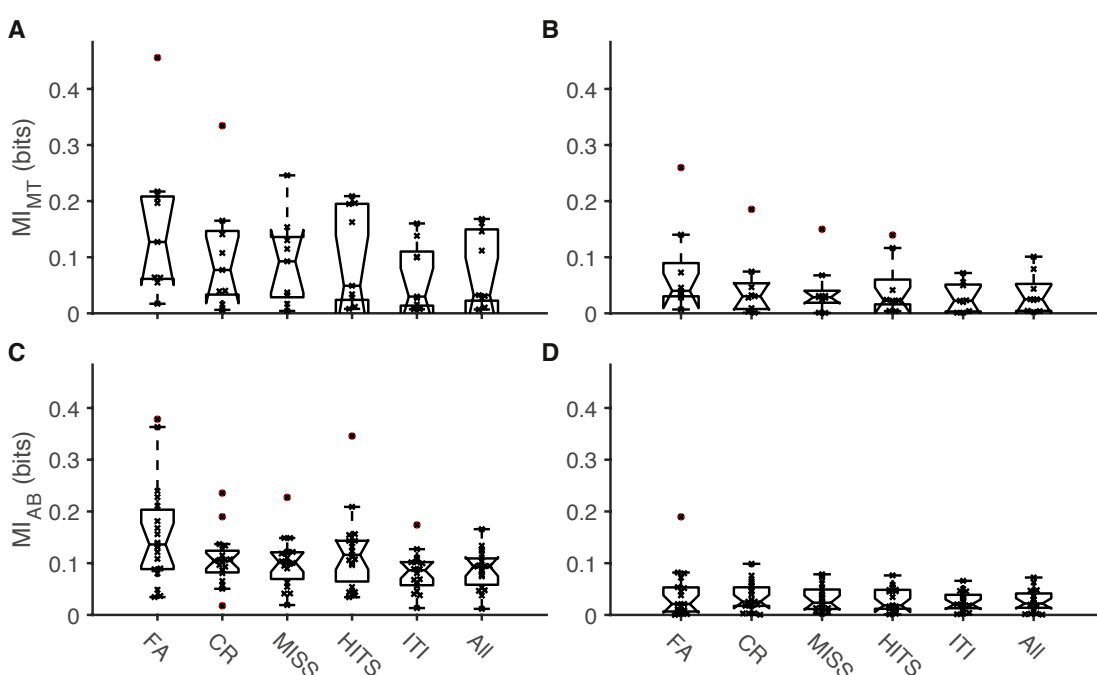


Figure 4.15: MI between pattern response and shanks is high and similar in all outcomes (5 ms bin width). MI (A) In MT's dataset animals reach MIs of around 0.1 bits, which does not differ significantly ($p > 0.003$, Wilcoxon rank sum, Bonferroni corrected). "All" denotes computing MI over the entire recordings. (B) Same as in (A) but for population FR. (C, D) same as in (A, B) but for AB.

The MI between each shank is one indicator of how correlated the shanks are in terms of cross-columnar co-activation. This is another important approach in understanding visual processing in V1. In this examination, $MI(R;shanks)$ is estimated as the information between neural signals (patterns or population FR) on one shank and the other shanks, at bin widths of 5 ms. To investigate whether the information conveyed by one

shank is affected by outcome type, Fig. 4.15 delineates the results separately for each behavioural state, and as well as across the whole recording (denoted "All").

Fig. 4.15 illustrates the results for $MI(R;shanks)$ estimated on MUA patterns (A, C) and population FR (B, D), also separated for the experimenters (A, B) from MT, and (C, D) from AB. The experimental sets were divided for experimenters, but statistical analysis indicated $MI(R;shanks)$ was not significantly different ($p > 0.05$, MWU test) between experimenters.

Assessing $MI(R;shanks)$ under differing conditions with Friedman tests resulted in significant differences for $MI(R;shanks)$ in (A) and (C) at $p < 0.001$, and $p < 0.05$ for population FR in (B), indicating that $MI(R;shanks)$ was significantly modulated by behavioural outcome. Yet, sign tests with multiple comparisons across outcomes (Bonferroni-corrected) were not significant.

The median MI between activity and shanks amounts to 0.08 bits for patterns (overall, across both experimenters) and 0.02 bits for population FR (estimated over "All" and both experimenters).

4.4 Discussion and conclusions

This chapter investigated how and if behavioural task outcome was reflected in the activity of simultaneously recorded populations of neurons. A new, efficient behavioural training protocol for head-fixed, water-restricted mice was developed, successfully evaluated and contrasted with a preceding protocol. Under the new protocol, mice learnt to differentiate between two gratings faster, reaching a discriminability index d' of 1 already after ten days, which was hardly reached under the previous protocol. Water-restricted, head-fixed C57BL/6 wild type young adult female mice were trained in an operant conditioning GO/NO-GO visual discrimination task to initiate or withhold a response (licking) upon visual presentation of one of two drifting gratings. Novel multi-shank, multi-laminar MUA data in in-vivo electrophysiology in V1 in the awake-behaving mouse was produced, quantitatively and qualitatively analysed and juxtaposed with data recorded by AB under the preceding protocol. MI of responses and behavioural outcome was determined, and JSD between pairwise groups of behavioural outcome classes examined.

Behaviour in a GO/NOGO task in head-fixed mice

In this study, an efficient behavioural protocol for head-fixed mice in a visual GO/NOGO task was devised. It improved over previous protocols (e.g. Berditchevskaia (2014)) as was indicated by the large deviation between success rates and discriminability during only 10 training sessions.

Fig. 4.5 suggested that mice were able to correctly discriminate between the gratings after roughly 10-15 sessions, when they reached a d' of 2. After this, the d' value reached a fluctuating plateau around 2 until the end of the training. Criterion fluctuated in a similar fashion for the first 10-20 sessions, whilst showing generally a slightly negative response bias. Other protocols involving whisker-stimulation in tactile behaviours (Guo et al. 2014) followed similar approaches as pursued in this study, reaching comparable values in discriminability after only ten sessions. Andermann, Kerlin and Reid (2010) achieved analogous results in head-fixed mice performing a GO/NOGO task, in chronic Ca^{2+} -imaging. Despite mice being nocturnal and having visual capacities inferior to carnivores or other higher mammals, e.g. (Prusky and R. M. Douglas 2004), mice were shown to be able to discriminate between stimulus features (Mangini and Pearlman 1980; Niell and Stryker 2008), and prove to be a suitable candidate for basic visual processing questions (Huberman and Niell 2011; Glickfeld, Reid and Andermann 2014).

It has been shown that visual responses are modulated by locomotion, another factor which could speed up the learning time (Andermann, Kerlin and Reid 2010; Dadarlat and Stryker 2017; Niell and Stryker 2010).

Although animals showed great progression during the training stage, performance sometimes decreased slightly during electrophysiological recordings. This may be attributable to increased stress or sub-optimal recovery after the general anaesthesia for the craniotomy. Alternatively, the current surgical protocol required an injection of 0.2 ml of sterile saline per hour of surgery. This fluid uptake, in connection with Buprenorphine jelly, may impede behavioural performance because the animal may no longer be sufficiently water deprived.

Significant difference in firing rates between rewarded and unrewarded stimulus

It was suggested that learning not only enhanced sensory responses in mouse V1, but that it also affected behaviour (Poort et al. 2015; Jurjut et al. 2017). Thus, training mice to respond differentially to distinct stimuli should be visible in behavioural

markers (such as task performance, accuracy or d') and as a correlate in the sensory representation.

Fig. 4.7 highlighted the significant difference in mean FR between S+ and S- ($p < 0.001$, 2-sample sign test) for high-performing (accuracy > 0.65), animals from experimenter MT. Normalised FR even amplified this finding. Considering that the FR before behavioural training is unknown, inference on what this difference signifies behaviourally is difficult. In conjunction with findings from Chapter 2, which indicated that leftward moving gratings evoked strongest responses in anaesthetised mice, it was now also observed in awake mice that the median FR for the leftward moving grating (S+) exceeded that of downward drifting grating.

In addition to an innate affinity of leftward moving gratings, repeated exposure to sinusoidal gratings can lead to SRP, which may have played a role in creating the difference in FRs as well. SRP is an example of experience-dependent plasticity in V1 without the involvement of acuity processing for low threshold visual stimuli (Duncan and Boynton 2003; Hager and Dringenberg 2010). Frenkel et al. (2006) investigated this perceptual learning and implicit memory in chronic Visually Evoked Potentials (VEP) recordings in L4 of V1 in mice passively viewing sinusoidal gratings. This stimulus-specific increase in amplitude is thought to originate from the local plasticity in V1. It is typical for early processing stages (Fahle 2004), and does not transfer across stimuli or between eyes. From a computational biology point of view, SRP can be thought of as a form of Hebbian plasticity realised as NMDA receptor-dependent Long-Term Potentiation (LTP) (Cooke and Bear 2014).

Related to this, Gavornik and Bear (2014) enquired into sequence recognition and prediction in V1, as SRP is highly specific to orientation presentation order and timing. They showed that V1 could recover the full sequence of stimuli even when single stimulus elements were excluded. The authors explained further that sequence learning did not transfer between trained and untrained eye, in line with the results of SRP, indicating that these changes in local plasticity appear at a stage where information processing from the eyes can still be separated. However, this sequence learning does not require NMDA receptor activation, and is thus based on a mechanism different from SRP (Gavornik and Bear 2014). Instead, sequence learning may involve a mechanism that makes use of input from the cholinergic system of the basal forebrain, as has been shown to be the case for several types of experience-dependent plasticity in V1 (Chubykin et al. 2013; Bear and Singer 1986). Given that in the present study stimuli were presented pseudorandomly, sampled from a Bernoulli distribution with variable length Poisson-

sampled ITI, sequence recognition should not be an issue in this study.

One possible way to test the involvement of SRP in the awake behaving task may be through injection of antagonists. Frenkel et al. (2006) showed that the induction of SRP required the activation of NMDARs, which they could abolish by applying an NMDA receptor antagonist CPP, leading to a blockage of AMPA insertion in V1 (with GluR1-CT). Thus, no LTP could evolve. However, this, and a similar study involving visual recognition memory (Cooke, Komorowski et al. 2015), was only shown in passively viewing, anaesthetised mice. It is still unknown if SRP was required for reward learning in the early visual system. Thus, an interesting extension would be to examine the effects of an abolished SRP and task performance of the mice.

Unfortunately, the dataset obtained by AB revealed findings dissimilar to MT indicating no apparent significance in the medians of the stimuli. In addition, mice were trained to different discriminability levels, with those achieved in the MT batch greatly exceeding AB's. Thus, it is not evident if the lack of reproducibility in median FR of the stimuli ensued from the different experimenters or the different performance levels of the mice.

Regrettably, we lack data of other sinusoidal gratings in this task, or data acquired before reward association took place, which could have been a valuable extension to describe these findings.

Behavioural response significantly influences stimulus-evoked firing rate

The two moving gratings evoked different FRs in V1. Through behavioural training, each stimulus was associated with either a reward or punishment. This entailed that the stimuli bore different meanings and required opposing responses from the mouse. Thus, beside changes attributable to habituation or SRP, mean FR for these associations could be affected by arousal or behavioural state (Vinck et al. 2015). One shortcoming of this study, however, is that pupil diameter was not recorded, a parameter that has been implicated in motivation (C. R. Lee and Margolis 2016).

Indeed, Fig. 4.8 indicated significant differences between FR distributions among behavioural task states (FA, CR, MISS, HITS, ITI, *pre*, *post*). This was an observation consistent across experimenters, and thus observable at different performance or discrimination levels. For example, FR during FA exceeded those recorded in CR, both states of the same visual stimulation. In conjunction with this, HIT FR exceeded those of MISS ($p < 0.001$, 2-sample sign test). These increases in FR during active licking behaviour (FA and HITS) may argue for an implication of top-down regulations (S. Zhang

et al. 2014; Moldakarimov, Bazhenov and Sejnowski 2014), enhancing the responses when a behavioural action is implemented. In addition to elevated FR of the stimuli themselves that may be ascribed to a form of SRP and inherent bias towards specific gratings as discussed in Chapter 2, motivational state and locomotion were shown to positively bias FR in V1 (Vinck et al. 2015; Poort et al. 2015; Jurjut et al. 2017; C. R. Lee and Margolis 2016; Dadarlat and Stryker 2017; Polack, Friedman and Golshani 2013), e.g. by shifting the gain of the neuron (Mineault et al. 2016).

Average PSTH shape varies between experimenters

The mouse and channel-averaged PSTH of Fig. 4.10 displayed a secondary peak for experiments executed by AB, which was not reproduced in MT. The peak frequency corresponded to roughly 5 Hz, which was different from the temporal frequencies associated with the visual stimuli, failing to explain it. Examination of individual PSTH traces (not shown) revealed these peaks to only occur in a subset of mice. Differences in average PSTH shape aligned with high- and low-performing mice, but also with different experimenters hinders interpretation. While it was shown that sensory responses may be enhanced by learning (Poort et al. 2015; Jurjut et al. 2017), which could be expressed by the shape of the PSTH, the current study lacks the within-group comparison at different performance levels. The effects of different experimenters cannot be disentangled from the observations at high and low performance with clear conscience.

MI between outcome and neural responses suggests V1 containing task-relevant information

Fig. 4.11 highlighted MI between session states (HITS, CR, FA, MISS, ITI) and neural responses, indicating substantial information ($p < 0.001$, 2-sample sign test against shuffled labels) of a median 0.02 bits for MI computed using 8-bit patterns with the CDM estimator for binary discrete data at 5 ms bins. Shuffling labels reduced this information to zero, and shuffling patterns spatially significantly reduced the information ($p < 0.001$, 2-sample sign test). MI computed over population FR via discrete entropies calculated with the PYM estimator presented substantial information at a median 0.02 bits ($p < 0.001$, 2-sample sign test against shuffled data), that label-shuffling reduced to zero, and was unaffected by spatially shuffling the bins.

Median MI of shuffled bins in (A) and data in (B) was approximately the same at 0.02 bits, and the distributions were not significantly different when treated as independent samples ($p > 0.05$, MWU). This would suggest that shuffling bins spatially reduced the

MI until it reached the limit of solely using population FR, since spatial information is discarded there as well. However, given that both MI estimates were computed on the same underlying data, the groups were dependent, and testing for a significant difference in MI medians resulted in $p < 0.001$ (2-sample sign test), thus rejecting the hypothesis that the median of the differences between the groups was zero. MI determined on shuffled bins consistently obtained higher values than with population FR ($p < 0.001$, 2-sample, one-sided sign test).

The inclusion of shanks greatly increased MI between task states and neural responses for entropies estimated on **patterns**, and at a lower rate for MI based on the population FR. Adding shanks, and thus increasing the state space induced partially large residual MI in the shuffled labels set in Fig. 4.12 (C), revealing high values at 2 or 3 shanks for higher bin widths, which may indicate a sample size problem, as they decreased at higher bin widths, thus artificially increasing MI by e.g. a negative entropy estimation bias. This bias may also be present in (A), which may have artificially inflated MI for the larger bin widths and 3-shank set. The real MI may thus be smaller, but still significant.

To conclude, the results indicate a substantial amount of information on task state in mouse V1.

JSD modulated by response types

Estimating the JSD for the pairwise outcome types (FA, CR, MISS, HITS), and comparing the distributions of JSD across resulting response types (*S-*, *Wrong*, *Lick*, *NoLick*, *Correct*, *S+*) revealed significant differences (all $p < 0.001$, MWU, Bonferroni corrected) between response type *NoLick* and all other response categories for both 8-bit **patterns** spare *Correct* in MT's dataset. In 16-bit **patterns**, the divergence distributions did not differ significantly in AB's dataset, and showed significant differences in MT's set for *NoLick* and *Lick*, *Correct* and *Wrong*, and *NoLick* and *Wrong*. If the animal refrained from licking, this could be interpreted as a case of passive viewing, non-alertness, no or low motivation, no or decreased attention (S. Zhang et al. 2014; Moldakarimov, Bazhenov and Sejnowski 2014), or no initiated motor activity - all parameters that were shown to be implicated in sensory processing (Andermann, Kerlin and Reid 2010; Dadarlat and Stryker 2017). Particularly locomotion was shown to positively influence FR in V1 (Niell and Stryker 2010; Saleem, Ayaz et al. 2013; Polack, Friedman and Golshani 2013). Although licking might not qualify as locomotion to the same extent as running on the tread ball as in the experiments by e.g. Dadarlat and

Stryker (2017), the motor signals sent to initiate a lick may (Zagha et al. 2013), which is particularly supported by the significant differences between *Lick* and *NoLick* divergence distributions. The divergences between response types may also be influenced by state changes during the sessions, e.g. from quiescent, aroused and focussed, which was discussed to play a role in sensory processing (Vinck et al. 2015; Reimer et al. 2014). These differences in divergence distributions arose in both groups that achieved high and low discriminability indices during training, and may thus not necessarily be a result of learning (Poort et al. 2015), although studies proposed an increase of processing already before a behavioural improvement could be detected (Jurjut et al. 2017).

Task-relevant information in V1 may be linked to decision-making

JSD, FR and MI among behavioural outcome types suggested neural correlates of task outcome in V1. This implies that V1 contains information beyond primarily visual input. In particular, FR of lick behaviour exceeded that of non-lick behaviour, as was also visible in differences in JSD between those response types. This information could be relayed top-down and affect the sensory response (Makino and Komiyama 2015; Moldakarimov, Bazhenov and Sejnowski 2014), which is supported by projections from Anterior Cingulate Cortex (ACC) to V1 described in A. Fiser et al. (2016) and S. Zhang et al. (2014). Such top-down inputs to V1 have been shown to contain stimulus-predictive signals that develop with experience (A. Fiser et al. 2016).

However, as the distributions were compared across the entire stimulus presentation periods, the differences in distributions may also be attributable to the motor actions. One way to test this could be to compare pattern distributions across all outcomes before any lick occurred to assess if this observation still holds. If the difference pertains and precedes the lick, this may argue for an involvement in the decision process. Otherwise, the differences in distributions of lick and non-lick behaviour may be ascribed to efference copies.

Another obstacle in analysing decision-making here lies in the experimental design of the GO/NOGO task and its inherent bias. A two-alternative forced choice design would circumvent this by forcing the animal to choose between two stimuli on each trial (Carandini and Churchland 2013).

It remains to be seen how sensory areas contribute to decision-making, and how separate brain regions integrate the different aspects leading to a decision (L. F. Abbott et al. 2017).

High MI between shanks indicates co-activation of cortical columns

$MI(R;shank)$ denoting how much the neural responses on one shank contain about the neural responses on another shank can be indicative of how correlated the shanks are, or if cross-columnar co-activation may be happening, which may particularly be the case for stimulus-driven activity.

Results were partitioned for experimenters, but did not demonstrate a significant difference ($p > 0.1$, MWU) between experimental sets. $MI(R;shank)$ was consistently high across session states and amounted to a median of 0.08 bits for estimates based on **patterns** with peaks of over 0.4 bits, and median 0.02 bits based on population FR.

In AB's recordings variance in HITs and FA appeared higher than CR and MISS, but it was not significantly different ($p > 0.003$). However, results of Fig. 4.10 indicated large increases in the mouse and site-averaged PSTH particularly of FA. Air puff artefacts could not be excluded as the source of the artefacts, which occurred in a subset of the recordings of AB. Air puff artefacts could induce correlated noise affecting all shanks, thus momentarily synchronising them, which could explain the increase in MI between shanks during FA. Neither the increase in PSTH nor in $MI(R;shanks)$ was visible in experiments by MT, potentially rendering this observation an outlier or artefact.

Shortcomings

Unfortunately, the datasets collected by different experimenters and under differing training protocols ensued in discrepancies in their results. In addition, performance levels in one dataset was high (accuracy over 65%), while the other was low, which may have had an effect on the results as well, rendering interpretation difficult.

Conclusions

Despite the shortcomings, it is possible to conclude that **pattern** probability distributions appear modulated by behavioural task state. Divergences between **pattern** distributions are lowest for *non – licking* behaviour, and MI between shanks was not significantly affected by different task states. MI of MUA and behavioural state was non-zero, which was significantly reduced to zero when task labels were shuffled, which was evident in **pattern** and population rate estimates. This implies V1 to contain information beyond visual input.

5

Population interactions are required to emulate observations of GO/NOGO data

Inference on incomplete data is a crucial aspect in the quest of deciphering the neural code. Varying stimulus conditions were shown to affect observed pattern distributions (cf. Chapter 2 and 3) – and an animal’s response was demonstrated to influence pattern distributions in the awake animal (Chapter 4).

In this chapter, the results of Chapter 4 are revisited with computational models that try to match some of the statistics of the data. It is enquired if differences in mean FR alone are able to account for the behavioural information in the neural signals, or if population interactions need to be included in the computations. In addition, statistical models are applied to recreate the pattern distributions to approximate the underlying processes that generated them; and the role of pairwise interactions and population coupling is investigated.

5.1 Introduction

Data analysis of experimental data is an important part of research. Recent advances in experimental techniques in Ca^{2+} imaging, methods in molecular biological interventions such as CRISPR, optogenetic perturbations or other imaging techniques created a large array of neuroscience data to be analysed (Yuste 2015), while experiments and theory require to be rejoined (Boomsma, Ferkinghoff-Borg and Lindorff-Larsen 2014). Sometimes, standard analysis techniques such as computing average FR across repetitions or experimental conditions are insufficient to provide a substantiated interpretation of the results. One reason may be that experimentalists may not be sufficiently trained in quantitative methods (Goldman and Fee 2017). Often, analysis focusses solely on rate-based examinations of single units instead of exploring the role of each neuron in its population, which is profoundly striking given the number of neurons and connections

in the brain (Stevenson and Körding 2011). An approach that goes beyond off-the-shelf analysis lies in developing computational models emulating features of empirical data, whilst accounting for different constraints that may influence the validity of the models.

Probabilistic and statistical approaches such as Bayesian or maximum entropy models have been subject matter in research investigations for many years (E. N. Brown et al. 1998; Pillow 2007; Tkačik, Marre, Mora et al. 2013; Boomsma, Ferkinghoff-Borg and Lindorff-Larsen 2014). One of the biggest challenges then is the biophysical interpretability of the models. The advent of neural networks, where deep learning techniques are of particular interest, often excel at reproducing empirical data, albeit lacking adequate means of being biologically feasible or interpretable (Ching et al. 2017).

Energy-Based-Model (EBM)s are a popular statistical technique of describing network states and transitions. They ascribe an energy proportional to its probability of occurring to each possible state of a network, where in line with thermodynamics, favourable states are assigned low energies (Spicher 2014; LeCun et al. 2006). Many models that are capable of describing small systems well do not necessarily perform well on higher order. This is often true for those models relying on a normalising constant requiring to count all possible states, which very quickly becomes a computationally intractable problem. Whilst such models used to be generally computationally expensive, recent advances in parameter estimation such as Minimum Probability Flow (MPF) (Sohl-Dickstein, Battaglino and DeWeese 2011) or maximum entropy flow models (Loaiza-Ganem, Y. Gao and Cunningham 2017) were able to create innovative approximations for intractable problems. One of the advantages in maximum entropy models is that they span from rudimentary models, such as the Independent model (IND) (which assumes each site to fire independently, with the only constraint being the mean FR) to very elaborate models featuring more and more complicated sets of constraints, approximating prior data more and more accurately. For example, pairwise correlations between neurons play a component part in their FR, and thus, their propensity to fire together, which is already elucidating how linked two potentially or seemingly (locally) disparate groups of neurons may be. Including correlation and population interactions is required particularly for larger neuronal populations as their effects on the spiking activity cannot be neglected (Schneidman 2016).

Although there is still a debate whether the true interactions in a network can be recovered from observational data or if interventional experiments are required (Pearl 2014), fitting an Ising model (Ising 1924) is one way to estimate a network with pairwise interactions for reproducing the functional connectivities seen in the data (Schneidman

et al. 2006; Hertz, Roudi and Tyrcha 2011). Ising models may not actually reveal the true interactions between the neurons as there are typically many physical interaction schemes that can reproduce the same functional connectivity patterns in a network (Hertz, Roudi and Tyrcha 2011). Hamilton, Sohl-Dickstein, Huth et al. (2013) successfully showed how Ising and maximum entropy models (Seiler et al. 2009) improved the presentation of laminar connectivity relationships over plain network correlation analysis. Yet, pairwise models may fail to explain higher-order interactions, whereas Restricted Boltzmann Machine (RBM) are capable of describing higher-order interactions shown to dominate the functional connectivity in microcolumns (Köster, Sohl-Dickstein et al. 2014). Alternatives to pairwise and higher-order modelling attempts may focus on the effects of population activity on each neuron and the dynamics observed for population rates (Y. Gao et al. 2016; Zhao and Park 2016). Complex couplings between an individual neuron and a population were shown to capture variability observed in neural recordings (Gardella, Marre and Mora 2016; Okun, Yger, Marguet et al. 2012; Schölvinck, Saleem et al. 2015; Huang 2016). Recently, it was suggested that low-level dynamics were able to explain large-scale phenomena as "by-products" of their population dynamics (Elsayed and Cunningham 2017; Pillow and Aoi 2017).

Given the scarcity in experimental research to account for pairwise or higher-order interactions in their analyses, this chapter attempts to approximate the empirical pattern probability distributions observed and described in the previous chapter in an effort to bring experiments and theory closer together (Boomsma, Ferkinghoff-Borg and Lindorff-Larsen 2014). The main focus lies on comparing generative models that approximate the same statistical properties as the true distributions to investigate which characteristics of the data may have given rise to our observations. One of the key questions to examine is: Can FR alone account for the pattern divergences observed in the previous chapter, or do pairwise or higher-order interactions need to be included to emulate the results found in the empirical data - and if so, is this the case for all stimulus conditions? Solving the problem of finding a suitable generative model is not trivial, as major challenges such as small sample sizes, incomplete observations and combinatorial problems need to be faced – on top of lacking sufficient information about what type of system generated the distributions. Thus, in the following, the information-theoretic techniques used to describe the data of the previous chapters are scrutinised for their validity, and tested on homogeneous Poisson process surrogate spiking data as a proxy for the IND where appropriate. Then, IND, Ising model, semi-Restricted Boltzmann Machine (sRBM)s and population tracking (O'Donnell et al. 2017), a statistical approach

that incorporates knowledge about the population rate, are fitted and tested against empirical data.

5.2 Methods - computational models

5.2.1 Independent model

The simplest model, often used as a baseline, is the IND. It is a first order maximum entropy model without (temporal) stimulus dependence. It assumes independence between cells, such that cells spike independently. It can be characterised by mean FR alone as shown in: $p_{ind}(x) = \prod_i (r_i x_i + (1 - r_i)(1 - x_i))$, where r_i defines the FR of neuron i (Köster, Sohl-Dickstein et al. 2014; Granot-Atedgi et al. 2013).

5.2.2 Energy-Based-Models

EBM are models that describe a system by assigning each state (configuration) an artificial energy (LeCun et al. 2006; Bengio 2009). They are inspired by statistical mechanics, where each state the system can be in has a certain energy. This is based on the notion of physical systems at thermal equilibrium, best described by the Boltzmann distribution. They have the maximum possible entropy given the mean energy of the system. Here, the main challenge is to find an energy function that accurately describes the system.

Often, instead of modelling the structure of the data, it is desired to learn how to generate the data. This involves learning the probability of the data, $p(x)$, instead of e.g. $p(\text{label}|x)$. Following the idea of thermal equilibrium, desirable data are required to have low energy (Bengio 2009). Decreasing the energy state of the model means making that particular state configuration of a system more likely to happen (since energy is inversely proportional to the probability of the state) (LeCun et al. 2006).

These energies are thus directly related to the probability of each state. The probability is proportional to the exponential of the negative energy: $p(x) = \frac{e^{-E(x)}}{Z}$, where x is the state, and Z is the partition function or scaling factor (Z stands for the German word for partition function, *Zustandssumme*), that ensures it adds up to 1. The idea behind EBMs is that it may be difficult to define a model that directly describes the probabilities of each state. Using $E(x)$ instead lets us describe probabilities indirectly, with the exponential guaranteeing for positive probabilities.

Ising models and RBM are the EBMs covered in this work. Because of their depend-

ence on the partition function, estimating their parameters is difficult as these models cannot be normalised in closed form. Exact solutions would require summing over the exponential number of states of the system. Summing over an exponential number of states quickly becomes infeasible, which is why approximate estimations are required.

Minimum Probability Flow Learning

MPF learning is a parameter estimation technique based on training your weights with detailed balance, developed by Sohl-Dickstein, Battaglino and DeWeese (2011) and applied e.g. in Schaub and S. R. Schultz (2012). This technique does neither require sampling from the equilibrium distribution, nor calculating a potentially intractable partition function. The idea behind MPF is to introduce deterministic dynamics, which interpolate between the empirical and the model distribution (Movellan 2008). To achieve this, stochastic transformations are applied to the data samples such that they appear to have come from the model distribution. Then, the aim is to minimise the KLD between data and the distribution that results from moving slightly away from the data distribution, towards the model distribution (i.e. evolving the deterministic dynamics for a very short time). The flow of probability out of data states into non-data states (model distribution) is then minimised when model and empirical distribution are equal, thus the KLD will be uniquely zero where the model distribution is identical to the data distribution.

With the KLD, MPF provides a convex objective function $k(\theta)$, for which it finds a solution via Taylor approximation that does not rely on a partition function. For any given initial energy, approximating a probability distribution (empirical true distribution) p_0 is achieved by moving on the tangent space (via Taylor approximation) and updating on the θ . This allows to fit networks with many nodes. It is an Markov-Chain-Monte-Carlo (MCMC)-inspired method whose biological interpretation is that of structural plasticity such as LTP, or Long-Term Depression (LTD) (Hager and Dringenberg 2010; Bliss and Lømo 1973; Lynch, Dunwiddie and Gribkoff 1977) and homeostatic plasticity.

Ising model

The Ising model (Ising 1924), a Markov Random Field, is a second order maximum entropy model over binary variables subject to first two statistics (mean and covariance matrix) (Köster, Sohl-Dickstein et al. 2014; Granot-Atedgi et al. 2013; Hertz, Roudi and Tyrcha 2011). It extends the independent model taking into account the mean and

variance to pairwise correlations $\langle x_i x_j \rangle = \frac{1}{T} \sum_{t=1}^T x_i(t) x_j(t)$ between cells i and j . In its basic form, this model does not take temporal order into account, thus, implicitly assumes stationarity. The maximum entropy distribution for the pairwise Ising model is the Gibbs equilibrium distribution: $p(x) = \frac{1}{Z} e^{\sum_{i=1}^N h_i x_i + \frac{1}{2} \sum_{i \neq j} J_{ij} x_i x_j}$. The Lagrange multipliers J_{ij} and h_i are chosen s.t. constraints are satisfied, where h_i stands for the bias of neuron i , and J_{ij} is the symmetric coupling strength between neuron i and j . Synaptic coupling is generally not symmetric, rendering interpretation of coupling matrix J_{ij} sometimes difficult. Fig. 5.1 (A) illustrates the lateral pairwise connections between visible nodes of an Ising model.

Parameter estimation in Ising models and their application has been a key research field in neuroscience (Tkačik, Schneidman and Berry II 2006; Broderick et al. 2007; Castellana and Bialek 2014; Hertz, Roudi and Tyrcha 2011; Gardella, Marre and Mora 2016; Schaub and S. R. Schultz 2012). In this study, Ising coupling parameters are estimated with MPF.

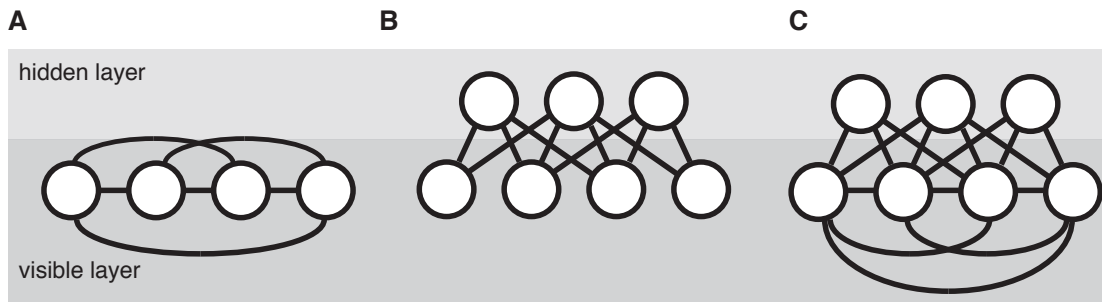


Figure 5.1: Connection schematic . (A) The Ising model has only pairwise connections and only visible nodes. (B) RBMs are a bipartite graph, with one layer of hidden and one layer of visible nodes. (C) sRBM are a combination of Ising and RBMs, i.e. with pairwise lateral connections in the visible layer.

Restricted Boltzmann Machines

Boltzmann machines are EBMs with an artificial neural network of undirected graphical structure and all-to-all connection, whose states are defined in terms of energies of joint configurations of visible and hidden units (LeCun et al. 2006; Bengio 2009). Like in all EBMs, the state's probability is proportional to the energy in $p(v, h) = \frac{1}{Z} e^{-E(v,h)}$. This means that the energy of any configuration is a linear function of the state. It is a

generative stochastic network capable of inferring a probability distribution over a set of input nodes (Salakhutdinov and Murray 2008).

RBM has a simplified, or restricted architecture in which no lateral connections occur between (the one layer of) hidden units, easing finding equilibrium distribution of hidden units given the visible units (Salakhutdinov, Mnih and Hinton 2007). This makes the model bipartite, symmetric, with weighted connections of binary, stochastic nodes. Fig. 5.1 (B) shows a schematic of nodes in hidden and visible layer and their undirected edges. The probability to activate the hidden unit is a logistic function of the input to the visible unit, and due to lack of lateral connections independent of the other units. Their energy function is $E(\mathbf{v}, \mathbf{h}) = -\mathbf{b}'\mathbf{v} - \mathbf{c}'\mathbf{h} - \mathbf{h}'\mathbf{W}\mathbf{v}$, where v and h are binary, and b , c , W are real number valued (b and c biases to visible and hidden units, and weight matrix W describing the connections between hidden and visible units), and v , h denote visible and hidden units (Hinton 2010).

A subset of RBMs are sRBMs, or semi-restricted Boltzmann machines (Köster, Sohl-Dickstein et al. 2014; Salakhutdinov and Murray 2008). They combine Ising and RBM models by including pairwise connections (or lateral connections) between the visible nodes (not the hidden ones), as is illustrated in Fig. 5.1 (C).

5.2.3 Population tracking model

The population tracking model (henceforth termed popTrack), developed by O'Donnell et al. (2017), is, in contrast to the preceding EBM models a statistical model that estimates the synchrony distribution and the probability of any neuron firing conditioned on the population rate. Thus, it includes a term of how coupled each neuron is to the population. As with the aforementioned EBM models, stationarity is assumed, and thus, each bin is assumed independent from the previous. For N neurons, the model fits two sets of parameters: a) N parameters for the population synchrony distribution (implicitly containing knowledge about the network dynamics and summed higher-order correlation effects) and b) $N^2 - N$ parameters describing the conditional probabilities of each neuron firing, given the population rate ($N + 1$ possible values of k , and N neurons, bar the silent and *all-on* states whose probabilities are trivial).

Pattern probability estimation comprises three parts: 1) Synchrony distribution $p(k)$, describing the probability of k neurons being simultaneously active. 2) Renormalisation factor a_k , that consists of the sum over the probabilities of all $\binom{N}{k}$ conditionally independent models at each k . 3) The conditional independent models of $p(x_i|k)$, denoting the probability of neuron i being active, given the synchrony of k neurons. These are

of the same form as the IND of 5.2.1, except r_i is replaced by $p(x_i|k)$, and there is one model for each k . Essentially, state estimation is broken down into k parts by constructing k conditional probability distributions, that mutually exclusively contain all possible patterns, $\sum_k \binom{N}{k} = 2^N$. Then, for any given k , the conditional probability distribution determines the probability of each neuron i being active (Bernoulli distributed). Together $p(x)$ can be described as $p(x) = \frac{p(k)}{a_k} \left(\prod_{i=1}^N [p(x_i|k) x_i + (1 - p(x_i|k))(1 - x_i)] \right)$.

Parameter estimation for $p(k)$ follows common histogram techniques with a fixed Dirichlet prior as regularisation, with $\alpha = 0.01$. Conditional probabilities use a Beta prior (with $\beta = 0.5$) over each $p(x_i|k)$, the conjugate to the Bernoulli distribution.

This model was used to generate surrogate data, to examine how much of the empirical results can be reproduced and explained by the structures. A conceptually similar idea based on population dynamics and their relation to individual FRs was proposed by Okun, Yger, Marguet et al. (2012) and Okun, Steinmetz et al. (2015).

5.2.4 Homogeneous Poisson surrogate data

Independent homogeneous Poisson process spiking surrogate data based on the mean FRs of each outcome type was generated to investigate if the results could be explained by FR effects alone. 200 trials were generated for each outcome type, and 400 for ITI. In probabilistic modelling approaches, independent homogeneous Poisson corresponds to the IND. The accuracy of the surrogate data was confirmed by comparing their mean FRs with those of the data, as well as confirming the Fano factor ($\frac{var}{mean}$) being equal to 1, a prerequisite for Poisson-distributed data (Eden and Kramer 2010). Theoretically, independent homogeneous Poisson results in maximum entropy, but given a fixed sample size matching the amount of recorded data, the modelled entropy might actually be lower (finite sampling bias). Moreover, the FR were not actually stationary over the recording. Thus, suitable alternatives for surrogate data to offset these effects may be the inhomogeneous Poisson process, that allows for temporally changing FR, or to include pairwise correlations as in the dichotomised Gaussian (Macke et al. 2009).

5.2.5 Modelling parameter details and model evaluation measures

Code implementations

In this work, Ising models, RBMs and sRBMs were trained using MPF (Sohl-Dickstein, Battaglini and DeWeese 2011). MPF learning is achieved with code adapted

from Jascha Sohl-Dickstein available at <https://github.com/Sohl-Dickstein/Minimum-Probability-Flow-Learning> in conjunction with optimisation code by Schmidt (2005).

Ising model implementations are based on code provided in the repositories on <https://github.com/libertyh/ising-model> (Hamilton, Sohl-Dickstein, Huth et al. 2013) and by Urs Köster <https://github.com/ursk/srbm> described in (Köster, Sohl-Dickstein et al. 2014). RBM and sRBM are computed with code based on <https://github.com/ursk/srbm> described in (Köster, Sohl-Dickstein et al. 2014). To allow comparison between models, the partition functions of the models were calculated using **Annealed Importance Sampling (AIS)** (Neal 2001; Salakhutdinov and Murray 2008) unless direct computation was possible.

Population tracking, fitting and model parameters were based on code available on <https://github.com/cianodonnell/PopulationTracking> (O'Donnell et al. 2017).

Modelling parameters and details

In order to infer pattern probabilities, the previously described models were fitted to subsets of empirical data, for each dataset. To avoid overfitting of Ising and RBM models, L2 regularisation ($L_2(w) = \frac{1}{2} \sum_i w_i^2$) was implemented with sparseness parameter λ of 0.005, which was found through 2-fold cross-validation (validated to yield the highest loglikelihood for most datasets). L2 regularisation was chosen based on its superior performance over L1 regularisation in creating a higher log-likelihood. The regularisation parameter was added to the objective function. Normalised likelihoods were computed using AIS (Neal 2001) with an AIS convergence wrapper implemented by Jascha Sohl-Dickstein and Urs Köster, if more than 2 shanks were compared. For patterns smaller than that the partition function could be computed directly by summing over all states. For three shanks (24 units), the partition function of each model was estimated by sampling 500 times at increasing annealing steps until 20 000 steps were reached. RBM and sRBM were fitted with 15 hidden and 15 visible units.

Loglikelihood gain

Loglikelihood gain is a measure to evaluate a model's success against a baseline model. It calculates in bits how much is gained choosing a particular model over a reference model, here IND. The larger the gain, the better the model over the alternative. Analogously, a negative loglikelihood gain means that the model is worse than the reference model. As described in Köster, Sohl-Dickstein et al. (2014), it was computed as the

sample expectation $\mathcal{L} = \frac{1}{n} \sum_{x=1}^n (\log_2 p_m(x) - \log_2 p_i(x))$, where p_m is the model probability and p_i the probability from the reference model. This value is normalised by μ_{popFR} per time bin to obtain a normalisation per spike, as was done in (Köster, Sohl-Dickstein et al. 2014), helping comparison across data sets of different activity.

Root mean square error

The other measure implemented to estimate model success is a variation of the Root Mean Square Error (RMSE). Since all estimates are probabilities, governed in logarithmic space, deviations are calculated on the logarithm of the probabilities. Refraining from this transformation would disregard information in low probabilities. For instance, if the model estimate is minute, while the empirical probability is high, the general RMSE would be low. However, with a logarithmic transformation, all values obtain equal weights. Eq. 5.1 provides the equation used to calculate this metric, across all n patterns.

$$RMSE_{log} = \sqrt{\frac{1}{n} \sum_{i=1}^n (\log_{10}(p_{emp,i}) - \log_{10}(p_{model,i}))^2} \quad (5.1)$$

5.3 Results

Computational modelling was based on in-vivo extracellular electrophysiology data from the awake mouse during a visual discrimination task reported in Chapter 4. Two types of surrogate data was generated: (I) homogeneous Poisson process data based on the mean FR, (II) population tracking model, taking into account individual FRs and their coupling to the population statistics (O'Donnell et al. 2017). With these, analyses presented in Chapter 4 were repeated to investigate if independent FRs alone were enough to account for the observed results, or if including population statistics served a better model. It was assessed how well surrogate models matched empirical statistics. Further, these homogeneous Poisson data was used to assess entropy estimators for finite sample bias to ensure validity of entropy estimates. Finally, different models were surveyed and evaluated in their abilities to recover data pattern distributions under varying conditions.

5.3.1 Evaluation of entropy estimators with surrogate homogeneous Poisson spiking data

Homogeneous Poisson spiking data facilitated evaluation of entropy estimators used in this work. The entropy estimators used in this study were CDM and PYM for binary and discrete data, and as a comparison, the plug-in estimator as well as a Dirichlet prior (emulating pseudocounts) with $\alpha = 1$ are presented. Fig. 5.2 displays the fractional bias of the entropy estimators as a function of sample size, for one, two and three shanks at 5 ms bins. Fractional bias is calculated as entropy estimate divided by the estimate at the highest number of samples (asymptotic value). 1000 trials of two seconds each were generated with homogeneous Poisson spiking data using the mean FR of each site. Entropies were calculated at 10 logarithmically spaced locations between 3 and 1000 trials. 3 trials amounted to 600 samples, 1000 trials corresponded to 4×10^5 samples at 5 ms.

Fig. 5.2 (A-E) delineates the fractional biases evaluated for one shank, 8-bit patterns, (F-J) for two shanks, and (K-O) for three shanks. (A) displays the plug-in estimator, which suffers substantial negative bias for poorly sampled distributions, which is evident from the figure. Horizontal pink dash-dotted lines represent $\pm 5\%$ of the asymptotic value. Vertical dash-dotted lines indicate 10^3 to 10^4 samples, equivalent to 10 to 100 trials, which is most commonly found in the empirical data for each outcome. Ideally, convergence is required within that box to ensure a reliable estimate on the empirical data. (B) shows the results for the CDM estimator, whose bias is diminished substantially over the plug-in results, converging much faster. (C) shows an estimator that uses a Dirichlet prior of $\alpha = 1$ not improving much over the plug-in estimator. PYM in (D) is an estimator made for discrete data, and thus not suitable for binary input data. (E) is again the PYM estimator but this time on the population FR, and thus non-binary discrete data, showing a fast convergence.

16-bit and 32-bit patterns in (F-J) and (K-O) converge much more slowly, or not at all as apparent for the plug-in and Dirichlet estimators. The CDM estimator achieves the best and fastest convergence for binary data, and it demonstrates that approximately 100 trials are required to obtain a reliable estimate (16-bit patterns). Using between 10 and 100 trials puts us in 95% of its asymptotic value. For all shanks, PYM converges fast for population FR (E, J, O). For three shanks, PYM contained singular matrices and pathological cases of only one symbol, which might explain the peculiar results in (N).

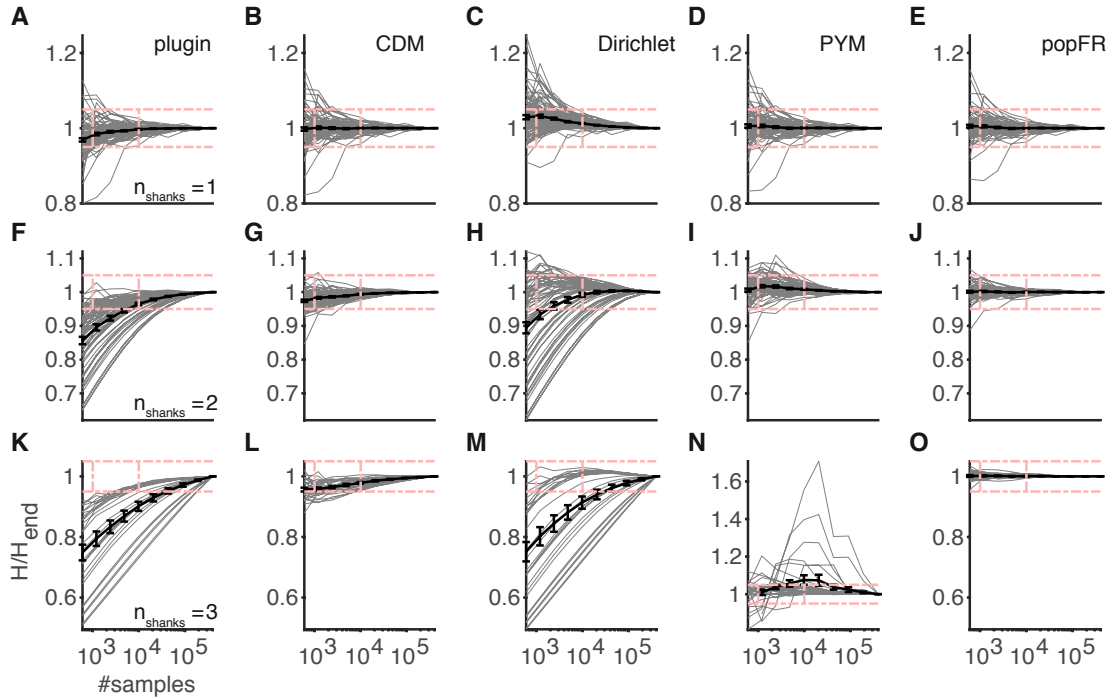


Figure 5.2: Fractional bias as a function of sample size. (A) Fractional bias for plug-in estimator as a function of sample size for one shank for 8-bit binary patterns approximately converges at 10^4 samples. Pink horizontal dash-dotted lines indicate $\pm 5\%$ of the asymptotic value, or the value at 1000 trials, H_{end} . Vertical lines indicate 10^3 and 10^4 samples, which were most commonly found in the empirical data, corresponding to 10 to 100 trials. (B) same as (A) for CDM estimator, (C) Dirichlet estimator with $\alpha = 1$, (D) PYM, and (E) PYM on population FR. (F-J) same as (A-E) for two shanks. (K-O) same as (A-E) for three shanks.

5.3.2 Homogeneous Poisson data fails to match features observed in empirical data

Entropy of homogeneous Poisson surrogate data overshoots empirical entropies

Entropies of Poisson surrogate data slightly but significantly exceed those of real data ($p < 0.001$, 2-sample sign test, Bonferroni corrected) in each behavioural task condition, as is evident from Fig. 5.3 (A-B). The violin graphs in Fig. 5.3 (A) show for each behavioural state that entropies (via CDM, 16-bit patterns) based on surrogate data steadily and significantly exceed data estimates ($p < 0.001$, 2-sample sign test, Bonferroni corrected), which is further illustrated in (B). The same is not true for popTrack estimates in (C), which approximately match experimental data (no significant difference apart

from FA condition, at $p < 0.01$, 2-sample sign test).

Inspection of entropies and μ_{popFR} in (B) and (D) illustrate the FR dependence of entropy estimates on population rate. In (B), Poisson surrogate pattern entropies are significantly higher than data entropies ($p < 0.001$, 2-sample sign test, upper traces), and population rate entropies significantly fall short of data estimates ($p < 0.001$, 2-sample sign test, lower traces). (D) reveals a close match between popTrack entropies and data estimates, differing marginally significantly at $p < 0.05$ (2-sample sign test) for pattern estimates (top traces), indicating no significant difference for population rate estimates ($p > 0.05$, 2-sample sign test). In both (B) and (D), R^2 values are provided for the function fits with the models and a cubic. (F) and (H) demonstrate the population rate entropy distributions. Direct comparison between surrogate pattern and data pattern entropies emphasises the consistency at which Poisson surrogates reach higher values, with no surrogate estimates crossing the identity line (G), whereas popTrack's in (I) are tightly distributed around the identity line.

MI of surrogate neural responses and behavioural outcome exceeds empirical results

MI between neural responses and behavioural outcome types including ITI resulted in independent homogeneous Poisson data (200 trials of two seconds length for each outcome type) significantly exceeding that of empirical data (visualised in Fig. 5.4). This is also true for popTrack surrogates (E-H). In both surrogate data, the number of trials was balanced, with 200 behavioural trials in each outcome, and 400 repetitions of ITI. Fig. 5.4 (A-D) provides the distributions of MI estimated on 8-bit patterns for Poisson surrogate data (black) and empirical data (grey, cf. Fig. 4.11), and (E-H) the same for popTrack. In all cases, shuffling the labels significantly reduced information ($p < 0.001$, 2-sample sign test), as did spatially shuffling the bins in pattern estimates. Overestimated MI was much larger in Poisson surrogates than in popTrack.

Surrogate data achieves higher MI(R;shanks) of neural responses and shanks

Re-examination of Fig. 4.15 with the inclusion of surrogate data reveals that MI(R;shanks) of neural responses, R, and shanks computed on homogeneous Poisson surrogate data in some cases exceeds empirical data, which is presented in Fig. 5.5. One-tailed Wilcoxon signed ranks tests between surrogate and empirical datasets suggest significant differences at $p < 0.01$ for all but FA in popTrack on MT's data. For Poisson surrogates, only MI based on all data exceeds experimental estimates. In (B),

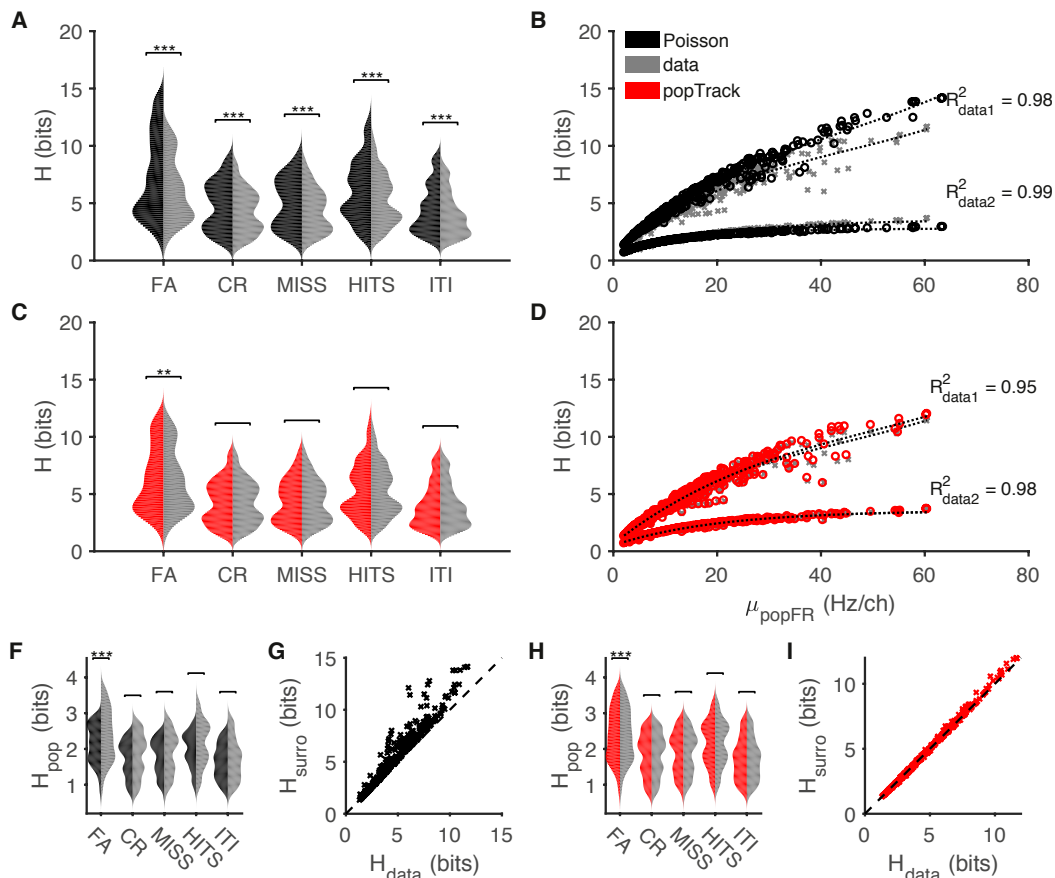


Figure 5.3: Entropy of homogeneous Poisson 16-bit patterns exceeds that of empirical data. (A) Violin graphs of entropies of surrogate (black, left) and data (grey, right) for each behavioural state indicate consistently higher entropy values for surrogate estimates. (B) Entropies against μ_{popFR} , top trace patterns, bottom population FR. (C, D) same as in (A, B) but for popTrack, showing a better match. (F) same as (A) but for population rate entropy estimates. (G) Direct comparison of entropies based on surrogate (y-axis) vs. data entropies (x-axis). (H, I) same as (F, G) for popTrack. **, *** indicate $p < 0.01$, and $p < 0.001$, respectively, 2-sample sign test, Bonferroni corrected.

MI(R;shanks) based on population FR indicate significant differences at $p < 0.01$ only for Poisson surrogates, and only for MISS, HIT and *All* ($p < 0.01$, one-tailed Wilcoxon signed ranks, Bonferroni corrected).

In AB's dataset, depicted in Fig. 5.5 (C-D), none of the pattern-based MI(R;shanks) estimates differ significantly between Poisson surrogate and empirical ($p > 0.008$, left-tailed Wilcoxon signed ranks, Bonferroni corrected). The same applies to values based

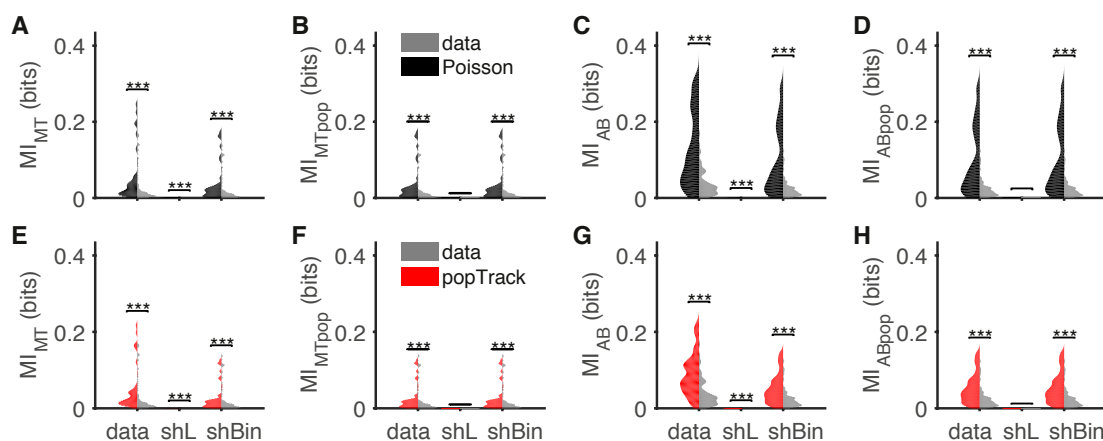


Figure 5.4: MI between behavioural outcomes including ITI, and neural response is significantly larger for surrogate than empirical data. (A) MI between MUA and behavioural outcome (including ITI) is significantly greater estimated on surrogate than on empirical data based on 8-bit patterns at 5 ms bins (one shank). Shuffling labels (shL) decreases the MI to zero, indicating no difference between surrogate and empirical set. Spatially shuffled bins significantly reduce MI over unshuffled patterns (all $p < 0.001$, 2-sample sign test, Bonferroni corrected), with surrogate yet again exceeding empirical data. (B) Same as (A) but for *popFR*. (C, D) same as (A, B) but for experimenter AB. (E-H) same as (A-D) but for data and popTrack (red). *** indicates $p < 0.001$, 2-sample sign test.

on population FR, portrayed in (D). Yet, popTrack estimates significantly exceed data values in all cases in (C), at ($p < 0.001$, one-tailed Wilcoxon signed ranks, Bonferroni corrected), yet also do not differ for population rate estimate in (D).

JSD is significantly smaller in surrogate data than in corresponding empirical data

JSD distributions of behavioural outcome states differ not only between experimenters and number of pattern sizes, but also among empirical, homogeneous Poisson and popTrack surrogate data, as detailed in Fig. 5.6. The distributions across all mice are significantly larger for empirical data than their matched homogeneous Poisson surrogate ($p < 0.01$ to $p < 0.001$, 2-sample one-tailed sign test, Bonferroni corrected). Fig. 5.6 (A-D) show divergences for 8-bit patterns, and (E-H) for two shanks, 16-bit patterns. Across experimenters and shanks, JSD based on surrogate data underestimates the true empirical divergences. Divergences are larger at 16-bit patterns for surrogate and empirical data, but still differ significantly at $p < 0.001$ (2-sample sign test) for all but one ($S-$, in AB's set) condition.

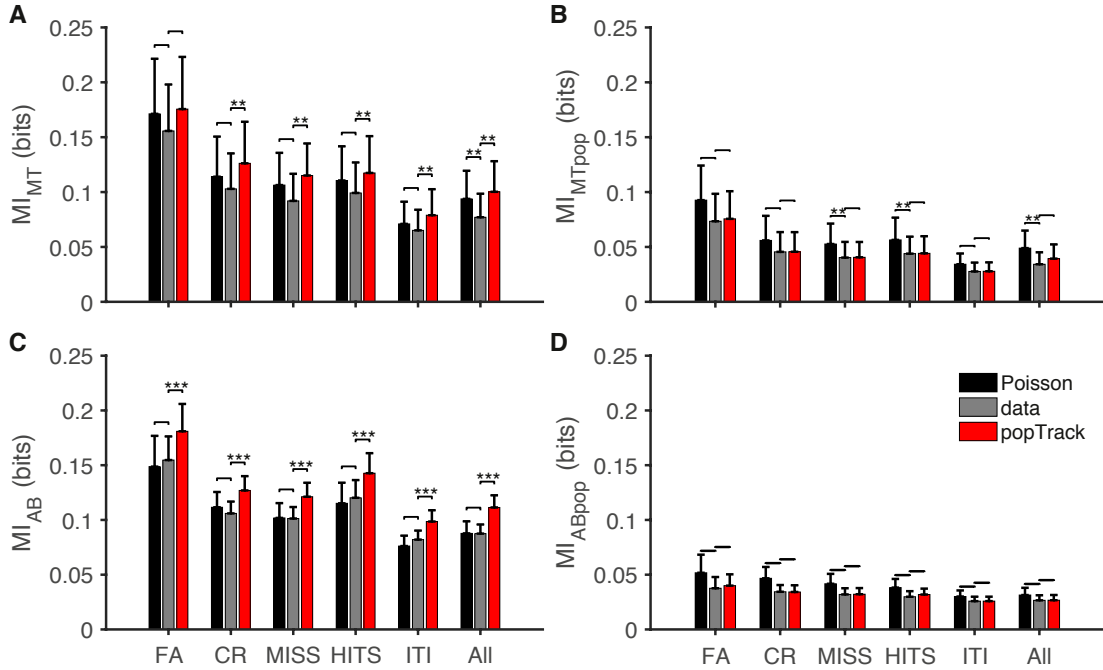


Figure 5.5: Poisson surrogate MI(R;shanks) between shanks matches data MI. (A) shows MI between MUA responses and shanks for each behavioural outcome for homogeneous Poisson surrogate data (black), empirical sets (grey) and popTrack (red) at 5 ms for 8-bit patterns in MT’s dataset. Indicated are mean and error bars (sem). PopTrack MI estimates sometimes significantly exceed empirical data (**, *** indicate $p < 0.01$ and $p < 0.001$, respectively, 2-sample sign test, Bonferroni corrected for multiple comparisons.) (B) same as (A) but for population FR data. (C, D) as (A, B) for AB dataset.

5.3.3 Loglikelihood gain and RMSE imply pairwise interactions are crucial

In the following section, models were trained on $\frac{2}{3}$ random partitions of binary patterns, and tested against the remaining hold-out $\frac{1}{3}$ data during stimulus presentation (S+ and S-).

Model success was estimated with gain in loglikelihood over the IND and is presented in Fig. 5.7 (A). The IND is often used as a baseline model for comparisons. Median popTrack loglikelihood gain was 0.28 bits/spike, Ising model 0.19 bits/spike, RBM 0.27 bits/spike, and sRBM 0.32 bits/spike. From these models, the Ising model performs most poorly, with the lowest gain in loglikelihood. The remaining models each obtain similar medians. Loglikelihood gains of sRBM exceed all other models at $p < 0.001$ (2-sample sign test, Bonferroni corrected). All models’ loglikelihood gains ex-

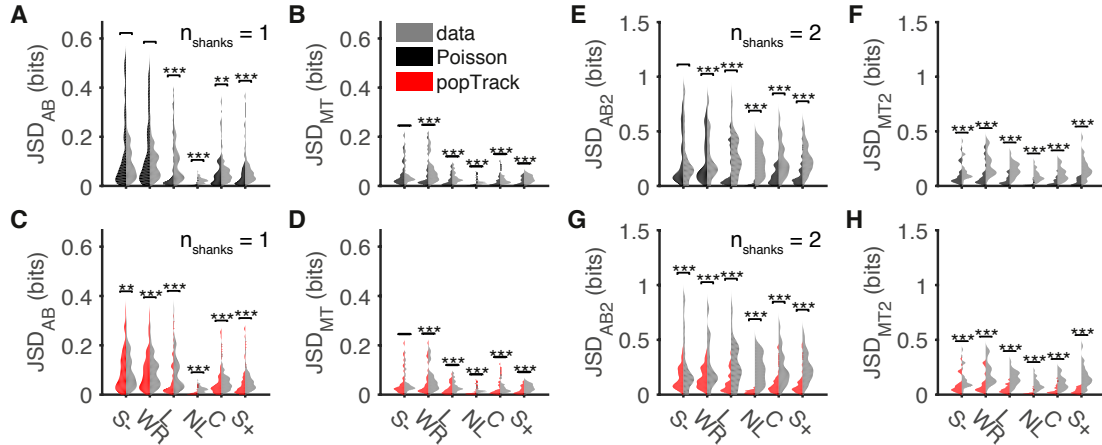


Figure 5.6: JSD of data exceeds surrogate data. Distributions of JSD between behavioural outcome states are significantly larger for empirical data than their matched homogeneous Poisson surrogate (2-sample right-tailed sign test). (A) JSD distributions for surrogate (black, left side) and empirical (grey, right side) dataset by AB for 8-bit patterns. (B) same as (A) but for MT dataset. (C, D) same as (A, B) but for popTrack. (E) JSD distributions for 16-bit patterns for AB indicating larger discrepancies between surrogate and empirical divergence distributions. (F) same as (E) but for MT. (G, H) same as (E, F) but for popTrack comparisons. Matched significant divergences are indicated by ** ($p < 0.01$) and *** ($p < 0.001$), 2-sample, one-tailed sign test. (E-H) same as (A-D) but for two shanks.

ceed Ising models ($p < 0.001$, one-sided 2-sample sign test). The distributions of RBMs and popTrack differ significantly at $p < 0.01$.

The insets of (A) present the scatter plots of the matched loglikelihood gain distributions to visualise their differences. Arrows indicate the side of the identity line where the majority of points lie. In the top inset, for sRBMs and Ising, the majority of points lies above the bisector line, only three points falling below it. The second inset shows popTrack and RBM, which differ less significantly. The third inset indicates that sRBMs consistently obtain larger loglikelihood gains compared with popTrack. The final inset shows popTrack obtains higher values than the Ising model.

Fig. 5.7 (B) delineates the RMSE between empirical probability and model probability estimates. Each dot represents one experimental set, for 16-bit patterns ($n=73$ sets), and grey dashed line connects the medians of each model. Inspection of the figure suggests that the RMSE achieved in sRBM models is consistently and significantly lowest ($p < 0.001$ against all other models but Ising, Wilcoxon signed ranks, Bonferroni corrected) at 0.24 (a.u.). Next is Ising with a median of 0.25, followed by popTrack at

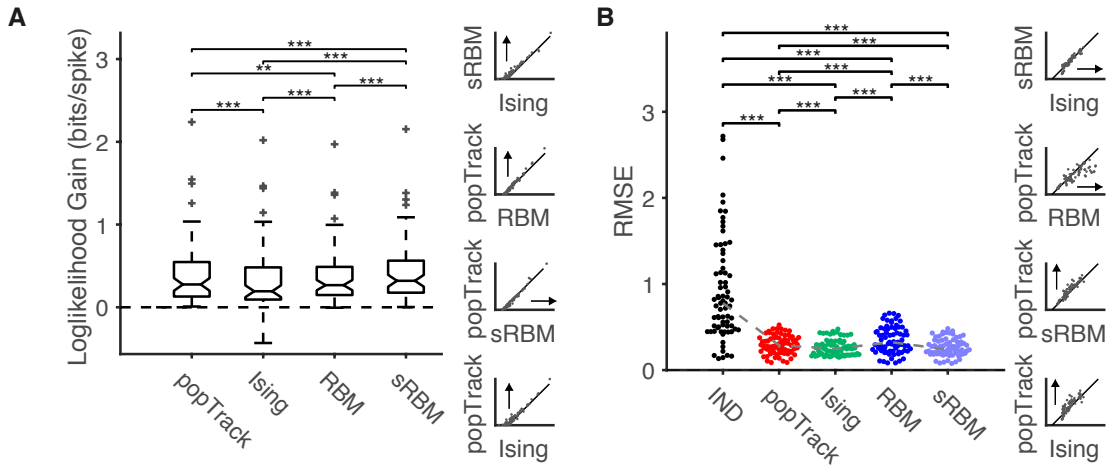


Figure 5.7: Loglikelihood gains and RMSE. (A) Loglikelihood gain over the IND for 16-bit patterns. Differences between model successes are significant at $p < 0.001$ (2-sample sign test, Bonferroni corrected) for popTrack and Ising, Ising and RBM, Ising and sRBM and sRBM and RBM. Loglikelihood gain of popTrack is significantly smaller than sRBM at $p = 0.002$ (2-sample sign test). Insets show scatter plots of loglikelihood gains between three distributions that had achieved similar medians, with arrows indicating on which side of the identity line the majority of points lies. (B) RMSE between empirical probability distribution and model estimates for $n = 73$ experimental sets. Grey dashed line indicates median of each distribution. Insets show scatters between sets of RMSE.

0.29, then RBM at 0.32. Median RMSE for IND amounts to 0.78, which is significantly larger than all other RMSE. Insets show pairwise RMSEs.

For two-shank patterns, popTrack obtained lowest RMSE in 10% of the cases, Ising models in 51 %, RBM in 1%, and sRBMs in 38%.

Model success depends on choice of training and test datasets

The figures presented were based on random subsets of training and test data from the same stimulus presentation type. However, the models' performances are contingent on training and testing data. Chapter 3 elaborated on differences in pattern spaces between SA and gratings, which may be visible in the models as well. To investigate this further, training and testing was done on the following subsets listed in Table 5.1, for one, two and three shanks separately. Models that performed well when trained and tested on evoked activities (S+ S-) do not necessarily perform well when tested on ITI, as is depicted in Fig. 5.8.

Descriptor name	Training	Testing
StimOnly	66% $S + S-$	33% $S + S-$
StimITI	100% $S + S-$	100% ITI
ITISTim	100% ITI	100% $S + S-$
All	66% $S + S-$ ITI	33% $S + S-$ ITI

Table 5.1: Training and testing on different subsets of data. When training and testing is done on the same or mixed set, training uses a random subset of 66% and testing the remaining 33%. If the sets are separate, 100% each are used.

As detailed in Fig. 5.8 (A-C), black line, IND consistently reaches the highest RMSE, for 8, 16 and 24-bit patterns and all training variations. Furthermore, all RMSE increase with the number of shanks used (A-C). Compared with the IND, all models perform equally well with regard to their RMSE. Because of their large overlap, (D-F) depict the ranked results to magnify the qualitative differences between the models. In doing this, the models are ranked in each experimental subset, and the mean and sem are presented. From (D-F) it is apparent that the sRBM consistently manifests lowest RMSE, across all shank variations. The ranks following sRBMs depend on the number of shanks and training/testing conditions particularly for the Ising model. The Ising model reveals a great variability depending on choice of training and testing data. At 8-bit patterns, Ising models are approximately at the median of all models if trained and tested on evoked activities only. For Ising models, then, the ranked RMSE deteriorates if trained on stimuli and tested on ITI, and attains highest ranks if trained on ITI and tested on evoked activities, before obtaining RMSEs in the lower half if trained and tested on subsets of both evoked and ITI data. This observation is similar for 16 and 24-bit patterns in (E) and (F). All other models remain roughly in the same relative constellation towards each other, where ITISTim consistently reveals the highest RMSE within each model apart from the Ising, at all shanks.

Focussing on the loglikelihood gain in (G-I) and their ranked versions of (J-L), a progression reminiscent of the RMSE of e.g. (C) emerges across all models and shanks. At StimOnly, the loglikelihood gain decreases at StimITI, after which it increases at ITISTim before it decreases again at All. The absolute values of the loglikelihood gain are roughly the same across all shanks at approximately 0.4 bits/spike, with the distributions at three shanks a bit higher and one shank a bit lower. Ranked loglikelihood gains in (J-L) enhance the differences between the models further, displaying that sRBMs attain the highest loglikelihood gains throughout training/test conditions

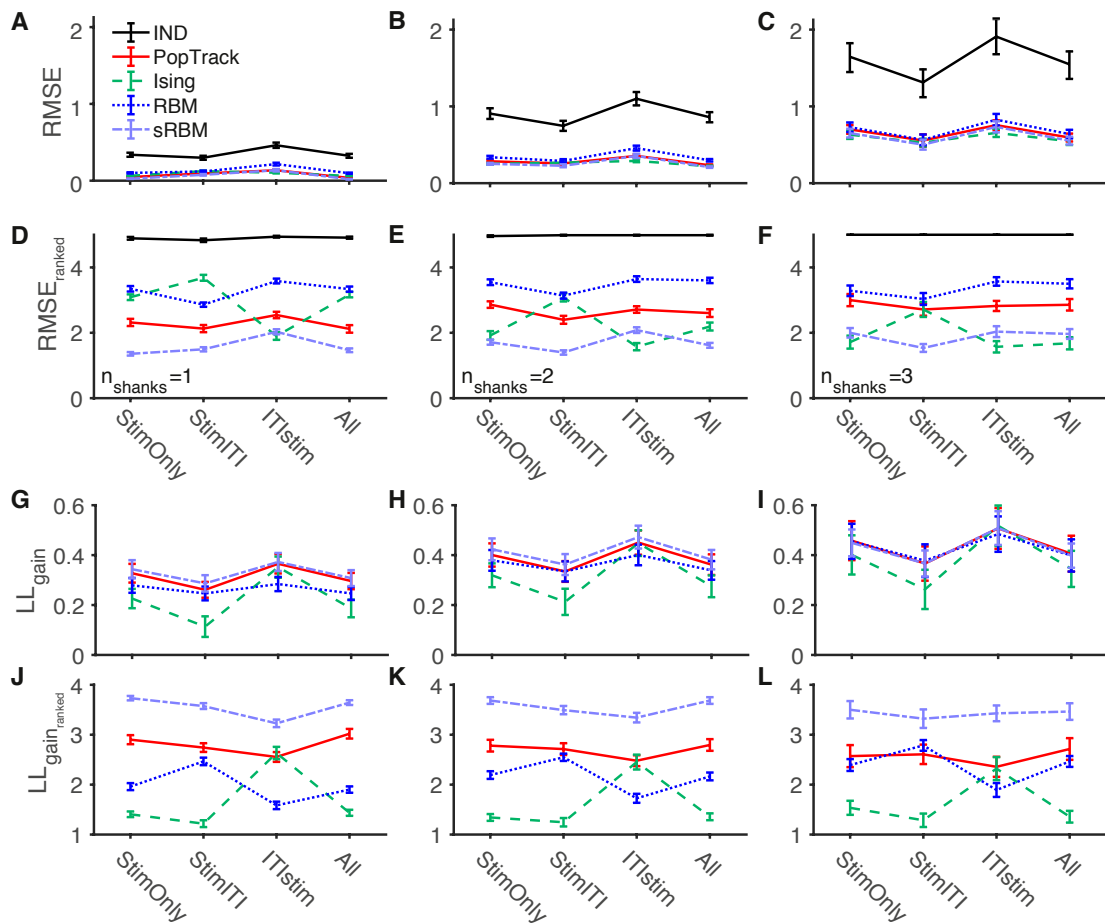


Figure 5.8: Model success depends on training and test subsets. (A-C) show mean RMSE for all models and training conditions for one, two and three shanks, respectively. (D-F) as in (A-C) but for each set ranked highest to lowest to emphasise differences. (G-I) same as (A-C) but for loglikelihood gain. (J-L) same as in (G-I) but ranked. Error bars show mean \pm sem.

and at all shanks, followed by popTrack, RBM and then Ising models. As was noted in RMSE, the Ising model emerges as deviant to the group appearance with achieving lowest loglikelihood gains in all but ITIstim training/test conditions, where it achieves values on par with popTrack, as depicted in e.g. (K).

Thus, if Ising models are trained on ITI and tested on evoked activities, their achieved RMSE is superior to all the other models while attaining loglikelihood gains similar to popTrack, rendering it an interesting model to investigate. Overall, the sRBM appears to perform best in both RMSE and loglikelihood gain, across training conditions and

regardless of pattern size.

5.3.4 Models successfully approximate empirical pattern probabilities

Ising model, popTrack, RBM and sRBM were fitted on patterns evoked by a subset of S+/S- and validated on a separate subset of the same kind (described in Tab. 5.1 as StimOnly). Fig. 5.9 demonstrates examples of scatters between modelled and empirical pattern probabilities, with their marginal distributions along the y and x-axes. Each symbol represents one unique pattern. The closer the symbol to the identity line, the better the prediction. Panel (A) shows the results for the IND model, with a high fraction of symbols assigned to low probabilities. The popTrack model in (B) reveals a much better match between pattern probabilities, particularly for more frequent patterns.

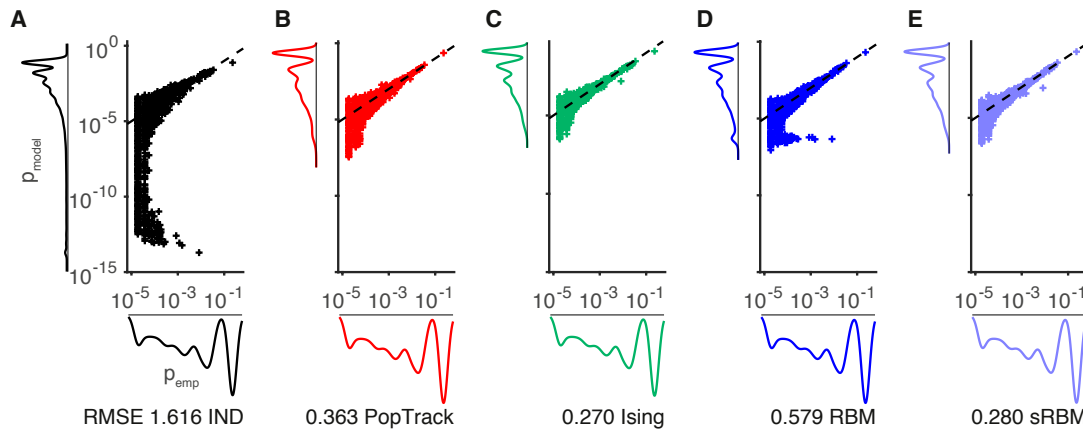


Figure 5.9: Pattern probability scatter between all models and p_{emp} . Each scatter is complemented by their marginal distributions along the y and x-axis. (A) IND introduces a large tail with low probabilities. (B) Symbols are much more centred along the identity line for the popTrack model. (C) The Ising model improves even more in RMSE. (D) RBMs allocating low probabilities to some particular patterns, increasing the RMSE. (E) sRBM reveals a much better fit than RBMs.

Fig. 5.10 illustrates pattern probability scatter plots of three example sets for the models IND, sRBM and popTrack. Each symbol represents one unique pattern. The x-axis indicates the empirical pattern probabilities, p_{emp} , while the y-axis indicates p_{model} , the probabilities estimated for each pattern by the different models. Marginal distributions for the models are shown along the y and marginal empirical distribution along the x-axis. Models assign probabilities much lower than those observed in the data, as evident from the y-axis.

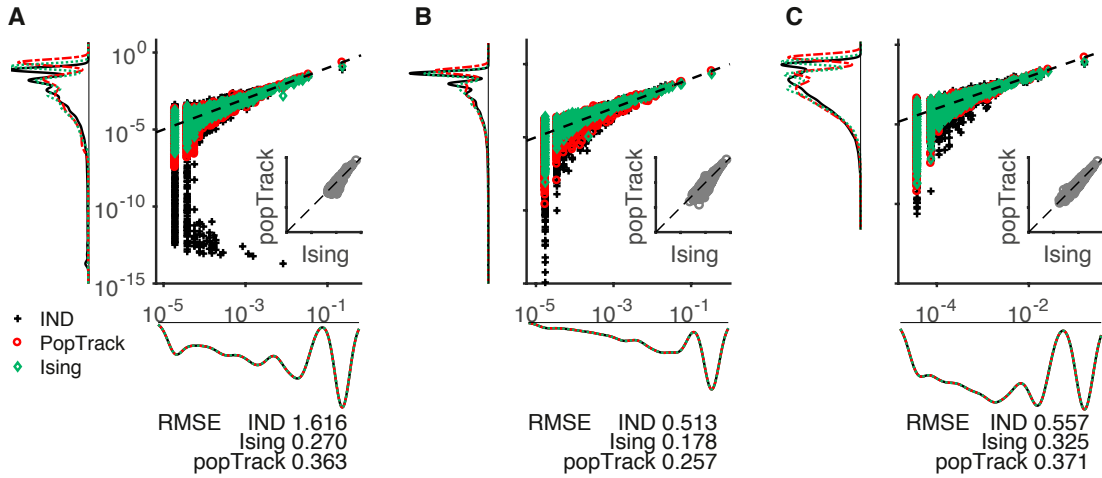


Figure 5.10: Pattern probability scatter between models and p_{emp} . Pattern probability scatter plots of IND, Ising model and popTrack for three example mice indicate varying success in matching empirical pattern probabilities for 16-bit patterns. Each symbol represents one pattern. Marginal distributions are presented along the y and x axis. Insets show predicted probabilities of popTrack against Ising. (B, C) same as (A) for different mice.

The IND model is black, Ising green, and popTrack in red markers. The closer the symbol to the identity line, the better the match between empirical and estimated probability. Since there are many possible patterns and thus many symbols obstructing or potentially skewing the presentation, the marginal distributions help interpret the scatter. The insets in each panel show scatters of the two models, popTrack and Ising, to illustrate how similar the pattern predictions of the two models are. In each of the examples, the IND model occupies the largest space, as apparent from the large subset of symbols afar from the identity line, with a long tail at very low estimates of down to 10^{-15} . For all models the predictions are best for frequent, or high-probability patterns.

Fig. 5.10 (B) serves as another example where the Ising model achieved the best fit between p_{emp} and model probabilities, as also evident from the low RMSE of 0.178. (C) is an example for an empirical probability distribution that occupies many patterns with large probabilities, such that the zero pattern is, albeit still being the most frequent one, not apparent as a single peak. Here, many popTrack symbols are obscured by the Ising estimates, indicating similar predictions, which can also be inferred from the inset of the two models tightly dispersed around the identity line.

5.3.5 Ising coupling matrices indicate consistent laminar connections

Although the Ising model performed poorest in terms of loglikelihood gains in comparison with the remaining models of this investigation, one of the Ising model's strengths is that its learnt parameters, the coupling matrix J_{ij} , can be visualised and interpreted as couplings between sites. In addition, it excelled at producing the lowest RMSE in 50% of the cases (StimOnly). Fig. 5.11 illustrates six examples of learnt Ising coupling matrices trained on 66% of the stimulation part $S + S^-$ of awake behaving data. All cases presented show strong laminar dependencies as indicated by the diagonal lines parallel to the main diagonal. Each shank is equipped with 8 sites, such that site 1 and 9, 2 and 10 etc. follow similar negative coupling terms as neighbouring sites on the same shank. The main diagonal illustrates the bias terms of the Ising model, or their propensity to spike and is positive for all sites shown. Each example mouse reveals negative couplings on the diagonals parallel to the major diagonal. In addition, (C) and (E) contain patterns reminiscent of a checker board. After 4 sites, the coupling terms change from negative to positive, and vice versa, and again when crossing to a different shank. This, again is a reminder of the probe architecture. The top four sites of each shank are located in the same or similar cortical depth, again pointing at the laminar structure.

5.4 Discussion and conclusions

In this chapter, two types of surrogate data were generated to evaluate the findings of Chapter 4: One was the homogeneous Poisson model (based on the mean FR of each behavioural state). The other was a novel probabilistic model: the population tracking model (popTrack) developed by O'Donnell et al. (2017), which tries to match each FR and the probability that each individual neuron fires conditioned on the population response. Homogeneous Poisson addressed if the results were attributable to mean FR alone, and popTrack also modelled population activities. Key results of Chapter 4 were contrasted with generated data. Homogeneous Poisson failed to match the observations in the data, proposing the observed features cannot be explained by FR differences alone, and while popTrack did not perfectly match results from data, it significantly improved upon the Poisson model, suggesting to reflect crucial elements inherent in the data.

To investigate connectivity structures further, different generative models were consulted: Starting with the IND, which stipulates cells fire independently, different EBMs (which allocate a probability to each observed spatial firing pattern) were investigated,

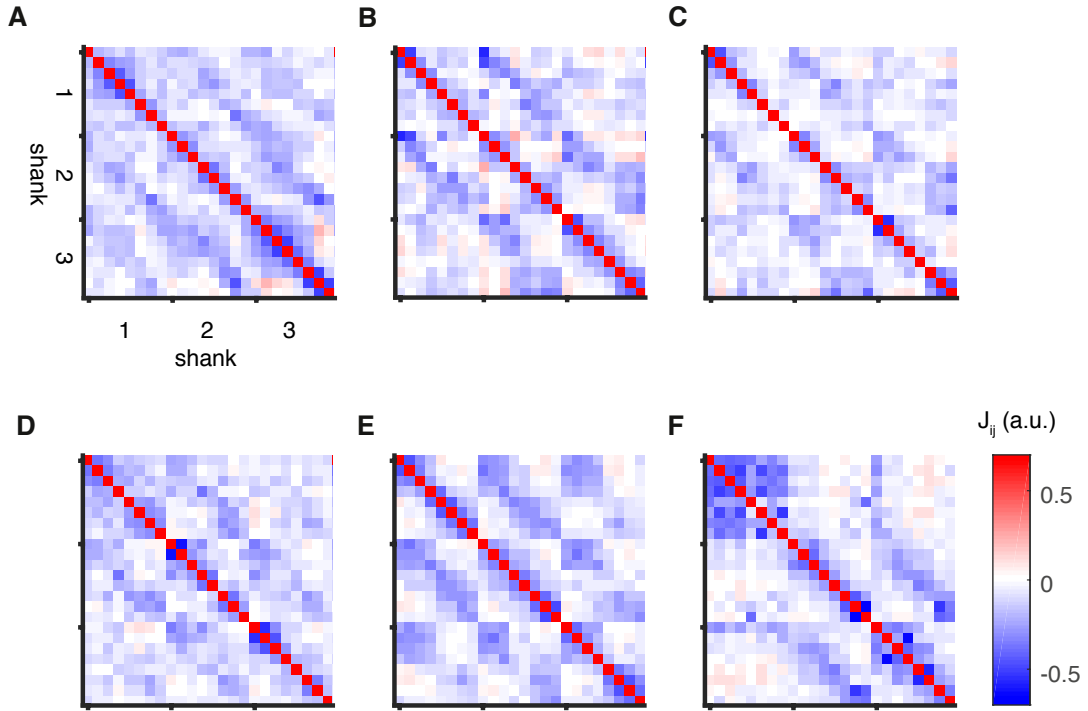


Figure 5.11: Ising coupling matrices for six example mice on 3 shanks each. Symmetric coupling matrices J_{ij} for six example datasets, illustrating laminar dependencies across shanks as suggested by the negative coupling terms parallel to the main diagonal bias terms. In addition, some sites indicate columnar structures as indicated by the squares around the diagonal (e.g. (E)). Sites on shanks are linearly arranged from top to bottom.

from the Ising model, assuming only pairwise couplings, over Restricted and semi-RBM, which also include higher-order interactions (Köster, Sohl-Dickstein et al. 2014), to the aforementioned popTrack model.

Population rates or higher-order dependencies are needed to explain the data

Entropies of Poisson surrogate data exceeded the real data's ($p < 0.001$, 2-sample sign test), whereas popTrack's entropies matched empirical data in all but one case (FA, $p < 0.01$, 2-sample sign test). Given that homogeneous Poisson reflects the maximum entropy solution for constraints on the first moment, it is not surprising, as was also discussed in O'Donnell et al. (2017). The popTrack model matched empirical entropies very well indicating its ability to capture structures beyond mean FR and the role of

population couplings on entropy. Both models underestimated the JSD between outcome states significantly ($p < 0.001$, 2-sample sign test), and overestimated MI between neural responses and behavioural outcomes for both population FR and pattern estimates. One reason why MI was higher in the surrogate data may be that the surrogate data had both higher and balanced numbers of trials, estimated on the statistics of the (unevenly) distributed outcomes of the empirical data. $MI(R;shanks)$ was mainly overestimated by popTrack, whereas Poisson did mostly not differ significantly. $MI(R;shanks)$ focusses on 8-bit patterns across shanks, thus, popTrack's poor performance here may be ascribed to its weakness in modelling small populations (O'Donnell et al. 2017). A Poisson process has no temporal coherence, but FR in experimental data are expected to fluctuate temporally both within a trial (which was evident from the PSTH Fig. 4.10 in Chapter 4), and as trial-to-trial variability. This can be linked to pairwise and/or population dependencies, and thus by increased stereotypical or synchronised firing patterns (Mineault et al. 2016) reduce entropy. Individual FRs alone may thus be unfit to capture the generative structure of the population.

An interesting extension of this analysis would be to choose a type of surrogate data that includes only pairwise correlations.

Perhaps the closest comparison of the results with literature regarding divergences is what Okun, Yger, Marguet et al. (2012), Okun, Yger and Harris (2013) and J. Fiser et al. (2013) presented. In their studies, the KLD between data and IND (there termed mean firing rate, MFR, model) vastly exceeded the KLD between two different subsets of the data. Similarly, Berkes et al. (2011) created a INDs, which were compared via KLD to the data distribution. Two major drawbacks with this comparison are that a) they used the KLD, and b) instead of comparing divergences that match the conditions (i.e. estimating the divergence within model data for matching conditions), they compared the data to the model distribution. However, in all cases divergences involving IND exceeded real data. An interesting investigation would be to test within-condition JSD on both Okun's and Berkes's datasets.

Models' performances are linked to choice of training and test data

The structure of Ising model coupling matrices revealed laminar couplings (Fig. 5.11), along with some columnar dependencies consistent with those described in Hamilton, Sohl-Dickstein and Huth (2013). Sites positioned more superficially were weakly negatively coupled, which was visible across shanks. This changed around site 5 or 6 to weak positive couplings with sites on other shanks around that site number, indicating that

deeper layers are positively and superficial ones negatively coupled. Including couplings among sites increased the likelihood of the data over the IND model by around 0.3 bit/spike (median at StimOnly), while improving the RMSE between empirical and model distribution. The improvement of Ising models over the IND was consistent across experiments and state spaces (numbers of shanks). The Ising model achieved RMSEs that could compete with more elaborate models such as popTrack and sRBM, emphasising the importance of pairwise interactions. Already in the seminal paper by Schneidman et al. (2006), weak, pairwise correlations were shown to play an important role, which was further explored in mouse V1 by Denman and Contreras (2014). In addition, Elsayed and Cunningham (2017) recently discussed how low-level features were often capable of accounting for large-scale effects. The high entropy estimates of the surrogate data and the fact that the inclusion of pairwise and higher-order dependencies or population features improved predicted **pattern** probabilities may confirm that only a subset of possible **patterns** are normally traversed (Sadovsky and MacLean 2014), and that the stimuli presented only stretch across a regime of stereotyped **patterns**.

The average loglikelihood gain in bits/s amounted to values comparable with the two experiments of similar state space as in Köster, Sohl-Dickstein et al. (2014), in which popTrack nicely fits in as well. In their study, the comparison between Single Unit Activity (SUA) and MUA was made, where MUA attained slightly higher loglikelihood gains than SUA.

Synchrony, or the population rate may change as a function of motivation or cortical state as was shown in Okun, Yger, Marguet et al. (2012) although in Urethane anaesthesia. Thus, each neuron's firing may be linked to the current cortical state. Yet, coupling parameters or strength may differ between synchronised desynchronised state - although it has been argued that coupling was unaffected by stimulus conditions (Okun, Steinmetz et al. 2015). Training on evoked activities and testing on SA resulted in poorest predictions of the different training/testing sets, which may argue for a reduction in dimensionality during stimulation (Mazzucato, Fontanini and La Camera 2016). Indeed, the Ising model trained on SA and tested on evoked activities performed best, arguing for stimulus independence, and supporting the idea that SA and stimuli govern similar activity spaces (Carrillo-Reid et al. 2015).

Shortcomings and future works

During visual stimulation, correlated inputs induce stimulus-dependent correlations, as well as temporal correlations (Renart et al. 2010). Including time-dependency was

shown to improve the models substantially elsewhere (Köster, Sohl-Dickstein et al. 2014; Granot-Atedgi et al. 2013) and would be feasible for some of the models, such as the sRBM.

An interesting extension of the popTrack model could be to fit the model to multiple population rates belonging to different cell assemblies, as inspired by approaches used in Gardella, Marre and Mora (2016). Assemblies could be discovered e.g. by a graph partitioning algorithm (Billeh et al. 2014). Then, a model with n FR parameters for each assembly could be built with one parameter to describe the interactions between cells in each assembly, and one describing the interaction between assemblies, while keeping the rest as random as possible according to maximum entropy principle. Including a pairwise assembly-population frequency interaction term could describe the correlations between population rates of the two (or n) assemblies.

6

Conclusions and outlook

This thesis investigated stimulus representation and signal processing factors via extracellular electrophysiology in mouse primary visual cortex under varying stimulus conditions in both the anaesthetised and awake mouse. Tuning characteristics of MUA were determined and state-of-the-art information-theoretic tools were used to explore spatial binary pattern statistics.

6.1 Summary

Neural processing in mouse V1 is part and parcel of modern neuroscience. For over half a century, orientation tuning in mouse V1 was reported as salt-and-pepper organised (Hubel and Wiesel 1962; Kaschube 2014; Jeyabalaratnam et al. 2013; Ringach et al. 2016; Hansel and van Vreeswijk 2012), lacking apparent structure as was found in e.g. cat or primates (Hirsch and Martinez 2006; Sun et al. 2015; Swisher et al. 2010). The majority of research focussed on characterising single cell properties, whilst the role of population activity on processing has only recently been moving into the focus of investigations (Montijn, Vinck and Pennartz 2014; Gutnisky et al. 2016; Gardella, Marre and Mora 2016; O'Donnell et al. 2017; Okun, Yger, Marguet et al. 2012).

This work comprises novel in-vivo electrophysiological experiments under different stimulus conditions in the Isoflurane-anaesthetised and head-fixed awake-behaving mouse and their information-theoretic analyses. The following briefly summarises the main findings of this study.

Chapter 2 and 3 focussed on the acquisition and analysis of neural responses to monocular full-field drifting gratings, natural scene movies and grey screens (as a proxy for ongoing activity), which were presented to anaesthetised mice. MUA was recorded from left hemisphere V1 and computationally evaluated on individual site and population level. FR analysis revealed that at the lowest SF used (0.01 cpd), left forward drifting gratings evoked highest responses across cortical layers and columns, whereas

upward moving gratings consistently elicited the lowest FRs, thus disagreeing with the established opinion of random organisation, in agreement with recent studies (Ringach et al. 2016; Kondo, Yoshida and Ohki 2016). However, higher SFs did not indicate similar levels of preferred directions, implying direction tuning to depend on the SF, in line with findings by Ayzenshtat, Jackson and Yuste (2016). Preferred directions varied with SF, with the mode moving from 180° over 270° to 360° , indicating the possibility to encode size and direction information efficiently in the same population.

Chapter 3 then extended the study of the anaesthetised experiments to their binary firing vectors (or word/pattern distributions) and population FR. With the aid of information-theoretic approaches the similarity of SA and evoked responses to natural movies was demonstrated, confirming results found in ferrets (Berkes et al. 2011), and their dissimilarities to sets of drifting gratings was presented. This analysis also conveyed that pattern probability distributions appear spatially but not directionally clustered, and that Shannon entropy and mean population FR follow a distinct relationship. MI of spatial patterns and stimulus could be shown to significantly decrease when spatial locations of the firing vectors were shuffled, pointing out the importance of spatial arrangement.

In Chapter 4, a novel, efficient training protocol for head-fixed, water-restricted mice was developed and evaluated against an alternative protocol by a different researcher. Under both protocols, mice were trained in a GO/NOGO visual discrimination task involving horizontal forward and downward drifting gratings. Subsequent in-vivo electrophysiology during the behavioural task unveiled V1 to contain substantial information about task outcome. Since protocols differed, results were contrasted and compared between experimenter and task performances. Information-theoretic methods were applied to examine the influence of the dichotomous choice (*to lick or not to lick*) on neural activities, which showed for both experimenters that JSD between outcome states was affected by behaviour.

Finally, in Chapter 5 a number of model computations on surrogate data was performed and results were compared with the findings of Chapter 4. Two types of surrogate data were used: 1) homogeneous Poisson process surrogate data based on the mean FR of each of the behavioural task states, to test if FR alone could account for the results. 2) popTrack surrogate data based on mean FR and a population activity interaction link (O'Donnell et al. 2017). Poisson data significantly overestimated entropy, whereas popTrack's greatly matched empirical estimates. Both surrogates significantly overestimate MI, and fail to meet JSD values present in the behavioural data. In addi-

tion, different models such as Ising models and sRBMs, were evaluated against the IND. Comparisons suggest that including pairwise interactions reduced discrepancies between empirical and model distributions significantly. Including higher-order interactions or population responses improved the predicted pattern distributions even more, as was shown using sRBM and popTrack models, suggesting the significant role of population dynamics particularly for larger ensemble sizes.

6.2 Shortcomings

In all experiments, stationarity was assumed, which is a strong assumption that is not necessarily well-founded (Tyrcha et al. 2013). Further, recording lengths or numbers of trials differed, which was partially accounted for by weighing the numbers, whenever possible. In anaesthetised recordings, anaesthesia length puts a limit on experimental duration. It is, therefore, important to find an optimum between stimulus duration, repetitions, and variety of stimuli presented to maximise, while balancing lengths. This problem is even more difficult in behaviour experiments, where a good performance (and thus few false responses) is desired, which entails low numbers of samples in FA and MISS.

It has been shown that activity patterns during the anaesthetised state differ from the awake state (Greenberg, Houweling and Kerr 2008; Aasebø et al. 2017), which is what a lot of computational models base their choice of parameters upon. That is why this study tried to examine model probabilities on datasets based on awake experiments, at the cost of lower sample sizes.

6.3 Future work

Inhibitory neurons in early visual processing seem to play an important role in visual perception (Hirsch, Martinez et al. 2003). Thus, an interesting variation of the experiments could be an optogenetic activation of e.g. PV+ interneurons in V1 to sharpen the neuronal feature selectivity, as this is assumed to improve the perceptual discrimination (S.-H. Lee et al. 2012) and decorrelate excitatory cells (King, Zylberberg and DeWeese 2013). An optogenetic approach targeting the Calcium-binding interneurons may help understand their role in visual discrimination processing (Pinto et al. 2013). This leads to a modulation of activated neurons in primary sensory cortices, mediated by populations that control the responsiveness of cortical outputs, here the PV+ in-

terneurons, which modify sensory responses in mouse visual cortex (Salinas and Thier 2000; J. Zhang and L. Abbott 2000).

An extension of the behavioural GO/NOGO may address the question how experience of a reward association alters brain circuitry in higher cognitive areas such as medial Prefrontal Cortex (mPFC) or ACC. Analysis of simultaneous electrophysiological recordings in e.g. mPFC and V1 could aim to relate the neural activities between the two not directly linked areas to behaviour and describe possible interactions between early visual system and higher areas. Simultaneous recordings across and along cortical layers over an extended time period (early vs. late learning stages) will enable elucidating the change in strength and direction of neural interactions in these two areas. This may help describe the decision-making and information flow across the primary sensory cortex and towards mPFC.

An interesting pharmacological investigation to probe the information content about task outcome in V1 during behaviour, could be to inject the NMDA receptor antagonist CPP, as mentioned in 4.4 to investigate if SRP was required in reward learning. Otherwise, when Gavornik et al. showed that sequence learning in V1 was not reliant on SRP (and thus NMDAR induction or AMPA insertion) but instead it was dependent on the cholinergic system as found through injection of scopolamine (acetylcholine antagonist), which suppressed sequence learning in V1 (Gavornik and Bear 2014).

The popTrack model showed great potential in analysing and emulating binary patterns. An interesting investigation could be to fit it to the anaesthetised datasets to examine population statistics under varying visual stimuli. Population couplings may differ between SA and evoked activities, and conditional probabilities could be contrasted across stimulus conditions. This could elucidate on how an individual site's propensity to fire given the population activity changes when population activity is driven by varying stimuli, e.g. if it is possible for a "chorister" under visual stimulation to change to a "soloist" under SA (Okun, Steinmetz et al. 2015).

Bibliography

- Aasebø, I. E. J. et al. (2017). ‘Temporal Processing in the Visual Cortex of the Awake and Anesthetized Rat’. *eNeuro* 4.
- Abbott, L. F. et al. (2017). ‘An International Laboratory for Systems and Computational Neuroscience’. *Neuron* 6, pp. 1213–1218.
- Adesnik, H. and M. Scanziani (2010). ‘Lateral Competition for Cortical Space by Layer-Specific Horizontal Circuits’. *Nature* 7292, pp. 1155–1160.
- Agarwal, G. et al. (2014). ‘Spatially Distributed Local Fields in the Hippocampus Encode Rat Position’. *Science* 6184, pp. 626–630.
- Agetsuma, M., J. P. Hamm, K. Tao, S. Fujisawa and R. Yuste (2017). ‘Parvalbumin-Positive Interneurons Regulate Neuronal Ensembles in Visual Cortex’. *Cerebral Cortex*, pp. 1–15.
- Andermann, M. L., A. M. Kerlin and R. C. Reid (2010). ‘Chronic Cellular Imaging of Mouse Visual Cortex During Operant Behavior and Passive Viewing’. *Frontiers in Cellular Neuroscience*.
- Archer, E. W., I. M. Park and J. W. Pillow (2012). ‘Bayesian Estimation of Discrete Entropy with Mixtures of Stick-Breaking Priors’. *NIPS* 1, pp. 2024–2032.
- Archer, E. W., I. M. Park and J. W. Pillow (2013a). ‘Bayesian and Quasi-Bayesian Estimators for Mutual Information from Discrete Data’. *Entropy* 5, pp. 1738–1755.
- Archer, E. W., I. M. Park and J. W. Pillow (2013b). ‘Bayesian Entropy Estimation for Binary Spike Train Data Using Parametric Prior Knowledge’. *NIPS*, pp. 1700–1708.
- Archer, E. W., I. M. Park and J. W. Pillow (2014). ‘Bayesian Entropy Estimation for Countable Discrete Distributions’. *Journal of Machine Learning Research* 1, pp. 2833–2868.
- Ardila Jiménez, S. C. (2016). ‘Analysis of Visual Responses in the Mouse Early Visual Pathway’. Doctoral dissertation. Imperial College London.
- Averbeck, B. B., P. E. Latham and A. Pouget (2006). ‘Neural Correlations, Population Coding and Computation.’ *Nature reviews. Neuroscience* 5, pp. 358–66.
- Ayzenshtat, I., J. Jackson and R. Yuste (2016). ‘Orientation Tuning Depends on Spatial Frequency in Mouse Visual Cortex’. *bioRxiv*.
- Balleine, B. W. (2007). ‘The Neural Basis of Choice and Decision Making’. *Journal of Neuroscience* 31, pp. 8159–8160.

- Barlow, H. B. (1997). ‘The Knowledge Used in Vision and Where It Comes From.’ *Philosophical Transactions of the Royal Society B: Biological Sciences* 1358, pp. 1141–7.
- Barlow, H. B. (2012). ‘Possible Principles Underlying the Transformations of Sensory Messages’. *Sensory Communication*. The MIT Press, pp. 216–234.
- Bathellier, B., L. Ushakova and S. Rumpel (2012). ‘Discrete Neocortical Dynamics Predict Behavioral Categorization of Sounds.’ *Neuron* 2, pp. 435–49.
- Bear, M. F. and W. Singer (1986). ‘Modulation of Visual Cortical Plasticity by Acetylcholine and Noradrenaline’. *Nature*.
- Bengio, Y. (2009). ‘Learning Deep Architectures for AI’. *Foundations and Trends® in Machine Learning* 1, pp. 1–127.
- Berditchevskaia, A. (2014). ‘Electrophysiological and Behavioural Correlates of Motivation and Choice in a Simple Visually Guided Task’. Doctoral dissertation. Imperial College London.
- Berens, P. (2009). ‘CircStat : A MATLAB Toolbox for Circular Statistics’. *Journal of Statistical Software* 10, p. 121108.
- Berkes, P., G. Orbán, M. Lengyel and J. Fiser (2011). ‘Spontaneous Cortical Activity Reveals Hallmarks of an Optimal Internal Model of the Environment.’ *Science* 6013, pp. 83–7.
- Billeh, Y. N., M. T. Schaub, C. A. Anastassiou, M. Barahona and C. Koch (2014). ‘Revealing Cell Assemblies at Multiple Levels of Granularity’. *Journal of Neuroscience Methods*, pp. 92–106.
- Biran, R., D. C. Martin and P. A. Tresco (2005). ‘Neuronal Cell Loss Accompanies the Brain Tissue Response to Chronically Implanted Silicon Microelectrode Arrays’. *Experimental Neurology*, pp. 115–126.
- Bishop, C. M. (2006). *Pattern Recognition and Machine Learning*. Springer.
- Bliss, T. V. P. and T. Lømo (1973). ‘Long-Lasting Potentiation of Synaptic Transmission in the Dentate Area of the Anaesthetized Rabbit Following Stimulation of the Perforant Path’. *Journal of Physiology* 2, pp. 331–356.
- Bonhoeffer, T. and A. Grinvald (1991). ‘Iso-Orientation Domains in Cat Visual Cortex Are Arranged in Pinwheel-like Patterns.’ *Nature* 6343, pp. 429–31.
- Boomsma, W., J. Ferkinghoff-Borg and K. Lindorff-Larsen (2014). ‘Combining Experiments and Simulations Using the Maximum Entropy Principle’. *PLoS Computational Biology* 2, pp. 1–9.

- Borst, A. and F. E. Theunissen (1999). ‘Information Theory and Neural Coding.’ *Nature Neuroscience* 11, pp. 947–57.
- Boyd, S. and L. Vandenberghe (2004). *Convex Optimization*. Ed. by C. U. Press. 3. Cambridge: Cambridge University Press. Chap. 1,10,11, pp. 487–487.
- Breiman, L., J. H. Friedman, R. A. Olshen and C. J. Stone (1984). *Classification and Regression Trees*. Chapman and Hall/CRC, p. 368.
- Broderick, T., M. Dudik, G. Tkačik, R. E. Schapire and W. Bialek (2007). ‘Faster Solutions of the Inverse Pairwise Ising Problem’. *arXiv*.
- Brown, E. N., L. M. Frank, D. Tang, M. C. Quirk and M. A. Wilson (1998). ‘A Statistical Paradigm for Neural Spike Train Decoding Applied to Position Prediction from Ensemble Firing Patterns of Rat Hippocampal Place Cells.’ *Journal of Neuroscience* 18, pp. 7411–25.
- Brunel, N. and J. P. Nadal (1998). ‘Mutual Information, Fisher Information, and Population Coding.’ *Neural computation* 7, pp. 1731–57.
- Busse, L. et al. (2011). ‘The Detection of Visual Contrast in the Behaving Mouse.’ *Journal of Neuroscience* 31, pp. 11351–61.
- Buzsáki, G. (2004). ‘Large-Scale Recording of Neuronal Ensembles.’ *Nature Neuroscience* 5, pp. 446–51.
- Buzsáki, G. and K. Mizuseki (2014). ‘The Log-Dynamic Brain: How Skewed Distributions Affect Network Operations.’ *Nature reviews. Neuroscience* 4, pp. 264–78.
- Carandini, M. and A. K. Churchland (2013). ‘Probing Perceptual Decisions in Rodents.’ *Nature Neuroscience* 7, pp. 824–831.
- Carrillo-Reid, L., J.-E. K. Miller, J. P. Hamm, J. Jackson and R. Yuste (2015). ‘Endogenous Sequential Cortical Activity Evoked by Visual Stimuli’. *Journal of Neuroscience* 23, pp. 8813–8828.
- Castellana, M. and W. Bialek (2014). ‘Inverse Spin Glass and Related Maximum Entropy Problems’. *Physical Review Letters* 11.
- Chadderton, P., A. T. Schaefer, S. R. Williams and T. W. Margrie (2014). ‘Sensory-Evoked Synaptic Integration in Cerebellar and Cerebral Cortical Neurons.’ *Nature reviews. Neuroscience* 2, pp. 71–83.
- Chalupa, L. M. and R. W. Williams (2008). ‘Eye, Retina, and Visual System of the Mouse’. *Journal of Neuro-Ophthalmology* 3, pp. 257–258.
- Ching, T. et al. (2017). ‘Opportunities and Obstacles for Deep Learning in Biology and Medicine’. *bioRxiv*.

- Chklovskii, D. B. and A. A. Koulakov (2004). ‘MAPS IN THE BRAIN: What Can We Learn from Them?’ *Annual Review of Neuroscience* Mitchison 1991, pp. 369–392.
- Chubykin, A. A., E. B. Roach, M. F. Bear and M. G. H. Shuler (2013). ‘A Cholinergic Mechanism for Reward Timing Within Primary Visual Cortex.’ *Neuron* 4, pp. 723–35.
- Constantinople, C. M. and R. M. Bruno (2013). ‘Deep Cortical Layers Are Activated Directly by Thalamus.’ *Science* 6140.
- Cooke, S. F. and M. F. Bear (2010). ‘Visual Experience Induces Long-Term Potentiation in the Primary Visual Cortex.’ *Journal of Neuroscience* 48, pp. 16304–13.
- Cooke, S. F. and M. F. Bear (2014). ‘How the Mechanisms of Long-Term Synaptic Potentiation and Depression Serve Experience-Dependent Plasticity in Primary Visual Cortex.’ *Philosophical Transactions of the Royal Society B: Biological Sciences*.
- Cooke, S. F., R. W. Komorowski, E. S. Kaplan, J. P. Gavornik and M. F. Bear (2015). ‘Visual Recognition Memory, Manifested As Long-Term Habituation, Requires Synaptic Plasticity in V1.’ *Nature Neuroscience* 2, pp. 262–271.
- Corey, J. and B. Scholl (2012). ‘Cortical Selectivity Through Random Connectivity.’ *Journal of Neuroscience* 30, pp. 10103–4.
- Cossell, L. et al. (2015). ‘Functional Organization of Excitatory Synaptic Strength in Primary Visual Cortex.’ *Nature*, pp. 1–5.
- Cover, T. M. and J. A. Thomas (1991). ‘Entropy, Relative Entropy and Mutual Information’. *Elements of Information Theory*.
- Cover, T. M. and J. A. Thomas (2012). *Elements of Information Theory*. Wiley.
- Cox, T. F. and M. A. A. Cox (2000). *Multidimensional Scaling*. Second Edi. Chapman and Hall/CRC, p. 328.
- Dadarlat, M. C. and M. P. Stryker (2017). ‘Locomotion Enhances Neural Encoding of Visual Stimuli in Mouse V1’. *Journal of Neuroscience* 14, pp. 3764–3775.
- De Franceschi, G., T. Vivattanasarn, A. B. Saleem and S. G. Solomon (2016). ‘Vision Guides Selection of Freeze or Flight Defense Strategies in Mice’. *Current Biology* 16, pp. 2150–2154.
- Denman, D. J. and D. Contreras (2014). ‘The Structure of Pairwise Correlation in Mouse Primary Visual Cortex Reveals Functional Organization in the Absence of an Orientation Map’. *Cerebral Cortex* 10, pp. 2707–2720.
- Dimitrov, A. G., A. A. Lazar and J. D. Victor (2011). ‘Information Theory in Neuroscience’. *Journal of Computational Neuroscience* 1, pp. 1–5.

- Douglas, R. J. and K. A. C. Martin (2004). ‘Neuronal Circuits of the Neocortex.’ *Annual Review of Neuroscience*, pp. 419–51.
- Duncan, R. O. and G. M. Boynton (2003). ‘Cortical Magnification Within Human Primary Visual Cortex Correlates with Acuity Thresholds’. *Neuron* 4, pp. 659–671.
- Eden, U. T. and M. A. Kramer (2010). ‘Drawing Inferences from Fano Factor Calculations.’ *Journal of Neuroscience Methods* 1, pp. 149–52.
- Elsayed, G. F. and J. P. Cunningham (2017). ‘Structure in Neural Population Recordings: An Expected Byproduct of Simpler Phenomena?’ *Nature Neuroscience* 9, pp. 1310–1318.
- Espinosa, J. S. and M. P. Stryker (2012). ‘Development and Plasticity of the Primary Visual Cortex.’ *Neuron* 2, pp. 230–49.
- Euston, D. R., A. J. Gruber and B. L. McNaughton (2012). ‘The Role of Medial Prefrontal Cortex in Memory and Decision Making.’ *Neuron* 6, pp. 1057–70.
- Fahle, M. (2004). ‘Perceptual Learning: A Case for Early Selection.’ *Journal of Vision* 2004, pp. 879–890.
- Fiser, A. et al. (2016). ‘Experience-Dependent Spatial Expectations in Mouse Visual Cortex’. *Nature Neuroscience* September.
- Fiser, J., M. Lengyel, C. Savin, G. Orbán and P. Berkes (2013). ‘How (not) to Assess the Importance of Correlations for the Matching of Spontaneous and Evoked Activity’. *arXiv*.
- Flint, R. D., Z. A. Wright, M. R. Scheid and M. W. Sutzky (2013). ‘Long Term, Stable Brain Machine Interface Performance Using Local Field Potentials and Multiunit Spikes.’ *Journal of Neural Engineering*.
- Frenkel, M. Y. et al. (2006). ‘Instructive Effect of Visual Experience in Mouse Visual Cortex.’ *Neuron* 3, pp. 339–49.
- Fu, Y. et al. (2014). ‘A Cortical Circuit for Gain Control by Behavioral State’. *Cell* 6, pp. 1139–1152.
- Furmanski, C. S., D. Schluppeck and S. A. Engel (2004). ‘Learning Strengthens the Response of Primary Visual Cortex to Simple Patterns’. *Current Biology* 7, pp. 573–578.
- Gao, E., G. C. DeAngelis and A. Burkhalter (2010). ‘Parallel Input Channels to Mouse Primary Visual Cortex.’ *Journal of Neuroscience* 17, pp. 5912–5926.
- Gao, Y., E. W. Archer, L. Paninski and J. P. Cunningham (2016). ‘Linear Dynamical Neural Population Models Through Nonlinear Embeddings’. *arXiv*.

- Gardella, C., O. Marre and T. Mora (2016). ‘A Tractable Method for Describing Complex Couplings Between Neurons and Population Rate’. *eNeuro* 4, pp. 1–13.
- Gatto, R. and S. R. Jammalamadaka (2007). ‘The Generalized Von Mises Distribution’. *Statistical Methodology*, pp. 341–353.
- Gavornik, J. P. and M. F. Bear (2014). ‘Learned Spatiotemporal Sequence Recognition and Prediction in Primary Visual Cortex’. *Nature Neuroscience*.
- Georgopoulos, A., A. Schwartz and R. Kettner (1986). ‘Neuronal Population Coding of Movement Direction’. *Science* 4771, pp. 1416–1419.
- Glickfeld, L. L., M. H. Histed and J. H. R. Maunsell (2013). ‘Mouse Primary Visual Cortex Is Used to Detect Both Orientation and Contrast Changes’. *Journal of Neuroscience* 50, pp. 19416–19422.
- Glickfeld, L. L., R. C. Reid and M. L. Andermann (2014). ‘A Mouse Model of Higher Visual Cortical Function’. *Current Opinion in Neurobiology* 1, pp. 28–33.
- Gold, J. I. and M. N. Shadlen (2007). ‘The Neural Basis of Decision Making’. *Annual Review of Neuroscience* 1, pp. 535–574.
- Goldman, M. S. and M. S. Fee (2017). ‘Computational Training for the Next Generation of Neuroscientists’. *Current Opinion in Neurobiology*, pp. 25–30.
- Goltstein, P. M., E. B. J. Coffey, P. R. Roelfsema and C. M. A. Pennartz (2013). ‘In Vivo Two-Photon Ca²⁺ Imaging Reveals Selective Reward Effects on Stimulus-Specific Assemblies in Mouse Visual Cortex.’ *Journal of Neuroscience* 28, pp. 11540–55.
- Granot-Atedgi, E., G. Tkačik, R. Segev and E. Schneidman (2013). ‘Stimulus-Dependent Maximum Entropy Models of Neural Population Codes’. *PLoS Computational Biology* 3.
- Greenberg, D. S., A. R. Houweling and J. N. D. Kerr (2008). ‘Population Imaging of Ongoing Neuronal Activity in the Visual Cortex of Awake Rats.’ *Nature Neuroscience* 7, pp. 749–51.
- Grubb, M. S. and I. D. Thompson (2003). ‘Quantitative Characterization of Visual Response Properties in the Mouse Dorsal Lateral Geniculate Nucleus.’ *Journal of Neurophysiology* 6, pp. 3594–3607.
- Guo, Z. V. et al. (2014). ‘Procedures for Behavioral Experiments in Head-Fixed Mice.’ *PLoS ONE* 2.
- Gutnisky, D. A., C. B. Beaman, S. E. Lew and V. Dragoi (2016). ‘Spontaneous Fluctuations in Visual Cortical Responses Influence Population Coding Accuracy’. *Cerebral Cortex*.

- Hager, A. M. and H. C. Dringenberg (2010). ‘Training-Induced Plasticity in the Visual Cortex of Adult Rats Following Visual Discrimination Learning.’ *Learning & Memory (Cold Spring Harbor, N.Y.)* 8, pp. 394–401.
- Hamilton, L. S., J. Sohl-Dickstein and A. G. Huth (2013). *Fitting Ising Models to Neural Data*. URL: <https://github.com/libertyh/ising-model> (visited on 31/08/2017).
- Hamilton, L. S., J. Sohl-Dickstein, A. G. Huth et al. (2013). ‘Optogenetic Activation of an Inhibitory Network Enhances Feedforward Functional Connectivity in Auditory Cortex’. *Neuron* 4, pp. 1066–1076.
- Han, F., N. Caporale and Y. Dan (2008). ‘Reverberation of Recent Visual Experience in Spontaneous Cortical Waves’. *Neuron* 2, pp. 321–327.
- Hansel, D. and C. van Vreeswijk (2012). ‘The Mechanism of Orientation Selectivity in Primary Visual Cortex Without a Functional Map.’ *Journal of Neuroscience* 12, pp. 4049–64.
- Harris, K. D. (2012). ‘Cell Assemblies of the Superficial Cortex.’ *Neuron* 2, pp. 263–5.
- Harris, K. D., J. Csicsvari, H. Hirase, G. Dragoi and G. Buzsáki (2003). ‘Organization of Cell Assemblies in the Hippocampus’. *Nature* 6948, pp. 552–556.
- Harris, K. D. and T. D. Mrsic-Flogel (2013). ‘Cortical Connectivity and Sensory Coding’. *Nature* 7474, pp. 51–58.
- Harris, K. D., R. Quiñones Quiroga, J. Freeman and S. L. Smith (2016). ‘Improving Data Quality in Neuronal Population Recordings’. *Nature Neuroscience* 9, pp. 1165–1174.
- Harris, K. D. and G. M. G. Shepherd (2015). ‘The Neocortical Circuit: Themes and Variations’. *Nature Neuroscience* 2, pp. 170–181.
- Hertz, J., Y. Roudi and J. Tyrcha (2011). ‘Ising Models for Inferring Network Structure from Spike Data’. *arXiv*, pp. 1–28.
- Hinton, G. (2010). ‘A Practical Guide to Training Restricted Boltzmann Machines’. *Momentum*, pp. 599–619.
- Hirsch, J. A. and L. M. Martinez (2006). ‘Laminar Processing in the Visual Cortical Column.’ *Current opinion in neurobiology* 4, pp. 377–84.
- Hirsch, J. A., L. M. Martinez et al. (2003). ‘Functionally Distinct Inhibitory Neurons at the First Stage of Visual Cortical Processing’. *Nature Neuroscience* 12, pp. 1300–1308.
- Histed, M. H., L. A. Carvalho and J. H. R. Maunsell (2012). ‘Psychophysical Measurement of Contrast Sensitivity in the Behaving Mouse.’ *Journal of Neurophysiology* 3.

- Hollerman, J. R. and W. Schultz (1998). ‘Dopamine Neurons Report an Error in the Temporal Prediction of Reward During Learning.’ *Nature Neuroscience* 4, pp. 304–9. arXiv: NIHMS150003.
- Horton, J. C. and D. L. Adams (2005). ‘The Cortical Column: A Structure Without a Function’. *Philosophical Transactions of the Royal Society B: Biological Sciences* 1456, pp. 837–862.
- Huang, H. (2016). ‘Theory of Population Coupling and Applications to Describe High Order Correlations in Large Populations of Interacting Neurons’. *arXiv*, pp. 1–14.
- Hubel, D. H. and T. N. Wiesel (1959). ‘Receptive Fields of Single Neurones in the Cat’s Striate Cortex.’ *Journal of Physiology*, pp. 574–591.
- Hubel, D. H. and T. N. Wiesel (1962). ‘Receptive Fields, Binocular Interaction and Functional Architecture in the Cat’s Visual Cortex’. *Journal of Physiology*, pp. 106–154.
- Hubel, D. H. and T. N. Wiesel (1968). ‘Receptive Fields and Functional Architecture of Monkey Striate Cortex’. *J.Physiol.(London)*, pp. 215–243.
- Hubel, D. H. and T. N. Wiesel (1974). ‘Uniformity of Monkey Striate Cortex: A Parallel Relationship Between Field Size, Scatter, and Magnification Factor’. *Journal of Comparative Neurology* 3, pp. 295–305.
- Hubel, D. H., T. N. Wiesel and S. LeVay (1976). ‘Functional Architecture of Area 17 in Normal and Monocularly Deprived Macaque Monkeys’. *Cold Spring Harbor Symposia on Quantitative Biology*, pp. 581–589.
- Huberman, A. D. and C. M. Niell (2011). ‘What Can Mice Tell Us About How Vision Works?’ *Trends in Neurosciences* 9, pp. 464–473.
- Ince, R. A. A., A. Mazzoni, A. Bartels, N. K. Logothetis and S. Panzeri (2012). ‘A Novel Test to Determine the Significance of Neural Selectivity to Single and Multiple Potentially Correlated Stimulus Features’. *Journal of Neuroscience Methods* 1, pp. 49–65.
- Ince, R. A. A., S. Panzeri and S. R. Schultz (2015). ‘Summary of Information Theoretic Quantities’. *arXiv*.
- Ising, E. (1924). ‘Beitrag Zur Theorie Des Ferromagnetismus’. *Zeitschrift für Physik* 1, pp. 253–258.
- Jeanne, J. M., T. O. Sharpee and T. Q. Gentner (2013). ‘Associative Learning Enhances Population Coding by Inverting Interneuronal Correlation Patterns.’ *Neuron* 2, pp. 352–63.

- Jeyabalaratnam, J. et al. (2013). ‘Adaptation Shifts Preferred Orientation of Tuning Curve in the Mouse Visual Cortex.’ *PLoS ONE* 5.
- Jiang, X., G. Wang, A. J. Lee, R. L. Stornetta and J. J. Zhu (2013). ‘The Organization of Two New Cortical Interneuronal Circuits.’ *Nature Neuroscience* 2.
- Jin, D. Z., V. Dragoi, M. Sur and H. S. Seung (2005). ‘Tilt Aftereffect and Adaptation-Induced Changes in Orientation Tuning in Visual Cortex.’ *Journal of Neurophysiology* 6, pp. 4038–50.
- Juavinett, A. L. and E. M. Callaway (2015). ‘Pattern and Component Motion Responses in Mouse Visual Cortical Areas’. *Current Biology* 13, pp. 1759–1764.
- Jurjut, O., P. Georgieva, L. Busse and S. Katzner (2017). ‘Learning Enhances Sensory Processing in Mouse V1 Before Improving Behavior’. *Journal of Neuroscience* 27, pp. 6460–6474.
- Kadir, S. N., D. F. M. Goodman and K. D. Harris (2014). ‘High-Dimensional Cluster Analysis with the Masked EM Algorithm’. *Neural Computation* 11, pp. 2379–2394.
- Kaschube, M. (2014). ‘Neural Maps Versus Salt-And-Pepper Organization in Visual Cortex’. *Current Opinion in Neurobiology* 1, pp. 95–102.
- Kass, R. E., V. Ventura and E. N. Brown (2005). ‘Statistical Issues in the Analysis of Neuronal Data.’ *Journal of Neurophysiology* 1, pp. 8–25.
- Keller, G. B., T. Bonhoeffer and M. Hübener (2012). ‘Sensorimotor Mismatch Signals in Primary Visual Cortex of the Behaving Mouse’. *Neuron* 5, pp. 809–815.
- Kenet, T., D. Bibitchkov, M. Tsodyks, A. Grinvald and A. Arieli (2003). ‘Spontaneously Emerging Cortical Representations of Visual Attributes’. *Nature* 6961, pp. 954–956.
- Kennerley, S. W. and M. E. Walton (2011). ‘Decision Making and Reward in Frontal Cortex: Complementary Evidence from Neurophysiological and Neuropsychological Studies.’ *Behavioral Neuroscience* 3, pp. 297–317.
- King, P. D., J. Zylberberg and M. R. DeWeese (2013). ‘Inhibitory Interneurons Decorrelate Excitatory Cells to Drive Sparse Code Formation in a Spiking Model of V1.’ *Journal of Neuroscience* 13, pp. 5475–85.
- Kipke, D. R., R. J. Vetter, J. C. Williams and J. F. Hetke (2003). ‘Silicon-Substrate Intracortical Microelectrode Arrays for Long-Term Recording of Neuronal Spike Activity in Cerebral Cortex’. *Electrical Engineering* 2, pp. 1–13.
- Kohn, A. (2007). ‘Visual Adaptation: Physiology, Mechanisms, and Functional Benefits’. *Journal of Neurophysiology*, pp. 3155–3164.
- Kohn, A. and J. A. Movshon (2003). ‘Neuronal Adaptation to Visual Motion in Area MT of the Macaque.’ *Neuron* 4.

- Kolb, B. et al. (2012). ‘Experience and the Developing Prefrontal Cortex.’ *Proceedings of the National Academy of Sciences*, pp. 17186–93.
- Kondo, S., T. Yoshida and K. Ohki (2016). ‘Mixed Functional Microarchitectures for Orientation Selectivity in the Mouse Primary Visual Cortex.’ *Nature Communications*, p. 13210.
- Köster, U. and B. A. Olshausen (2013). ‘Testing Our Conceptual Understanding of V1 Function’. *arXiv*.
- Köster, U., J. Sohl-Dickstein, C. M. Gray and B. A. Olshausen (2014). ‘Modeling Higher-Order Correlations Within Cortical Microcolumns’. *PLoS Computational Biology* 7. Ed. by J. H. Macke.
- Koulakov, A. A. and D. B. Chklovskii (2002). ‘Direction of Motion Maps in the Visual Cortex: A Wire Length Minimization Approach’. *Neurocomputing*, pp. 489–494.
- Kozai, T. D. Y., K. Catt et al. (2014). ‘Mechanical Failure Modes of Chronically Implanted Planar Silicon-Based Neural Probes for Laminar Recording.’ *Biomaterials*, pp. 25–39.
- Kozai, T. D. Y., X. Li et al. (2014). ‘Effects of Caspase-1 Knockout on Chronic Neural Recording Quality and Longevity: Insight into Cellular and Molecular Mechanisms of the Reactive Tissue Response.’ *Biomaterials* 36, pp. 9620–34.
- Kralik, J. D. et al. (2001). ‘Techniques for Long-Term Multisite Neuronal Ensemble Recordings in Behaving Animals.’ *Methods (San Diego, Calif.)* 2, pp. 121–150.
- Kraskov, A., H. Stögbauer and P. Grassberger (2004). ‘Estimating Mutual Information’. *Physical Review E* 6, p. 066138.
- Kullback, S. and R. A. Leibler (1951). ‘on Information and Sufficiency’. *The Annals of Mathematical Statistics* 1, pp. 79–86.
- Land, R., G. Engler, A. Kral and A. K. Engel (2013). ‘Response Properties of Local Field Potentials and Multiunit Activity in the Mouse Visual Cortex’. *Neuroscience*, pp. 141–151.
- LeCun, Y., S. Chopra, R. Hadsell, M. Ranzato and F. J. Huang (2006). ‘A Tutorial on Energy-Based Learning’. *Predicting Structured Data*, pp. 191–246.
- Lee, C. R. and D. J. Margolis (2016). ‘Pupil Dynamics Reflect Behavioral Choice and Learning in a Go/NoGo Tactile Decision-Making Task in Mice’. *Frontiers in Behavioral Neuroscience*, pp. 1–14.
- Lee, S.-H. et al. (2012). ‘Activation of Specific Interneurons Improves V1 Feature Selectivity and Visual Perception.’ *Nature* 7411, pp. 379–83.

- Lin, J. (1991). ‘Divergence Measures Based on the Shannon Entropy’. *IEEE Transactions on Information Theory* 1, pp. 145–151.
- Loaiza-Ganem, G., Y. Gao and J. P. Cunningham (2017). ‘Maximum Entropy Flow Networks’. *arXiv*, pp. 1–13.
- Luczak, A., P. Barthó and K. D. Harris (2009). ‘Spontaneous Events Outline the Realm of Possible Sensory Responses in Neocortical Populations.’ *Neuron* 3, pp. 413–25.
- Luczak, A., P. Barthó and K. D. Harris (2013). ‘Gating of Sensory Input by Spontaneous Cortical Activity’. *Journal of Neuroscience* 4, pp. 1684–95.
- Luczak, A., B. L. McNaughton and K. D. Harris (2015). ‘Packet-Based Communication in the Cortex’. *Nature reviews. Neuroscience* 12, pp. 745–755.
- Lynch, G. S., T. Dunwiddie and V. Gribkoff (1977). ‘Heterosynaptic Depression: A Postsynaptic Correlate of Long-Term Potentiation.’ *Nature* 5604, pp. 737–739.
- MacKay, D. M. and W. S. McCulloch (1952). ‘The Limiting Information Capacity of a Neuronal Link’. *The Bulletin of Mathematical Biophysics* 2, pp. 127–135.
- Macke, J. H., P. Berens, A. S. Ecker, A. S. Tolias and M. Bethge (2009). ‘Generating Spike Trains with Specified Correlation Coefficients’. *Neural Computation* 2, pp. 397–423.
- Makino, H. and T. Komiyama (2015). ‘Learning Enhances the Relative Impact of Top-down Processing in the Visual Cortex’. *Nature Neuroscience* 8, pp. 1116–1122.
- Mangini, N. J. and A. L. Pearlman (1980). ‘Laminar Distribution of Receptive Field Properties in the Primary Visual Cortex of the Mouse.’ *Journal of Comparative Neurology* 1, pp. 203–222.
- Martinez, L. M. et al. (2005). ‘Receptive Field Structure Varies with Layer in the Primary Visual Cortex’. *Nature Neuroscience* 3, pp. 372–379.
- Mazurek, M., M. Kager and S. D. Van Hooser (2014). ‘Robust Quantification of Orientation Selectivity and Direction Selectivity’. *Frontiers in Neural Circuits*.
- Mazzucato, L., A. Fontanini and G. La Camera (2016). ‘Stimuli Reduce the Dimensionality of Cortical Activity’. *Frontiers in Systems Neuroscience*.
- Miller, J.-E. K., I. Ayzenshtat, L. Carrillo-Reid and R. Yuste (2014). ‘Visual Stimuli Recruit Intrinsically Generated Cortical Ensembles’. *Proceedings of the National Academy of Sciences* 38.
- Mineault, P. J., E. Tring, J. T. Trachtenberg and D. L. Ringach (2016). ‘Enhanced Spatial Resolution During Locomotion and Heightened Attention in Mouse Primary Visual Cortex.’ *Journal of Neuroscience* 24, pp. 6382–92.

- Moldakarimov, S., M. Bazhenov and T. J. Sejnowski (2014). ‘Top-down Inputs Enhance Orientation Selectivity in Neurons of the Primary Visual Cortex During Perceptual Learning.’ *PLoS Computational Biology* 8.
- Montijn, J. S., M. Vinck and C. M. A. Pennartz (2014). ‘Population Coding in Mouse Visual Cortex: Response Reliability and Dissociability of Stimulus Tuning and Noise Correlation’. *Frontiers in Computational Neuroscience*.
- Mountcastle, V. B. (1997). ‘The Columnar Organization of the Neocortex.’ *Brain*, pp. 701–22.
- Movellan, J. R. (2008). *A Minimum Velocity Approach to Learning*. URL: <http://mplab.ucsd.edu/wp-content/uploads/MinimumVelocity.pdf> (visited on 31/08/2017).
- Namoodiri, V. M. K., M. A. Huertas, K. J. Monk, H. Z. Shouval and M. G. H. Shuler (2015). ‘Visually Cued Action Timing in the Primary Visual Cortex’. *Neuron* 1, pp. 319–330.
- Neal, R. M. (2001). ‘Annealed Importance Sampling’. *Statistics and Computing* 2, pp. 125–139.
- Nelson, M. (2012). ‘Understanding and Applying Extracellular Recordings in Awake, Behaving Animals’. Doctoral dissertation. California Institute of Technology.
- Nemenman, I. (2011). ‘Coincidences and Estimation of Entropies of Random Variables with Large Cardinalities’. *Entropy* 12, pp. 2013–2023.
- Nemenman, I., W. Bialek and R. R. de Ruyter van Steveninck (2004). ‘Entropy and Information in Neural Spike Trains: Progress on the Sampling Problem’. *Physical Review E* 5, p. 056111.
- Nemenman, I., F. Shafee and W. Bialek (2002). ‘Entropy and Inference, Revisited’. *NIPS*, pp. 95–100.
- Niell, C. M. (2013). ‘Vision: More Than Expected in the Early Visual System’. *Current Biology* 16, R681–R684.
- Niell, C. M. and M. P. Stryker (2008). ‘Highly Selective Receptive Fields in Mouse Visual Cortex’. *Journal of Neuroscience* 30, pp. 7520–7536.
- Niell, C. M. and M. P. Stryker (2010). ‘Modulation of Visual Responses by Behavioral State in Mouse Visual Cortex.’ *Neuron* 4, pp. 472–9.
- Nielsen, F. (2010). ‘A Family of Statistical Symmetric Divergences Based on Jensen’s Inequality’. *arXiv*, p. 15.
- O’Donnell, C., J. T. Gonçalves, N. Whiteley, C. Portera-Cailliau and T. J. Sejnowski (2017). ‘The Population Tracking Model: A Simple, Scalable Statistical Model for Neural Population Data’. *Neural Computation* 1, pp. 50–93.

- Obien, M. E. J., K. Deligkaris, T. Bullmann, D. J. Bakkum and U. Frey (2015). ‘Revealing Neuronal Function Through Microelectrode Array Recordings’. *Frontiers in Neuroscience*.
- Ohki, K., S. Chung, Y. H. Ch’ng, P. Kara and R. C. Reid (2005). ‘Functional Imaging with Cellular Resolution Reveals Precise Micro-Architecture in Visual Cortex.’ *Nature* 7026, pp. 597–603.
- Okun, M., A. Lak, M. Carandini and K. D. Harris (2016). ‘Long Term Recordings with Immobile Silicon Probes in the Mouse Cortex’. *PLoS ONE* 3, pp. 1–17.
- Okun, M., N. A. Steinmetz et al. (2015). ‘Diverse Coupling of Neurons to Populations in Sensory Cortex’. *Nature* 7553, pp. 511–515.
- Okun, M., P. Yger and K. D. Harris (2013). ‘How (not) to Assess the Importance of Correlations for the Matching of Spontaneous and Evoked Activity’. *arXiv*, pp. 1–4.
- Okun, M., P. Yger, S. L. Marguet et al. (2012). ‘Population Rate Dynamics and Multineuron Firing Patterns in Sensory Cortex’. *Journal of Neuroscience* 48, pp. 17108–17119.
- Olsen, S. R., D. S. Bortone, H. Adesnik and M. Scanziani (2012). ‘Gain Control by Layer Six in Cortical Circuits of Vision’. *Nature* 7387, pp. 47–52.
- Olshausen, B. A. (2013). ‘20 Years of Learning About Vision: Questions Answered, Questions Unanswered, and Questions Not Yet Asked’. *20 Years of Computational Neuroscience*, pp. 243–270.
- Olshausen, B. A. and D. J. Field (2005). ‘How Close Are We to Understanding V1?’ *Neural Computation* 8, pp. 1665–99.
- Palmer, S. E., O. Marre, M. J. Berry II and W. Bialek (2015). ‘Predictive Information in a Sensory Population’. *Proceedings of the National Academy of Sciences* 22, pp. 6908–6913.
- Paninski, L. (2003). ‘Estimation of Entropy and Mutual Information’. *Neural Computation* 6, pp. 1191–1253.
- Panzeri, S. and S. R. Schultz (2001). ‘A Unified Approach to the Study of Temporal, Correlational, and Rate Coding’. *Neural Computation*, pp. 1311–1349.
- Panzeri, S., R. Senatore, M. A. Montemurro and R. S. Petersen (2007). ‘Correcting for the Sampling Bias Problem in Spike Train Information Measures’. *Journal of Neurophysiology* 3, pp. 1064–72.
- Park, I. M. (2014). *A Guide to Discrete Entropy Estimators*. URL: <https://memming.wordpress.com/2014/02/09/a-guide-to-discrete-entropy-estimators/> (visited on 06/04/2017).

- Park, I. M., E. W. Archer, K. Latimer and J. W. Pillow (2013). ‘Universal Models for Binary Spike Patterns Using Centered Dirichlet Processes’. *NIPS*, pp. 2463–2471.
- Patterson, C. A., S. C. Wissig and A. Kohn (2013). ‘Distinct Effects of Brief and Prolonged Adaptation on Orientation Tuning in Primary Visual Cortex.’ *Journal of Neuroscience* 2, pp. 532–43.
- Pearl, J. (2014). *Probabilistic Reasoning in Intelligent Systems: Networks of Plausible Inference*. English. San Mateo, Calif.: Morgan Kaufmann.
- Petersen, C. C. H. and S. Crochet (2013). ‘Synaptic Computation and Sensory Processing in Neocortical Layer 2/3.’ *Neuron* 1, pp. 28–48.
- Pillow, J. W. (2007). ‘Likelihood-Based Approaches to Modeling the Neural Code’. *Bayesian Brain: Probabilistic Approaches to Neural Coding*, pp. 53–70.
- Pillow, J. W. and M. C. Aoi (2017). ‘Is Population Activity More Than the Sum of Its Parts?’ *Nature Neuroscience* 9, pp. 1196–1198.
- Pillow, J. W. and P. E. Latham (2007). ‘Neural Characterization in Partially Observed Populations of Spiking Neurons.’ *NIPS*, pp. 1–8.
- Pinto, L. et al. (2013). ‘Fast Modulation of Visual Perception by Basal Forebrain Cholinergic Neurons.’ *Nature Neuroscience* 12, pp. 1857–63.
- Pola, G., S. R. Schultz, R. S. Petersen and S. Panzeri (2003). ‘A Practical Guide to Information Analysis of Spike- Trains’. *Neuroscience Databases*, pp. 137–152.
- Polack, P.-O. O., J. Friedman and P. Golshani (2013). ‘Cellular Mechanisms of Brain State-Dependent Gain Modulation in Visual Cortex’. *Nature Neuroscience* 9, pp. 1331–1339.
- Poort, J. et al. (2015). ‘Learning Enhances Sensory and Multiple Non- Sensory Representations in Primary Visual Cortex’. *Neuron* 6, pp. 1478–1490.
- Prusky, G. T., N. M. Alam, S. Beekman and R. M. Douglas (2004). ‘Rapid Quantification of Adult and Developing Mouse Spatial Vision Using a Virtual Optomotor System’. *Investigative Ophthalmology & Visual Science* 12, p. 4611.
- Prusky, G. T. and R. M. Douglas (2004). ‘Characterization of Mouse Cortical Spatial Vision’. *Vision Research*, pp. 3411–3418.
- Quian Quiroga, R. and S. Panzeri (2009). ‘Extracting Information from Neuronal Populations: Information Theory and Decoding Approaches.’ *Nature reviews. Neuroscience* 3, pp. 173–85.
- Raj, A. and C. H. Wiggins (2008). ‘A Non-Negative Expansion for Small Jensen-Shannon Divergences’. *arXiv* 3, p. 4.

- Rauss, K. and G. Pourtois (2013). ‘What Is Bottom-up and What Is Top-down in Predictive Coding?’ *Frontiers in Psychology*.
- Ré, M. A. and R. K. Azad (2014). ‘Generalization of Entropy Based Divergence Measures for Symbolic Sequence Analysis’. *PLoS ONE* 4, pp. 1–11.
- Reig, R., Y. Zerlaut, R. Vergara, A. Destexhe and M. V. Sanchez-Vives (2015). ‘Gain Modulation of Synaptic Inputs by Network State in Auditory Cortex in Vivo’. *Journal of Neuroscience* 6, pp. 2689–2702.
- Reimer, J. et al. (2014). ‘Pupil Fluctuations Track Fast Switching of Cortical States During Quiet Wakefulness’. *Neuron* 2, pp. 355–362.
- Renart, A. et al. (2010). ‘The Asynchronous State in Cortical Circuits.’ *Science* 5965, pp. 587–90.
- Rescorla, R. A. and A. R. Wagner (1972). ‘A Theory of Pavlovian Conditioning: Variations in the Effectiveness of Reinforcement and Nonreinforcement’. *Classical Conditioning II Current Research and Theory* 6, pp. 64–99.
- Rikhye, R. V. and M. Sur (2015). ‘Spatial Correlations in Natural Scenes Modulate Response Reliability in Mouse Visual Cortex’. *Journal of Neuroscience* 43, pp. 14661–14680.
- Ringach, D. L. (2004). ‘Mapping Receptive Fields in Primary Visual Cortex.’ *Journal of Physiology*, pp. 717–728.
- Ringach, D. L. et al. (2016). ‘Spatial Clustering of Tuning in Mouse Primary Visual Cortex.’ *Nature Communications*, p. 12270.
- Rodieck, R. W. (1965). ‘Quantitative Analysis of Cat Retinal Ganglion Cell Response to Visual Stimuli’. *Vision Research* 12, pp. 583–601.
- Romano, S. A. et al. (2015). ‘Spontaneous Neuronal Network Dynamics Reveal Circuit’s Functional Adaptations for Behavior’. *Neuron*, pp. 1070–1085.
- Rossant, C. et al. (2016). ‘Spike Sorting for Large, Dense Electrode Arrays’. *Nature Neuroscience* 4, pp. 634–641.
- Rothschild, G., I. Nelken and A. Mizrahi (2010). ‘Functional Organization and Population Dynamics in the Mouse Primary Auditory Cortex.’ *Nature Neuroscience* 3.
- Roudi, Y., E. Aurell and J. Hertz (2009). ‘Statistical Physics of Pairwise Probability Models.’ *Frontiers in Computational Neuroscience*.
- Saarinen, J. and D. M. Levi (1995). ‘Perceptual Learning in Vernier Acuity: What Is Learned?’ *Vision Research* 4, pp. 519–527.

- Sadeh, S. and S. Rotter (2015). ‘Orientation Selectivity in Inhibition-Dominated Networks of Spiking Neurons: Effect of Single Neuron Properties and Network Dynamics’. *PLoS Computational Biology* 1.
- Sadovsky, A. J. and J. N. MacLean (2014). ‘Mouse Visual Neocortex Supports Multiple Stereotyped Patterns of Microcircuit Activity’. *Journal of Neuroscience* 23, pp. 7769–7777.
- Sakata, S. and K. D. Harris (2009). ‘Laminar Structure of Spontaneous and Sensory-Evoked Population Activity in Auditory Cortex.’ *Neuron* 3, pp. 404–18.
- Salakhutdinov, R., A. Mnih and G. Hinton (2007). ‘Restricted Boltzmann Machines for Collaborative Filtering’. *ICML*, pp. 791–798.
- Salakhutdinov, R. and I. Murray (2008). ‘On the Quantitative Analysis of Deep Belief Networks’. *ICML*, pp. 872–879.
- Saleem, A. B., A. Ayaz, K. J. Jeffery, K. D. Harris and M. Carandini (2013). ‘Integration of Visual Motion and Locomotion in Mouse Visual Cortex’. *Nature Neuroscience* 12, pp. 1864–1869.
- Saleem, A. B., P. Chadderton, J. Apergis-Schoute, K. D. Harris and S. R. Schultz (2010). ‘Methods for Predicting Cortical UP and DOWN States from the Phase of Deep Layer Local Field Potentials.’ *Journal of Computational Neuroscience* 1-2, pp. 49–62.
- Salinas, E. and P. Thier (2000). ‘Gain Modulation: A Major Computational Principle of the Central Nervous System’. *Neuron*, pp. 15–21.
- Schaub, M. T. and S. R. Schultz (2012). ‘The Ising Decoder: Reading out the Activity of Large Neural Ensembles.’ *Journal of Computational Neuroscience* 1, pp. 101–18.
- Schmidt, M. (2005). *minFunc: Unconstrained Differentiable Multivariate Optimization in Matlab*. URL: <http://www.cs.ubc.ca/~schmidtm/Software/minFunc.html>.
- Schneidman, E. (2016). ‘Towards the Design Principles of Neural Population Codes’. *Current Opinion in Neurobiology*, pp. 133–140.
- Schneidman, E., M. J. Berry II, R. Segev and W. Bialek (2006). ‘Weak Pairwise Correlations Imply Strongly Correlated Network States in a Neural Population.’ *Nature* 7087, pp. 1007–12.
- Schölvinck, M. L., K. J. Friston and G. Rees (2012). ‘The Influence of Spontaneous Activity on Stimulus Processing in Primary Visual Cortex’. *NeuroImage* 3, pp. 2700–2708.

- Schölvinck, M. L., A. B. Saleem, A. Benucci, K. D. Harris and M. Carandini (2015). ‘Cortical State Determines Global Variability and Correlations in Visual Cortex.’ *Journal of Neuroscience* 1.
- Schuett, S., T. Bonhoeffer and M. Hübener (2002). ‘Mapping Retinotopic Structure in Mouse Visual Cortex with Optical Imaging.’ *Journal of Neuroscience* 15, pp. 6549–59.
- Schultz, W., P. Dayan and P. R. Montague (1997). ‘A Neural Substrate of Prediction and Reward’. *Science* 5306, pp. 1593–1599.
- Seiler, H. et al. (2009). ‘Maximum Entropy Decoding of Multivariate Neural Spike Trains’. *BMC Neuroscience*.
- Shannon, C. E. (1948). ‘A Mathematical Theory of Communication’. *The Bell System Technical Journal*.
- Shlens, J. (2007). ‘Notes on Kullback-Leibler Divergence and Likelihood Theory’. *Systems Neurobiology Laboratory, Salk Institute for Biological Studies*, pp. 1–4.
- Skinner, B. F. (1938). ‘The Behavior of Organisms: An Experimental Analysis’. *The Psychological Record*, p. 486.
- So, Y. T. and R. Shapley (1981). ‘Spatial Tuning of Cells in and Around Lateral Geniculate Nucleus of the Cat: X and Y Relay Cells and Perigeniculate Interneurons’. *Journal of Neurophysiology* 1, pp. 107–120.
- Sohl-Dickstein, J., P. B. Battaglino and M. R. DeWeese (2009). ‘Minimum Probability Flow Learning’. *arXiv*.
- Sohl-Dickstein, J., P. B. Battaglino and M. R. DeWeese (2011). ‘New Method for Parameter Estimation in Probabilistic Models: Minimum Probability Flow’. *Physical Review Letters* 22.
- Spicher, D. (2014). ‘Modeling Multi-Neuron Spike Trains with Energy-Based Models’. Master’s Thesis. Humboldt Universität zu Berlin, TU Berlin, University of Edinburgh.
- St. John-Saaltink, E., P. Kok, H. C. Lau and F. P. de Lange (2016). ‘Serial Dependence in Perceptual Decisions Is Reflected in Activity Patterns in Primary Visual Cortex’. *Journal of Neuroscience* 23, pp. 6186–6192.
- Stanislaw, H. and N. Todorov (1999). ‘Calculation of Signal Detection Theory Measures.’ *Behavior Research Methods, Instruments, & Computers* 1, pp. 137–149.
- Stark, E. and M. Abeles (2007). ‘Predicting Movement from Multiunit Activity’. *Journal of Neuroscience* 31, pp. 8387–8394.

- Sterratt, D. C., D. Lyngholm, D. J. Willshaw and I. D. Thompson (2013). ‘Standard Anatomical and Visual Space for the Mouse Retina: Computational Reconstruction and Transformation of Flattened Retinae with the Retistruct Package’. *PLoS Computational Biology* 2.
- Stevenson, I. H. and K. P. Körding (2011). ‘How Advances in Neural Recording Affect Data Analysis.’ *Nature Neuroscience* 2.
- Strong, S. P., R. Koberle, R. R. de Ruyter van Steveninck and W. Bialek (1998). ‘Entropy and Information in Neural Spike Trains’. *Physical Review Letters* 1, pp. 197–200.
- Stüttgen, M. C., C. Schwarz and F. Jäkel (2011). ‘Mapping Spikes to Sensations’. *Frontiers in Neuroscience*, pp. 1–17.
- Sun, W., Z. Tan, B. D. Mensh and N. Ji (2015). ‘Thalamus Provides Layer 4 of Primary Visual Cortex with Orientation- and Direction-Tuned Inputs’. *Nature Neuroscience* 2, pp. 308–315.
- Swindale, N. V. (1998). ‘Orientation Tuning Curves: Empirical Description and Estimation of Parameters.’ *Biological Cybernetics*, pp. 45–56.
- Swisher, J. D. et al. (2010). ‘Multiscale Pattern Analysis of Orientation-Selective Activity in the Primary Visual Cortex’. *Journal of Neuroscience* 1, pp. 325–330.
- Tan, A. Y. Y., B. D. Brown, B. Scholl, D. Mohanty and N. J. Priebe (2011). ‘Orientation Selectivity of Synaptic Input to Neurons in Mouse and Cat Primary Visual Cortex.’ *Journal of Neuroscience* 34, pp. 12339–50.
- Tan, A. Y. Y., Y. Chen, B. Scholl, E. Seidemann and N. J. Priebe (2014). ‘Sensory Stimulation Shifts Visual Cortex from Synchronous to Asynchronous States’. *Nature* 7499, pp. 226–229.
- Tang, J. (2015). ‘Characterization of Response Properties in the Mouse Lateral Geniculate Nucleus Jiaying Tang February 2015’. Doctoral dissertation. Imperial College London.
- Tkačik, G. and W. Bialek (2014). ‘Information Processing in Living Systems’. *Exploring Complexity Fall 2011/ Information Processing In LivingSystems*, pp. 1–21.
- Tkačik, G., O. Marre, D. Amodei et al. (2014). ‘Searching for Collective Behavior in a Large Network of Sensory Neurons’. *PLoS Computational Biology* 1. Ed. by O. Sporns.
- Tkačik, G., O. Marre, T. Mora et al. (2013). ‘The Simplest Maximum Entropy Model for Collective Behavior in a Neural Network’. *Journal of Statistical Mechanics: Theory and Experiment* 03, P03011.

- Tkačik, G., E. Schneidman and M. J. Berry II (2006). ‘Ising Models for Networks of Real Neurons’. *arXiv* 3, pp. 3–6.
- Tolkieln, M. and S. R. Schultz (2015). ‘Multi-Unit Activity Contains Information About Spatial Stimulus Structure in Mouse Primary Visual Cortex’. *Proceedings of the Annual International Conference of the IEEE Engineering in Medicine and Biology Society, EMBS*, pp. 3771–3774.
- Treves, A. and S. Panzeri (1995). ‘The Upward Bias in Measures of Information Derived from Limited Data Samples’. *Neural Computation* 2, pp. 399–407.
- Tse, P. U. and P. Cavanagh (2000). ‘Chinese and Americans See Opposite Apparent Motions in a Chinese Character.’ *Cognition* 3, B27–32.
- Tyrcha, J., Y. Roudi, M. Marsili and J. Hertz (2013). ‘The Effect of Nonstationarity on Models Inferred from Neural Data’. *Journal of Statistical Mechanics: Theory and Experiment* 03.
- Umino, Y., E. Solessio and R. B. Barlow (2008). ‘Speed, Spatial, and Temporal Tuning of Rod and Cone Vision in Mouse.’ *Journal of Neuroscience* 1, pp. 189–198.
- Victor, J. D. (2002). ‘Binless Strategies for Estimation of Information from Neural Data’. *Physical Review E* 5.
- Vinck, M., R. Batista-Brito, U. Knoblich and J. A. Cardin (2015). ‘Arousal and Locomotion Make Distinct Contributions to Cortical Activity Patterns and Visual Encoding’. *Neuron* 3, pp. 740–754.
- Võikar, V., A. Polus, E. Vasar and H. Rauvala (2005). ‘Long-Term Individual Housing in C57BL/6J and DBA/2 Mice: Assessment of Behavioral Consequences’. *Genes, Brain and Behavior* 4, pp. 240–252.
- Vreysen, S., B. Zhang, Y. M. Chino, L. Arckens and G. Van den Bergh (2012). ‘Dynamics of Spatial Frequency Tuning in Mouse Visual Cortex’. *Journal of Neurophysiology* 11, pp. 2937–2949.
- Vu, M. (2012). *Lecture 2 : Entropy and Mutual Information*. URL: http://www.info612.ece.mcgill.ca/lecture%7B%5C_%7D02.pdf (visited on 31/08/2017).
- Wallace, D. J. et al. (2013). ‘Rats Maintain an Overhead Binocular Field at the Expense of Constant Fusion’. *Nature* 7452, pp. 65–69.
- Wang, P. and D. Nikolić (2011). ‘An LCD Monitor with Sufficiently Precise Timing for Research in Vision’. *Front Hum Neurosci*.
- Welzl, H. and J. Bureš (1977). ‘Lick-Synchronized Breathing in Rats’. *Physiology and Behavior* 4, pp. 751–753.

- Wickelmaier, F. (2003). ‘An Introduction to MDS’. *Reports from the Sound Quality Research Unit, {...}*, p. 26.
- Williams, J. C., R. L. Rennaker and D. R. Kipke (1999). ‘Long-Term Neural Recording Characteristics of Wire Microelectrode Arrays Implanted in Cerebral Cortex’. *Brain Research Protocols* 3, pp. 303–313.
- Womelsdorf, T., C. A. Bosman and P. Fries (2013). ‘Selective Neuronal Synchronization and Attentional Stimulus Selection in Visual Cortex’. *New Visual Neurosciences*, pp. 1013–1030.
- Yilmaz, M. and M. Meister (2013). ‘Rapid Innate Defensive Responses of Mice to Looming Visual Stimuli’. *Current Biology* 20, pp. 2011–2015.
- Yuste, R. (2015). ‘From the Neuron Doctrine to Neural Networks’. *Nature reviews. Neuroscience* 8, pp. 487–497.
- Zagha, E., A. E. Casale, R. N. S. Sachdev, M. J. McGinley and D. A. McCormick (2013). ‘Motor Cortex Feedback Influences Sensory Processing by Modulating Network State.’ *Neuron* 3, pp. 567–78.
- Zhang, J. and L. Abbott (2000). ‘Gain Modulation of Recurrent Networks’. *Neurocomputing*, pp. 623–628.
- Zhang, K., I. Ginzburg, B. L. McNaughton and T. J. Sejnowski (1998). ‘Interpreting Neuronal Population Activity by Reconstruction: Unified Framework with Application to Hippocampal Place Cells.’ *Journal of Neurophysiology* 2, pp. 1017–44.
- Zhang, S. et al. (2014). ‘Selective Attention. Long-Range and Local Circuits for Top-down Modulation of Visual Cortex Processing’. *Science* 6197, pp. 660–665.
- Zhao, Y. and I. M. Park (2016). ‘Variational Latent Gaussian Process for Recovering Single-Trial Dynamics from Population Spike Trains’. *Neural Computation* 5, pp. 1293–1316.
- Zucker, R. S. and W. G. Regehr (2002). ‘Short-Term Synaptic Plasticity.’ *Annual Review of Physiology*, pp. 355–405.

Appendices

1 Statistical Tests

All statistical tests were evaluated at $\alpha = 0.05$, which was Bonferroni-corrected if multiple comparisons were performed.

- MWU was used for comparing two independent variables of non-normal, unsymmetric, independent groups.
- 1-sample median test or 1-sample sign test was used to test the hypothesis of one non-normally distributed population having zero median.
- Kolmogorov-Smirnov test and normal quantile-quantile-plots were used to test for normality.
- Symmetry about the median was assessed with the skewness of the difference between the two distributions and graphically via boxplots of the differences.
- Kruskal-Wallis was used to compare 2 or more non-normally distributed independent groups, where otherwise for normally distributed populations one-way Analysis of Variance (ANOVA) was used.
- Wilcoxon signed ranks was used for independent variables with 2 matched, dependent or paired groups, when the distributions are symmetric under the assumption that distributions are equal.
- 2-sample sign test was used for independent variables with 2 matched, dependent or paired groups, when the distributions were non-symmetric, only under the assumption that the median of differences is zero, without assuming the shapes of the distributions.
- ANCOVA was used to compare regression results, with MATLAB's function *aoctool.m*.
- Friedman test was used to test when Wilcoxon signed ranks would have been used for 2 pairs, only for more than 2 groups (dependent, matched, paired groups) the null hypothesis that the column effects are all the same against the alternative that they are not all the same.
- Rayleigh test was used to test for non-uniformity in circular variables, implemented by Philipp Berens for MATLAB's Circular Statistics Toolbox (Directional Statistics), (Berens 2009).

2 Supplementary figures of 2

2.1 Direction decoding performances of different decoders as a function of bin size and number of shanks

The different decoders varied in their performance for the direction and SF decoding tasks.

Inspecting Fig. 1 - Fig. 4, suggests the Naive Bayes (NB) decoder to be most successful in decoding stimulus direction. Most decoders (apart from Linear Discriminant Analysis (LDA) for the population FR features in Fig. 4) improved their classification rate when incorporating a larger number of shanks. This is particularly pronounced in Fig. 1 (A) and (G) for the Spatio-temporal Multi-Unit Activity (STMUA) feature, where four shanks achieve classification rates over 60%, while two shanks reach only around 40%.

Fig. 1 further reveals that Spike Count (SC) features offer the lowest correct prediction rates, which is similar across all decoders.

With the NB decoder, bin size does not appear to play an important role in decoding performance as is evident from the similar values across bin widths, for all feature types. This cannot be observed in the k-nearest neighbour (knn) classifier in Fig. 2, which reveals a weak tendency to perform better with increasing bin widths, particularly for STMUA features (A, D, G). The other features, SC and population FR, however, attain similar values across bin widths.

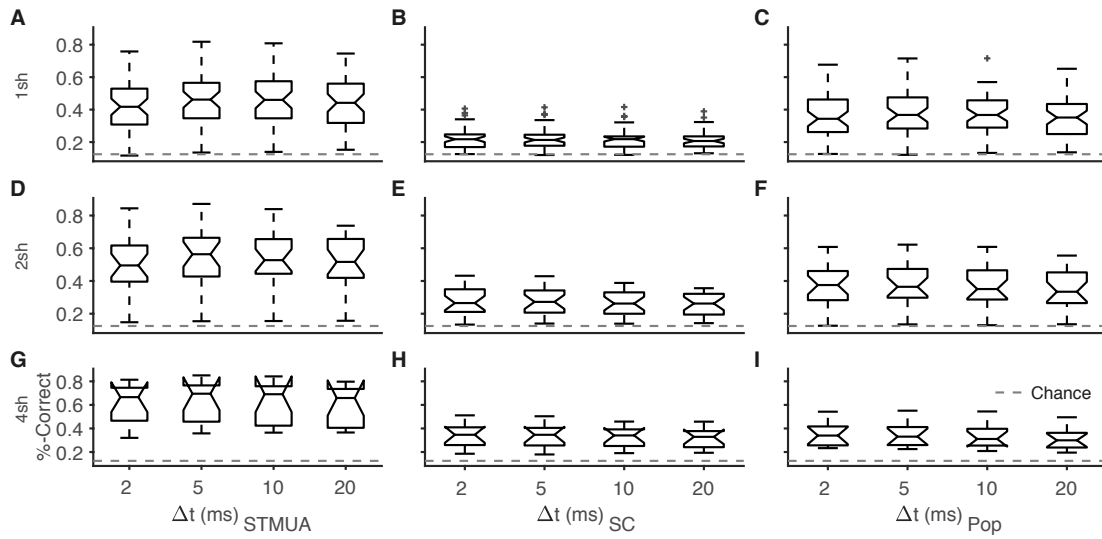


Figure 1: Direction decoding performance, NB classifier for varying numbers of shanks. (A, D, G) shows averaged classification rate for STMUA features, (B, E, H) for SC features, and (C, F, I) for population FR. (A, B, C) use one shank, (D, E, F) two shanks, and (G, H, I) four shanks. Chance level is indicated with a dashed line at 12.5%.

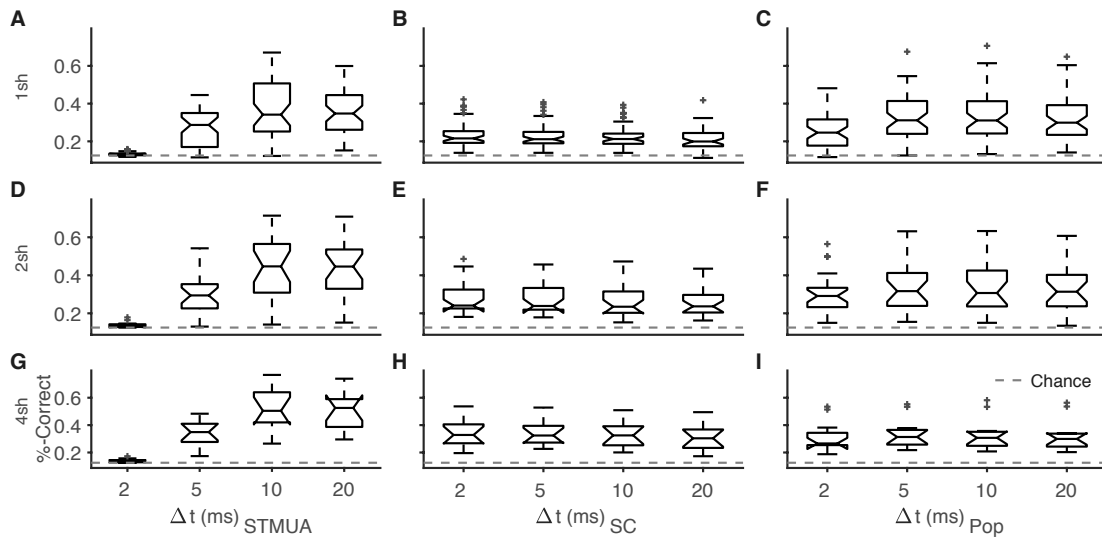


Figure 2: Direction decoding, knn classifier, description as in Fig. 1.

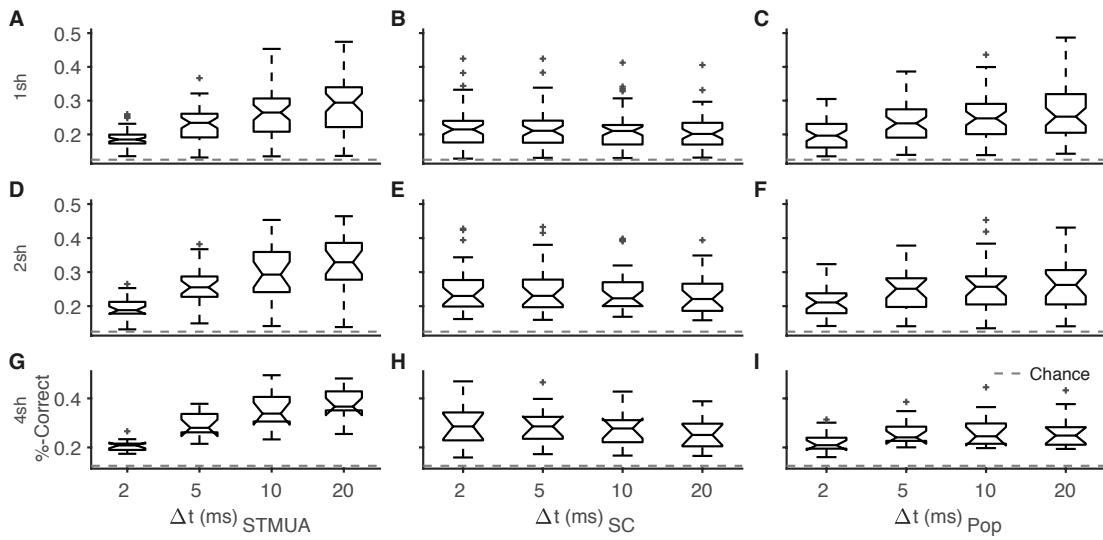


Figure 3: Direction decoding, classification tree classifier, description as in Fig. 1.

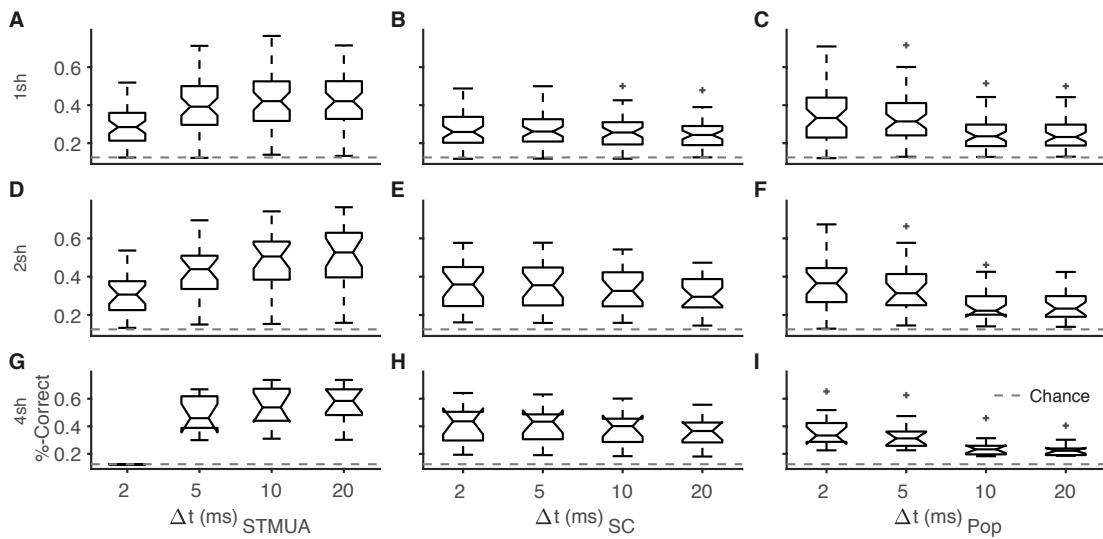


Figure 4: Direction decoding, LDA classifier, description as in Fig. 1.

2.2 Spatial frequency decoding performances of different decoders as a function of bin size and number of shanks

In overall terms, for SF decoding the NB also appears to be the most successful decoder as can be seen comparing Fig. 5 - 8. Having investigated Fig. 1 - Fig. 4, where we saw that SC features offered the lowest correct prediction rates, we can now appreciate the superiority of SC predictions over the other features, particularly for a high number of shanks, where classification rates exceed those of STMUA features (e.g. in Fig. 5 for NB classifier). The SC feature appears most unaffected by bin width with steadily high performances across decoders and bin widths.

The LDA decoder provides us with an interesting result, where STMUA features indicate an increase in classification rates with bin widths, whereas population FR features reveal the opposite effect, decreasing performance over bin widths, while SC features appear impervious to bin width changes.

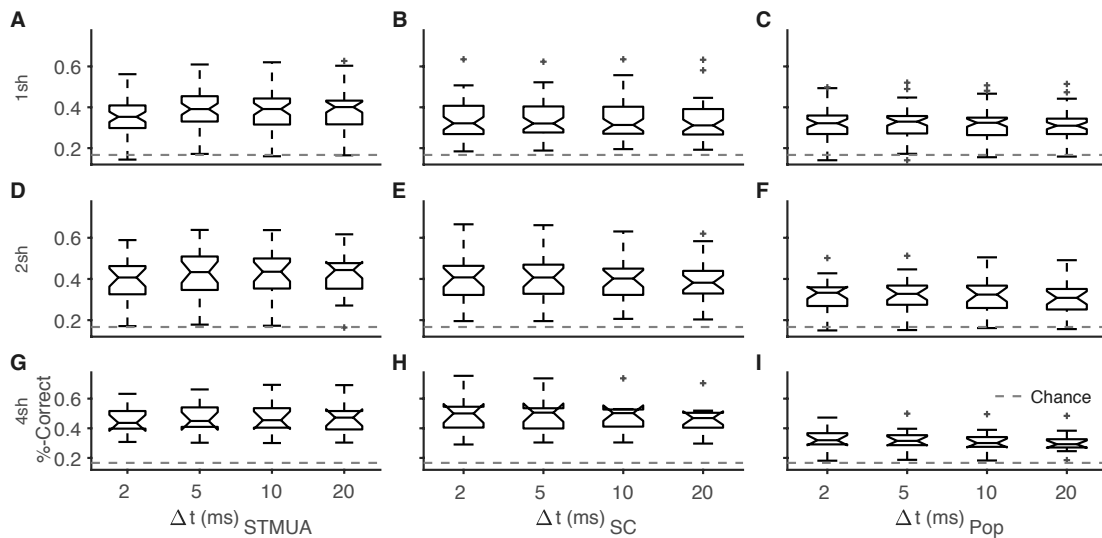


Figure 5: SF decoding performance, NB classifier for varying numbers of shanks. (A, D, G) shows averaged classification rates for STMUA features, (B, E, H) for SC features, and (C, F, I) for population FR. (A, B, C) use one shank, (D, E, F) two shanks, and (G, H, I) four shanks. Chance level is indicated with a dashed line at 16.6%.

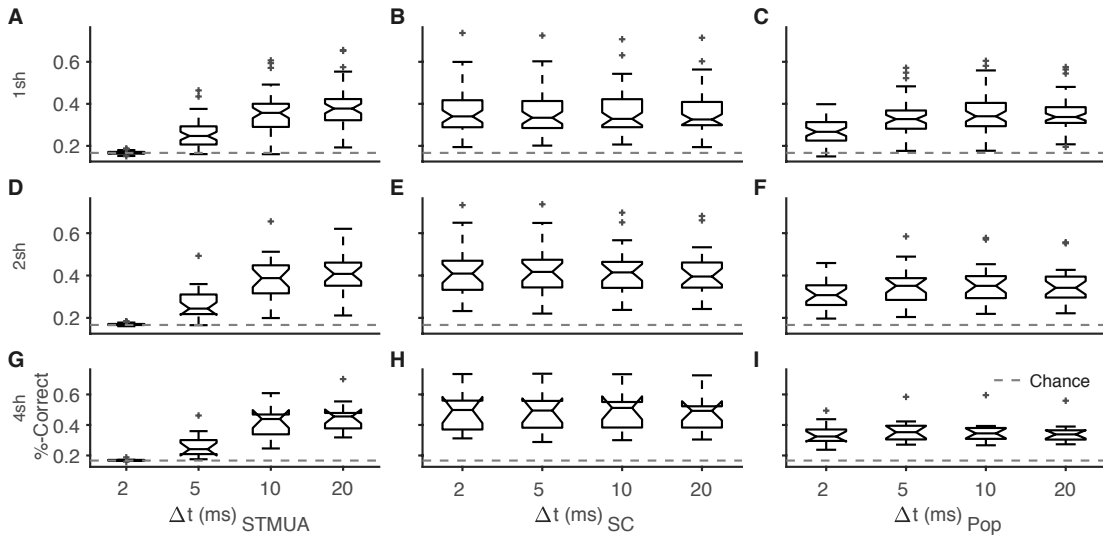


Figure 6: SF decoding, knn classifier, description as in Fig. 5.

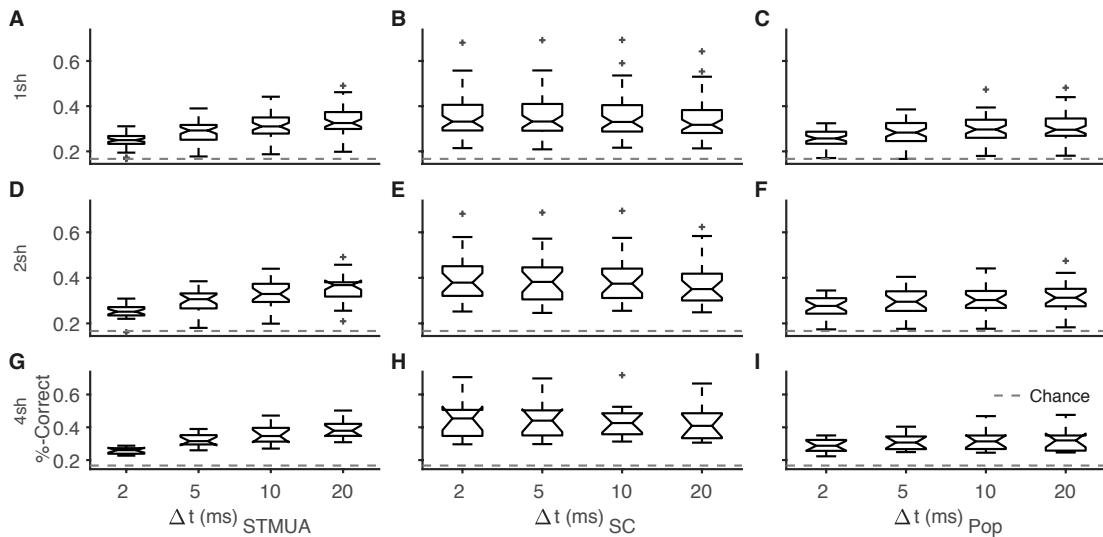


Figure 7: SF decoding, classification tree classifier, description as in Fig. 5.

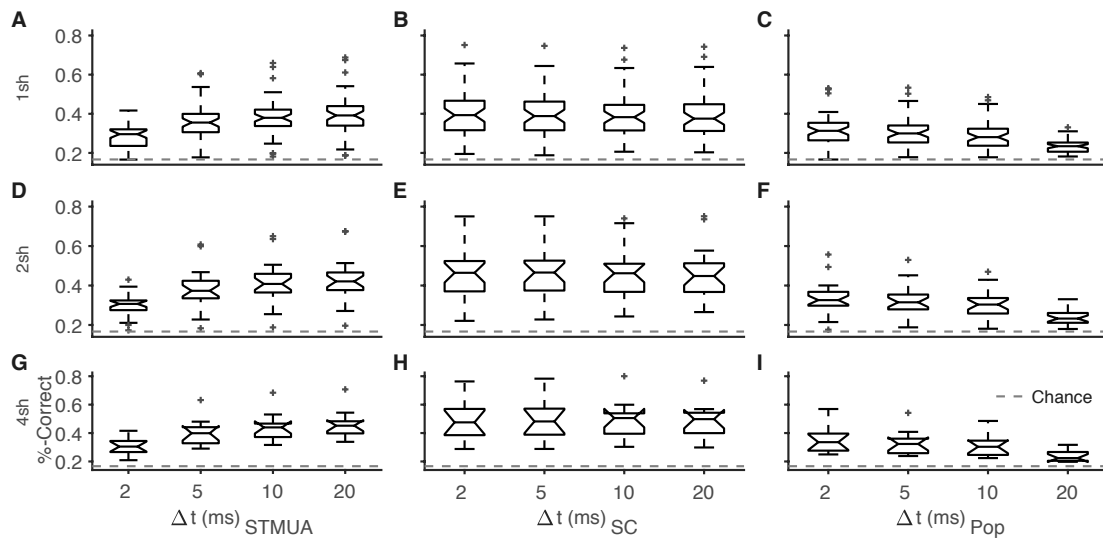


Figure 8: SF decoding, LDA classifier, description as in Fig. 5.

3 Supplementary figures of Chapter 3

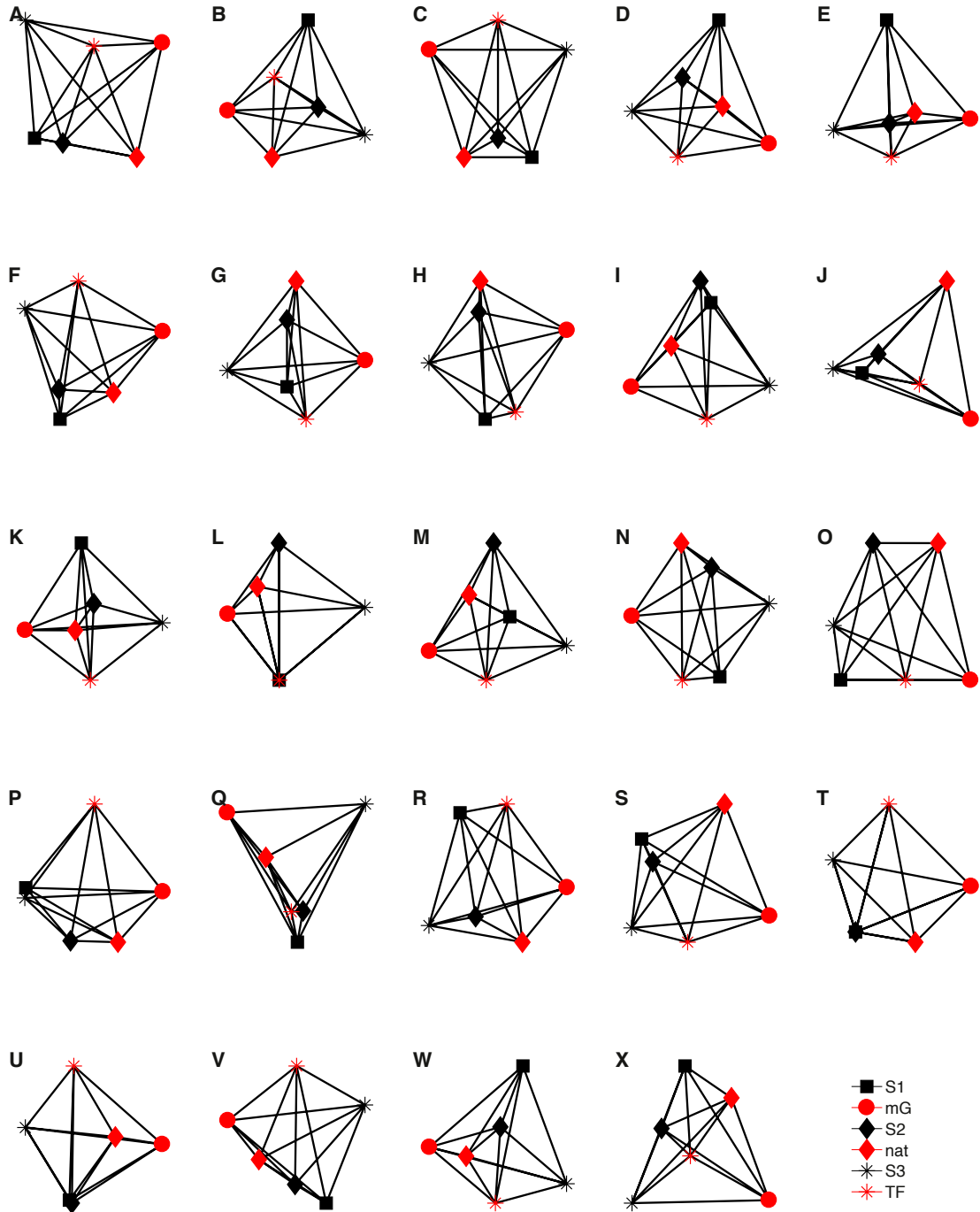


Figure 9: All MDS graphs of Chapter 3

Carprofen

Dilution for mice:		Prescribed Dose	You dilute this		Final Volume	Resulting Concentration	LOWER		UPPER	
1:100	Stock Solution [mg/ml]	[lower...upper] in [mg/kg]	Carprofen [ml]	Sterile Saline [ml]	[ml]	at hand in [mg/ml]	15	20	15	20
SC	50	5	0.2	19.8	20	0.5	0.15	0.2	0.15	0.2
	50	5	0.1	9.9	10	0.5	0.15	0.2		

Buprenorphine

Dilution for mice:		Prescribed Dose	You dilute this		Final Volume	Resulting Concentration	LOWER		UPPER	
1:10	Stock Solution [mg/ml]	[lower...upper] in [mg/kg]	Vetergesic [ml]	Sterile Saline [ml]	[ml]	at hand in [mg/ml]	15	20	15	20
SC	0.3	0.05	0.1	1	9	0.03	0.025	0.033	0.05	0.067
	0.3	0.05	0.1	0.5	4.5	0.03	0.025	0.033	0.05	0.067

Lidocaine

Dilution for mice:		Prescribed Dose	You dilute this		Final Volume	Resulting Concentration	LOWER		UPPER	
1:4 or 1:10	Stock Solution [mg/ml]	[lower...upper] in [mg/kg]	Lidocaine [ml]	Sterile Saline [ml]	[ml]	at hand in [mg/ml]	15	20	15	20
SC	20	2	5	15	20	5	0.006	0.008		
	100 mg/5ml	2								
	2g/100ml	2	1	9	10	2	0.015	0.02		

CBS direction, do not exceed 2mg/kg of total dose = 0.002mg/g. for a 20g mouse that's equal to 0.04mg, which is contained in 0.01ml of 0.5% lidocaine.

Enrofloxacin

Dilution for mice:		Prescribed Dose	You dilute this		Final Volume	Resulting Concentration	LOWER		UPPER	
1:10	Stock Solution [mg/ml]	[lower...upper] in [mg/kg]	Baytril [ml]	Sterile Saline [ml]	[ml]	at hand in [mg/ml]	15	20	15	20
SC	25	5	0.5	4.5	5	2.5	0.03	0.04	0.06	0.08
	25	5	0.1	0.9	1	2.5	0.03	0.04	0.06	0.08

Sulfamethoxazole/Trimethoprim

Dilution for mice:		Prescribed Dose	You dilute this		Final Volume	Resulting Concentration	LOWER		UPPER	
1:33 (3:100)	Stock Solution [mg/5ml]	[lower...upper] in [mg/kg]	Septin [ml]	Tap Water [ml]	[ml]	at hand in [mg/ml]	15	20	15	20
	40	95	7.5	250	257.5					
	200		(CBS recommendation)							

Drinking Water
Shake the bottle daily
Replace every 3 days

Fluid Requirements

per hour of surgery		Prescribed Dose (without extra losses)	LOWER		UPPER	
SC		10 [ml/kg/h]	15	20	15	20
			0.15	0.2	0.15	0.2

Volume of fluid = [surgical time (hours) x basic fluid rate (ml) x weight of mouse (kgs)] + [blood loss] + [volume of fluid mouse would normally intake over 3 hours]

LASA		Recommended maximum volumes of doses (SC)	20 [ml/kg]	Mouse Weight	
				15g	20g
				0.3	0.4

5 Copyright Permissions

Rightslink® by Copyright Clearance Center

10/09/2017, 17:57



Title: Multi-Unit Activity contains information about spatial stimulus structure in mouse primary visual cortex

Conference Proceedings: 2015 37th Annual International Conference of the IEEE Engineering in Medicine and Biology Society (EMBC)

Author: Marie Tolkiehn; Simon R. Schultz

Publisher: IEEE

Date: 25-29 Aug. 2015

Copyright © 2015, IEEE

LOGIN

If you're a **copyright.com** user, you can login to RightsLink using your copyright.com credentials. Already a **RightsLink** user or want to [learn more?](#)

Thesis / Dissertation Reuse

The IEEE does not require individuals working on a thesis to obtain a formal reuse license, however, you may print out this statement to be used as a permission grant:

Requirements to be followed when using any portion (e.g., figure, graph, table, or textual material) of an IEEE copyrighted paper in a thesis:

- 1) In the case of textual material (e.g., using short quotes or referring to the work within these papers) users must give full credit to the original source (author, paper, publication) followed by the IEEE copyright line © 2011 IEEE.
- 2) In the case of illustrations or tabular material, we require that the copyright line © [Year of original publication] IEEE appear prominently with each reprinted figure and/or table.
- 3) If a substantial portion of the original paper is to be used, and if you are not the senior author, also obtain the senior author's approval.

Requirements to be followed when using an entire IEEE copyrighted paper in a thesis:

- 1) The following IEEE copyright/ credit notice should be placed prominently in the references: © [year of original publication] IEEE. Reprinted, with permission, from [author names, paper title, IEEE publication title, and month/year of publication]
- 2) Only the accepted version of an IEEE copyrighted paper can be used when posting the paper or your thesis on-line.
- 3) In placing the thesis on the author's university website, please display the following message in a prominent place on the website: In reference to IEEE copyrighted material which is used with permission in this thesis, the IEEE does not endorse any of [university/educational entity's name goes here]'s products or services. Internal or personal use of this material is permitted. If interested in reprinting/republishing IEEE copyrighted material for advertising or promotional purposes or for creating new collective works for resale or redistribution, please go to http://www.ieee.org/publications_standards/publications/rights/rights_link.html to learn how to obtain a License from RightsLink.

If applicable, University Microfilms and/or ProQuest Library, or the Archives of Canada may supply single copies of the dissertation.



Copyright © 2017 Copyright Clearance Center, Inc. All Rights Reserved. [Privacy statement](#). [Terms and Conditions](#). Comments? We would like to hear from you. E-mail us at customer-care@copyright.com

**JOHN WILEY AND SONS LICENSE
TERMS AND CONDITIONS**

Sep 08, 2017

This Agreement between Miss. Marie Tolkiehn ("You") and John Wiley and Sons ("John Wiley and Sons") consists of your license details and the terms and conditions provided by John Wiley and Sons and Copyright Clearance Center.

License Number	4184261103686
License date	Sep 08, 2017
Licensed Content Publisher	John Wiley and Sons
Licensed Content Publication	Journal of Physiology
Licensed Content Title	Receptive fields and functional architecture of monkey striate cortex
Licensed Content Author	D. H. Hubel,T. N. Wiesel
Licensed Content Date	Mar 1, 1968
Licensed Content Pages	29
Type of use	Dissertation/Thesis
Requestor type	University/Academic
Format	Print and electronic
Portion	Figure/table
Number of figures/tables	1
Original Wiley figure/table number(s)	Text-fig. 2.
Will you be translating?	No
Title of your thesis / dissertation	Information-theoretic investigation of multi-unit activity properties under different stimulus conditions in mouse primary visual cortex
Expected completion date	Sep 2017
Expected size (number of pages)	200
Requestor Location	Miss. Marie Tolkiehn Department of Bioengineering Imperial College London South Kensington Campus London, London SW7 2AZ United Kingdom Attn: Miss. Marie Tolkiehn
Publisher Tax ID	EU826007151
Billing Type	Invoice
Billing Address	Miss. Marie Tolkiehn Department of Bioengineering Imperial College London South Kensington Campus London, United Kingdom SW7 2AZ Attn: Miss. Marie Tolkiehn

Total 0.00 GBP

[Terms and Conditions](#)

TERMS AND CONDITIONS

This copyrighted material is owned by or exclusively licensed to John Wiley & Sons, Inc. or one of its group companies (each a "Wiley Company") or handled on behalf of a society with which a Wiley Company has exclusive publishing rights in relation to a particular work (collectively "WILEY"). By clicking "accept" in connection with completing this licensing transaction, you agree that the following terms and conditions apply to this transaction (along with the billing and payment terms and conditions established by the Copyright Clearance Center Inc., ("CCC's Billing and Payment terms and conditions"), at the time that you opened your RightsLink account (these are available at any time at <http://myaccount.copyright.com>).

Terms and Conditions

- The materials you have requested permission to reproduce or reuse (the "Wiley Materials") are protected by copyright.
- You are hereby granted a personal, non-exclusive, non-sub licensable (on a stand-alone basis), non-transferable, worldwide, limited license to reproduce the Wiley Materials for the purpose specified in the licensing process. This license, **and any CONTENT (PDF or image file) purchased as part of your order**, is for a one-time use only and limited to any maximum distribution number specified in the license. The first instance of republication or reuse granted by this license must be completed within two years of the date of the grant of this license (although copies prepared before the end date may be distributed thereafter). The Wiley Materials shall not be used in any other manner or for any other purpose, beyond what is granted in the license. Permission is granted subject to an appropriate acknowledgement given to the author, title of the material/book/journal and the publisher. You shall also duplicate the copyright notice that appears in the Wiley publication in your use of the Wiley Material. Permission is also granted on the understanding that nowhere in the text is a previously published source acknowledged for all or part of this Wiley Material. Any third party content is expressly excluded from this permission.
- With respect to the Wiley Materials, all rights are reserved. Except as expressly granted by the terms of the license, no part of the Wiley Materials may be copied, modified, adapted (except for minor reformatting required by the new Publication), translated, reproduced, transferred or distributed, in any form or by any means, and no derivative works may be made based on the Wiley Materials without the prior permission of the respective copyright owner. **For STM Signatory Publishers clearing permission under the terms of the [STM Permissions Guidelines](#) only, the terms of the license are extended to include subsequent editions and for editions in other languages, provided such editions are for the work as a whole in situ and does not involve the separate exploitation of the permitted figures or extracts**, You may not alter, remove or suppress in any manner any copyright, trademark or other notices displayed by the Wiley Materials. You may not license, rent, sell, loan, lease, pledge, offer as security, transfer or assign the Wiley Materials on a stand-alone basis, or any of the rights granted to you hereunder to any other person.
- The Wiley Materials and all of the intellectual property rights therein shall at all times

remain the exclusive property of John Wiley & Sons Inc, the Wiley Companies, or their respective licensors, and your interest therein is only that of having possession of and the right to reproduce the Wiley Materials pursuant to Section 2 herein during the continuance of this Agreement. You agree that you own no right, title or interest in or to the Wiley Materials or any of the intellectual property rights therein. You shall have no rights hereunder other than the license as provided for above in Section 2. No right, license or interest to any trademark, trade name, service mark or other branding ("Marks") of WILEY or its licensors is granted hereunder, and you agree that you shall not assert any such right, license or interest with respect thereto

- NEITHER WILEY NOR ITS LICENSORS MAKES ANY WARRANTY OR REPRESENTATION OF ANY KIND TO YOU OR ANY THIRD PARTY, EXPRESS, IMPLIED OR STATUTORY, WITH RESPECT TO THE MATERIALS OR THE ACCURACY OF ANY INFORMATION CONTAINED IN THE MATERIALS, INCLUDING, WITHOUT LIMITATION, ANY IMPLIED WARRANTY OF MERCHANTABILITY, ACCURACY, SATISFACTORY QUALITY, FITNESS FOR A PARTICULAR PURPOSE, USABILITY, INTEGRATION OR NON-INFRINGEMENT AND ALL SUCH WARRANTIES ARE HEREBY EXCLUDED BY WILEY AND ITS LICENSORS AND WAIVED BY YOU.
- WILEY shall have the right to terminate this Agreement immediately upon breach of this Agreement by you.
- You shall indemnify, defend and hold harmless WILEY, its Licensors and their respective directors, officers, agents and employees, from and against any actual or threatened claims, demands, causes of action or proceedings arising from any breach of this Agreement by you.
- IN NO EVENT SHALL WILEY OR ITS LICENSORS BE LIABLE TO YOU OR ANY OTHER PARTY OR ANY OTHER PERSON OR ENTITY FOR ANY SPECIAL, CONSEQUENTIAL, INCIDENTAL, INDIRECT, EXEMPLARY OR PUNITIVE DAMAGES, HOWEVER CAUSED, ARISING OUT OF OR IN CONNECTION WITH THE DOWNLOADING, PROVISIONING, VIEWING OR USE OF THE MATERIALS REGARDLESS OF THE FORM OF ACTION, WHETHER FOR BREACH OF CONTRACT, BREACH OF WARRANTY, TORT, NEGLIGENCE, INFRINGEMENT OR OTHERWISE (INCLUDING, WITHOUT LIMITATION, DAMAGES BASED ON LOSS OF PROFITS, DATA, FILES, USE, BUSINESS OPPORTUNITY OR CLAIMS OF THIRD PARTIES), AND WHETHER OR NOT THE PARTY HAS BEEN ADVISED OF THE POSSIBILITY OF SUCH DAMAGES. THIS LIMITATION SHALL APPLY NOTWITHSTANDING ANY FAILURE OF ESSENTIAL PURPOSE OF ANY LIMITED REMEDY PROVIDED HEREIN.
- Should any provision of this Agreement be held by a court of competent jurisdiction to be illegal, invalid, or unenforceable, that provision shall be deemed amended to achieve as nearly as possible the same economic effect as the original provision, and the legality, validity and enforceability of the remaining provisions of this Agreement shall not be affected or impaired thereby.

- The failure of either party to enforce any term or condition of this Agreement shall not constitute a waiver of either party's right to enforce each and every term and condition of this Agreement. No breach under this agreement shall be deemed waived or excused by either party unless such waiver or consent is in writing signed by the party granting such waiver or consent. The waiver by or consent of a party to a breach of any provision of this Agreement shall not operate or be construed as a waiver of or consent to any other or subsequent breach by such other party.
- This Agreement may not be assigned (including by operation of law or otherwise) by you without WILEY's prior written consent.
- Any fee required for this permission shall be non-refundable after thirty (30) days from receipt by the CCC.
- These terms and conditions together with CCC's Billing and Payment terms and conditions (which are incorporated herein) form the entire agreement between you and WILEY concerning this licensing transaction and (in the absence of fraud) supersedes all prior agreements and representations of the parties, oral or written. This Agreement may not be amended except in writing signed by both parties. This Agreement shall be binding upon and inure to the benefit of the parties' successors, legal representatives, and authorized assigns.
- In the event of any conflict between your obligations established by these terms and conditions and those established by CCC's Billing and Payment terms and conditions, these terms and conditions shall prevail.
- WILEY expressly reserves all rights not specifically granted in the combination of (i) the license details provided by you and accepted in the course of this licensing transaction, (ii) these terms and conditions and (iii) CCC's Billing and Payment terms and conditions.
- This Agreement will be void if the Type of Use, Format, Circulation, or Requestor Type was misrepresented during the licensing process.
- This Agreement shall be governed by and construed in accordance with the laws of the State of New York, USA, without regards to such state's conflict of law rules. Any legal action, suit or proceeding arising out of or relating to these Terms and Conditions or the breach thereof shall be instituted in a court of competent jurisdiction in New York County in the State of New York in the United States of America and each party hereby consents and submits to the personal jurisdiction of such court, waives any objection to venue in such court and consents to service of process by registered or certified mail, return receipt requested, at the last known address of such party.

WILEY OPEN ACCESS TERMS AND CONDITIONS

Wiley Publishes Open Access Articles in fully Open Access Journals and in Subscription journals offering Online Open. Although most of the fully Open Access journals publish open access articles under the terms of the Creative Commons Attribution (CC BY) License only, the subscription journals and a few of the Open Access Journals offer a choice of Creative Commons Licenses. The license type is clearly identified on the article.

The Creative Commons Attribution License

The [Creative Commons Attribution License \(CC-BY\)](#) allows users to copy, distribute and transmit an article, adapt the article and make commercial use of the article. The CC-BY license permits commercial and non-

Creative Commons Attribution Non-Commercial License

The [Creative Commons Attribution Non-Commercial \(CC-BY-NC\)License](#) permits use, distribution and reproduction in any medium, provided the original work is properly cited and is not used for commercial purposes.(see below)

Creative Commons Attribution-Non-Commercial-NoDerivs License

The [Creative Commons Attribution Non-Commercial-NoDerivs License](#) (CC-BY-NC-ND) permits use, distribution and reproduction in any medium, provided the original work is properly cited, is not used for commercial purposes and no modifications or adaptations are made. (see below)

Use by commercial "for-profit" organizations

Use of Wiley Open Access articles for commercial, promotional, or marketing purposes requires further explicit permission from Wiley and will be subject to a fee.

Further details can be found on Wiley Online Library

<http://olabout.wiley.com/WileyCDA/Section/id-410895.html>

Other Terms and Conditions:

v1.10 Last updated September 2015

Questions? customercare@copyright.com or +1-855-239-3415 (toll free in the US) or +1-978-646-2777.

NATURE PUBLISHING GROUP LICENSE TERMS AND CONDITIONS

Sep 08, 2017

This Agreement between Miss. Marie Tolkiehn ("You") and Nature Publishing Group ("Nature Publishing Group") consists of your license details and the terms and conditions provided by Nature Publishing Group and Copyright Clearance Center.

License Number	4184260423428
License date	Sep 08, 2017
Licensed Content Publisher	Nature Publishing Group
Licensed Content Publication	Nature
Licensed Content Title	Cortical connectivity and sensory coding
Licensed Content Author	Kenneth D. Harris, Thomas D. Mrsic-Flogel
Licensed Content Date	Nov 6, 2013
Licensed Content Volume	503
Licensed Content Issue	7474
Type of Use	reuse in a dissertation / thesis
Requestor type	academic/educational
Format	print and electronic
Portion	figures/tables/illustrations
Number of figures/tables/illustrations	1
High-res required	no
Figures	Figure 3 Proposed relationship between feature mapping and coding in rodent visual cortex, cat visual cortex and rodent auditory cortex
Author of this NPG article	no
Your reference number	
Title of your thesis / dissertation	Information-theoretic investigation of multi-unit activity properties under different stimulus conditions in mouse primary visual cortex
Expected completion date	Sep 2017
Estimated size (number of pages)	200
Requestor Location	Miss. Marie Tolkiehn Department of Bioengineering Imperial College London South Kensington Campus London, London SW7 2AZ United Kingdom Attn: Miss. Marie Tolkiehn
Billing Type	Invoice
Billing Address	Miss. Marie Tolkiehn

Department of Bioengineering
Imperial College London
South Kensington Campus
London, United Kingdom SW7 2AZ
Attn: Miss. Marie Tolkiehn

Total 0.00 GBP

Terms and Conditions

Terms and Conditions for Permissions

Nature Publishing Group hereby grants you a non-exclusive license to reproduce this material for this purpose, and for no other use, subject to the conditions below:

1. NPG warrants that it has, to the best of its knowledge, the rights to license reuse of this material. However, you should ensure that the material you are requesting is original to Nature Publishing Group and does not carry the copyright of another entity (as credited in the published version). If the credit line on any part of the material you have requested indicates that it was reprinted or adapted by NPG with permission from another source, then you should also seek permission from that source to reuse the material.
2. Permission granted free of charge for material in print is also usually granted for any electronic version of that work, provided that the material is incidental to the work as a whole and that the electronic version is essentially equivalent to, or substitutes for, the print version. Where print permission has been granted for a fee, separate permission must be obtained for any additional, electronic re-use (unless, as in the case of a full paper, this has already been accounted for during your initial request in the calculation of a print run). NB: In all cases, web-based use of full-text articles must be authorized separately through the 'Use on a Web Site' option when requesting permission.
3. Permission granted for a first edition does not apply to second and subsequent editions and for editions in other languages (except for signatories to the STM Permissions Guidelines, or where the first edition permission was granted for free).
4. Nature Publishing Group's permission must be acknowledged next to the figure, table or abstract in print. In electronic form, this acknowledgement must be visible at the same time as the figure/table/abstract, and must be hyperlinked to the journal's homepage.
5. The credit line should read:
Reprinted by permission from Macmillan Publishers Ltd: [JOURNAL NAME] (reference citation), copyright (year of publication)
For AOP papers, the credit line should read:
Reprinted by permission from Macmillan Publishers Ltd: [JOURNAL NAME], advance online publication, day month year (doi: 10.1038/sj.[JOURNAL ACRONYM].XXXXX)

Note: For republication from the *British Journal of Cancer*, the following credit lines apply.

Reprinted by permission from Macmillan Publishers Ltd on behalf of Cancer Research UK: [JOURNAL NAME] (reference citation), copyright (year of publication) For AOP papers, the credit line should read:
Reprinted by permission from Macmillan Publishers Ltd on behalf of Cancer Research UK: [JOURNAL NAME], advance online publication, day month year (doi: 10.1038/sj.[JOURNAL ACRONYM].XXXXX)

6. Adaptations of single figures do not require NPG approval. However, the adaptation should be credited as follows:

Adapted by permission from Macmillan Publishers Ltd: [JOURNAL NAME] (reference citation), copyright (year of publication)

Note: For adaptation from the *British Journal of Cancer*, the following credit line applies.

Adapted by permission from Macmillan Publishers Ltd on behalf of Cancer Research UK: [JOURNAL NAME] (reference citation), copyright (year of publication)

7. Translations of 401 words up to a whole article require NPG approval. Please visit <http://www.macmillanmedicalcommunications.com> for more information. Translations of up to a 400 words do not require NPG approval. The translation should be credited as follows:

Translated by permission from Macmillan Publishers Ltd: [JOURNAL NAME] (reference citation), copyright (year of publication).

Note: For translation from the *British Journal of Cancer*, the following credit line applies.

Translated by permission from Macmillan Publishers Ltd on behalf of Cancer Research UK: [JOURNAL NAME] (reference citation), copyright (year of publication)

We are certain that all parties will benefit from this agreement and wish you the best in the use of this material. Thank you.

Special Terms:

v1.1

Questions? customer-care@copyright.com or +1-855-239-3415 (toll free in the US) or +1-978-646-2777.
